

Integration of magnetic gravity compensation and spherical actuation for robotic applications

Citation for published version (APA):

van Ninhuijs, B. (2016). *Integration of magnetic gravity compensation and spherical actuation for robotic applications: a novel actuator concepts towards a smart arm-support system*. [Phd Thesis 1 (Research TU/e / Graduation TU/e), Electrical Engineering]. Technische Universiteit Eindhoven.

Document status and date:

Published: 06/06/2016

Document Version:

Publisher's PDF, also known as Version of Record (includes final page, issue and volume numbers)

Please check the document version of this publication:

- A submitted manuscript is the version of the article upon submission and before peer-review. There can be important differences between the submitted version and the official published version of record. People interested in the research are advised to contact the author for the final version of the publication, or visit the DOI to the publisher's website.
- The final author version and the galley proof are versions of the publication after peer review.
- The final published version features the final layout of the paper including the volume, issue and page numbers.

[Link to publication](#)

General rights

Copyright and moral rights for the publications made accessible in the public portal are retained by the authors and/or other copyright owners and it is a condition of accessing publications that users recognise and abide by the legal requirements associated with these rights.

- Users may download and print one copy of any publication from the public portal for the purpose of private study or research.
- You may not further distribute the material or use it for any profit-making activity or commercial gain
- You may freely distribute the URL identifying the publication in the public portal.

If the publication is distributed under the terms of Article 25fa of the Dutch Copyright Act, indicated by the "Taverne" license above, please follow below link for the End User Agreement:

www.tue.nl/taverne

Take down policy

If you believe that this document breaches copyright please contact us at:

openaccess@tue.nl

providing details and we will investigate your claim.

Integration of Magnetic Gravity Compensation and Spherical Actuation for Robotic Applications

A Novel Actuator Concept Towards a Smart Arm-Support System

PROEFSCHRIFT

ter verkrijging van de graad van doctor
aan de Technische Universiteit Eindhoven,
op gezag van de rector magnificus, prof.dr.ir. F.P.T. Baaijens,
voor een commissie aangewezen door het College voor Promoties
in het openbaar te verdedigen
op maandag 6 juni 2016 om 16.00 uur

door

Bob van Nindhuijs

geboren te Helden

Dit proefschrift is goedgekeurd door de promotoren en de samenstelling van de promotiecommissie is als volgt:

voorzitter:	prof.dr.ir. A.B. Smolders
promotor:	prof.dr. E.A. Lomonova MSc
copromotoren:	dr.ir. J.W. Jansen dr. B.L.J. Gysen MSc (Prodrive Technologies)
leden:	prof.dr.ir. S. Stramigioli (UT) dr. B. Dehez (UCL) prof.dr. K. Ito
adviseur:	prof.dr. C.V.C. Bouten

Het onderzoek dat in dit proefschrift wordt beschreven is uitgevoerd in overeenstemming met de TU/e Gedragscode Wetenschapsbeoefening

Aan mijn ouders



This research is part of the Pieken in de Delta program and is funded by Rijksdienst voor Ondernemend Nederland (RVO), an agency of the Dutch Ministry of Economical Affairs, and the provinces Noord-Brabant and Limburg, the Netherlands.

This research received funding from the Promobilia Foundation.

B. van Nindhuijs, *Integration of Magnetic Gravity Compensation and Spherical Actuation for Robotic Applications*, Eindhoven University of Technology, 2016

A catalogue record is available from the Eindhoven University of Technology Library.
ISBN: 978-90-386-4088-4

Copyright © 2016 by B. van Nindhuijs. All rights reserved.

Summary

Integration of Magnetic Gravity Compensation and Spherical Actuation for Robotic Applications

A Novel Actuator Concept Towards a Smart Arm-Support System

Mobile arm-support systems provide an aid during the activities of daily living to enhance the user's quality of life. With this robotic application the user's independence increases and, consequently, the demand for caretakers reduces. The goal of a smart arm-support system is to improve the user's independence by extending the functionality in mobile system. The arm-support systems found in the literature show that there is a balance between functionality and mobility. Functionality is defined as how many degrees of freedom of support can be provided, which of these degrees are actuated and whether gravity compensation is applied. The current devices use single-degree-of-freedom actuators to actuate each degree of freedom. Consequently, to mimic the shoulder joint at least three actuators are necessary. In addition, the applied constructions have a predefined sequence of axes and are often bulky and cumbersome. To avoid these issues, a novel spherical actuator topology is proposed. In this actuator, a passive magnetic gravity compensator is integrated to reduce the power dissipation. Therefore, the proposed design is more suitable for mobile applications in contrast to the spherical actuator topologies from the literature. This thesis presents the theoretical description, design, and experimental validation of a 'first in the world' spherical actuator with integrated gravity compensator.

The spherical actuator with integrated gravity compensator has a three dimensional design. Therefore, alternative computational methods to finite element analysis (FEA) are investigated to reduce the computation time. Two semi-analytical modeling methods are evaluated, namely spherical harmonic modeling and magnetic charge modeling. These methods are extended and applied in the spherical coordinate system. The harmonic model can include infinitely permeable boundaries and an uneven number of permanent magnets in a spherical array. The magnetic charge model obtains the magnetic flux density for each permanent magnet

segment separately. Therefore, this method can include more diverse permanent magnet arrays, whereas the harmonic model can only be applied for a closed spherical permanent magnet array. Furthermore, infinitely permeable boundaries are taken into account with the implementation of spherical imaging. A discrepancy of 4% between the semi-analytical models and finite element analysis has been achieved. Hence, with both models the magnetic flux density of spherical shaped permanent magnets and magnet arrays can be accurately predicted.

A spherical magnetic spring is researched to realize the integrated gravity compensator. The spherical shape supports the multi-degree-of-freedom motion necessary to mimic the shoulder joint. This spring is composed out of two concentric hemispherical permanent magnets. Different combinations of radial and parallel magnetization are investigated. The torque production of these combinations have been predicted with the magnetic charge model. For the applications of arm-support systems, a sinusoidal torque characteristic is required to compensate for the gravity force. The topology that complies with this characteristic combines a radial and parallel magnetization for the outer and inner hemispherical permanent magnet, respectively. For the concept of the spherical magnetic spring, a patent has been filed.

The spherical actuator requires an unconventional hemispherical design because of the integrated gravity compensator. This unique design complies with the requirements for the range of motion of the arm-support system. Only slotless topologies are considered because in case of sudden power failure a user may not be able to control the arm-support system. The changing pole pitch due to the spherical geometry requires a single-phase commutation algorithm to excite the coils. This algorithm applies a two-norm minimization of the torque constants which are obtained with the magnetic charge model. A comparison is made between multiple topologies based on their predicted power dissipation. The topology with the lowest power dissipation is integrated with the gravity compensator. In this integration, the back-iron behind the permanent magnet array has to be segmented to minimize the interaction between both devices.

The spherical actuator with integrated gravity compensator has been experimentally verified with measurements on a proof-of-principle. In this demonstrator, segmentation and scaling of the theoretical design are applied due to manufacturing limitations. The measurements on the separated gravity compensator show a 3.6% deviation with respect to FEA on the expected sinusoidal torque characteristic. The torque measurements of the spherical actuator have an rms error of 7% and 11% with the FEA and the analytical model, respectively. The commutation of the coils to create a torque about one axis have a rms discrepancy within 9% over the complete range of motion. The integrated device has a cross-coupling of 0.6% and 0.7% with respect to the separated gravity compensator and spherical actuator respectively.

Contents

List of symbols	xi
1 Introduction	1
1.1 Background	1
1.2 Research goals and objectives	3
1.3 Thesis outline	4
2 Overview of actuated arm-support systems and their applications	5
2.1 Introduction on arm-support systems	6
2.2 Actuated mobile arm-support requirements	7
2.2.1 Applications	7
2.2.2 Actuation principle	9
2.2.3 Compliant and back-drivable actuation	11
2.2.4 Actuator configuration	12
2.2.5 Specifications	17
2.2.6 Discussion of the literature research	22
2.3 Human shoulder joint specification	22
2.3.1 Movement definitions	22
2.3.2 Properties of the human arm	24
2.3.3 Torque analysis	26
2.3.4 Range of motion	29
2.4 Actuator design consideration	29
2.5 Conclusions	30
3 Modeling of spherical magnetic structures	33
3.1 Introduction on spherical modeling	34
3.2 Electromagnetic modeling	35
3.3 Torque calculations	36
3.3.1 Lorentz force	37
3.3.2 Maxwell stress tensor	38
3.4 Charge modeling	40

3.4.1	General solution	40
3.4.2	Parallel magnetization	42
3.4.3	Radial magnetization	45
3.5	Imaging	46
3.6	Harmonic modeling	48
3.6.1	General solution	49
3.6.2	Boundary conditions	50
3.6.3	Magnetization description	50
3.6.4	Parallel magnetization	51
3.7	Benchmark topology	54
3.7.1	Parallel magnetization	55
3.7.2	Radial magnetization	56
3.8	Comparison	57
3.8.1	Parallel magnetization	57
3.8.2	Radial magnetization	62
3.9	Conclusions	64
4	Spherical magnetic gravity compensator	69
4.1	Passive compensation	70
4.2	Specifications	71
4.3	Spherical magnetic spring design	72
4.4	Magnetic gravity compensator design	78
4.4.1	Optimization of the geometry	78
4.4.2	Force analysis	80
4.4.3	Demagnetization	81
4.5	Manufacturability	84
4.6	Conclusions	85
5	Integrated design of a spherical actuator	87
5.1	System topology and specifications	88
5.1.1	Spherical actuation	88
5.1.2	User scenarios	90
5.1.3	Mechanics	90
5.1.4	Specifications	91
5.2	Analysis method	92
5.2.1	Flux density	92
5.2.2	Commutation algorithm	94
5.2.3	Optimization strategy	97
5.3	Topology optimization	97
5.3.1	Permanent magnet arrays	97
5.3.2	Coil arrays	98
5.3.3	Power dissipation	99
5.4	Integration of the gravity compensator	107
5.5	Optimization of the geometry	115

5.6	Thermal analysis	117
5.7	Cogging torque	120
5.8	Final design	123
5.9	Conclusions	125
6	Realization and experimental verification	129
6.1	Prototype design	130
6.2	Test benches	130
6.3	Magnetic gravity compensator	131
6.3.1	Construction	131
6.3.2	Measurement results	139
6.4	Spherical actuator with gravity compensator	140
6.4.1	Spherical actuator measurement results	145
6.4.2	Integration	152
6.5	Conclusions	157
7	Conclusions and recommendations	159
7.1	Conclusions	160
7.2	Scientific contributions	164
7.3	Recommendations	165
A	Definition of the Spherical coordinate system	167
B	Spherical vector analysis	169
C	Definition of the Cylindrical coordinate system	171
	Bibliography	173
	Acknowledgements	187
	Curriculum Vitae	191

List of symbols

Symbol	Unit	Description	Page
\vec{B}	[T]	Magnetic flux density	35
B_r	[T]	Remanent magnetic flux density	55
C_w	[deg]	Coil gap width	100
\vec{D}	[C/m ²]	Electrical flux density	35
\vec{E}	[V/m]	Electrical field strength	35
\vec{F}	[N]	Force	36
\vec{f}	[Nm ⁻³]	Force density	37
F_g	[N]	Gravity force	28
F_{gs}	[N]	Gravity of the upper arm and forearm	26
g	[m/s ²]	Acceleration due to gravity	26
g_a	[m]	Airgap length	74
G_l	[deg]	Coil gap length	100
G_w	[deg]	Conductor bundle width	100
h	[W/m ² K]	Convection heat-transfer coefficient	118
\vec{H}	[A/m]	Magnetic field strength	35
h_b	[m]	Wall thickness	132
h_{bc}	[m]	Coil back-iron height	93
h_{bm}	[m]	Permanent magnet back-iron height	93
h_c	[m]	Coil height	93
h_d	[m]	Diameter of cylindrical magnets	132
h_m	[m]	Permanent magnet height	93
h_{mc}	[m]	Height of cylindrical magnets	132
j	[-]	Imaginary unit	49
k	[m]	Inversion circle radius	47
l_{egt}	[m]	Elbow grip length	26
l_{ua}	[m]	Length of the upper arm	26
\vec{M}	[A/m]	Magnetization	35
m	[-]	Harmonic number	49

\vec{M}_0	[A/m]	Remanent magnetization	35
m_{add}	[kg]	Mass of the additional mass	26
m_f	[kg]	Mass of the forearm	26
m_h	[kg]	Mass of the hand	26
m_{ua}	[kg]	Mass of the upper arm	26
n	[-]	Harmonic number	49
P_n^m	[-]	Associated Legendre function of the first kind	49
P_n	[-]	Legendre polynomial	49
P_ϕ	[-]	Total number of magnets in the ϕ -direction	55
p_ϕ	[-]	Magnet number in the ϕ -direction	55
P_θ	[-]	Total number of magnets in the θ -direction	55
p_θ	[-]	Magnet number in the θ -direction	55
P_x	[W]	Power dissipation for a torque about the x -axis	104
P_y	[W]	Power dissipation for a torque about the y -axis	104
P_z	[W]	Power dissipation for a torque about the z -axis	104
Q	[W]	Heat flow rate	118
q	[C]	Electric charge	37
\vec{r}_d	[m]	Displacement vector	36
R_x	[deg]	Rotation about the x -axis	94
R_y	[deg]	Rotation about the y -axis	94
R_z	[deg]	Rotation about the z -axis	94
R_{in}	[m]	Inner radius	54
R_{out}	[m]	Outer radius	54
R_s	[m]	Infinite permeable boundary radius	54
\vec{T}	[Nm]	Torque	36
T	[°C]	Temperature	118
$t_{ambient}$	[s]	Cool down time to ambient temperature	120
T_{con}	[Nm]	Continuous torque	91
T_d	[Nm]	Desired torque	94
T_p	[°C]	Peak temperature	120
T_{da}	[Nm]	Dynamic torque of the additional mass	28
T_{ds}	[Nm]	Dynamic torque of the human arm	28
T_{ga}	[Nm]	Torque due to the gravity of the additional mass	26
T_{sa}	[Nm]	Static torque of the additional mass	26
T_{ds}	[Nm]	Static torque of the human arm	26
T_{ss}	[Nm]	Total static torque	27
w_c	[deg]	Stator width	126
x, y, z	[m]	Cartesian coordinates	43

Symbol	Unit	Description	Page
α	[rad/s ²]	Angular acceleration	26
α_c	[deg]	Rotation angle of the elongated coil	100
β	[deg]	Flexion angle	23
γ	[deg]	Horizontal flexion	23
χ	[–]	Magnetic susceptibility	36
δ	[–]	Duty cycle	91
ϵ_{rms}	[–]	Rms error	58
ζ	[deg]	Angle	23
λ_ϕ	[deg]	Magnetization angle in the ϕ -direction	55
λ_θ	[deg]	Magnetization angle in the θ -direction	55
μ_0	[H/m]	Permeability of free space	36
μ_r	[–]	Relative permeability	36
φ	[A]	Magnetic scalar potential	36
ρ	[m]	Radius spherical coordinate system	168
ρ_c	[C/m ³]	Electric charge density	35
ρ_m	[A/m ²]	Magnetic volume charge density	41
σ_m	[A/m]	Magnetic surface charge density	41
τ_c	[deg]	Coil pitch	101
τ_m	[deg]	Pole pitch in the θ -direction and ϕ -direction	101
τ_ϕ	[deg]	Pole pitch in the ϕ -direction	57
τ_θ	[deg]	Pole pitch in the θ -direction	57
θ, ϕ	[deg]	Angles spherical coordinate system	168
\vec{v}	[m/s]	Velocity	37
ξ	[deg]	Permanent back-iron angle	113

Abbreviation	Explanation	Page
2D	Two-dimensional	56
3D	Three-dimensional	50
AAS	Ambulatory arm support	8
ADL	Activities of daily living	6
DC	Direct current	9
DoF	Degree of freedom	9
FEA	Finite element analysis	3
HSBA	Hydraulic bilateral-servo actuator	10
IAS	Industrial arm support	9
MEC	Magnetic equivalent circuit model	34
MJM	Multijet modeling	138
MR	Magnetorheological	11
pMA	Pneumatic muscle actuator	10
PM	Permanent magnet	34
RAS	Rehabilitation arm support	8
rHEA	Rotational hydroelastic actuator	10
ROM	Range of motion	8
SEA	Series elastic actuator	11

Chapter 1

Introduction

1.1 Background

A world without any robotic systems becomes evermore harder to imagine nowadays. Especially in industrial environments, such systems are widely applied. It started in the 1960s [29] when robots replaced the human operators in factories to carry out hazardous and harmful tasks. The market for robotics that automate industrial processes has been growing ever since. The major reason for this growth is the declining costs of such systems while the costs of human labor increases. Especially through the 1990s the robotic market grew fast. Furthermore, robots are not only getting cheaper, but robotic systems become better: more effective, faster, more accurate, and more flexible [20].

Parallel to the industrial robotic evolution, other types of robots made their entrance such as mobile robotics and walking robots in 1968, and humanoid robots in 1972 [29]. Another robotic technology idea, as presented in [19], is to create an exoskeleton that enhances the human capabilities or that can be used for telemanipulation. This idea was developed in 1965 and is intended to be used in military or industrial environments. Eventually, the first applications of an exoskeleton arm were proposed for telemanipulation [115].

One of the first upper extremities support system is the rancho electric arm [87] which uses exoskeleton technology and was developed in 1969. This arm-support system uses tongue-switches to control the actuators. In the period between 1969 and 2000 only a handful of comparable systems were developed. A review of arm-support systems published in 1995 [41] presents 20 prototypes. Today, there are tens of prototypes and several commercial devices [36, 71, 74, 108]. From the

overview of actuated arm-support systems as presented in [90] it can be found that 93% of the discussed prototypes have been developed after the year 2000.

In contrast to the widely employed industrial robotics, the application of automated rehabilitation in clinics is rare. In [107] three main reasons are given namely, robots lack the skills, robots are unsafe, and robots might replace the therapist. Therapists gain their skills through experience and guidance by expert mentors. Furthermore, an alert and perceptive therapist adjusts the ongoing therapy on the patient's state and progress. When robots would move the arm and are not intelligent enough to detect contra-indications, they could harm the patient. The fear for replacement comes from industrial robots that took the place of assembly workers in factories. In contrast to industrial robotics, rehabilitation robots are developed to provide an aid during therapy, not to replace the therapist. Hence, the patient can practise therapy on their own resulting in more therapy at less costs (i.e. partial automation).

Aside from the use in rehabilitation centres, arm-support systems are being developed to be used at home. In general, these systems have to be small and mobile because they are mounted on an (electric) wheelchair. Currently, arm-support systems that are used at home, provide gravity compensation using a mechanical spring. Some designs can adjust the tension with an electrical machine. There are currently no commercially available actuated mobile arm-support systems that can control more than one degree of freedom. A multi-degree-of-freedom arm-support can provide more support during activities of daily living. Hence, the level of independence increases and, consequently, the quality of life improves. To some extent such systems could also be used for rehabilitation through e.g. serious gaming [89]. Furthermore, such smart arm-support system can extend the time that an individual with, for example, a neuromuscular disorder is able to use its own arm before a robotic manipulator is necessary. Recent research shows that the functional deterioration in wheelchair-dependent boys with Duchenne Muscular Dystrophy could be delayed with assisted training [52].

To provide the necessary support during the activities of daily living, at least the shoulder and elbow joint of the human arm have to be mimicked by an arm-support system. The elbow joint has only one degree of freedom and can be assisted with an one-degree-of-freedom actuator. The shoulder joint has multiple degrees of freedom. Furthermore, this joint needs a support a longer arm length and higher mass than the elbow joint; hence, it requires a higher torque. Consequently, the largest challenge is to create a design of an actuated solution for the shoulder joint. Therefore, this thesis is focused on the design of a multi-degrees-of-freedom actuator.

1.2 Research goals and objectives

In robotic applications such as arm-support systems, there is always a trade off between the actuated degrees-of-freedom and the mobility of the robotic arm. When multiple joints are actuated, a separate actuator is usually used for every degree of freedom. In addition, arm-support systems need to compensate for a static load due to the weight of the human arm. Consequently, the multi-degrees-of-freedom joints result in large, cumbersome, and sometimes complex constructions that have a predefined sequence of rotation axes.

To reduce the power consumption and provide free robotic arm movement, an integrated design of a gravity compensator and an actuator with multi-degrees-of-freedom is proposed. An electromagnetic solution is considered which is capable of providing these requirements in a configuration such that the active and passive device does not influence each other's electromagnetic behavior.

This thesis is concerned with the research, three-dimensional modeling, analysis, design, and realization of a spherical actuator with integrated gravity compensator for the application in a smart arm-support system. The following objectives concerning this matter are identified and researched:

- **Investigation of the electromechanical specifications for an actuator to mimic a human shoulder joint.** A set of specifications is required to design a realistic spherical actuator with integrated gravity compensator. These specifications are obtained by combining a categorization of the reported actuated arm-support systems in the literature and an analysis of the shoulder joint.
- **Extension of fast semi-analytical magnetostatic field modeling techniques in the spherical coordinate system.** Research is performed on the application of semi-analytical modeling techniques in the spherical coordinate system. These techniques allow fast and comprehensive evaluations of multiple actuator and compensator topologies, in contrast to existing numerical techniques such as finite element analysis (FEA).
- **Research of topologies and designs of passive spherical magnetic springs.** Arm-support systems have large static loads due to the weight of the human arm. Therefore, passive compensation can significantly reduce the power consumption in an arm-support system. Such spherical gravity compensator should demonstrate a spring type behavior in one rotational direction while have zero stiffness in the other rotational directions.
- **Design of a spherical actuator in which the gravity compensator can be integrated.** It is a necessity to integrate a spherical actuator with the gravity compensator to actively control the arm-support system. This unique integrated design has to provide an extended range of motion to

mimic the shoulder joint movements during a basic set of activities of daily living. For that reason, an unconventional hemispherical actuator design has been optimized using the semi-analytical magnetostatic field modeling tools.

- **Experimental verification of a realized spherical actuator with integrated gravity compensator.** Realization of the integrated actuator demonstrates the working principle of the gravity compensator, the spherical actuator, and their integration. The cross coupling between the gravity compensator and spherical actuator is validated. Furthermore, the performance of the actuator is quantified through measurements.

1.3 Thesis outline

The thesis continues in **Chapter 2** with an overview of actuated arm-support systems. The aim of this chapter is to obtain a set of actuator specifications for an arm-support system. The retrieved information from the literature about the applied actuators is investigated and analysed. In addition, the performance of the human shoulder joint is evaluated to obtain the requirements for a basic set of activities of daily living.

In **Chapter 3**, Maxwell's equations are used to derive expressions that describe magnetostatic fields in spherical coordinates. These expressions are obtained with two different methods which result in a spherical harmonic model and a magnetic charge model. The discrepancies among the obtained models and FEA including the corresponding calculation time are compared.

Novel spherical magnetic spring topologies, based on only permanent magnets, are researched in **Chapter 4**. It is demonstrated that the spring behavior is determined by the magnetization pattern. The design that complies with the arm support specifications is optimized with respect to its volume. Subsequently, manufacturing issues are discussed.

Chapter 5 presents a design methodology for the spherical actuator with integrated gravity compensator. Two optimization procedures are performed. The first optimization routine determines the actuator topology with the lowest power dissipation. Multiple topologies for the hemispherical permanent magnet array, coils and coil arrays are investigated. For the second optimization procedure, a parametric search is performed on the geometry to achieve the smallest volume that complies with the thermal specifications.

In **Chapter 6**, a scaled prototype of the spherical actuator with integrated gravity compensator is realized. With this prototype, the working principle of the gravity compensator, spherical actuator and their integration are validated through measurements.

Finally, the conclusions and recommendations of the thesis are given in **Chapter 7**.

Chapter 2

Overview of actuated arm-support systems and their applications

Abstract - During the last decades a large diversity of actuated arm-support systems have been developed to provide support throughout daily tasks, during training or for persons in an industrial environment. The arm support systems found in the literature are categorized to obtain an overview of the actuator specifications. In addition, the human shoulder joint is analysed to determine the torque delivered during the activities of daily living. By comparing the shoulder joint properties with the categorization a set of requirements for a novel spherical actuator towards a smart arm support system is obtained.

This chapter is based on

- B. van Nindhuijs, L. A. van der Heide, J. W. Jansen, B. L. J. Gysen, D. J. van der Pijl, and E. A. Lomonova, "Overview of actuated arm support systems and their applications," *Actuators*, vol. 2, nr. 4, pp. 86-110, 2013.
- L. A. van der Heide, B. van Nindhuijs, A. Bergsma, G. J. Gelderblom, D. J. van der Pijl and L. P. de Witte, "An overview and categorization of dynamic arm supports for people with decreased arm function" *Prosthetics and Orthotics Int.*, vol. 38, nr. 4, pp. 287-302, 2013.

2.1 Introduction on arm-support systems

Arm-support systems are developed to complement the capabilities of the human arm. Assistive arm-support systems augment the arm functionalities of persons with upper extremity limitations. These systems are used during activities of daily living (ADL) [42, 46, 48] or for training and rehabilitation purposes [75, 99, 101]. Other arm-support systems enhance the human capabilities of healthy persons [9, 77, 128] or facilitate teleoperation and virtual reality [8, 27, 84].

Various overviews and reviews on arm-support systems with a different focus are presented in the literature. The majority of these overviews and reviews consider rehabilitation devices used for neurological lesions. A categorization of these devices is given by Loureiro et al. [74] on the mechanical construction and the supporting segments (i.e. shoulder, elbow, etc.). The clinical use is evaluated with respect to the mechanical degrees of freedom by Riener et al. [108]. Reinkensmeyer et al. [106] reviews the costs reduction by automating some aspects of therapeutic help. Van der Heide et al. [43] analyses the user functionality of arm-support systems designed for use at home. Reviews from a more technical perspective are also provided in the literature. The global development of exoskeletons is presented by Guizzo and Goldstein [36]. The progression of control strategies for rehabilitation devices is evaluated by Marchal-Crespo and Reinkensmeyer [76]. The mechanical requirements are classified for active upper limb exoskeletons on the supporting segments, degrees of freedom, actuation technology, power transmission method, and purpose of the robot by Gopura and Kiguchi [32]. An analysis of rehabilitation robots including the actuator technology, mechanical construction, and control is presented in [71]. A more general review of robotic systems is provided by van der Smagt et al. [118] on actuation principles, sensing methods, and control strategies.

In this chapter a technical overview is given with the focus on the specifications of the applied actuators in arm-support systems. The found arm-support systems in the literature are categorized on application, used actuation principle, and the actuator configuration. The actuator configuration depicts the position of the actuators with respect to the mechanical construction. For each application a subdivision is made on the actuation technology which is again subdivided by the actuation configuration. This categorization is illustrated in Fig. 2.1. Furthermore, the torque required by the human arm during activities of daily living is determined. The correlation between this torque and the actuator specifications found in the literature is investigated. In addition, other aspects of the actuators in arm-support systems are discussed in more detail such as compliance, bandwidth, backdrivability, and the degrees of freedom. More insight is gained in the operation of actuators in arm-support system with this analysis.

The literature study in this chapter has been performed with the Inspec database. The majority of the used data has been published in journals. The reported results,

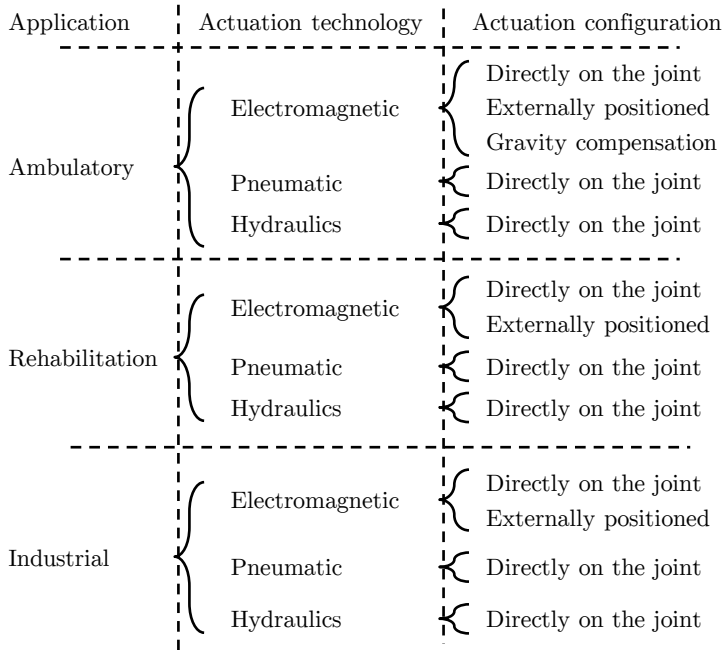


Figure 2.1: Proposed overview of the arm-support systems

facts, numbers, and recommendations have not been validated.

2.2 Actuated mobile arm-support requirements

2.2.1 Applications

The arm-support systems found in the literature can be categorized on their applications namely, ambulatory, rehabilitation, and industrial applications. These categories are in relation with the usage environment such as at home, rehabilitation center or in the workplace. The functionality necessary for these applications define the requirements of the arm-support system.

Ambulatory

Ambulatory arm-support (AAS) systems are intended for users with diminished arm functionality, due to e.g. neuromuscular disorders, to help during the activities of daily living. These activities consist of, for example, eating, drinking, using the computer or writing. Usually, a partial range of motion (ROM) of a healthy human body is covered to compensate for the muscle activity lost or to avoid muscle fatigue. For this category of arm-support systems, it can be desirable to be inconspicuous; hence, stigmatization can be avoided. Additionally, a certain movement characteristic can be required, such as following the arm movements naturally or providing a stable support. Flexibility and simple mounting, e.g. on a wheelchair, are often required. When mounted on an electric wheelchair, the energy consumption has to be small to avoid recharging of the wheelchair battery during the day. A typical example of this category is the Armon arm-support system [78]. This work shows the evolution of the arm-support design to provide support during activities of daily living. It is also suggested that AAS systems can be used for people who suffer from, for example, repetitive strain injury and muscle fatigue.

Rehabilitation

Rehabilitation arm-support (RAS) systems are developed to assess the human arm impairments [123] and to regain the arm functionality by training [101]. People who suffer from, e.g. the repercussions of a stroke or an accident benefit from these support systems. The research of Jansen et al. [52] shows that the progressive neuromuscular disorder Duchenne can be delayed with assisted training. A RAS design is proposed by Perry et al. [101] that can provide assistance during the therapeutic exercises over the range of motion required for the activities of daily living. Usually, RAS systems are situated in rehabilitation centers, and are designed to be stationary. However, some devices provide rehabilitation at home [3, 130, 135]. These systems have a small lightweight mechanical construction; hence, they are easy to carry, occupy a small volume, and have a low power consumption. For therapy sessions, it can be beneficial to store the progress for monitoring, which is used to evaluate the effectiveness of RAS systems by Riener et al. [108]. In general, stationary RAS systems have a larger volume, more complex mechanical structures, and more powerful actuators in comparison with mobile rehabilitation systems and AAS systems.

Industrial

Industrial arm-support (IAS) systems are intended to enhance the physical capabilities of healthy humans or to use them as master/slave devices. The designed IAS system of Martinez et al. [77] enhances the human capabilities to perform heavy physical work and to improve ergonomics. For such functionality, an additional energy supply is necessary. Master/slave devices are used to carry out procedures remotely (i.e. teleoperated) such as dismantling nuclear installations [25], or in virtual environments [8]. In the research of Frey et al. [27] it has been shown that haptics can provide the user a more realistic experience in this environment. In general, enhancing the human capabilities requires high torque, whereas the teleoperated and virtual environments only need to provide haptic feedback.

2.2.2 Actuation principle

In the literature, three actuation principles and one damping method can be distinguished: electromagnetic, pneumatic, hydraulic, and semi-active damping.

Electromagnetic actuators

Electromagnetic actuators convert electrical energy into mechanical motion. The majority of arm-support systems use electrical rotary motors which provide one-degree-of-freedom (DoF) rotary motion. Most of the applied electrical motors are permanent-magnet machines. From the permanent magnet motors, brushed DC motors [3, 33, 79, 83, 86, 87, 94, 95, 103] and brushless DC motors [31, 48, 60, 104, 110, 130] are selected the most.

Permanent magnet brushed DC motors are excited using brushes and a DC source such as the battery of an electric wheelchair. Brushless DC motors (without brushes) have more than one phase, in general three phases, that need excitation to produce a torque. For both machine topologies, a drive is required to control the mechanical motion. This drive is usually not taken into account in the power-to-weight calculations. The catalog [2] shows that for the electrical machine sizes used in the arm-support systems found in the literature, the brushed DC motors provide a higher efficiency, and higher torque than brushless motors.

High-speed and low-torque electrical motors have a smaller volume and are preferred over high-torque low-speed electrical motors to avoid large and cumbersome constructions and to lower the costs. The output speed can be reduced and the torque can be increased by using gears. Commonly, gear ratios of 100:1, 300:1 or even higher are selected. The disadvantage of such high gearing is their low efficiency. For example, the efficiency of standard Maxon gears [2] are equal to 70%

(100:1) to 50% (300:1 and higher). These values are obtained when the maximum continuous torque is applied to the gear.

Pneumatic actuators

Three different pneumatic actuators are applied in arm-support systems namely, pneumatic cylinders, McKibben muscles, and pneumatic muscle actuators (pMAs).

In pneumatic cylinders, pressurized air is injected which produces a force that moves the piston in the cylinder in a linear direction. Pneumatic cylinders can be double-acting (push and pull) or single-acting (push or pull). The McKibben muscle injects pressurized air into a pneumatic bladder. As a result, the bladder expands and the end parts contracts. This actuator is also referred to as an artificial muscle because it is similar to the human muscle. The McKibben muscle is only single-acting (pull). The pMA presented by Davis et al. [23] is an improvement of the McKibben muscle using enhanced modeling techniques and a novel construction. In [77] the modeling and control of a commercial pneumatic muscle required extra work due to its high non-linearity, in comparison with electrical DC machines.

The power-to-weight ratio of pneumatic actuators considering only the cylinder is high. However, the required compressor is not included in this ratio. The air can also be compressed externally and transported to the actuator. However, for mobile applications this can be very inconvenient, especially for AAS systems. Additionally, pneumatic actuators are often associated with noise which can be experienced as unpleasant.

Hydraulic actuators

From the applied actuator principles in arm-support systems, it is shown by Brown et al. [11] that hydraulic actuators have the highest power-to-weight ratio and positional stiffness. Similar to the pneumatic actuator, this ratio is determined without the hydraulic pump. In the literature, the following hydraulic actuation principles can be distinguished: hydraulic cylinders [67], a hydraulic bilateral-servo actuator (HBSA) [127], and a rotational hydroelastic actuator rHEA [122].

With a hydraulic pump, fluid is injected into a hydraulic cylinder and, similar to the pneumatic actuator, a force is generated to move the piston in a linear direction. Hydraulic cylinders can be constructed to be double-acting or single-acting. To increase the actuators force output and decrease the mass of the arm-support system a HBSA is proposed by Umemura et al. [127]. The HBSAs are very similar to the hydraulic cylinders, however, an electric motor is combined with a lead screw to pressurize the fluid. The motor is directly attached or placed

very close to the hydraulic cylinder. Therefore, this combination can be seen as one actuator. This actuator has low transmission losses because of the nearby placement of the compressor. If multiple HBSAs are incorporated, each HBSA requires its own electric motor, whereas multiple hydraulic cylinders require only one hydraulic pump. The rHEA is a rotational hydraulic actuator combined with a mechanical spring. Comparable with hydraulic cylinders, a rotational hydraulic actuator uses blades to produce a force that is converted to a rotational motion.

The risk of leakages in hydraulic actuators, even when carefully designed, is underlined by Brown et al. [11]. Therefore, a high level of maintenance is required.

Semi-active damping

Technically, semi-active dampers cannot be classified as an actuator since they provide a (speed-dependent) reaction force and not an active force. Semi-active dampers consist of a piston, and a fluid which viscosity can be adjusted using an electromagnetic field. One of the semi-active dampers used in arm-support systems is the magnetorheological (MR) damper. By using this damper as a clutch, it was found in [39] that a minimal reaction torque is present when no magnetic field is applied, and the reaction torque can be enlarged by increasing the magnetic field. The semi-active damper design proposed in [14] for arm-support systems to suppress tremors shows a reaction torque of 1.1 Nm.

2.2.3 Compliant and back-drivable actuation

A compliant actuator moves when an external force is applied, and it returns to its original state when the force is no longer present. This corresponds with an elastic output behavior. Compliant actuators are designed into arm-support systems to provide more comfort [103], safety [134] or a combination of both [67]. These actuators have a smaller impact force compared to stiff actuators, and a sudden external force on the output of the system is less likely to damage the mechanical construction or gears.

A back-drivable actuator moves when an external force is applied, and it does not return to its original state when the force is no longer present. Direct-drive electromagnetic actuators can be highly back-drivable if the controller does not anticipate on the external force. A comparison between direct-drive and geared actuators has been presented in [141] which underlines this property. In this work, it is concluded that with a rigid (i.e. non back-drivable) implementation, the gearbox can be damaged by a sudden impact of a high external force on its output.

Pneumatic actuators are inherently compliant because of the compressibility of air [82, 124, 126, 134, 137]. For other actuation principles such as, electromag-

netic actuators with high gearing and hydraulic actuators, back-drivability and compliance can be accomplished through hardware and software. An often used hardware solution for compliant actuation is the series elastic actuator (SEA) [67, 96, 103, 122]. The SEA has a mechanical spring in series with the actuator output and the mechanical construction. An adjustable compliant actuator was investigated in [130, 131] by controlling the tension of the mechanical spring with an additional electrical motor. A SEA can also be applied to pressurize the fluid of a hydraulic disk brake for passive actuation, as concluded by Stienen et al. [121]. Back-drivability is achieved by Johnson et al. [55] with slip clutches to provide safety for people with spasms. Compliant and back-drivable systems can also be realized through control. By measuring the force exerted on the output of the actuator with an additional sensor, the position can be adjusted [13, 27, 33, 42].

Actuators can be made inherently compliant or back-drivable with a hardware solution, whereas with a software solution a delay exists that limits the maximum achievable actuator bandwidth. Therefore, a hardware implementation copes better with sudden impacts. However, adding a mechanical spring, introduces more or lower resonances in the mechanical system that can result in a reduction of bandwidth. In human-machine interactions, compliant and back-drivable actuation by hardware is preferred because of safety [106]. When no power is available or when a sudden power loss occurs, compliant and back-drivable actuation achieved by hardware is still present, whereas a software controller is no longer functional.

2.2.4 Actuator configuration

The actuator configuration defines the position of the actuators within the mechanical construction of the arm-support system. Several actuation configurations can be distinguished: directly-on-the-joint, externally positioned, and gravity compensated. In addition, the inertia, the actuator bandwidth, the number of DoFs, and the difference between exoskeleton and end-effector are discussed in this section.

Configurations

The mechanical construction of the directly-on-the-joint arm-support system is illustrated in Fig. 2.2a for rotational actuators and in Fig. 2.2b for translational actuators. In this configuration the actuators are placed close to or aligned at the joint that they control. Both illustrations show one DoF in the shoulder joint and one DoF in the elbow joint.

Externally positioned actuators are usually placed on the stationary part of the arm-support system and use cable-drive transmissions to transfer a force or torque. In the literature two mechanical constructions can be distinguished namely: an exoskeleton design and a cable suspension design. The exoskeleton design uses

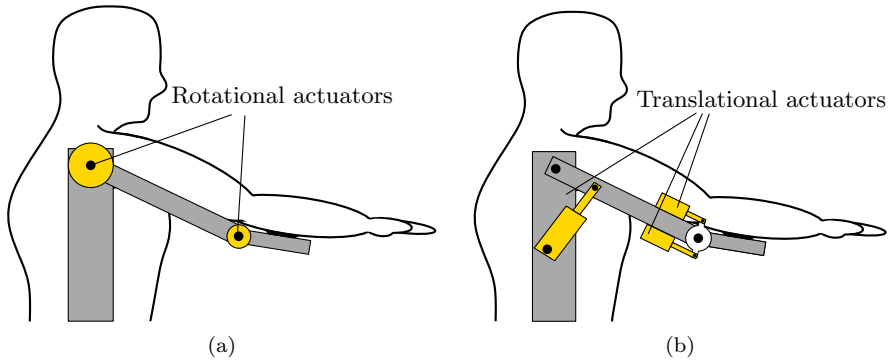


Figure 2.2: Schematic examples of directly-on-the-joint actuation configuration for: (a) rotational, (b) translational.

cable-drive transmission that follows the human arm as illustrated in Fig. 2.3a [6, 98, 101], whereas the cable suspension design approaches the human arm from above as shown in Fig. 2.3b [73, 75, 94, 111]. A cable suspension is able to provide a larger range of motion with less DoF compared to the exoskeleton structure. A cable suspended RAS systems is developed in [111] with only three degrees of freedom that can include non-trivial spatial paths for upper limb rehabilitation. In [75, 94], the constructions are optimized to include a large range of motion.

Devices with gravity compensation generally use a compressed mechanical spring that can be adjusted by an actuator as illustrated in Fig. 2.4. This compressed mechanical spring provides a passive force; hence, no energy is consumed. Designs are proposed in which the user can adjust the spring tension with a button to account for extra load, e.g. to lift a cup of water [46, 59]. These designs provide support in only one DoF, and therefore, have less functionality compared to the aforementioned actuated arm-support systems. According to [7] the long-term acceptance of such systems depend on simplicity and cosmetics.

Inertia

In general, multi-DoF arm-support systems which use directly-on-the-joint actuator configurations have stacked single-DoF actuators. This is visualized in the simplified schematic in Fig. 2.2a. In this figure, the first actuator (i.e. the shoulder joint actuator) of the 2-DoF arm-support system needs to account for the gravity and inertia of the second actuator (i.e. the elbow joint actuator). The more DoFs, the more actuators are stacked, which results in bulky systems.

The stacked actuator construction is avoided by externally positioning the actuators, for example, at the base of the arm-support system. Because of this

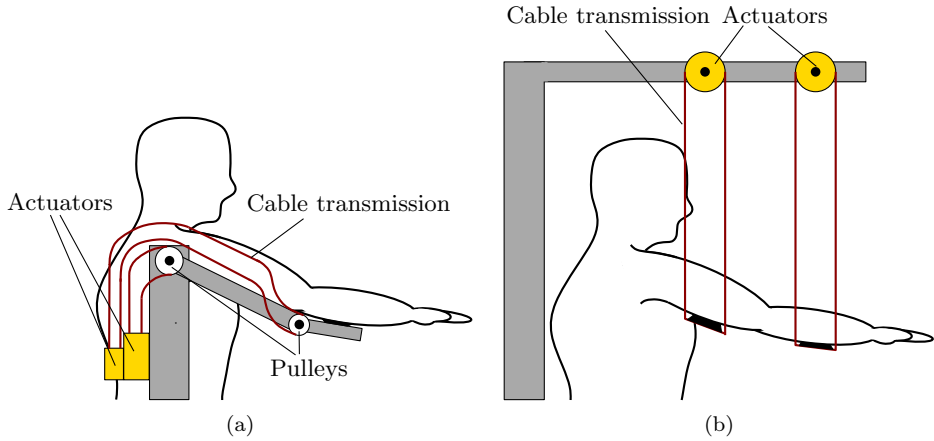


Figure 2.3: Schematic examples of external positioned actuation configuration for: (a) placed on the stationary part, (b) cable suspended.

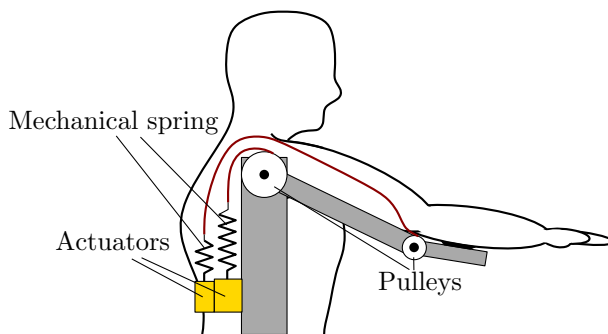


Figure 2.4: Schematic example of adjustable gravity compensation using mechanical springs.

positioning, the mass of the dynamic part of the arm-support system decreases. Additionally, a low-mass structure has less inertia which provides a better dynamical performance. By placing the actuators externally, a mass reduction of 60% was achieved in [101]. To exert the torque at the joint a cable-drive transmission can be used. The analysis in [75] shows the disadvantages which are: maintaining the tension of the cable-drive transmission, friction or even variable friction can be caused by the cables and pulleys, only a pulling force can be achieved and the mechanical design poses complexity e.g. cables may not interfere with the user's movement.

A combination of directly-on-the-joint and externally positioned actuation is also possible. Such design is proposed in [99] to create space near the subject's head. Another combination of a pneumatic actuator as shown in Fig. 2.2b and the gravity compensation as shown in Fig. 2.4 is presented in [134]. In this design, the pneumatic actuator is placed parallel to the mechanical spring; hence, the actuator has to account for only the acceleration and deceleration of the arm-support system.

Bandwidth

For arm-support systems, a closed-loop control bandwidth is desirable which has the same or a higher range than that of a human. These human properties have been investigated by Brooks [10]. From a survey it was shown that the position control bandwidth of a healthy human depends on the experience that is present. For newly introduced actions, the bandwidth is in the range of 1 Hz-2 Hz, for repetitive actions the bandwidth range is 2 Hz-5 Hz, for learned actions a bandwidth of 5 Hz can be obtained, and for reflexive actions 10 Hz is reached.

Each actuator configuration has its own set of specifications and adding hardware such as gears and mechanical springs can have a significant impact on the system bandwidth. Electrical actuators have a high force control bandwidth (typically higher than 100 Hz) that is in general significantly higher than the mechanical resonances of the arm-support system. These resonances occurred around 6 Hz to 8 Hz in [48, 101] and 40 Hz in [116]. The combination of a low gear ratio (35:1) and a brushed DC motor limited the mechanical bandwidth to approximately 50 Hz in [116]. The SEA developed in [103] consists of a brushed DC motor and a spring with a stiffness of 2.51 Nm/rad, resulting in a force control bandwidth of 3.15 Hz. The rHEA of Stienen et al. [122] has a torque bandwidth of 18 Hz with a spring stiffness of 150 Nm/rad. A position control bandwidth in the range of 6.5 Hz-7.2 Hz was achieved in [67] using a linear hydraulic actuator in series with a adjustable mechanical spring.

Pneumatic actuators have a bandwidth in the same range of the mechanical resonances. Using pneumatic muscles, a force control bandwidth of 3.5 Hz was achieved

while tracking a 5 cm peak to peak sine wave in [134]. In [12] A positional control bandwidth of approximately 1.4 Hz was achieved.

Degrees of freedom

The human arm can be simplified by 7 active DoFs, namely: 3 DoFs for the shoulder joint, 1 DoF for the elbow, 1 DoF for the forearm and 2 DoFs for the wrist [18, 42, 85]. Additionally, active or passive DoFs can be added to e.g. provide joint alignment with the operator's physiological joints, although these DoFs are redundant. Usually, a limited number of DoFs are applied to decrease the complexity of the mechanical design and the control strategy. It is not necessary to provide 7 DoFs of support during ADL, for example gravity compensators can have 5 DoFs [8, 46, 59] (3 DoFs for the shoulder, 1 DoF for the elbow, and 1 DoF for the forearm). In [117], the applicability of 1 DoF to suppress tremors is investigated. The system in [27] provides in total 10 DoF (7 DoFs for the arm and 3 DoFs for the fingers). In [116] an exoskeleton system is designed with 14 DoFs (6 DoFs for the shoulder, 2 DoFs for the elbow, 1 DoF for the forearm, 2 active DoFs and 3 passive DoFs for the wrist) to mimic the human arm.

Support type

The design of the arm-support system depends on the type of support that is demanded. Different designs can be applied, such as placement of the arm-support system behind, aside, or in front of the user as illustrated in Fig. 2.5.

An exoskeleton type of arm-support system is attached to the upper arm, forearm and sometimes also the wrist/hand as shown in Fig. 2.5a [8, 31, 42, 55, 67, 75, 101, 104, 116]. With this configuration, each individual movement of the limb can be controlled accurately; this can be beneficial for training. A disadvantage is the possible damage that occurs in the human joints when these are not perfectly aligned with the exoskeleton joints. Especially the shoulder joint is fragile since it is easily dislocated.

An arm-support system can consist out of multiple systems that provide support independently from each other as illustrated in Fig. 2.5b. These systems are both attached to the solid world and the human arm. In [49, 125] two commercially available industrial robotic arms are used. Another commercial robot, the HapticMaster, is applied for exploring the possibilities of using virtual reality in rehabilitation [72] and for assessment of human motor impairments [123].

Providing support at a single point, e.g. at the forearm from the back or aside the user, as illustrated in Fig. 2.5c, is referred to as an end-effector [46, 59, 103, 127, 134]. Such a device can also be positioned in front of the user in [4, 60] and is attached to the forearm and human hand as illustrated in Fig. 2.5d. End-effectors

provide support on one point of the human arm; hence, no joint alignment is required. This simplifies the installation and there is no direct danger of damaging a joint. Furthermore, the kinematics do not have to be exactly the same as a human arm. However, the motion of the human arm cannot be controlled accurately.

2.2.5 Specifications

The specifications of the applied actuators in arm-support systems, which have been found in the literature, are analysed in this section. These systems are categorized according to their application, the actuation principle, and the actuation configuration. A summary is given in Tables 2.1, 2.2 and, 2.3 for the three applications, namely ambulatory, rehabilitation, and industrial, respectively. In general, it is found that all arm-support systems can be placed in one of these three tables, however, some of them can be placed in more than one. In this case, the found system is placed in the category with the most comparable actuators based on their volume. In each table, the developed prototypes are sorted on their publication year. In this thesis the focus is on the shoulder joint and, therefore, the speed and power of this joint are included.

Ambulatory arm-support systems

The number of publications that give the specification of the actuator is too limited to obtain a trend from Table 2.1. The directly-on-the-joint actuation configurations have a torque range of 7 Nm-23 Nm. An externally positioned actuator is able to provide a torque of 98 Nm for the shoulder joint and 28.4 Nm for the elbow joint [34]. The distinction in torque between these configurations is explained by the difference in power and speed. The gravity compensators only specify a force to indicate the amount of support on the forearm. The systems with gravity compensation have a comparable force of 45 N and 50 N [46, 59].

Only one publication specified the force of the applied pneumatic muscle [134]. The applied actuator in this work is able to provide a force of 220 N and has the most power usage of the listed AAS actuation specifications.

There is one arm-support system with a hydraulic actuator which specifies the torque properties [127]. This actuator is the HBSA and provides an elbow torque of 89 Nm. The shoulder joint torque in this arm-support design provides a torque of 63.6 Nm which is lower than the elbow joint. This difference is the result of the applied mechanical construction of the arm-support system. Furthermore, this arm-support system has the highest torque for the elbow compared with the other actuation principles.

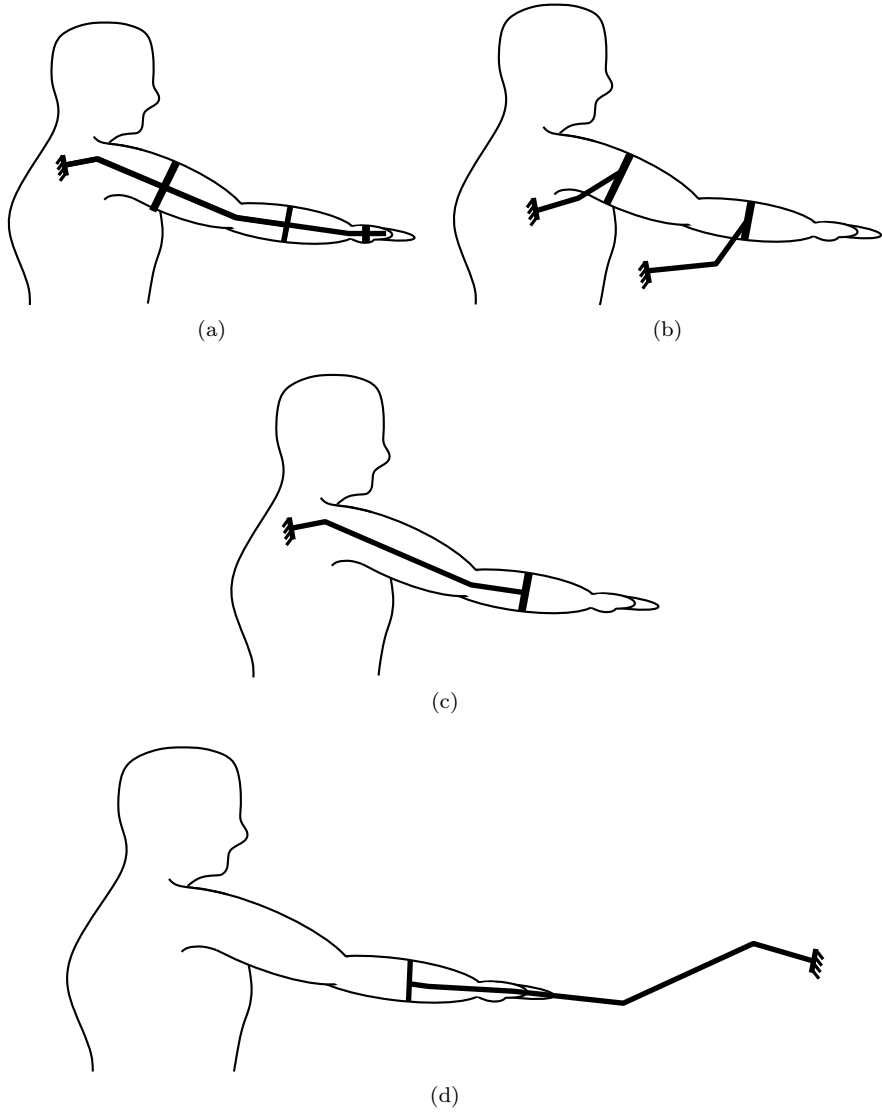


Figure 2.5: Arm-support systems configurations: (a) exoskeleton, (b) multiple end-effectors, (c) end-effector placed behind or aside the user, (d) end-effector placed in front of the user.

Rehabilitation arm-support systems

In rehabilitation arm-support (RAS) systems, a large variety of actuator configurations are applied which results in a large diversity of force, torque, and power specifications as shown in Table 2.2. The directly-on-the-joint actuator configuration presented by [86] provides a force of 151 N with a ball screw and a 150 W electric motor. Only one publication specifies a shoulder joint torque which is 20 Nm [13]. This arm-support system has a remarkable high speed specification, namely 1146°/s. This speed is by far the highest compared to the other arm-support systems.

Two externally positioned electromagnetic actuators have a specified torque that has a large variation for the shoulder joint, namely 62 Nm and 200 Nm, whereas, for the elbow joint a torque of about 32 Nm is applied. The force range of the cable suspended arm-support systems [75, 111] are both in the same range, namely 45 N-50 N. The power needed to produce 50 N in [111] is 231 W, whereas the dedicated RAS in [86] produces 150 N and requires only 150 W. This difference is caused by incorporating a high gear ratio by means of a ball screw.

The two pneumatic actuators provide a torque of 15 Nm and 30 Nm for the shoulder joint. The specifications of the elbow joint are 6 Nm and 15 Nm. The arm-support system in [124] uses the same torque for the shoulder joint as for elbow joint namely, 15 Nm. The other system in [126] produces a torque of 30 Nm for the shoulder joint and 6 Nm for the elbow joint.

The torque provided by the hydraulic actuator, 15 Nm, is in the same range as the torque generated by the pneumatic actuators. However, the hydraulic actuator provides a speed that is 9.38 times higher. Therefore, this actuator has a larger power consumption compared to the pneumatic actuator.

In the listed specifications, some numbers stand out such as the 200 Nm torque used for the shoulder joint actuation [99] and the applied force of 151 N in [86]. The force of 151 N can be explained because the majority of this force is necessary to lift the arm support itself, however, the 200 Nm is probably oversized.

Industrial arm-support systems

Two types of arm-support systems can be distinguished in the literature, master/slave devices and for enhancement of the human body. For master/slave devices, a haptic feedback is provided in the range of 19 Nm to 20 Nm for the shoulder joint and 4 Nm to 10 Nm for the elbow joint [8, 116]. A pneumatic actuator is employed for enhancing the human body and can exert a force of 200 N [128].

Table 2.1: Specified actuator properties of the torque and force applied in AAS systems

Actuation technology	Actuator configuration	T_{max} [Nm]		F_{max} [N]	Speed	Power [W]	Reference	Publication year
		Shoulder	Elbow					
Electromagnetic actuators	Directly-on-the-joint	23	23	-	48°/s	19	[87]	1969
		15 ^a	7.2 ^a	-	75°/s	19.6	[55]	2001
	External positioned	98	28.4	-	95°/s	185 ^b	[34]	2008
	Gravity compensation	-	-	45	0	0	[46]	2006
-		-	50	0	0	[59]	2007	
Pneumatic	Directly-on-the-joint	-	-	220 ^c	1.1m/s	242	[134]	2006
Hydraulic	Directly-on-the-joint	63.6	89	-	-	-	[127]	2009

^aDesign specifications^bCatalog specification^cpressure of 600kPa used

Table 2.2: Specified actuator properties of the torque and force applied in RAS systems

Actuation technology	Actuator configuration	T_{max} [Nm]		F_{max} [N]	Speed	Power [W]	Reference	Publication year
		Shoulder	Elbow					
Electromagnetic actuators	Directly-on-the-joint	-	28	151	-	150 ^d	[86]	2006
		-	-	12	-	-	[49]	2007
		20	-	-	1146°/s	400	[13]	2008
	Externally positioned	-	-	50	-	312 ^d	[111]	2007
		62 ^e	33 ^e	-	-	-	[101]	2007
		200	32	-	35°/s	122	[99]	2008
-	-	-	45	-	-	[75]	2012	
Pneumatic	Directly-on-the-joint	30	6	-	64°/s ^f	33.5 ^f	[126]	2003
		15	15	-	50°/s	13	[124]	2007
Hydraulic	Directly-on-the-joint	-	15	-	469 °/s ^{fg}	123 ^{fg}	[67]	2011

^dCatalog specification of rated power

^eTorque based on gear ratio

^fEstimated from figure

^gA 1.1kW compressor used

Table 2.3: Specified actuator properties of the torque and force applied in IAS systems

Actuation technology	Actuator configuration	T_{max} [Nm]		F_{max} [N]	Speed	Power [W]	Reference	Publication year
		Shoulder	Elbow					
Electromagnetic actuators	Directly-on-the-joint	20	10	-	-	-	[8]	1994
	Externally positioned	19.3	4.5	-	-	150 ^h	[116]	2011
Pneumatic	Directly-on-the-joint	-	-	200 ⁱ	10°/s	-	[128]	1999

^hCatalog specified rated power

ⁱpressure of 400kPa used

2.2.6 Discussion of the literature research

In the literature only a limited number of publications provided the specifications of the actuators applied in the arm-support systems. The AAS system category is the most related to the smart arm-support system researched in this thesis. For this category only seven arm-support systems are listed that provide the actuator specifications. From this list, no coherent set of requirements can be derived, however, an overall typical torque of 20 Nm is shown. In addition, the torque range of the directly-on-the-joint configuration is equal to 7 Nm-23 Nm and corresponds with the desirable functionality of the smart arm-support system. The obtained actuator specifications show a high dependency on the application and the functionalities. These elements influence the eventual design of the arm-support system and, therefore, the requirements of the actuators.

From this literature study, it appears that the shoulder joint poses the most challenges for the mechanical construction and actuator design. The highest torque is required compared to the elbow, forearm and wrist. Furthermore, this joint has multiple degrees of freedom. By designing a novel multi-degree-of-freedom actuator which can mimic the shoulder joint, the complexity of the arm-support construction can be significantly reduced.

2.3 Human shoulder joint specification

The intention of the smart arm-support system is to assist during activities of daily living. Therefore, the set of requirements can also be obtained by analysing the movements of the human arm during the activities of daily living. A set of torque requirements for the actuator design can be derived with this analysis. In addition, the performance to lift an additional mass such as a can or cup is taken into account.

2.3.1 Movement definitions

The human shoulder consists of multiple bones (collarbone, shoulder blade, upper arm bone) that form a ball and socket joint. This joint is kept in position with different muscle groups that can produce movements in multiple degrees of freedom. Each movement has a name that depends on the used muscle group. These movements are flexion, horizontal flexion, and rotation as illustrated in Fig. 2.6 [57]. At rest, the arm points to the ground, with the palm of the hand pointing towards the human body as shown in Fig. 2.7. For the activities of daily living, only a reduced set of arm movements is considered.

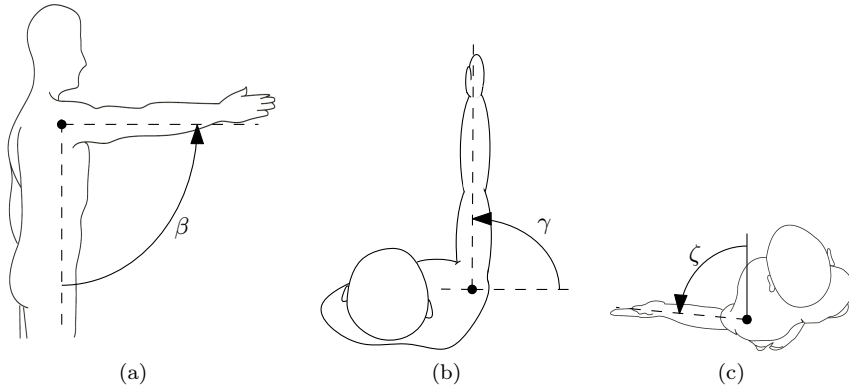


Figure 2.6: Shoulder movements: (a) flexion, (b) horizontal flexion, (c) rotation.

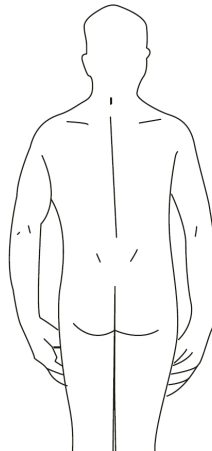


Figure 2.7: The rest position of the human arm.

Table 2.4: Male human arm length of Dutch adults of 20-30 years using a gaussian distribution [1]

Dimensions in sitting position	Mean [m]	Standard deviation [mm]	90% [mm]	95% [mm]
Shoulder height	624	34	44	56
Elbow height	262	28	36	46
Elbow grip length	364	20	26	34

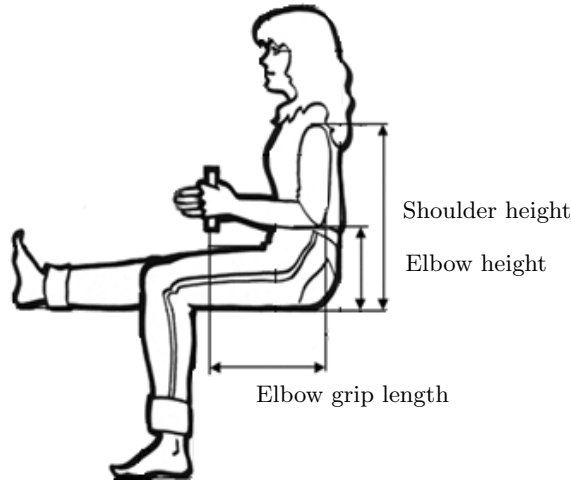


Figure 2.8: The parameters of the human arm as defined by the DINED project [1].

2.3.2 Properties of the human arm

The uniqueness of every human body results in different dimensions of the human arm. Therefore, a range is considered that provides a maximum and minimum torque requirement. The dimensions of a large quantity of Dutch subjects are obtained in the DINED anthropometric database [1]. This database provides a Gaussian distribution of different arm lengths as defined in Fig. 2.8. The arm length of male subjects in the age of 20-30 years has a mean and standard deviation as listed in Table 2.4. The length of the upper arm, the elbow height and the shoulder height have a variation. The database has not specified the length of the upper arm separately. However, from the analysis of the shoulder height and the elbow height, it shows that the elbow grip length is about the same length as the upper arm. Hence, the elbow grip length is also used as upper arm length.

The mass of all body parts have a ratio with respect to the total body mass. This ratio has been obtained from [40] and is listed in Table 2.5. According to

Table 2.5: Percentages of the body part with respect to the total human weight [40]

Body part	Ratio [%]
Head	7
Trunk	43
Upper arm	3.5
Forearm	2.3
Hand	0.7
Thigh	11.4
Lower leg	5.3
Foot	1.8

Table 2.6: Estimated human arm specifications of people with diminished arm functionality.

Body part	Mass [kg]	
	min	max
Upper arm	1.1	2.2
Elbow grip length	0.90	1.8
Total	2.0	4.0

the DINED database the mean body mass of a male between 20-30 years is 80 kg with a standard deviation of 10 kg. This results in a range of minimal 4.29 kg and maximum 6.11 kg for the human arm. However, the arm support is intended for people with diminished arm functionality. Especially, for subject with neurological disorders, the muscles deteriorate and the mass of the human arm decreases. It is assumed that this deterioration causes a reduction of about 2 kg of the human forearm. This results in a human arm mass range of minimum 2 kg and maximum 4 kg as listed in Table 2.6.

The required acceleration is estimated with an inertial measurement unit, iNEMO, attached to the wrist of a healthy person. This estimation is based on movements during activities of daily living such as drinking coffee and using the computer. The resulting acceleration of the shoulder joint were obtained for movements with a stretched and 90° bent elbow. A range for the angular acceleration is obtained which is listed in Table 2.7. These accelerations take the range of the human arm length and mass into account.

During the activities of daily living, it is sometimes required to lift an additional mass such as a cup of water or a can of cola. This extra mass also needs to be considered in the arm support design. For the requirements of the arm-support

Table 2.7: Angular acceleration of the shoulder joint with a stretched and bent forearm measured on a healthy subject

Shoulder joint	α [rad/s ²]	
	min	max
Stretched arm	2.3	5.0
Elbow bent 90°	4.5	7.6

system the minimum mass that needs to be considered is 0.35 kg (can of cola) and a maximum of 0.5 kg.

2.3.3 Torque analysis

Static

A static torque is required from the shoulder joint to keep the arm in a steady position. To calculate this torque for the human arm, an equal distributed mass is assumed as illustrated in Fig. 2.9. The length difference of 2 mm between the elbow grip length and the upper arm length together with the mass difference of 0.5% are neglectable with respect to the total length and mass. The upper limit of this static torque for the shoulder joint, (T_{sj}), can be calculated with

$$T_{sj} = l_{ua} F_{gs} \quad (2.1)$$

$$= l_{ua} (m_{ua} + m_f + m_h) g \quad (2.2)$$

where l_{ua} is the length of the upper arm, F_{gs} is the gravity force of the upper arm and forearm, m_{ua} is the mass of the upper arm, m_f is the mass of the forearm, m_h is the mass of the hand and g is the gravitational acceleration. The torque required to lift an additional object is not included in the distributed mass. The weight of this object is not a static load such as the human arm and, therefore, needs to be actively compensated. Hence, the torque required from the shoulder joint to lift an additional mass, T_{sa} , is obtained by

$$T_{sa} = (l_{ua} + l_{egl}) F_{ga} \quad (2.3)$$

$$= (l_{ua} + l_{egl}) m_{add} g. \quad (2.4)$$

where l_{egl} is the elbow grip length, m_{add} is the additional mass, and F_{ga} is the gravity of the additional mass. This equation accounts for the torque required for a stretched arm; hence it provides the upper torque limit. If the elbow is bent at 90°, the elbow grip length will be zero.

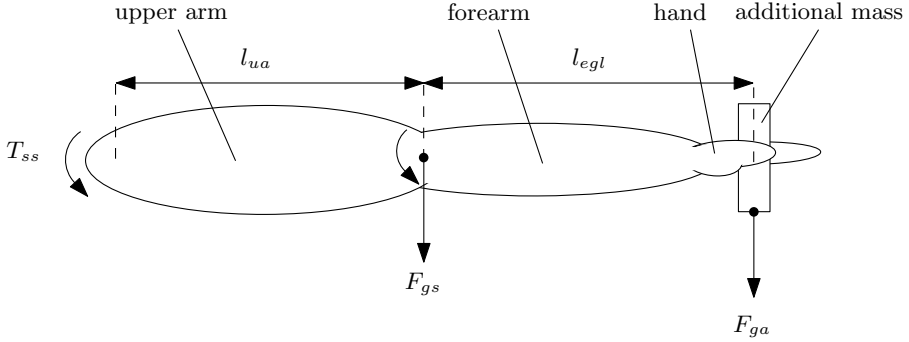


Figure 2.9: Used model of the human arm to obtain the static torque requirements.

Table 2.8: Required static torque for the gravity compensation at $\beta = 90^\circ$

Shoulder flexion	Torque [Nm]			
	Additional mass		Human arm	
	min	max	min	max
Stretched arm	2.2	3.9	6.5	16
Elbow bent 90°	1.1	1.9	4.3	10

Motion in the vertical direction needs to account for the gravity force as illustrated in Fig. 2.10a. The static torque to counteract gravity is obtained by

$$T_{ss}(\beta) = (T_{sj} + T_{sa}) \sin(\beta). \quad (2.5)$$

This equation shows that the movement of the human arm requires a sinusoidal torque characteristic as function of the β displacement. Furthermore, it indicates an instable point at the initial position of $\beta = 0^\circ$. Movement in the horizontal plane, indicated as the γ -direction in Fig. 2.10b, is not dependent on the gravity force. Hence, during this movement the static torque has to remain constant.

For the sinusoidal torque characteristic the torque amplitude value is at the arm position of 90° shoulder flexion movement. Therefore, the torque is obtained in this position and the required torque in the other positions can be obtained with (2.5). The static torque is determined with the properties obtained of the human arm as listed in Table 2.6 and the specified additional mass. The results for this load are listed in Table 2.8 for a stretched arm and the arm with the elbow bent 90° .

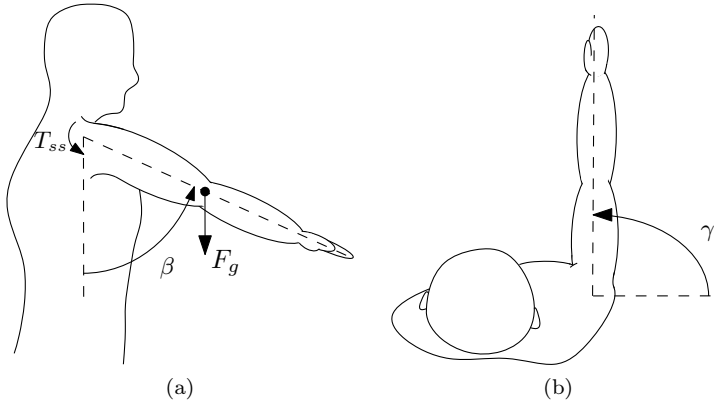


Figure 2.10: Schematic representation of a human upper limb and the torque generated by the shoulder joint: (a) top view, (b) side view.

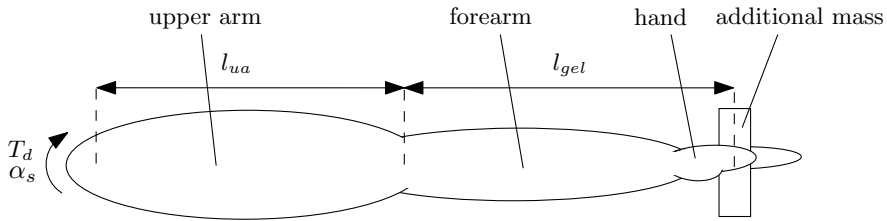


Figure 2.11: Used model of the human arm to obtain the dynamic torque requirements.

Dynamic

The accelerations of the human arm and lifting an additional mass during activities of daily living are considered as the dynamic behavior. The dynamic torque is determined with the human arm model as illustrated in Fig. 2.11. With an equally distributed arm mass, this torque can be obtained for the shoulder joint by

$$T_{ds} = (m_{ua} + m_f + m_h) l_{ua}^2 \alpha_s \quad (2.6)$$

where α_s is the angular acceleration. The torque required to accelerate the additional mass is obtained by

$$T_{da} = m_{add} (l_{ua} + l_{egl})^2 \alpha_s. \quad (2.7)$$

This equation gives the upper torque limit required to accelerate the additional mass. With the obtained acceleration measurements as listed in Table 2.7 the dynamic performance range is obtained and listed in Table 2.9.

Table 2.9: Required torque for the acceleration of the additional mass and human arm

Shoulder joint	Torque [Nm]			
	Additional mass		Human arm	
	min	max	min	max
Stretched arm	0.33	1.6	0.50	3.2
Elbow bent 90°	0.17	0.60	0.44	2.7

The dynamic performance of the shoulder joint only needs to consider the acceleration and deceleration to a certain speed. No torque is necessary when the human arm is at a constant speed and its gravity is compensated. Therefore, the derived torque requirement is not a continuous specification. For the design of the actuator, these specifications will be translated into a continuous torque requirement.

2.3.4 Range of motion

By analysing the activities of daily living, a range of motion for the shoulder joint can be found. The most essential activities to be performed independently are eating and drinking. Other activities such as writing and using a computer are also taken into account. By monitoring the shoulder joint during these activities, a movement space as listed in Table 2.10 is found. This table shows that for the daily routine a range of minimal 55° and maximal 90° is required.

Activities such as grabbing something from the floor or petting a small dog are not considered because these tasks would also involve the motion of the upper body. Other activities for which a larger angle than 90° are necessary such as reaching to a top shelf or opening a hanging cupboard are not included. Instead of providing support for these activities, it is easier to adjust the surroundings. For example, lowering the kitchen counter such that people in an electric wheelchair can cook on it.

2.4 Actuator design consideration

Comparison of the results from the shoulder joint analysis and the literature overview shows that there is a correlation between these two. The human shoulder joint requires a static torque range of 4.3 Nm to 16 Nm and an active torque range of 0.56 Nm to 3.2 Nm. This range is comparable with the range found for the AAS directly-on-the-joint configuration which is 7 Nm to 23 Nm.

Table 2.10: Important activities of daily living and their range of motion specifications

Tasks	Movement	Min angle [°]	Max angle [°]
Eating, drinking	Flexion	0-20	75-90
	Horizontal flexion	0-20	75-90
	Rotation	0-20	75-90
Computer, writing	Flexion	0	10-15
	Horizontal flexion	0	10-15
	Rotation	90	10-15

To mimic the shoulder joint during the activities of daily living at least three degrees of freedom are necessary. In the literature, this is achieved with complex mechanical constructions that have a predefined sequence of rotation axes. To avoid this complexity and the predefined sequence, a multi-degree-of-freedom actuator can be employed that has a ball and socket joint construction similar to the human shoulder joint. The inclusion of multiple degrees of freedom in a single electrical actuator such as planar motion [51], spherical motion [139] and, combined rotary and linear motion [81] has been intensively researched. From these actuators, the spherical actuator provides the suggested ball and socket joint construction. This actuator topology is a direct drive and, therefore, it is back-drivable and can be made compliant through control. Because of these properties, the spherical actuator is considered for the smart controlled arm-support system.

Only support during activities of daily living is considered with the obtained set of requirements for the smart arm-support system. Such an arm support can also provide rehabilitation. In general, RAS systems have a higher torque range compared to the AAS systems as found in the literature. Therefore, only a limited set of rehabilitation exercises can be performed and to include the complete set an actuator with a higher torque specification is needed.

2.5 Conclusions

The arm-support systems obtained from the literature have been divided based on their applications, actuation technology, and actuator configuration. Three different applications have been distinguished namely, ambulatory, rehabilitation, and industrial. Ambulatory arm-support systems are used at home and their power consumption is often limited by a mobile power source such as a battery. A wide range of rehabilitation arm-support systems exists for a wide variety of neurologic lesions and to provide training possibilities. Therefore, more flexibility is required for this application compared to the ambulatory application. However, mobile

rehabilitation arm supports are usually dedicated and, therefore, less flexible. Industrial arm-support systems are designed for enhancement of the human body or to function as a master/slave device. For enhancement of the human body, powerful actuators are needed, whereas master/slave devices require haptics. The degrees of freedom necessary for these applications depend on the supported activities.

The actuation principles that are applied in existing arm-support systems are electromechanical actuators, pneumatic actuators, hydraulic actuators, and semi-active dampers. For safety reasons, compliance and back-drivability are important properties when choosing the actuation technology. If actuators do not have one of these properties inherently such as pneumatic actuators, it can be achieved with hardware or software.

The actuation configuration is the mechanical construction method of the actuation technology in the arm-support system. Positioning the actuators externally decreases the mass and inertia of the arm support itself, which is beneficial for the dynamic behavior. However, a more complex mechanical construction is required. The configuration with externally positioned actuators have been subdivided into two groups, exoskeletons and cable suspensions. A cable suspension provides a larger range of motion with less degrees of freedom compared to other arm-support systems. However, a construction above the user is required. The gravity compensator is an actuation configuration that provides support in only one degree of freedom. To compensate for the gravity, a mechanical spring or counterweight is used that is adjustable with an actuator. Consequently, a low power consumption is required by prestressing the mechanical spring.

The provided torque of the human shoulder joint is determined with a set of arm properties obtained from the literature. This torque is separated in the required static torque and dynamic torque. A static torque range of 4.3 Nm to 16 Nm and an active torque of 0.44 Nm to 3.2 Nm has been found. This range corresponds to the found AAS directly-on-the-joint configuration. Additionally, it has been found that at least three degrees of freedom are required to mimic the shoulder joint.

A three degrees of freedom motor can be realized with one spherical actuator because of the similar ball and socket joint construction as the shoulder joint. This actuator topology has no predefined sequence of axes and, therefore, reduces the complexity of the mechanical construction.

Chapter 3

Modeling of spherical magnetic structures

Abstract - Fast semi-analytical modeling techniques are researched to design multi-degree-of-freedom spherical electromechanical systems. Two techniques are investigated, namely the magnetic charge model and the harmonic model. Both modeling techniques are extended to model a region with an infinitely permeable material. This region is included in the boundary conditions of the harmonic model. For the magnetic charge model, this region is modeled with the extension of spherical imaging. Furthermore, the magnetic flux density of a radial magnetization is predicted with this modeling technique. Both models are applied to a benchmark problem to compare the results on accuracy and limitations.

This chapter is based on

- B. van Nindhuijs, T. E. Motoasca, B. L. J. Gysen, and E. A. Lomonova, "Modeling of spherical magnet arrays using the magnetic charge model," *IEEE Transactions on Magnetics*, vol. 49, no. 7, pp. 4109-4112, 2013.
- B. van Nindhuijs, T. E. Motoasca, and E. A. Lomonova, "Accurate analytical computation of magnetic flux density of spherical permanent magnet arrays," in 2012 XXth International Conference on Electrical Machines (ICEM), Sept 2012, pp. 2746-2751.
- B. van Nindhuijs, J. W. Jansen, B. Gysen, and E. A. Lomonova, "Comparison of Harmonic and Magnetic Charge Model for Spherical Magnetic Structures with a Neumann Boundary," *IEEE Transactions on Magnetics*, vol.51, no.11, pp.1-4, 2015

3.1 Introduction on spherical modeling

The interaction of electromagnetic fields in a spherical structure produce forces and torques in multiple directions. These fields can originate from permanent magnets, coils, or a combination of both and their behavior is described by Maxwell's equations. Spherical actuators use a combination of permanent magnets and coils to produce a torque. This torque can be controlled by the excitation of the current through the coils. Combining multiple permanent magnets, a passive torque can be produced which can be used for a spherical magnetic spring in a gravity compensator application. These applications are investigated in Chapter 4 and Chapter 5.

The torque of electromagnetic spherical constructions can be predicted by solving Maxwell's equations with semi-analytical models or finite element analysis (FEA). FEA divides the solution region into a finite number of subregions [28]. This discretization requires a large computational effort and time, especially, for 3D problems. To decrease this computational time significantly, semi-analytical are researched that provide a fast and accurate prediction. This reduction is especially beneficial for a broad optimization of multiple actuator topologies.

Semi-analytical modeling techniques such as the magnetic equivalent circuit model (MEC), harmonic model, and a distributed multipole model have been applied to spherical magnetic structures. A lumped element network for the magnetic circuit is created for each permanent magnet (PM) array with the MEC method. Changes in the PM topology, e.g. the number and magnetization directions of PMs, require the construction of a new MEC model. Hence, this is a time-consuming technique for design and optimization. This method has been applied on spherical magnetic structures in [68]. The harmonic modeling method provides a solution to a boundary value problem [37]. This model has been applied on a two by four spherical permanent magnet array in [133] to obtain a semi-analytical model. A full analytical expression is found considering only the first harmonic in [139] and the first three harmonics in [112]. The distributed multipole model, which uses a known analytical solution, utilizes the magnetic charge of every dipole and the summation of all dipoles provide the total magnetic field solution [64, 66]. Another modeling method is the magnetic charge model. This technique replaces the permanent magnets by an equivalent spatial (volume or surface) distribution of magnetic charges [53].

The magnetic charge model and harmonic model are derived from Maxwell's equations and both models are extended in this chapter. The magnetic charge model is applied in the spherical domain. In addition to a parallel magnetization, the magnetic field of a radial magnetization can be predicted with this modeling technique. To model a boundary of highly permeable material, the magnetic charge is further extended with spherical imaging. Further, a harmonic model is derived that can

also include such boundaries. This model can include an asymmetrical spherical permanent magnet array. The spherical coordinate system which is applied in this chapter is defined in Appendix A. The modeling techniques are compared with a bench mark model that has 32 spherical permanent magnets.

3.2 Electromagnetic modeling

The magnetic field solution is derived from the Maxwell equations. In differential form, these equations are given by,

$$\nabla \times \vec{H} = \vec{J} + \frac{\partial \vec{D}}{\partial t} \quad (3.1)$$

$$\nabla \cdot \vec{B} = 0 \quad (3.2)$$

$$\nabla \times \vec{E} = -\frac{\partial \vec{B}}{\partial t} \quad (3.3)$$

$$\nabla \cdot \vec{D} = \rho_c \quad (3.4)$$

where \vec{H} is the magnetic field strength, \vec{J} is the current density, \vec{D} is the electric flux density, \vec{B} is the magnetic flux density, \vec{E} is the electrical field strength and ρ_c is the free electric charge density. To obtain the magnetic flux density from the static Maxwell equations, the magnetic flux density, \vec{B} , and the electric flux density, \vec{D} , are assumed to be independent of time, which results in

$$\frac{\partial \vec{B}}{\partial t} = 0 \quad (3.5)$$

$$\frac{\partial \vec{D}}{\partial t} = 0. \quad (3.6)$$

With this assumption the static Maxwell equations can be listed as

$$\nabla \times \vec{H} = \vec{J} \quad (3.7)$$

$$\nabla \cdot \vec{B} = 0. \quad (3.8)$$

The magnetic material is modeled by introducing a magnetization vector \vec{M} . In general, the magnetization vector consists of two components, described by

$$\vec{M} = \vec{M}_0 + \vec{M}_s. \quad (3.9)$$

The vector \vec{M}_0 results from the remanent magnetization present in hard magnetized material such as permanent magnets. Due to this magnetization a resulting magnetic field \vec{H} arises, which causes a secondary magnetization, M_s , since the

material has a finite magnetic susceptibility χ . The relation of the secondary magnetization \vec{M}_s with the magnetic field strength is given by

$$\vec{M}_s = \chi \vec{H}. \quad (3.10)$$

Using these definitions it can be shown that the magnetic flux density and the magnetic field strength is related as given by

$$\vec{B} = \mu_0(\vec{H} + \vec{M}) \quad (3.11)$$

$$= \mu_0\mu_r\vec{H} + \mu_0\vec{M}_0 \quad (3.12)$$

where μ_0 is the permeability of vacuum and

$$\mu_r = (1 + \chi) \quad (3.13)$$

is the relative permeability. By introducing a magnetic scalar potential φ which is defined as

$$\vec{H} = -\nabla\varphi \quad (3.14)$$

and assuming a current free region and substituting (3.14) in (3.8), and (3.12) the magnetic scalar potential can be expressed as

$$\nabla^2\varphi = \frac{\nabla \cdot \vec{M}_0}{\mu_r}. \quad (3.15)$$

This type of equation is also referred to as the Poisson equation. This equation can be solved in two ways. Either with separation of variables and solving the boundary value problem with harmonic modeling or by using the free space Green's function with the magnetic charge modeling.

3.3 Torque calculations

An accurate prediction of the mechanical torque that is produced by interacting electromagnetic fields, is essential to obtain a design that complies with a predefined set of specifications. The torque is obtained by

$$\vec{T} = \vec{r}_d \times \vec{F} \quad (3.16)$$

where \vec{T} is the torque, \vec{r}_d is the displacement vector, and \vec{F} is the force. The force \vec{F} can be obtained with the Lorentz force and Maxwell stress tensor method.

3.3.1 Lorentz force

The Lorentz force equation describes the relation between the force \vec{F} on a charged particle q which moves through an external magnetic field \vec{B} with a velocity of \vec{v} or in an electric field \vec{E}

$$\vec{F} = q(\vec{E} + \vec{v} \times \vec{B}). \quad (3.17)$$

For magnetostatic problems it is assumed that the electric field \vec{E} is zero. Consequently, the force density, as provided by [136], can be written as,

$$\vec{f} = \lim_{\delta V \rightarrow 0} \sum_i \frac{q_i \vec{v}_i \times \vec{B}_i}{\delta V} \quad (3.18)$$

where q_i , and \vec{v}_i refer to all the particles in the volume δV and \vec{B}_i is the flux density experienced by q_i . When it is assumed that all particles within δV experience the same flux density \vec{B} and with the definition of free current density as given by

$$\vec{J} = \lim_{\delta V \rightarrow 0} \sum_i \frac{q_i \vec{v}_i}{\delta V} \quad (3.19)$$

the Lorentz force density can be written as

$$\vec{F} = \int_V \vec{J} \times \vec{B} \, dV. \quad (3.20)$$

Assuming perfectly spherical shaped coils with no current flowing in the radial direction, the force is given by

$$\vec{F} = \int_V ((J_\theta B_\phi - B_\theta J_\phi) \vec{e}_\rho + B_\rho J_\phi \vec{e}_\theta - J_\theta B_\rho \vec{e}_\phi) \, dV. \quad (3.21)$$

The torque is obtained as described in (3.16) with a displacement vector equal to

$$\vec{r} = \begin{bmatrix} \rho \vec{e}_\rho \\ 0 \vec{e}_\theta \\ 0 \vec{e}_\phi \end{bmatrix} \quad (3.22)$$

which results in

$$\vec{T} = \rho \int_V (-J_\theta B_\rho \vec{e}_\theta + B_\rho J_\phi \vec{e}_\phi) \, dV. \quad (3.23)$$

This equation shows that the produced torque is not dependent on the tangential magnetic flux density components B_θ and B_ϕ .

3.3.2 Maxwell stress tensor

The force resulting from a magnetic field interactions can be calculated with the Maxwell stress tensor. This method is usually given in the Cartesian coordinate system [53] and in the cylindrical coordinate system [80]. The Maxwell stress tensor is derived for the components of a spherical coordinate system starting from the Lorentz force equation (3.20). Assuming a magnetostatic system, Ampère's circuit law can be substituted. This results in

$$\vec{F} = \int_V (\nabla \times \vec{H}) \times \vec{B} dV. \quad (3.24)$$

The constitutive relation (3.12) in a source free medium with a constant relative permeability results in

$$\vec{B} = \mu \vec{H}. \quad (3.25)$$

Substituting this relation in the force equation (3.24) results in

$$\vec{F} = \frac{1}{\mu} \int_V (\nabla \times \vec{B}) \times \vec{B} dV. \quad (3.26)$$

Applying the vector identity

$$(\nabla \times \vec{A}) \times \vec{A} = (\vec{A} \cdot \nabla) \vec{A} - \frac{1}{2} \nabla (\vec{A} \cdot \vec{A}) \quad (3.27)$$

it can be found that

$$\vec{F} = \frac{1}{\mu} \int_V (\vec{B} \cdot \nabla) \vec{B} - \frac{1}{2} \nabla (\vec{B} \cdot \vec{B}) dV. \quad (3.28)$$

With the assumption of a right-handed orthogonal coordinate system with three axes, ν_1 , ν_2 and, ν_3 , the found expression of the force results in

$$\vec{F} = \frac{1}{\mu} \int_V \left[(B_1 \frac{\partial}{\partial \nu_1} + B_2 \frac{\partial}{\partial \nu_2} + B_3 \frac{\partial}{\partial \nu_3}) \begin{bmatrix} B_1 \vec{e}_{\nu_1} \\ B_2 \vec{e}_{\nu_2} \\ B_3 \vec{e}_{\nu_3} \end{bmatrix} - \frac{1}{2} \begin{bmatrix} \frac{\partial}{\partial \nu_1} \vec{e}_{\nu_1} \\ \frac{\partial}{\partial \nu_2} \vec{e}_{\nu_2} \\ \frac{\partial}{\partial \nu_3} \vec{e}_{\nu_3} \end{bmatrix} (B_1^2 + B_2^2 + B_3^2) \right] dV. \quad (3.29)$$

In the Cartesian coordinate system these vectors are described by the magnetic flux density components. Because the spherical coordinate system is also a right-handed orthogonal coordinate system, the spherical magnetic flux density components B_ρ , B_θ , and B_ϕ can be applied in the same way as the Cartesian components. Simplification of the found expression [136] results in:

$$F_m = \frac{1}{\mu} \int_V B_n \frac{\partial B_m}{\partial \nu_n} - \frac{1}{2} \frac{\partial}{\partial \nu_m} B_k^2 dV \quad (3.30)$$

where n is the index of the scalar component, m is the index of the vector component,

$$B_k^2 = B_1^2 + B_2^2 + B_3^2 \quad (3.31)$$

and

$$B_n \frac{\partial}{\partial \nu_n} = B_1 \frac{\partial}{\partial \nu_1} + B_2 \frac{\partial}{\partial \nu_2} + B_3 \frac{\partial}{\partial \nu_3} \quad (3.32)$$

$$= B \cdot \nabla. \quad (3.33)$$

By introducing the Kronecker delta

$$\delta_{mn} = \begin{cases} 1 & \text{when } m = n \\ 0 & \text{when } m \neq n \end{cases} \quad (3.34)$$

it is found that

$$F_m = \frac{1}{\mu} \int_V B_n \frac{\partial B_m}{\partial \nu_n} - \frac{\delta_{mn}}{2} \frac{\partial}{\partial \nu_n} B_k^2 dV. \quad (3.35)$$

The products of derivatives can also be stated as

$$F_m = \frac{1}{\mu} \int_V \frac{\partial B_n B_m}{\partial \nu_n} - B_m \frac{\partial B_n}{\partial \nu_n} - \frac{\delta_{mn}}{2} \frac{\partial}{\partial \nu_n} B_k^2 dV \quad (3.36)$$

where

$$B_m \frac{\partial B_n}{\partial \nu_n} = B_m \nabla \cdot B_n = 0. \quad (3.37)$$

Hence, the expression for the force results in

$$F_m = \frac{1}{\mu} \int_V \frac{\partial}{\partial \nu_n} \left(B_n B_m - \frac{\delta_{mn}}{2} B_k^2 \right) dV \quad (3.38)$$

where the Maxwell stress tensor is given by

$$\mathbb{T} = B_n B_m - \frac{\delta_{mn}}{2} B_k^2. \quad (3.39)$$

An expression of the force in function of the Maxwell stress tensor is provided by

$$\vec{F} = \frac{1}{\mu} \int_V \nabla \cdot \mathbb{T} dV. \quad (3.40)$$

Applying the Divergence theorem [28] this expression can be written as

$$\vec{F} = \frac{1}{\mu} \oint_S \mathbb{T} \cdot \vec{n} ds. \quad (3.41)$$

Because the spherical coordinate system is a right-handed orthogonal coordinate system, the tensor in the spherical domain results in

$$\mathbb{T} = \begin{bmatrix} \frac{B_\rho^2 - B_\theta^2 - B_\phi^2}{2} & B_\rho B_\theta & B_\rho B_\phi \\ B_\theta B_\rho & \frac{B_\theta^2 - B_\rho^2 - B_\phi^2}{2} & B_\theta B_\phi \\ B_\phi B_\rho & B_\phi B_\theta & \frac{B_\phi^2 - B_\rho^2 - B_\theta^2}{2} \end{bmatrix}. \quad (3.42)$$

The force produced between two concentric spherical permanent magnets can be obtained with the Maxwell stress tensor and results in

$$\vec{F} = \frac{1}{\mu} \oint_S \left(\frac{B_\rho^2 - B_\theta^2 - B_\phi^2}{2} \vec{e}_\rho + B_\theta B_\rho \vec{e}_\theta + B_\phi B_\rho \vec{e}_\phi \right) ds \quad (3.43)$$

with the spherical displacement vector as defined in (3.22), the expression of the torque results in

$$\vec{T} = \frac{\rho}{\mu} \oint_S (-B_\phi B_\rho \vec{e}_\theta + B_\theta B_\rho \vec{e}_\phi) ds. \quad (3.44)$$

3.4 Charge modeling

The magnetic charge model replaces the permanent magnets with a distribution of equivalent magnetic charges. In the magnetostatic field equations, these equivalent magnetic charges are used as source terms and the magnetic fields can be obtained by e.g. the free space Green's function [28]. This model calculates the magnetic field solution of one single spherical shaped magnet and the total field solution of the spherical permanent magnet array is obtained by means of superposition. Since the magnetic charge model obtains the magnetic flux density for each spherical permanent magnet separately, this method can include different spherical magnetic structures such as hemispheres.

3.4.1 General solution

Assuming a free-space problem, i.e. no boundary surfaces, and a relative permeability of one, a general solution to the Poisson equation (3.15) is obtained with the free-space Green's function

$$\varphi = -\frac{1}{4\pi} \int \frac{\nabla' \vec{M}_0(\vec{r}')}{|\vec{r} - \vec{r}'|} dv' \quad (3.45)$$

where \vec{r} is the observation point, \vec{r}' is the source point and, ∇' operates on the primed coordinates. Assuming that the magnetization \vec{M}_0 is confined to a volume

V (of permeability μ_0) and falls abruptly to zero outside this volume. The magnetic scalar potential can be written as

$$\varphi = \frac{1}{4\pi} \int_V \frac{\rho_m(\vec{r}')}{|\vec{r} - \vec{r}'|} dV' + \frac{1}{4\pi} \oint_S \frac{\sigma_m(\vec{r}')}{|\vec{r} - \vec{r}'|} ds' \quad (3.46)$$

where

$$\rho_m = -\nabla' \cdot \vec{M}_0 \quad (3.47)$$

is the magnetic volume charge density and

$$\sigma_m = \vec{M}_0 \cdot \vec{n} \quad (3.48)$$

is the magnetic surface charge density and \vec{n} is the normal vector of the closed surface S [28].

The magnetic volume charge density and magnetic surface charge density are obtained with a divergence or a scalar product, hence, both densities are scalars. Therefore, the magnetization can be expressed in the Cartesian coordinate system or the spherical coordinate system as long as the other component of the scalar product is expressed in the same coordinate system. This can be beneficial when a certain magnetization topology is easier to describe in one of the two coordinate systems.

The scalar potential has a relation to the magnetic field strength \vec{H} as defined in (3.14) and substitution of the magnetic scalar potential (3.46), provides the following expression for the magnetic field strength

$$\vec{H} = \frac{1}{4\pi} \int_V \rho_m(\vec{r}') \nabla \frac{1}{|\vec{r} - \vec{r}'|} dV' + \frac{1}{4\pi} \oint_S \sigma_m(\vec{r}') \nabla \frac{1}{|\vec{r} - \vec{r}'|} ds'. \quad (3.49)$$

The Euclidean distance between the observation point and the source point in the Cartesian coordinate system can be written as

$$|\vec{r} - \vec{r}'| = \sqrt{(x - x')^2 + (y - y')^2 + (z - z')^2}. \quad (3.50)$$

After conversion of this expression to the spherical coordinate system (A.5), the Euclidian distance is obtained by

$$|\vec{r} - \vec{r}'| = \sqrt{\rho^2 + \rho'^2 - 2\rho\rho' [\sin(\theta) \sin(\theta') \cos(\phi - \phi') + \cos(\theta) \cos(\theta')]}. \quad (3.51)$$

The gradient in the spherical coordinate system results in

$$\begin{aligned} \nabla \frac{1}{|\vec{r} - \vec{r}'|} = & - \frac{\rho + \rho' [\sin(\theta) \sin(\theta') \cos(\phi - \phi') + \cos(\theta) \cos(\theta')]}{a^{3/2}} \vec{e}_\rho \\ & + \frac{\rho' [\cos(\theta) \sin(\theta') \cos(\phi - \phi') - \sin(\theta) \cos(\theta')]}{a^{3/2}} \vec{e}_\theta \\ & - \frac{\rho' \sin(\theta') \sin(\phi - \phi')}{a^{3/2}} \vec{e}_\phi \end{aligned} \quad (3.52)$$

where

$$a = \rho^2 + \rho'^2 - 2\rho\rho' [\sin(\theta) \sin(\theta') \cos(\phi - \phi') + \cos(\theta) \cos(\theta')]. \quad (3.53)$$

The magnetic flux density is obtained outside the permanent magnets with the relation between the magnetic field strength and the magnetic flux density as shown in (3.12) and (3.49).

Analogously, an expression for the magnetic field of a cylindrical permanent magnet can be obtained. The Euclidian distance between two points in this coordinate system can be obtained by

$$|\vec{r} - \vec{r}'| = \sqrt{\rho^2 + \rho'^2 - 2\rho\rho' \cos(\phi - \phi') + (z - z')^2} \quad (3.54)$$

and the gradient is determined by

$$\nabla \frac{1}{|\vec{r} - \vec{r}'|} = \frac{-\rho + \rho' \cos(\phi - \phi')}{a^{3/2}} \vec{e}_\rho - \frac{\rho' \sin(\phi - \phi')}{a^{3/2}} \vec{e}_\phi + \frac{z - z'}{a^{3/2}} \vec{e}_z, \quad (3.55)$$

where

$$a = \rho^2 + \rho'^2 - 2\rho\rho' \cos(\phi - \phi') + (z - z')^2. \quad (3.56)$$

With this expression, the magnetic field of a radial and parallel magnetized cylindrical permanent magnet can be obtained [105]. As alternative to a radial magnetized spherical permanent magnet, a segmentation of parallel magnetized cylindrical magnets can be applied to achieve this magnetization as is presented later on in this thesis (Chapter 4).

3.4.2 Parallel magnetization

To find the magnetic flux density with the magnetic charge model, an expression for the magnetic volume density and magnetic charge density has to be found. A parallel magnetization is uniform inside the permanent magnet and, therefore, the volume charge density is zero inside this volume, i.e. $\nabla \cdot \vec{M}_0 = 0$; hence, only the surface charge density remains. In addition, it is assumed that the problem consists of three different regions as illustrated in Fig. 3.1. Regions 1 and 3 contain air and in region 2 a magnetic source is employed, such as a permanent magnet. For all three regions the magnetic charge model assumes a relative permeability of $\mu_r = 1$, including the region that contains the permanent magnets.

The magnetic surface charge density (3.48) depends on the magnetization vector and the normal vector of the surface. This implies that, the magnetic surface charge distribution is different for each surface. A spherical segment with six

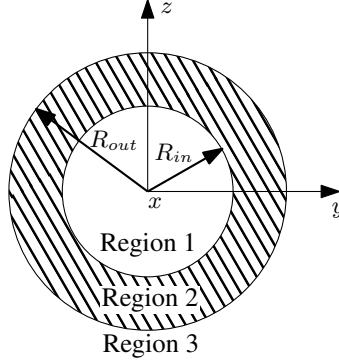


Figure 3.1: Regions and geometric parameters definitions of a spherical permanent magnet array.

different surfaces is shown in Fig. 3.2. The normal vectors of these surfaces can be defined in the spherical coordinate system as

$$\begin{aligned}
 \vec{n}_1 &= \begin{bmatrix} 1 \vec{e}_\rho \\ 0 \vec{e}_\theta \\ 0 \vec{e}_\phi \end{bmatrix} & \vec{n}_2 &= \begin{bmatrix} -1 \vec{e}_\rho \\ 0 \vec{e}_\theta \\ 0 \vec{e}_\phi \end{bmatrix} \\
 \vec{n}_3 &= \begin{bmatrix} 0 \vec{e}_\rho \\ 1 \vec{e}_\theta \\ 0 \vec{e}_\phi \end{bmatrix} & \vec{n}_4 &= \begin{bmatrix} 0 \vec{e}_\rho \\ -1 \vec{e}_\theta \\ 0 \vec{e}_\phi \end{bmatrix} \\
 \vec{n}_5 &= \begin{bmatrix} 0 \vec{e}_\rho \\ 0 \vec{e}_\theta \\ 1 \vec{e}_\phi \end{bmatrix} & \vec{n}_6 &= \begin{bmatrix} 0 \vec{e}_\rho \\ 0 \vec{e}_\theta \\ -1 \vec{e}_\phi \end{bmatrix}.
 \end{aligned} \tag{3.57}$$

With the six normal vectors, the magnetic charge densities of the surfaces can be obtained depending on the magnetization.

The magnetic surface charges can be obtained by substitution of the parallel magnetization vector (3.115) and the normal vectors of each surface (3.48) in (3.48) which results in

$$\sigma_{m;1} = M_\rho(\theta, \phi) \tag{3.58}$$

$$\sigma_{m;2} = -M_\rho(\theta, \phi) \tag{3.59}$$

$$\sigma_{m;3} = M_\theta(\theta, \phi) \tag{3.60}$$

$$\sigma_{m;4} = -M_\theta(\theta, \phi) \tag{3.61}$$

$$\sigma_{m;5} = M_\phi(\theta, \phi) \tag{3.62}$$

$$\sigma_{m;6} = -M_\phi(\theta, \phi). \tag{3.63}$$

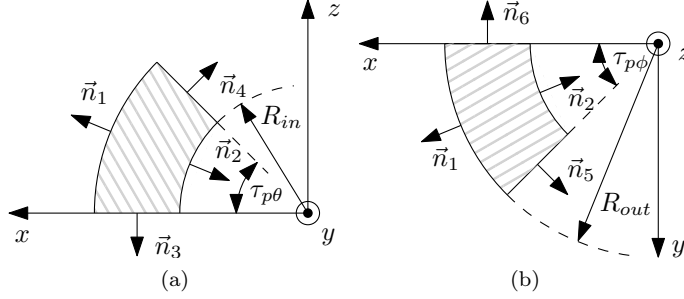


Figure 3.2: Side view of a single permanent magnet segment defining the normal vectors of the six surfaces: (a) xz -view, (b) xy -view.

A spherical permanent magnet array can be defined with a pole pitch of $\tau_{p\theta}$ in the θ -direction, $\tau_{p\phi}$ in the ϕ -direction, an inner radius R_{in} and an outer radius R_{out} . The definition of these pole pitches is shown in Fig. 3.2. Substitution of these geometric parameters, the surface charge densities in (3.49), and (3.12), the magnetic flux density of every surface of a single permanent magnet segment is obtained by

$$\vec{B}_{1,2} = -\frac{\mu_0}{4\pi} \int_{\tau_{p\theta}(p_\theta-1)}^{\tau_{p\theta}p_\theta} \int_{\tau_{p\phi}(p_\phi-1)}^{\tau_{p\phi}p_\phi} \sigma_{m;1,2} \nabla \frac{1}{|\vec{r} - \vec{r}'|} \rho'^2 \sin(\theta') d\theta' d\phi' \quad (3.64)$$

$$\vec{B}_{3,4} = -\frac{\mu_0}{4\pi} \int_{\tau_{p\theta}(p_\theta-1)}^{\tau_{p\theta}p_\theta} \int_{R_{in}}^{R_{out}} \sigma_{m;3,4} \nabla \frac{1}{|\vec{r} - \vec{r}'|} \rho' \sin(\Theta) d\rho' d\phi' \quad (3.65)$$

$$\vec{B}_{5,6} = -\frac{\mu_0}{4\pi} \int_{\tau_{p\theta}(p_\theta-1)}^{\tau_{p\theta}p_\theta} \int_{R_{in}}^{R_{out}} \sigma_{m;5,6} \nabla \frac{1}{|\vec{r} - \vec{r}'|} \rho' d\rho' d\theta'. \quad (3.66)$$

where p_θ and p_ϕ are the magnet numbers in the θ - and ϕ -direction respectively.

The total magnetic flux density produced by one permanent magnet segment is obtained by

$$\vec{B}_{p_\theta:p_\phi} = \sum_{i=1}^6 \vec{B}_i \quad (3.67)$$

where the subscript of $B_{p_\theta:p_\phi}$ denotes the magnetic flux density of the p_θ^{th} permanent magnet segment in the θ -direction and p_ϕ^{th} permanent magnet segment in the ϕ -direction where the subscript i represents the flux density generated by the i^{th} surface. The magnetic flux density of the complete spherical permanent magnet array is obtained by

$$\vec{B}_{tot} = \sum_{p_\theta=1}^{P_\theta} \sum_{p_\phi=1}^{P_\phi} \vec{B}_{p_\theta:p_\phi}. \quad (3.68)$$

For a spherical segment consisting of less than six surfaces such as a hemispherical shell, only three normal vectors exist. Such spherical magnet only has three normal vectors. The same model as presented above can be applied; however, only (the relevant) three magnetic flux densities will be nonzero.

The expression for the magnetic flux density has a combination of a square root of trigonometric functions in the denominator because of the spherical coordinate system. Therefore, the required integration is solved numerically. For each observation point this numerical integration needs to be performed. The calculation time depends mainly on the number of included observation points and the size of the spherical permanent magnet array.

3.4.3 Radial magnetization

To find the magnetic flux density with the magnetic charge model of a radially magnetized magnet, an expression for the magnetic volume charge density and magnetic surface charge density has to be found. As the magnetization is not uniform through the volume of the magnets, a volume charge density exists. This volume charge density can be evaluated with (3.47) and (B.2) which results in

$$\rho_m = -\frac{2M_0}{\rho}. \quad (3.69)$$

Contrary to a parallel magnetization, the magnetic charge density is distributed over only two surfaces, resulting in two magnetic surface charges for a permanent magnet segment. Only on the surfaces with a constant radius, a magnetic charge density exist, namely at $\rho = R_{out}$ and $\rho = R_{in}$. The normal vectors of these surfaces are

$$\vec{n}_1 = \begin{bmatrix} 1 \vec{e}_\rho \\ 0 \vec{e}_\theta \\ 0 \vec{e}_\phi \end{bmatrix} \quad (3.70)$$

$$\vec{n}_2 = \begin{bmatrix} -1 \vec{e}_\rho \\ 0 \vec{e}_\theta \\ 0 \vec{e}_\phi \end{bmatrix} \quad (3.71)$$

and the surface charge densities are given by

$$\sigma_{m;1} = M_0 \quad (3.72)$$

$$\sigma_{m;2} = -M_0. \quad (3.73)$$

The magnetic flux density produced by a spherical permanent magnet can be separated into three components, firstly, the magnetic volume charge density, \vec{B}_{vol} ,

secondly, the magnetic surface charge density, \vec{B}_1 , of the first surface with radius R_{out} , and finally the magnetic surface charge density, \vec{B}_2 , of the second surface with radius R_{in} . The magnetic flux density as function of the pole pitches of the spherical permanent magnet array is given by.

$$\vec{B}_{vol} = -\frac{\mu_0}{4\pi} \int_{\tau_{p\theta}(p_\theta-1)}^{\tau_{p\theta}P_\theta} \int_{\tau_{p\phi}(p_\phi-1)}^{\tau_{p\phi}P_\phi} \int_{R_{in}}^{R_{out}} \rho_m \nabla \frac{1}{|\vec{r}' - \vec{r}|} \rho'^2 \sin(\theta') d\rho' d\theta' d\phi' \quad (3.74)$$

$$\vec{B}_1 = -\frac{\mu_0}{4\pi} \int_{\tau_{p\theta}(p_\theta-1)}^{\tau_{p\theta}P_\theta} \int_{\tau_{p\phi}(p_\phi-1)}^{\tau_{p\phi}P_\phi} \sigma_{m;1} \nabla \frac{1}{|\vec{r}' - R_{in}|} \rho'^2 \sin(\theta') d\theta' d\phi' \quad (3.75)$$

$$\vec{B}_2 = -\frac{\mu_0}{4\pi} \int_{\tau_{p\theta}(p_\theta-1)}^{\tau_{p\theta}P_\theta} \int_{\tau_{p\phi}(p_\phi-1)}^{\tau_{p\phi}P_\phi} \sigma_{m;2} \nabla \frac{1}{|\vec{r}' - R_{out}|} \rho'^2 \sin(\theta') d\theta' d\phi'. \quad (3.76)$$

The magnetic flux density of one permanent magnet segment is obtained by

$$\vec{B}_{p_\theta:p_\phi} = \vec{B}_{vol} + \vec{B}_1 + \vec{B}_2 \quad (3.77)$$

where the subscript of $B_{p_\theta:p_\phi}$ denotes the magnetic flux density of the p_θ^{th} permanent magnet segment in the θ -direction and p_ϕ^{th} permanent magnet segment in the ϕ -direction. The magnetic flux density of the complete spherical permanent magnet array is calculated by superposition:

$$\vec{B}_{tot} = \sum_{p_\theta=1}^{P_\theta} \sum_{p_\phi=1}^{P_\phi} \vec{B}_{p_\theta:p_\phi}. \quad (3.78)$$

The integrals to obtain the magnetic flux density are solved numerically. Instead of six surfaces, the radial magnetization consists of two numerical surface integrals and a numerical volume integration.

3.5 Imaging

The method of images reduces a boundary-value problem, i.e. with material interfaces, into a free-space problem, i.e. without material interfaces. In this method the material is replaced by image sources that provide the appropriate boundary conditions at the interface. With these image sources, free-space models such as the aforementioned magnetic charge model, can take an interface with a constant radius and a different relative permeability into account.

The position and size of the image source, i.e. the imaged spherically shaped permanent magnet, can be obtained with the method of inversion [50]. This method

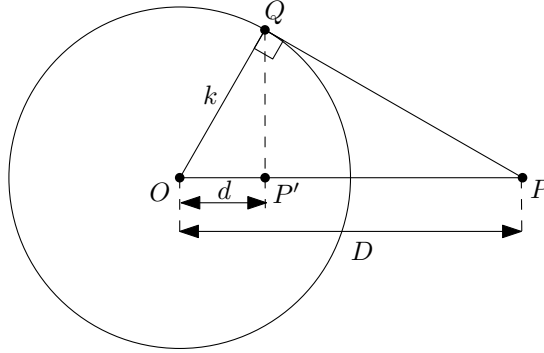


Figure 3.3: The inversion circle theory [50].

can be explained by means of the circle inversion illustrated in Fig. 3.3. From the similar triangles, OQP and OQP' , it follows that

$$\frac{OP}{k} = \frac{k}{OP'} \quad (3.79)$$

where k is the inversion radius. From this equation, it can be derived that

$$dD = k^2. \quad (3.80)$$

A sectional view of a spherical magnet with a continuous boundary is shown in Fig. 3.4a. The equivalent of this figure, according to the method of inversion, is depicted in Fig. 3.4b. Hence, the position of the imaged magnetic charges to model a highly permeable boundary is obtained with this method.

As the geometry of the image source is different with respect to the original source, the magnetic volume charge density and magnetic surface charge density alter. According to the method of inversion, the relation between the radius of the original permanent magnet and imaged permanent magnet is given by

$$\rho'' = \frac{k^2}{\rho} \quad (3.81)$$

where k is the radius of the high permeability boundary, ρ is the radius of the original permanent magnet and ρ'' is the radius of the image source. The magnetic volume charge density of the image source results in [50]

$$\rho_m''(\rho'', \theta, \phi) = \left(\frac{k}{\rho''}\right)^5 \rho_m\left(\frac{k^2}{\rho''}, \theta, \phi\right) \quad (3.82)$$

and the magnetic surface charge density can be obtained by

$$\sigma_m''(\rho'', \theta, \phi) = \left(\frac{k}{\rho''}\right)^3 \sigma_m\left(\frac{k^2}{\rho''}, \theta, \phi\right). \quad (3.83)$$

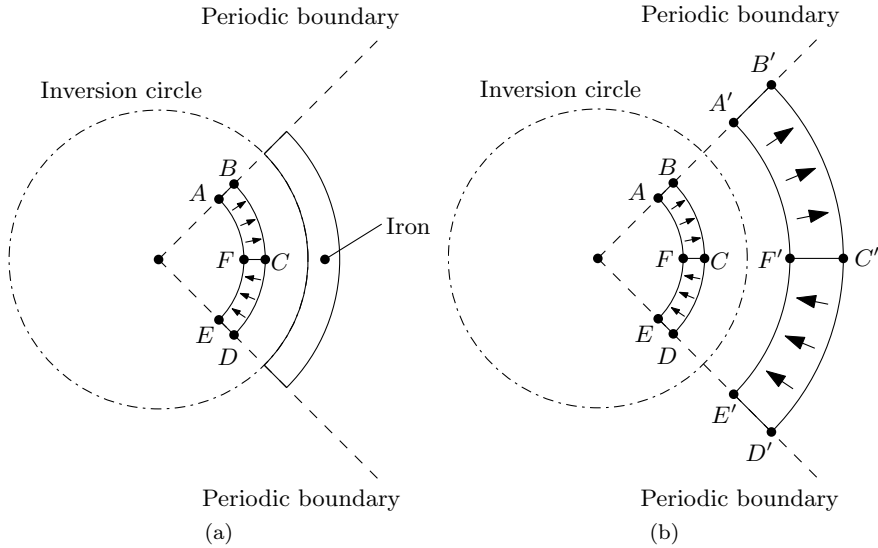


Figure 3.4: Sectional view with continuous boundaries of a spherical permanent magnet array with: (a) the iron boundaries, (b) imaged permanent magnets.

The magnetic flux density of the image source is obtained in the same way as the original source. The complete magnet field solution is obtained by the superposition principle. With this method the magnetic flux density of the region between the spherical permanent magnets and the infinitely permeable boundary can be obtained. The magnetic flux density inside the region that contains the highly permeable material cannot be obtained with this method. Additionally, only a completely enclosed spherical boundary can be included. A region that partially consists of a highly permeable material cannot be included.

3.6 Harmonic modeling

The harmonic modelling method provides a solution to a boundary value problem. A boundary value problem considers multiple regions which can have a different relative permeability μ_r or a source present. Each region is described by differential equations and can be solved by means of separation of variables. This separation results in a harmonic expression for every region. By linking these expressions together with the boundary conditions, the set of equations is solved.

3.6.1 General solution

A Poisson equation has been solved to find the solution to the magnetic scalar potential, (3.15). The solution to this equation depends on the applied magnetization. When an equally distributed magnetization is applied, its divergence is zero which results in a Laplace equation given by

$$\nabla^2 \varphi = 0. \quad (3.84)$$

The homogeneous solution for the Laplace equation can be obtained with the spherical harmonics [35] described by

$$\varphi(\rho, \theta, \phi) = \sum_{n=0}^{\infty} \sum_{m=-n}^n (a\rho^n + b\rho^{-(n+1)}) S_n^m P_n^m(\cos(\theta)) e^{jm\phi} \quad (3.85)$$

where m and n are the harmonic numbers, j is the imaginary unit and, $P_n^m(\cos(\theta))$ is the associated Legendre function of the first kind described by

$$P_n^m(x) = (n - x^2)^{|m|/2} \left(\frac{d}{dx} \right)^{|m|} P_n(x) \quad (3.86)$$

and $P_n(x)$ is the n^{th} Legendre polynomial, defined by the Rodrigues formula:

$$P_n(x) = \frac{1}{2^n n!} \left(\frac{d}{dx} \right)^n (x^2 - 1)^n. \quad (3.87)$$

and S_n^m is a normalization factor defined as,

$$S_n^m = \sqrt{\frac{2n+1}{4\pi} \frac{(n-|m|)!}{(n+|m|)!}}. \quad (3.88)$$

In the literature, the dependencies of θ and ϕ are often abbreviated to [35, 112, 133, 139]

$$Y_n^m(\theta, \phi) = S_n^m P_n^m(\cos(\theta)) e^{jm\phi}. \quad (3.89)$$

To find a solution to the Poisson equation, first a solution to the spherical differential equation (B.7) has to be found. A solution to this equation is presented in [112] by considering only the first three harmonics of a radial magnetization. However, a general solution for a radial magnetization has not been found. Therefore, a harmonic model that can predict the magnetic flux density produced by a radial magnetization is not included in this thesis.

3.6.2 Boundary conditions

For the application of spherical permanent magnet arrays, the problem is divided into spherical shells with different radii. Each different shell represents a region. Certain conditions on the boundaries of these regions should hold to find the magnetic field solution [38].

The boundary conditions depend on the region and the material of the region. Firstly, the magnetic flux density at the origin has to be finite and the far field has to be zero, which results in

$$\vec{B}|_{\rho \rightarrow 0} \neq \infty \quad (3.90)$$

$$\vec{B}|_{\rho \rightarrow \infty} = 0. \quad (3.91)$$

Secondly, the magnetic flux density has to be continuous at the boundaries; this means that the normal component of the magnetic flux density of region i is equal to region $i + 1$ which can be defined in the spherical domain as

$$B_{i\rho} = B_{(i+1)\rho} \quad (3.92)$$

Furthermore, the tangential component of the magnetic field strength has to be continuous. In the 3D domain and in the absence of a free surface current density, this boundary condition can be written in terms of the scalar potential [102, 120] and is given by

$$\varphi_i = \varphi_{(i+1)}. \quad (3.93)$$

Both aforementioned conditions are referred to as continuous boundary conditions. Lastly, when adding a region consisting of highly permeable material [88] it is often assumed that $\mu_r = \infty$. With this assumption it has to hold at the boundary that

$$\varphi_i = 0 \quad (3.94)$$

where the subscript i denotes the region which is adjacent to the region that contains highly permeable material.

The regions that contain highly permeable material have to be completely spherically enclosed with this method. Hence, a region that partially consists of highly permeable material cannot be modeled.

3.6.3 Magnetization description

The magnetization of the spherical permanent magnets is included in the boundary conditions and also in the Poisson equation if $\nabla M \neq 0$. An expression for this

magnetization is found with the spherical harmonics [139] by

$$M_{\kappa}(\theta, \phi) = \sum_{n=0}^{\infty} \sum_{m=-n}^n C_{n;\kappa}^m e^{jm\phi} S_n^m P_n^m(\cos(\theta)) \quad (3.95)$$

where

$$C_{n;\kappa}^m = \epsilon \int_0^{2\pi} \int_0^{\pi} M_{\kappa}(\theta, \phi) \sin(\theta) S_n^m P_n^m(\cos(\theta)) e^{-jm\phi} d\theta d\phi \quad (3.96)$$

where

$$\epsilon = \begin{cases} (-1)^m & \text{if } m \geq 0 \\ 1 & \text{if } m \leq 0 \end{cases}$$

and subscript κ denotes one of the spherical variables ρ , θ or ϕ and, $M_{\kappa}(\theta, \phi)$ is the magnetization vector. Application to a spherical permanent magnet array, the spherical harmonics can be written as

$$C_{n;\kappa}^m = (-1)^m \sum_{p_{\phi}=1}^{P_{\phi}} \sum_{p_{\theta}=1}^{P_{\theta}} (-1)^{p_{\theta}-1} (-1)^{p_{\phi}-1} \int_{\tau_{p_{\phi}}(p_{\phi}-1)}^{\tau_{p_{\phi}} p_{\phi}} \int_{\tau_{p_{\theta}}(p_{\theta}-1)}^{\tau_{p_{\theta}} p_{\theta}} M_{\kappa}(\theta, \phi) \sin(\theta) S_n^m P_n^m(\cos(\theta)) e^{-jm\phi} d\theta d\phi \quad (3.97)$$

where $\tau_{p_{\theta}}$ is the pole pitch in the θ -direction, and $\tau_{p_{\phi}}$ is the pole pitch in the ϕ -direction as indicated in Fig. 3.8. The magnetization of each permanent magnet is modeled separately, and the magnetization of the complete spherical permanent magnet array is obtained by summation of all harmonics. Hence, an uneven permanent magnet array in the ϕ - and θ -direction can be described. Despite an asymmetric array can be modeled, this formulation of the harmonic model cannot account for a hemispherical permanent magnet array. In addition, the integral of this expression can be solved analytically for the ϕ -dependency once the magnetizations are known because this integration concerns a complex exponential function. The integration for the θ -dependency needs to be solved numerically. This expression involves the Legendre functions and, therefore, no analytical expression has been found.

3.6.4 Parallel magnetization

The harmonic model is applied to an example problem considering three regions and an infinitely permeable boundary as illustrated in Fig. 3.5. Regions 1 and 3 contain air, and region 2 is a source region which consists of permanent magnets. Each region has its own general solution for the magnetic scalar potential. This

results in

$$\varphi_i(\rho, \theta, \phi) = \sum_{n=0}^{\infty} \sum_{m=-n}^n (a_{m,i}^n \rho^n + b_{m,i}^n \rho^{-(n+1)}) S_n^m P_n^m(\cos(\theta)) e^{jm\phi} \quad (3.98)$$

where the subscript i of φ_i , $a_{m,i}^n$ and $b_{m,i}^n$ denotes the region. To comply with the boundary condition in the origin (3.90), the coefficient $b_{m,1}^n$ has to be zero. The remaining coefficients can be obtained with the other boundary conditions described by

$$\varphi_1|_{\rho=R_{in}} = \varphi_2|_{\rho=R_{in}} \quad (3.99)$$

$$\varphi_2|_{\rho=R_{out}} = \varphi_3|_{\rho=R_{out}} \quad (3.100)$$

$$\varphi_3|_{\rho=R_s} = 0 \quad (3.101)$$

$$\mu_0 \mu_{r;1} H_{1;\rho}|_{\rho=R_{in}} = \mu_0 \mu_{r;1} H_{2;\rho}|_{\rho=R_{in}} + \mu_0 M_\rho \quad (3.102)$$

$$\mu_0 \mu_{r;2} H_{2;\rho}|_{\rho=R_{out}} + \mu_0 M_\rho = \mu_0 \mu_{r;3} H_{3;\rho}|_{\rho=R_{out}} \quad (3.103)$$

where $\mu_{r;i}$ denotes the permeability of region i . To compare the harmonic model with the magnetic charge model, a relative permeability of one is chosen for this example. In practice, sintered NdFeB permanent magnets have a relative permeability in the order of 1.03-1.10 [129]. By solving the set of equations the solution of the coefficients is given by

$$a_{m;1}^n = M_\rho(\theta, \phi) \frac{R_{in}^{-n} R_s^{-2n-1} R_{out}^{-n} (R_s^{2n+1} (R_{out} R_{in}^n - R_{in} R_{out}^n) + R_{in}^n R_{out}^n (R_{in}^{n+2} - R_{out}^{n+2}))}{(1+2n) S_n^m P_n^m(\cos(\theta)) e^{jm\phi}} \quad (3.104)$$

$$a_{m;2}^n = M_\rho(\theta, \phi) \frac{R_s^{-2n-1} R_{out}^{-n} (R_{out}^n (R_{in}^{n+2} - R_{out}^{n+2}) + R_{out} R_s^{2n+1})}{(1+2n) S_n^m P_n^m(\cos(\theta)) e^{jm\phi}} \quad (3.105)$$

$$b_{m;2}^n = M_\rho(\theta, \phi) \frac{-R_{in}^{n+2}}{(1+2n) S_n^m P_n^m(\cos(\theta)) e^{jm\phi}} \quad (3.106)$$

$$a_{m;3}^n = M_\rho(\theta, \phi) \frac{R_s^{-2n-1} (R_{in}^{n+2} - R_{out}^{n+2})}{(1+2n) S_n^m P_n^m(\cos(\theta)) e^{jm\phi}} \quad (3.107)$$

$$b_{m;3}^n = M_\rho(\theta, \phi) \frac{(R_{out}^{n+2} - R_{in}^{n+2})}{(1+2n) S_n^m P_n^m(\cos(\theta)) e^{jm\phi}}. \quad (3.108)$$

With these coefficients the magnetic flux density in all three regions can be calculated. Hence, the magnetic flux density in region 3 results in

$$B_{3;\rho}(\rho, \theta, \phi) = \sum_{n=0}^{\infty} \sum_{m=-n}^n -\frac{\mu_0 C_{n;\rho}^m}{2n+1} \rho^{-n-2} R_s^{-2n-1} (R_{in}^{n+2} - R_{out}^{n+2}) \\ (n\rho^{2n+1} + (n+1)R_s^{2n+1}) S_n^m P_n^m(\cos(\theta)) e^{jm\phi} \quad (3.109)$$

$$B_{3;\theta}(\rho, \theta, \phi) = \sum_{n=0}^{\infty} \sum_{m=-n}^n \frac{\mu_0 C_{n;\theta}^m}{2n+1} \frac{\rho^{-n-2}}{\sin(\theta)} R_s^{-2n-1} (\rho^{2n+1} - R_s^{2n+1}) \\ (R_{in}^{n+2} - R_{out}^{n+2}) S_n^m((n+1)\cos(\theta)P_n^m(\cos(\theta)) \\ + (m-n-1)P_{n+1}^m(\cos(\theta))) e^{jm\phi} \quad (3.110)$$

$$B_{3;\phi}(\rho, \theta, \phi) = \sum_{n=0}^{\infty} \sum_{m=-n}^n -\frac{\mu_0 C_{n;\phi}^m}{2n+1} \frac{jm}{\sin(\theta)} \rho^{-n-2} R_s^{-2n-1} (\rho^{2n+1} - R_s^{2n+1}) \\ (R_{in}^{n+2} - R_{out}^{n+2}) S_n^m P_n^m(\cos(\theta)) e^{jm\phi} \quad (3.111)$$

The harmonic model provides a solution in terms of a finite number of harmonic components. For the presented harmonic model, an analytical expression is found for the dependency in the ϕ -direction, whereas the dependency in the θ -direction is solved numerically. An analytical solution for the integration of the Legendre function to obtain the variable $C_{n;\kappa}^m$ is not known. This numerical integration depends on the integration step size in the θ -direction and the harmonic numbers. Consequently, the calculation time mainly depends on the number of harmonics taken into account. Therefore, the time to calculate one harmonic is taken as a measure to indicate the time performance of this method.

If two regions are considered (only regions 2 and 3 in Fig. 3.1), and the center is modeled as infinitely permeable material as presented in [88], the expression for the coefficients are less susceptible for an arithmetic overflow. Furthermore, when the relative permeability of multiple regions are taken into account, the complexity increases significantly. Due to this complexity, the expression for the magnetic flux density earlier reaches an arithmetic overflow. This overflow is caused by an expression such as $(n+1)R_s^{2n+1}$ in (3.109). This operation is returned as infinite when the number of harmonics becomes too high. The influence of this overflow is shown in the next sections.

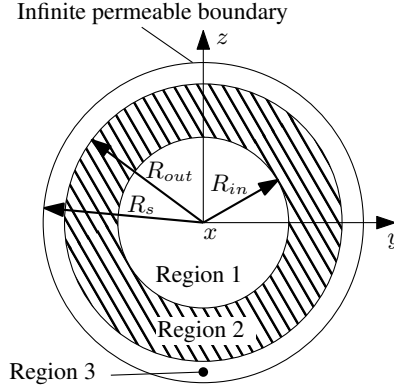


Figure 3.5: Regions and geometric parameters definitions of a spherical permanent magnet array with an infinitely permeable boundary.

Table 3.1: Geometric parameters of the benchmark topologies

Parameter	Value	Unit	Description
R_{in}	40	[mm]	Inner radius of the benchmark
R_{out}	55	[mm]	Outer radius of the benchmark
R_s	56	[mm]	Infinite permeable boundary radius
B_r	1.3	[T]	Remanent magnetic flux density
μ_r	1	[-]	Relative permeability

3.7 Benchmark topology

The derived semi-analytical models are applied to a benchmark model to compare their accuracy and limitations. This benchmark consists of 32 spherically shaped permanent magnets as shown Fig. 3.6 and has the same three regions for the modeling example as illustrated in Fig. 3.5. The spherical permanent magnets have an angular size of $\tau_{p\theta} = 45^\circ$ and $\tau_{p\phi} = 45^\circ$. Due to the spherical shape they do not have equal volumes. To comply with the assumptions of the magnetic charge model, both benchmarks consist of a free-space problem considering a relative permeability of one. To validate the results, the FEA is also carried out with a relative permeability of one. The dimensions of this benchmark model are listed in Table 3.1.

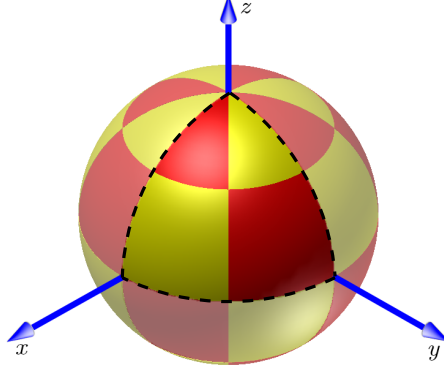


Figure 3.6: Spherical permanent magnet structure to validate the modeling techniques consisting of 32 permanent magnets.

3.7.1 Parallel magnetization

The function to characterize the parallel magnetization vector is derived in the Cartesian coordinate system. In this coordinate system, the magnetization vector of each permanent magnet can be described with the angles λ_θ and λ_ϕ as indicated in Fig. 3.7. For the benchmark model, the angles are chosen in the centre of each spherical permanent magnet segment and are obtained with

$$\lambda_\theta = \frac{\pi}{P_\theta} \left(p_\theta - \frac{1}{2} \right) \quad (3.112)$$

$$\lambda_\phi = \frac{2\pi}{P_\phi} (p_\phi - 1) \quad (3.113)$$

where P_θ is the total number of permanent magnets in the θ -direction, $p_\theta = 1, 2, \dots, P_\theta$, P_ϕ is the total number of permanent magnets in the ϕ -direction and $p_\phi = 1, 2, \dots, P_\phi$. Based on these angles the Cartesian components of the magnetization vector are given by

$$\vec{M}_0 = \begin{bmatrix} M_x \vec{e}_x \\ M_y \vec{e}_y \\ M_z \vec{e}_z \end{bmatrix} = \begin{bmatrix} M_0 \sin(\lambda_\theta) \cos(\lambda_\phi) \vec{e}_x \\ M_0 \sin(\lambda_\theta) \sin(\lambda_\phi) \vec{e}_y \\ M_0 \cos(\lambda_\theta) \vec{e}_z \end{bmatrix} \quad (3.114)$$

where $M_0 = \frac{B_r}{\mu_0}$ and B_r is the remanent magnetic flux density of the permanent magnets. The magnetization vector is converted to the spherical coordinate system, as described in (A.1), for the harmonic model, which results in

$$\vec{M}_0 = (-1)^{p_\theta + p_\phi} M_0 \begin{bmatrix} (\cos(\lambda_\phi - \phi) \sin(\lambda_\theta) \sin(\theta) + \cos(\lambda_\theta) \cos(\theta)) \vec{e}_\rho \\ (\cos(\lambda_\phi - \phi) \sin(\lambda_\theta) \cos(\theta) - \cos(\lambda_\theta) \sin(\theta)) \vec{e}_\theta \\ \sin(\lambda_\theta) \sin(\lambda_\phi - \phi) \vec{e}_\phi \end{bmatrix}. \quad (3.115)$$

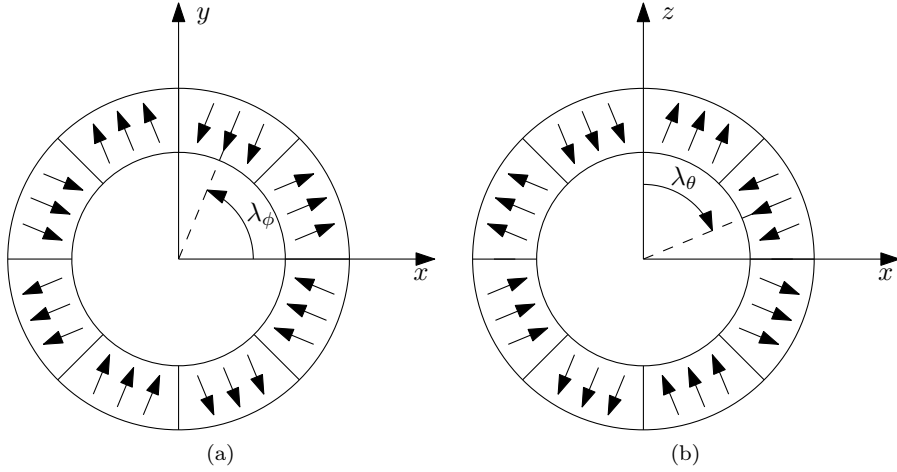


Figure 3.7: The 2D projection of the benchmark topology with a parallel magnetization in the xy -plane (a), and zx -plane (b).

3.7.2 Radial magnetization

The radial magnetization of a sphere can be defined directly in the spherical coordinate system. As the word radial already suggests the direction of the magnetization vector of each permanent magnet is in the ρ -direction. The resulting 2D projection of the benchmark with a radial magnetization is shown in Fig. 3.8. This magnetization pattern can be described by

$$\vec{M}_0 = \begin{bmatrix} (-1)^{p_\theta+p_\phi} M_0 \vec{e}_\rho \\ 0 \vec{e}_\theta \\ 0 \vec{e}_\phi \end{bmatrix} \quad (3.116)$$

where $p_\theta = 1, 2, \dots, P_\theta$, $p_\phi = 1, 2, \dots, P_\phi$, P_θ is the total number of permanent magnets in the θ -direction and P_ϕ is the total number of permanent magnets in the ϕ -direction.

A radial magnetization in a spherical direction poses some manufacturing challenges. For anisotropic material, a radial magnetic field has to be applied during the manufacturing process. If an isotropic material is used, a magnetizer that can produce a radial field is required to create this magnetization.

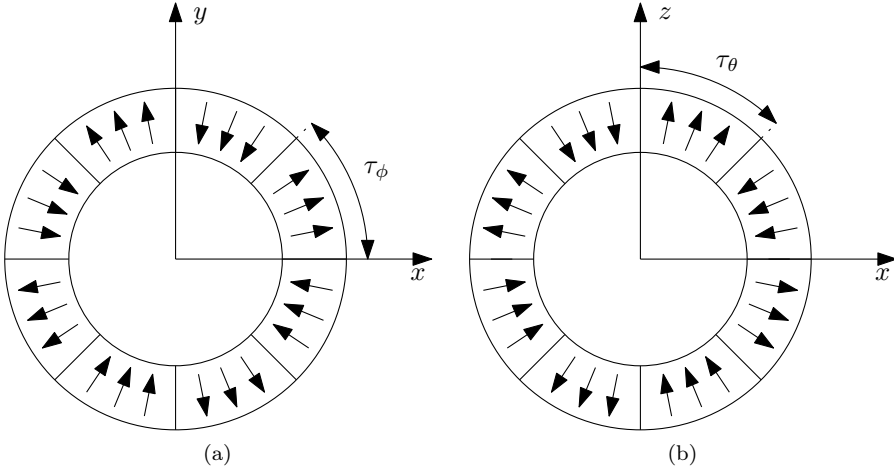


Figure 3.8: The 2-D projection of the benchmark topology with a radial magnetization in the xy -plane (a), and zx -plane (b).

3.8 Comparison

The magnetic flux density of the benchmark topology is obtained with the magnetic charge model, harmonic model and the commercial FEA software Maxwell. This benchmark has 32 spherical permanent magnets for which a radial and parallel magnetization is considered. Since no harmonic expression is found to model a radial magnetization, the harmonic model is not included in the comparison of this magnetization.

The magnetic flux density on the radius of 56 mm is calculated. An airgap of 1 mm is simulated with this radius. The results are shown over a range of $\theta = 0^\circ$ - 90° and $\phi = 0^\circ$ - 90° as indicated in Fig. 3.6.

3.8.1 Parallel magnetization

Application to the unbounded benchmark topology

The magnetic flux density of the benchmark model, predicted with the magnetic charge model, is shown in Fig. 3.10. These results are obtained with a numerical integration $d\theta = \pi/N$ and $d\phi = 2\pi/2N$ where N is 300. This integration step size is determined for a rms discrepancy below 0.1%. The convergence of the numerical integration as function of the integration step N is shown in Fig. 3.9. The applied numerical integration step size corresponds with a spatial step size of 0.42 mm for

the surfaces at R_{in} and 0.58 mm for the surfaces at R_{out} . The resulting calculation time for this step size is equal to 0.36 s for each observation point. In addition, this integration step can be decreased further because the magnetic charge model is not numerically limited. Therefore, the discrepancy of the harmonic model and FEA is obtained with respect to the magnetic charge model. This discrepancy is calculated by

$$\epsilon_{\text{rms}} = \frac{\text{rms}(B_{ref}) - \text{rms}(B)}{\text{rms}(B_{ref})} \quad (3.117)$$

where B is the magnetic flux density compared to the reference magnetic flux density B_{ref} .

The obtained discrepancy between the harmonic model and the magnetic charge model is shown in Fig. 3.11. These results are obtained with a numerical integration of $d\theta = \pi/300$. This integration step resulted in a calculation time per harmonic of 0.071 s. For the obtained results a maximum of 149 harmonics could be taken into account. This corresponds with a spatial period of 2.4 mm. Increasing the number of harmonics resulted in an arithmetic overflow. This can be avoided with numerical methods, however, this also increases the computation time. The discrepancy with the harmonic model shows a remainder of the harmonic description due to the limited number of harmonics that can be taken into account. Further, there is the Gibbs effect [30] that occurs at the transition between the spherical permanent magnet segments. The discrepancy of the harmonic model with respect to the magnetic charge model is calculated with (3.117). The resulting discrepancies, listed in Table 3.2, are within 0.03%. Hence, it can be concluded that the harmonic method and the charge modeling are in very good agreement with each other.

The resulting discrepancy between the obtained results from the FEA and the magnetic charge model is shown in Fig. 3.11. These results show a small amplitude difference for the radial magnetic flux density of 7.9 mT. Furthermore, numerical noise of the FEA and the numerical integration of the magnetic charge model is visible. The discrepancies as listed in Table 3.2 of the magnetic flux density components are all within 1%.

FEA discretizes the problem into elements to approximate the solution of the complete problem. The accuracy of this model depends on the distribution of the mesh elements. When the complete solution is obtained, the magnetic flux density on each arbitrary point can be interpolated. The simulation time of FEA strongly depends on the number of mesh elements used to solve the problem. A mesh of 2 mm was assigned at a radius of 56 mm. The total number of 947015 mesh elements required a simulation time of 39.5 min. For this simulation, FEA was limited by the 16GB of internal memory of the pc.

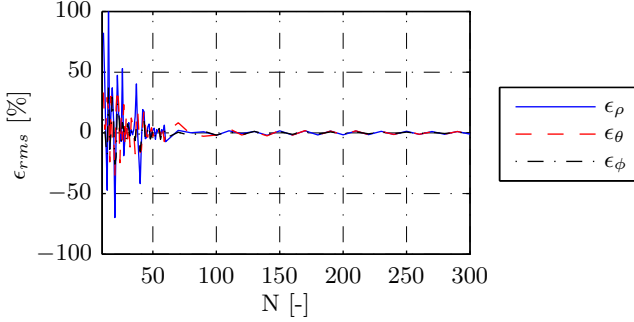


Figure 3.9: Convergence of the numerical integration of the magnetic charge model.

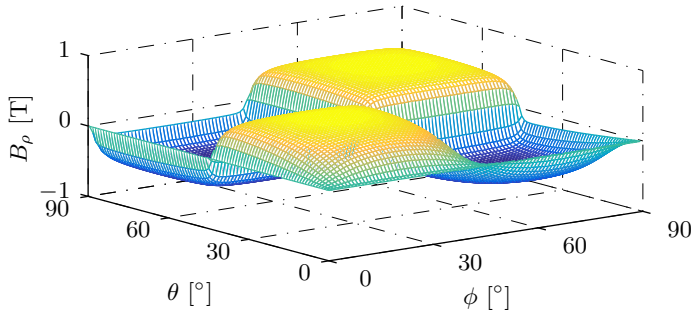
Application to the bounded benchmark topology

An region of infinite permeable material encloses the benchmark topology to evaluate the magnetic charge model in combination with spherical imaging. The magnetic flux density at this boundary is evaluated where a zero tangential field is assumed, therefore, only the radial magnetic field component is considered in this analysis. The radius of this boundary is 56 mm and is listed with the rest of the geometry properties in Table 3.1.

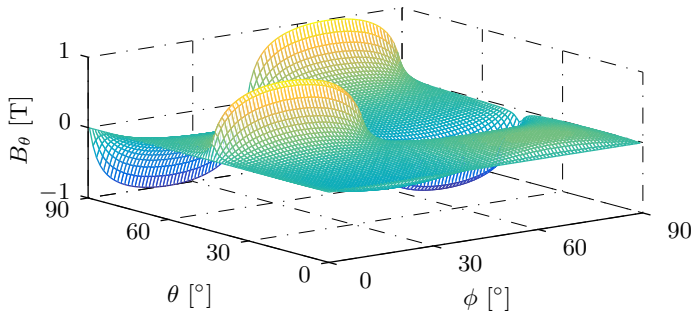
The obtained magnetic flux density with the magnetic charge model is shown in Fig. 3.12. These results show a magnetic flux density increase of 47% by adding an infinite permeable boundary. For the numerical integration it is chosen that $d\theta = \pi/N$ and $d\phi = 2\pi/2N$ where $N=300$. This resulted in a 0.72 s calculation time per observation point including the original source and image source. This time is doubled with respect to the unbounded benchmark topology due to the imaged sources.

The harmonic model has a discrepancy with the magnetic charge model as shown in Fig. 3.12. In this figure the remainder of the harmonic description is visible in the ϕ -direction and the Gibbs effect is present. Due to the inclusion of an infinitely permeable boundary, the number of harmonics is limited to 122 before reaching the arithmetic overflow. This corresponds with a spatial period of 2.9 mm. The discrepancy with respect to the magnetic charge model is equal to 1.6%; hence, the models are in good agreement of each other.

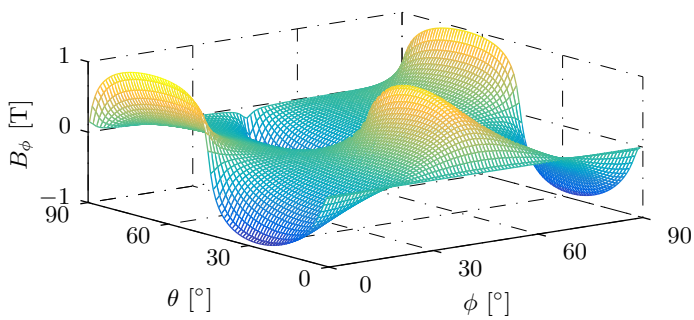
In the FEA, a region with a relative permeability of $\mu_r = 4000$ is simulated that surrounds the permanent magnet array. In this analysis, a mesh size of 2 mm is assigned at the boundary. This result in a discrepancy as shown in Fig. 3.12c with respect to the magnetic charge model. In this simulation, 1185710 mesh elements are used and a calculation time of 35.7 min is required. In this figure mostly numerical noise is visible and a small amplitude of about 7 mT is present. The



(a)



(b)



(c)

Figure 3.10: Magnetic flux density of the unbounded benchmark topology obtained with the magnetic charge model at a radius of 56 mm in the third region of component: (a) B_ρ , (b) B_θ , and (c) B_ϕ .

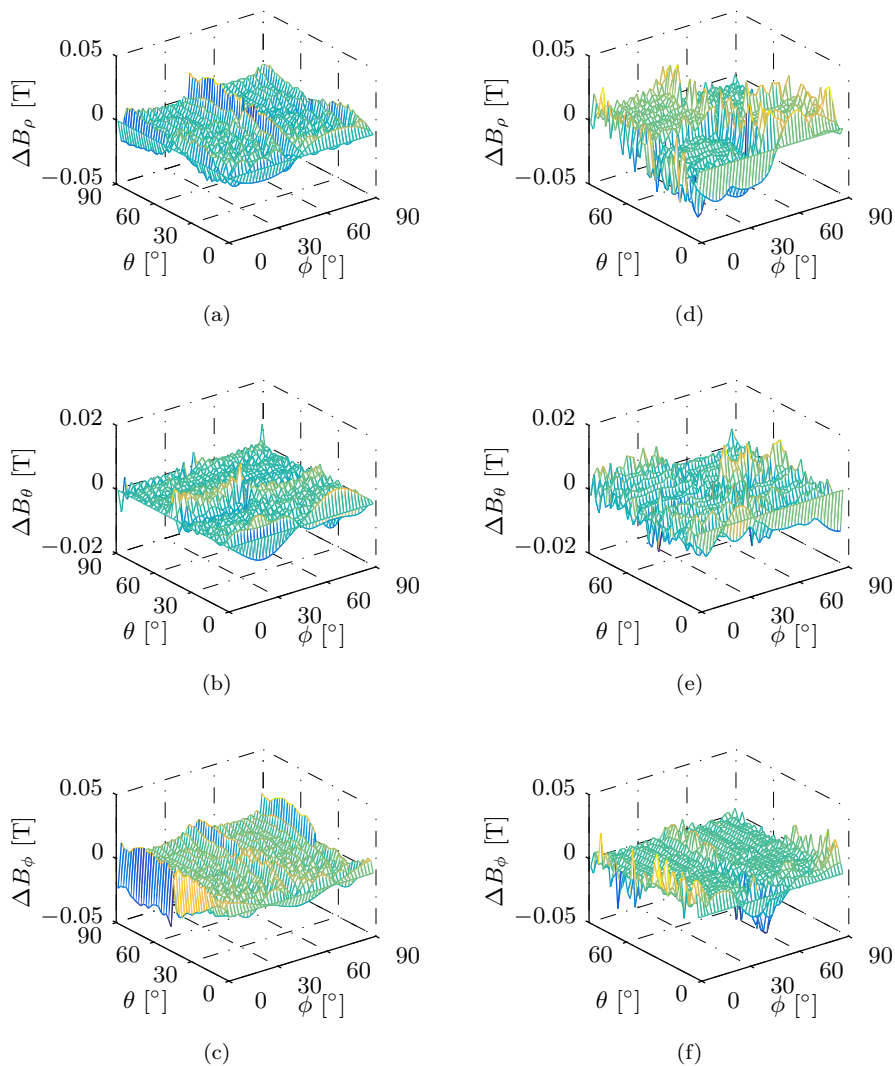


Figure 3.11: The discrepancy of the magnetic charge model with respect to the harmonic model: (a) ΔB_ρ , (b) ΔB_θ , (c) ΔB_ϕ , and to the FEA: (d) ΔB_ρ , (e) ΔB_θ , (f) ΔB_ϕ .

Table 3.2: The rms discrepancy of FEA and the harmonic modeling with respect to the magnetic charge models considering the 32 spherical permanent magnet array with a parallel magnetization Table 3.1, Fig. 3.11.

Boundary	Modeling method	B_ρ [%]	B_θ [%]	B_ϕ [%]
Unbounded	Harmonic	0.025	0.028	0.0017
	FEA	1.0	0.63	0.88
Bounded	Harmonic	1.6	-	-
	FEA	1.6	-	-

discrepancy is the highest at the transitions between the permanent magnets.

3.8.2 Radial magnetization

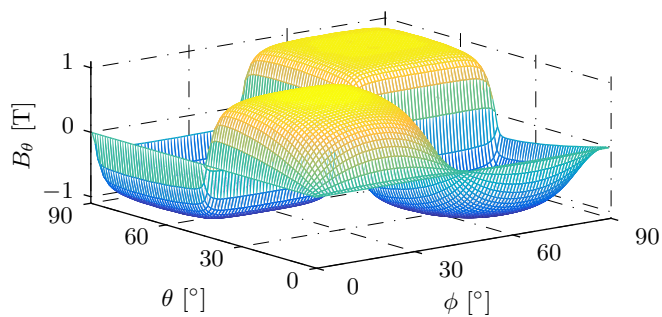
A radial magnetization is modeled with the magnetic charge model and FEA. Since no semi-analytical harmonic expression is found for the radial magnetization, this model is not included for the comparison of the radial magnetizations.

The magnetic flux density is obtained with the magnetic charge model and the results are shown in Fig. 3.13. These results show a concave radial magnetic flux density, whereas with a parallel magnetization a convex radial magnetic flux density is produced. The amplitude of the radial magnetic flux density is 20% smaller compared to the parallel magnetization.

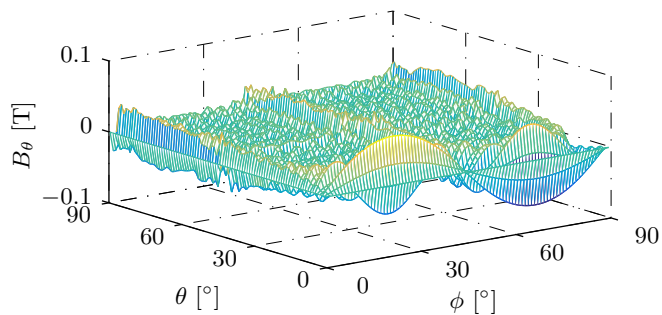
For the magnetic charge densities, a numerical integration step of $d\theta = \pi/N$ and $d\phi = 2\pi/2N$ with $N = 300$ is used. An numerical integration of the volume charge density is performed with $d\rho = R_{out}/N$, $d\theta = \pi/N$ and $d\phi = 2\pi/2N$ where N is 150. The convergence is below 0.1% with this numerical integration step size. The calculation time is equal to 0.60 s for each observation point. The computation time per observation point is 1.3 s for the method of imaging. In comparison to the unbounded benchmark topology, this time is more than twice the simulation time because the imaged geometry is larger and the integration step is kept equal. Furthermore, the volume charge density which requires a numerical volume integration. Due to this integration, more computation time is necessary. Hence, there is a trade of between accuracy and computation time.

The discrepancy between the two modeling techniques is shown in Fig. 3.14. The majority of the visible discrepancy is noise and the visible amplitude of the radial magnetic flux density is neglectable small. The simulation time of FEA is 36 min with an assigned mesh of 2 mm at the boundary.

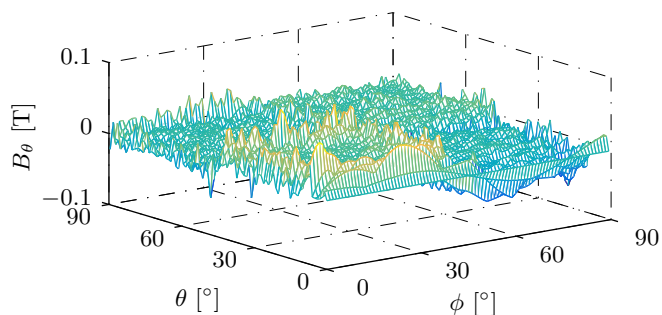
The rms discrepancies of the unbounded and unbounded benchmark topologies with a radial magnetization are obtained with (3.117) and listed in Table 3.3. For



(a)



(b)



(c)

Figure 3.12: Application to the bounded benchmark topology: (a) Radial magnetic flux density at $R_s = 56$ mm obtained with the magnetic charge model, (b) discrepancy between the harmonic model and magnetic charge model, (c) discrepancy between FEA and the magnetic charge model.

Table 3.3: The rms discrepancy of the FEA with respect to the magnetic charge models considering the benchmark topology with 32 radial magnetized permanent magnets

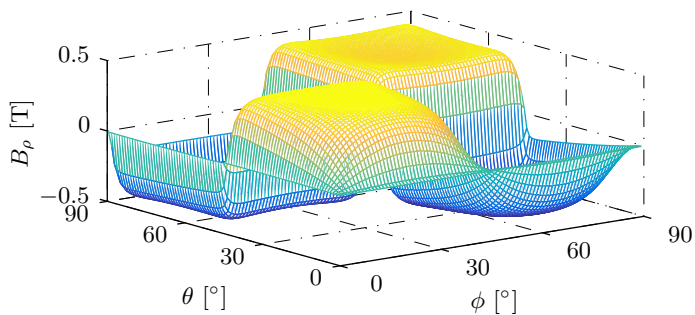
Boundary	B_ρ [%]	B_θ	B_ϕ
Unbounded	1.4	1.0	1.3
Bounded	3.8	-	-

the unbounded topology, the magnetic charge model and FEA have a discrepancy within 2%. Hence they are in good agreement with each other. For the bounded topology, a discrepancy of 3.8% is obtained; hence, also for this topology the models are in good agreement.

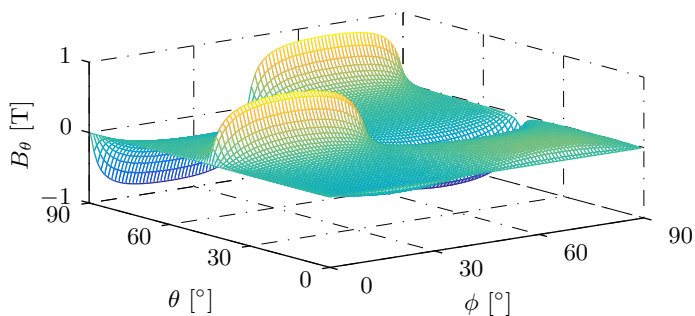
3.9 Conclusions

Two different 3D semi-analytical models to obtain the magnetostatic field solution of spherical magnetic structures have been presented. The scalar potential, obtained from Maxwell's equations, is solved by separation of variables resulting in a harmonic model and by the free-space Green's function resulting in a magnetic charge model. With these semi-analytical models the interaction between multiple spherical permanent magnets or with coils can be obtained. The effect of this interaction can be predicted in terms of force and torque with the Lorentz force method and the Maxwell stress tensor. It has been shown that the Lorentz force method only requires the radial magnetic flux density to obtain the torque for spherical magnetic structures. In addition, the Maxwell stress tensor has been derived from the Lorentz force law in the spherical coordinate system.

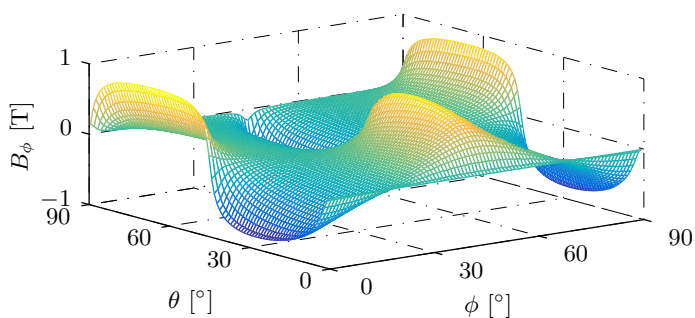
The magnetic charge model is implemented in the spherical coordinate system to model parallel and radial magnetizations. The radial magnetization requires the inclusion of the magnetic volume charge density. Furthermore, these models are extended with spherical imaging by applying the method of inversion; hence, the magnetic charge model can account for an infinitely permeable boundary for both magnetizations. In addition, the field solution in each observation point is obtained for each permanent magnet individually, and by superposition the total field solution is found. Therefore, this method provides a high flexibility because partially spherical permanent magnet arrays can be taken into account. This model is completely solved numerically. A higher accuracy than the presented harmonic model and FEA can be achieved because in the magnetic flux density prediction of the benchmark topology it has not been numerically limited. The FEA was limited by the internal memory of the computer, and the harmonic model had an arithmetic overflow at a certain number of harmonics.



(a)



(b)



(c)

Figure 3.13: Magnetic flux density results of the unbounded benchmark topology with 32 radial magnetized permanent magnets obtained with the magnetic charge model at a radius of 56 mm of component: (a) B_ρ , (b) B_θ , and (c) B_ϕ .

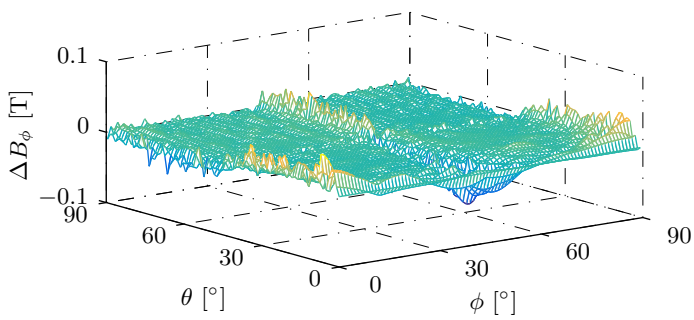
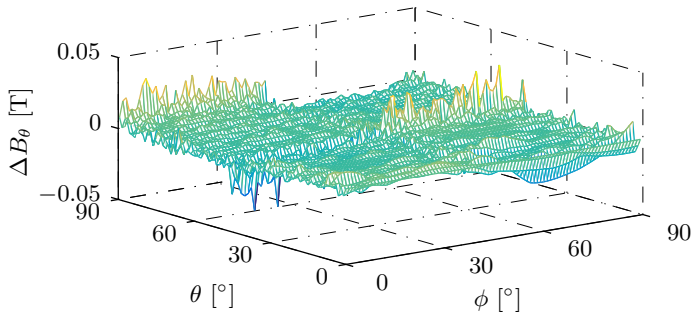
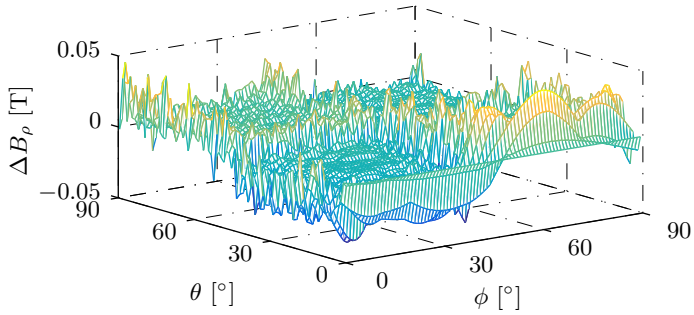


Figure 3.14: Discrepancy between the charge model and FEA of the unbounded benchmark topology with 32 radial magnetized permanent magnets of component: (a) ΔB_ρ , (b) ΔB_θ , and (c) ΔB_ϕ .

A harmonic model has been presented that can include a boundary of highly permeable material and is extended to account for asymmetrical permanent magnet arrays. In contrast to the magnetic charge model, the presented harmonic model cannot account for hemispherical permanent magnet arrays. However, the magnetic flux density of an array with an uneven number of permanent magnets can be predicted. Due to the numerical limitations a maximum number of harmonics that can be taken into account, the solution of the benchmark always has a certain discrepancy.

The magnetic charge model and harmonic model are applied to a spherical permanent magnet array containing 32 permanent magnets. The magnetic flux density produced by a parallel magnetization is obtained with both semi-analytical models and FEA. For both the bounded and unbounded benchmark topology, a maximum discrepancy of 1.6% has been achieved between the models; hence, the three modeling methods are in good agreement with each other. The presented harmonic model cannot include a radial magnetization and, therefore, the magnetic flux density of the spherical permanent magnet array has been obtained with the magnetic charge model and FEA. For this magnetization a discrepancy within 4% has been calculated and it can be concluded that both models are in good agreement with each other.

Chapter 4

Spherical magnetic gravity compensator

Abstract - A passive gravity compensator that is integrated in an actuator could significantly reduce the power consumption in robotic applications. To compensate for the gravity, a rotational spherical magnetic spring is investigated. This spring is constructed out of two concentric hemispherical permanent magnets. All combinations of a parallel and radial magnetization are investigated to find the topology which has the required torque characteristic. Consequently, the spring topology with a parallel and radial magnetization is designed as a gravity compensator for an arm support application.

This chapter is based on

- B. van Nindhuijs, B. L. J. Gysen, J. W. Jansen, and E. A. Lomonova, "Multi-degree-of-freedom spherical permanent-magnet gravity compensator for mobile arm support systems," *IEEE Transactions on Industry Applications*, vol. 50, nr.6, pp. 3628-3636, 2014.
- B. van Nindhuijs, B. L. J. Gysen, J. W. Jansen, and E. A. Lomonova, "Gravity compensation using a spherical magnetic spring," patent 2015/0137923, 2015.
- B. van Nindhuijs, B. L. J. Gysen, J. W. Jansen, and E. A. Lomonova, "Multi-degree-of-freedom spherical permanent magnet gravity compensator for mobile arm support systems," *Proceedings of the 2013 IEEE International Electric Machines and Drives Conference (IEMDC)*, Chicago, Illinois, May 12-15, pp. 1443-1449, 2013.

4.1 Passive compensation

The gravity is a constant force in a known direction. Therefore, this force can be compensated passively to reduce the required power consumption of a system. For devices that operate only in a plane perpendicular to the gravity force, such as vibration isolators [53, 142] and tray systems [58], this force is equal to the gravity force. Idealized, these systems have zero stiffness in all directions. The vibration isolator presented in [53] creates positive and negative stiffness with permanent magnets to suspend a mass of 750 kg. This system is designed for minimal stiffness with an achieved power consumption of only 0.3 W to keep the mass in position. Devices such as a robotic arm with only rotational joints that operate in the complete three dimensional space have to compensate for the gravity with a varying counteracting force.

In contrast to the aforementioned gravity compensators, a variable force/torque is required to provide gravity compensation during rotational movement. In Chapter 2 it is shown that there is a sinusoidal relation between the necessary torque and the angle formed by the arm and the axis of gravity. However, the compensation torque is not position dependent for motion in the plane perpendicular to the gravity force. Hence, a constant torque (zero stiffness) is required. A compensator design for a smart arm-support system has to comply with both requirements. Therefore, a rotational spring with multi-degrees of freedom is required.

With permanent magnets, a magnetic spring can be realized. The repulsion of two equal poles or the attraction of two different poles provides a positive or negative stiffness, respectively. The force is produced by the interaction between the magnetic fields of the magnets and contact is not necessary. The torque is reduced proportionally to the square of the magnetic field which decreases rapidly and nonlinearly as function of the distance to the magnet. Therefore, linear systems as illustrated in Fig. 4.1a can have difficulties coping with a large stroke. The production of torque and force can be manipulated by changing the configuration of the permanent magnets. Hence, spring configurations can be designed for linear and rotary motion. Multiple spring designs are presented in [109] from a simple two pole vertical spring as illustrated in Fig. 4.1a to multipole permanent magnet array designs for linear motion. In the patent of [97] multiple magnetic spring topologies are proposed such as a magnetic spring for rotational movement with multiple equilibrium points. One of these topologies consists of two cylindrical quasi-Halbach arrays as illustrated in Fig. 4.1b. The torque as function of the displacement has a period of 120° with a total of three equilibrium positions. Because the cylinders are concentric, the distance between both magnet arrays (the airgap) does not change in contrast to the topology for linear motion as illustrated in Fig. 4.1a. Another shape besides a cube and cylindrical, is a sphere. A magnetic spring constructed out of concentric spherically shaped permanent magnets as illustrated in Fig. 4.2 allows rotation about the three Cartesian axes.

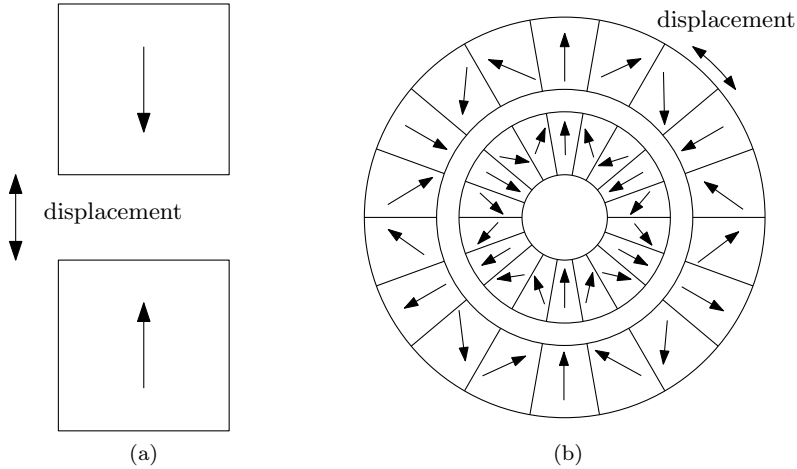


Figure 4.1: Examples of magnetic spring topologies for: (a) linear motion, (b) rotational motion.

In this chapter, a spherical magnetic spring is designed to provide gravity compensation in a robotic arm application. The spherical gravity compensator is designed for the robotic application of a smart arm-support system. The ball and socket joint construction of the spherical gravity compensator, which is similar to the human shoulder joint, enables it to provide the required support specified for the smart arm-support system. Especially the ability to provide multiple degrees of freedom is beneficial in mimicking the shoulder in particular.

4.2 Specifications

The specifications to provide gravity compensation in an arm-support system are derived from the human shoulder joint analysis presented in Chapter 2. In this analysis it is shown that to compensate for the gravity, a sinusoidal torque is required. In the spherical coordinate system, the sinusoidal torque is necessary for $T_\phi(\theta, \phi)$ as function of θ . For motion in a plane perpendicular to the gravity force which corresponds to $T_\phi(\theta, \phi)$ as function of ϕ zero stiffness is required. The coordinate definitions of θ and ϕ are shown in Fig. 4.2. Furthermore, the torque $T_\theta(\theta, \phi)$ has to be zero, otherwise this would create a movement about the z -axis. The amplitudes of the sinusoidal torque characteristic for multiple scenarios are listed in Table 2.8. For the gravity compensator design it is assumed that the elbow is bent at 90° during most of the time during the activities of daily living. For this scenario, it is shown that a torque of 10 Nm is required to compensate for the mass

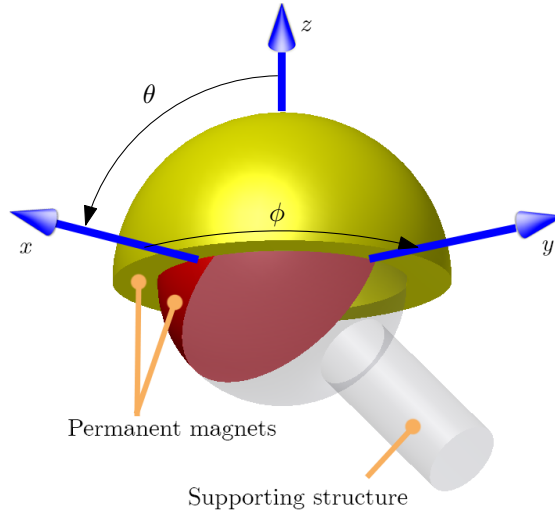


Figure 4.2: Proposed spherical permanent magnet gravity compensator.

of the human arm. For the mass of the arm support itself including an actuator to actively control the shoulder joint, an additional 2 Nm is added. Hence, a total torque of 12 Nm is required from the gravity compensator. In this arm support design no actuation for the elbow joint is taken into account. However, if an elbow actuation of 2 kg is added an average additional torque of 7 Nm is required.

4.3 Spherical magnetic spring design

The properties of the human arm show two equilibrium points, when the arm is at rest position (stable point) and when the arm is pointing upwards parallel to the gravity force (unstable point). The angle between these points is $\beta = 180^\circ$, where β is in the opposite direction of θ as shown in Fig. 4.2. To provide these equilibrium points, the gravity compensator can consist of only two permanent magnets that rotate with respect to each other. According to the maximum range of motion (β) $0 - 90^\circ$, the gravity compensator will only cross one equilibrium point namely, the rest position. For the gravity compensator this is an unstable point because according to (2.5) an increasing torque is required when moving out of this position. This behavior can be provided with two spherically shaped permanent magnets with an opposite magnetization direction. In this direction, the gravity compensator has a negative rotational stiffness, whereas the motion in the γ -direction requires zero rotational stiffness (as defined in Fig. 2.10). The angle γ is equal to the ϕ -direction. To realize zero rotational stiffness, a symmetrical mag-

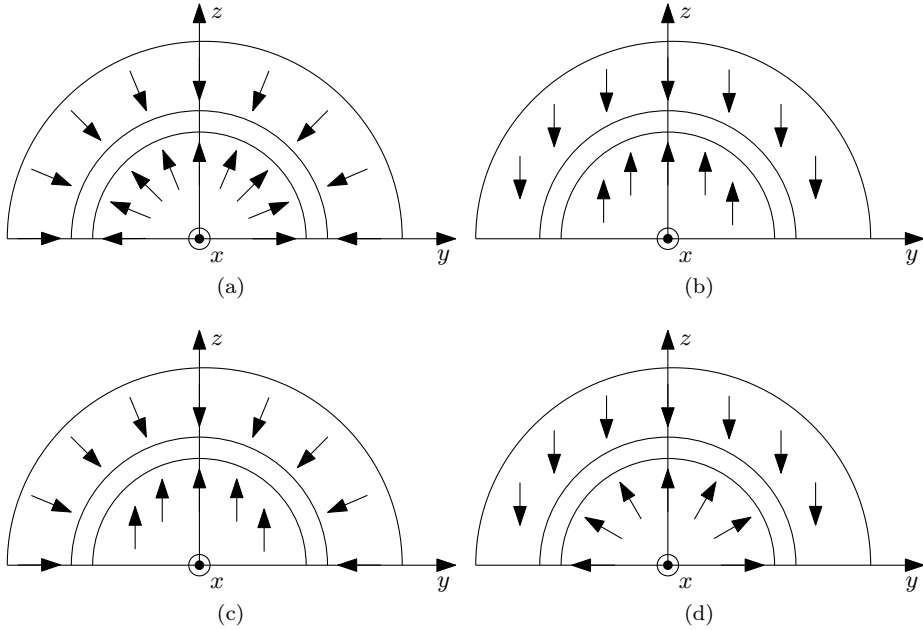


Figure 4.3: The magnetization topologies of the outer and the inner hemispheres: (a) radial-radial, (b) parallel-parallel, (c) radial-parallel, (d) parallel-radial.

netization configuration about the z -axis is employed. Hence, the magnetization direction with respect to each other does not change when one of the permanent magnets is rotated about this axis.

For the initial spring design, two permanent magnets with a hemispherical geometry are chosen for practicality reasons. The specified torque characteristic has a rotational period of 180° . This period corresponds to a hemispherical and a full spherical shape of the permanent magnets. For the inner permanent magnet a hemispherical shape is preferred because it is easier to mount it on a supporting structure as indicated in Fig. 4.2. The outer permanent magnet has an hemispherical shape because it otherwise cannot achieve the specified range of motion. For example, a full spherical shape for the outer permanent magnet interferes with the supporting structure of the inner permanent magnet.

The research on gravity compensators and magnetic springs shows that the force and torque characteristics depend on the magnetization combination chosen. Examples of such combinations are aligned magnetizations [109], perpendicular magnetizations [142] or the usage of a combination of both in for example a quasi-Hallbach magnet array [5, 54]. For the spherical spring, a magnetization in the radial (spherical) direction, parallel (axial) direction and the combination of both

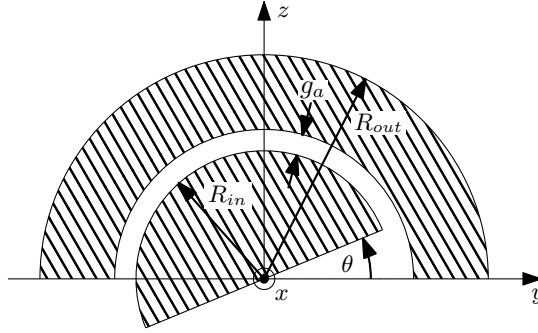


Figure 4.4: The magnetic gravity compensator geometry parameters.

Table 4.1: Geometric parameters of the investigated gravity spherical springs

Parameter	Value	Unit	Description
R_{in}	25	[mm]	Outer radius of the inner magnet
g_a	1	[mm]	Airgap length
R_{out}	36	[mm]	Outer radius of the outer magnet
B_r	1.3	[T]	Remanent magnetic flux density
μ_r	1	[-]	Relative permeability

as illustrated in Fig. 4.3 are investigated.

The geometric parameters which are listed in Table 4.1 and defined in Fig. 4.4 are applied for the evaluation of the magnetization combinations. The resulting torque characteristics of the compensator topologies are shown in Figs. 4.5 through 4.8. The results have been obtained with the magnetic charge model and the torque is predicted with the Maxwell stress tensor in the airgap. All topologies have no torque production for $T_\theta(\theta, \phi)$. The torque, $T_\phi(\theta, \phi)$, shows different torque characteristics that all have zero stiffness as function of ϕ .

A radial magnetization for both hemispheres, as shown in Fig. 4.3a, results in a square wave torque characteristic and is presented in Fig. 4.5. The radial magnetization creates an constant magnetic flux distribution in the airgap of both hemispheres. This topology provides a square-wave torque characteristic and, therefore, has almost zero stiffness over a range from $\theta = 20^\circ$ to $\theta = 160^\circ$. This torque behavior corresponds with gravity compensators as used for vibration isolators as presented in [53]. However, this is not the desirable characteristic for a robotic arm. When the topology arrives at its meta-stable (initial position) and stable position the torque goes relatively fast to zero.

With a parallel magnetization for both permanent magnets as shown in Fig. 4.3b, a torque as visualized in Fig. 4.6 has been found. With the combination of the spherical geometry and the parallel magnetization, the magnetic flux is focused at the top of the sphere inside the airgap. This results in an almost constant stiffness in the range of $\theta = 40^\circ$ and $\theta = 140^\circ$. In addition, this magnetization topology has two stable positions, namely the initial ($\theta = 0^\circ$) and the end position $\theta = 180^\circ$ (of the human arm). In the middle, at $\theta = 90^\circ$ a meta-stable position is present. In the initial position as depicted in Fig. 4.3b, the magnetization direction are opposed to each other. Because of the symmetry and flux focussing there is magnetic field interaction on the flat size of the hemisphere which is referred to as end-effects. These end-effect produce a negative torque that is larger than the positive torque that results from the opposite magnetizations, that create a stable position.

The combination of a radial magnetized outer hemispherical permanent magnet and a parallel magnetized inner spherical permanent magnet, as shown in Fig. 4.3c, produces a torque as shown in Fig. 4.7. This topology combines the constant magnetic flux density of the radial magnetization with the flux focussing of the parallel magnetization. This results in a sinusoidal torque characteristic as shown in the figure. This topology provides a positive stiffness in the first part, $\theta = 0^\circ$ to $\theta = 90^\circ$ and a negative stiffness for the second part, $\theta = 90^\circ$ to $\theta = 180^\circ$.

The inverted combination, radial-parallel as shown in Fig. 4.3d, provides a torque characteristic as given in Fig. 4.8. The torque characteristic shown in this figure is similar to the torque characteristic of the parallel-parallel magnetization combination, but it is inverted. The torque amplitude, however, is very low in comparison to the other topologies. Because the magnetic flux density of the outer hemispherical permanent magnet closes within its own structure [91], the magnetic fields only have little interaction. Consequently, there is almost no coupling between the hemispheres.

To ensure the torque characteristics are consistent for different geometric parameters, the ratio between the inner and outer sphere radii is investigated. This investigation is performed with a variable outer radius R_{out} and a constant inner radius, R_{in} , and airgap, g_a . Consequently, the airgap volume in which the magnetic field interacts, is kept constant. The resulting torque for the different ratios is shown in Fig. 4.9. According to these results, the topologies, except for the radial-parallel configuration, show a range where the stiffness is zero or a constant that decreases when the radius increases. This range can be extended by expanding the outer spherical shape of the permanent magnet towards a full sphere. The radial-parallel configuration only shows a change in amplitude and, therefore, it is concluded that the geometry change does not influence the torque characteristic. In these 2D figures the torque characteristics are more clearly visible for the different topologies such as the almost zero stiffness in Fig. 4.9a and the almost linear stiffness in Fig. 4.9b.

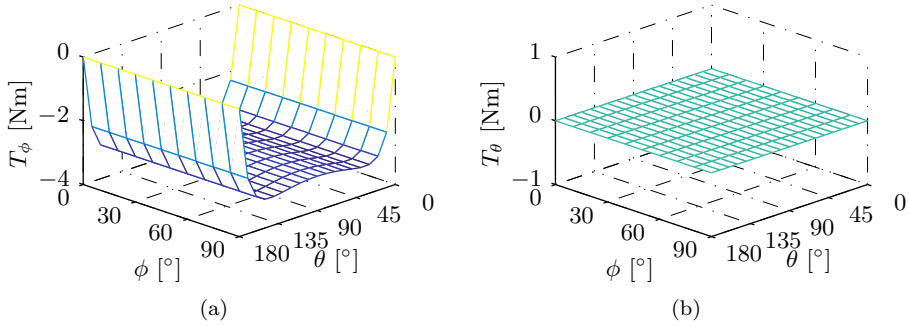


Figure 4.5: Torque of the radial-radial magnetization combination rotating the outer permanent magnet about: (a) ϕ -axis, (b) θ -axis.

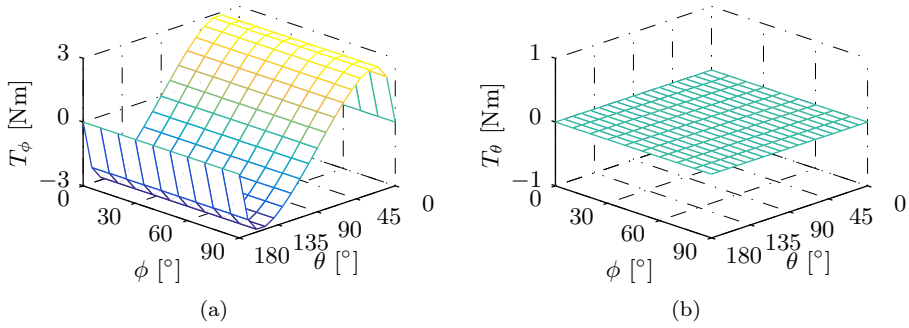


Figure 4.6: Torque of the parallel-parallel magnetization combination rotating the outer permanent magnet about: (a) ϕ -axis, (b) θ -axis.

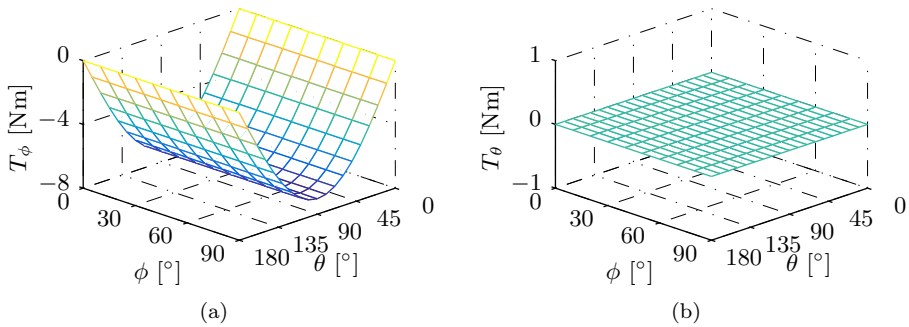


Figure 4.7: Torque of the radial-parallel magnetization combination rotating the outer permanent magnet about: (a) ϕ -axis, (b) θ -axis.

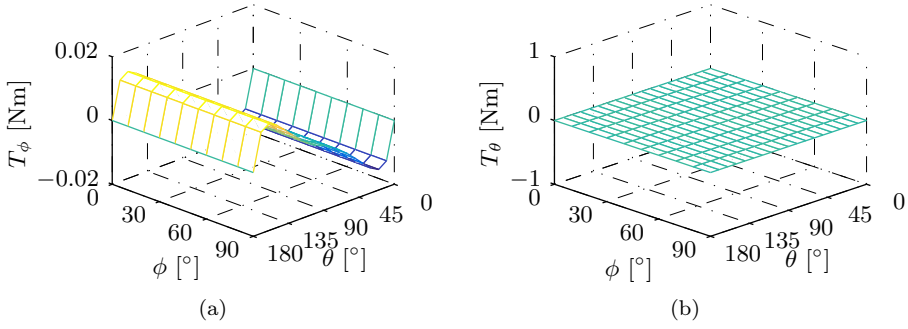


Figure 4.8: Torque of the parallel-radial magnetization combination rotating the outer permanent magnet about: (a) ϕ -axis, (b) θ -axis.

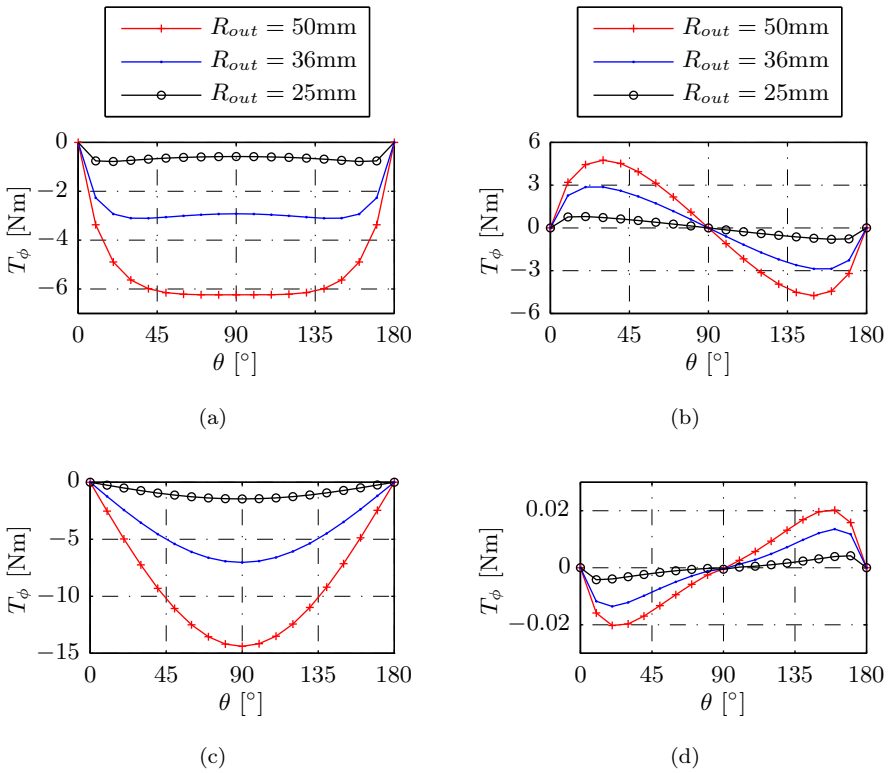


Figure 4.9: The torque of the different magnetization combinations for different ratios at $R_x = 0^\circ$: (a) radial-radial magnetization, (b) parallel-parallel magnetization, (c) radial-parallel magnetization, (d) parallel-radial magnetization.

4.4 Magnetic gravity compensator design

To compensate for the gravity in the robotic application of a mobile arm-support system it is shown in Chapter 2 that a sinusoidal torque characteristic is required. This torque characteristic corresponds with the radial-parallel spherical spring topology and, therefore, investigated further. Additionally, this magnetic spring has zero stiffness in the other rotation as shown in Fig. 4.7, which corresponds with movement in the horizontal plane (perpendicular to the gravity direction). Therefore, a magnetic gravity compensator is designed and optimized using this spherical magnetic spring topology.

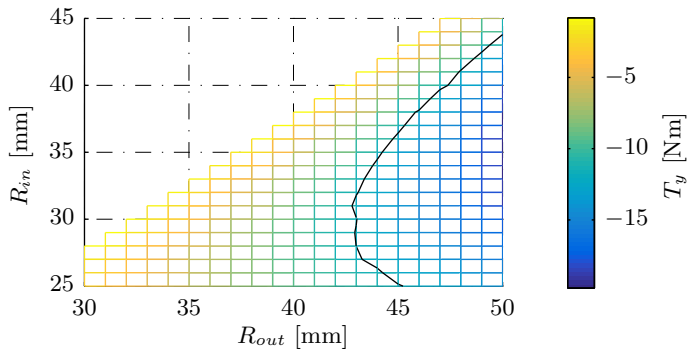
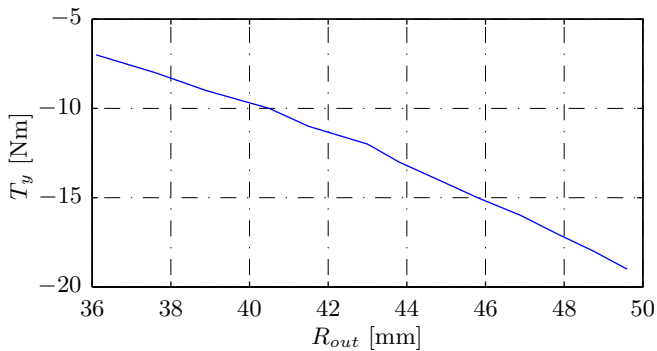
4.4.1 Optimization of the geometry

The magnetic gravity compensator has to provide a torque of 12 Nm with the aforementioned magnetization topology. For the smart arm-support system, it is desirable to minimize its volume to guarantee flexible mounting on an electric wheelchair. In addition, the geometrical optimization also results in minimized mass which is beneficial for the mobility of the system. This optimization is performed with the magnetic charge model that assumes a relative permeability of $\mu_r = 1$. A parametric search for a range of inner and outer radii and a fixed airgap length of $g_a = 1$ mm has been carried out to. The analysis in Fig. 4.9c shows that the radial-parallel spherical spring topology produces a sinusoidal torque characteristic for different R_{out} . Therefore, only $\theta = 90^\circ$ is evaluated. The amplitude of the torque, T_ϕ , as function of the inner and outer radius is shown in Fig. 4.10. The minimal magnet thickness is equal to 1 mm. From the parametric search, the optimal torque as function of the outer radius can be obtained and is shown in Fig. 4.11. Identification of this figure, shows a quadratic relation between the torque production and the outer radius of the gravity compensator.

From the figures created with the parametric search (4.10 and 4.11), the optimal design for the spherical gravity compensator is obtained. For the design with a specified torque of $T = 12$ Nm a dimension of 43 mm for the outer radius and 29 mm for the inner radius is found. The geometric parameters for this final design are listed in Table 4.2. For alternative cases, for example when the smart arm support is equipped with an actuator for the elbow joint, the minimal radii can be obtained from Fig. 4.11. This results in an outer radius of 49.6 mm and an inner radius of 35 mm. Hence, a smart arm-support design with an actuated shoulder joint requires a torque increase of 58% that can be achieved by increasing the volume with 36%.

Table 4.2: Geometric parameters of the final design for the gravity compensator

Parameter	Value	Unit	Description
R_{in}	29	[mm]	Outer radius of the inner magnet
R_{out}	43	[mm]	Outer radius of the outer magnet
g_a	1	[mm]	Airgap length
B_r	1.3	[T]	Remanent magnetic flux density
μ_r	1	[-]	Relative permeability

Figure 4.10: The torque about the y -axis as a function of R_{in} and R_{out} obtained at the position $\theta = 90^\circ$ where the black line represents the torque requirement 12 Nm.Figure 4.11: The amplitude of the torque production as function of the outer radius obtained from the position $\theta = 90^\circ$.

4.4.2 Force analysis

The magnetic spring consists of two permanent magnets that are configured in a radial-parallel magnetization that have an opposite direction. Aside from a sinusoidal torque production, forces are produced. These forces between the hemispherical permanent magnets as function of the rotation angle θ are shown in Fig. 4.12. Although, the instable initial position might suggest a repulsive force, this figure shows an attraction force of 533 N instead. According to the flux lines as shown in Fig. 4.13, the radial magnetization at the end of the hemispheres pulls the parallel magnetized inner hemisphere towards the outer hemisphere. These end-effects have such a concentration of flux lines that it counteracts the repulsion of the oppositely directed magnetizations. At an angle of $\theta = 36^\circ$ the force in the z -direction becomes negative and the outer permanent magnet repels the inner permanent magnet. This force reaches its maximum of 124 N at $\theta = 60^\circ$. In this position there are less end-effects.

For a correct operation of the magnetic gravity compensator, it is important that the hemispherical permanent magnets are concentric. Otherwise, the sinusoidal torque characteristic cannot be maintained. The bearing has to withstand both attractive and repulsion forces. The forces in the x - and y -directions always push the inner hemisphere towards the outer hemisphere because of the enclosing spherical geometry. A positive force in the z -direction is also an attraction force between the hemispheres. To account for the negative force in the z -direction, the bearing has to include an additional mechanical construction mounted on the outer hemispherical permanent magnet that encloses the inner hemispherical permanent magnet.

There are multiple possible bearings to employ the gravity compensator with, such as an air, plain, and ball bearing. The airgap in an air bearing can be made very small and has the least friction among the mentioned bearings. However, external equipment is necessary to produce pressurized air. A plain bearing uses material that has a low friction coefficient. Despite this low friction, it has the largest stick and slip effect of the aforementioned bearing topologies. A ball bearing has less friction than the plain bearing. However, the gravity compensator requires a spherical spacer to keep the balls at their position. With this type of bearing, the airgap depends on the size of the bearing balls. Furthermore, these balls cannot be made of magnetic material because they would disrupt the magnetic field. Hence, other material has to be used such as non-magnetic stainless steel or ceramic. A spherical ball bearing for the gravity compensator is presented in Chapter 6.

4.4.3 Demagnetization

The produced magnetic field by a permanent magnet is characterized by the magnetic flux density, B , and the magnetic field strength, H . The $B(H)$ -curve describes the magnetic hysteresis loop of the magnetic material. This loop intersects the positive side of the ordinate at the remanence magnetic flux density, B_r at $H = 0$ A/m. This curve is part of the hysteresis loop and has a knee point at which the permanent magnet is permanently demagnetized. The NdFeB permanent magnet material is more susceptible for demagnetization at higher temperatures because the location of the knee point is influenced. This knee point is in direct relation to the coercivity of the permanent magnet, indicated by the magnetic field strength, often indicated with H_{cj} . This magnetic field strength is defined as the point at which the polarization of the magnetic field is zero.

To determine the working point of the permanent magnet, the magnetic flux density component in the direction of the magnetization is obtained. These components are radial, B_ρ , for the outer and in the z -direction, B_z , in the inner hemispherical permanent magnet. The minimum demagnetizing flux density as function of the rotation, θ , is shown in Fig. 4.14. Both hemispherical permanent magnets have the highest opposite magnetic flux density at the initial position, $\theta = 0^\circ$. These magnetic flux densities are visualized with a sectional view in Fig. 4.15.

The magnetic flux density of the inner permanent magnet in Fig. 4.15a shows that the hemisphere is the most susceptible at the corners on the bottom of the hemisphere. This corresponds with the end-effects as shown with the flux lines in Fig. 4.13. The lowest magnetic flux density in the system is equal to -0.1 T and it mostly occurs at the corners.

The magnetic flux density in the outer permanent magnet is visualized in the sectional view of Fig. 4.15b. In this figure the lowest magnetic flux density in the system occurs about the z -axis. This corresponds with the flux lines as shown in Fig. 4.13 where the lines of the inner hemispherical permanent magnet closes through the outer hemispherical permanent magnet. The maximum opposite radial magnetic flux density is equal to -0.6 T.

For the demagnetization of the hemispherical permanent magnets, it can be concluded that mainly the radial magnetized permanent magnet has a risk to be permanently demagnetized. In the design of this passive device it is assumed that it does have high temperature rises. Therefore, a remanent of 1.3 T is realistically chosen for the radial permanent magnet. For the inner hemispherical permanent magnet, this remanent magnetic flux density is conservatively chosen. Hence, the presented design is considered feasible.

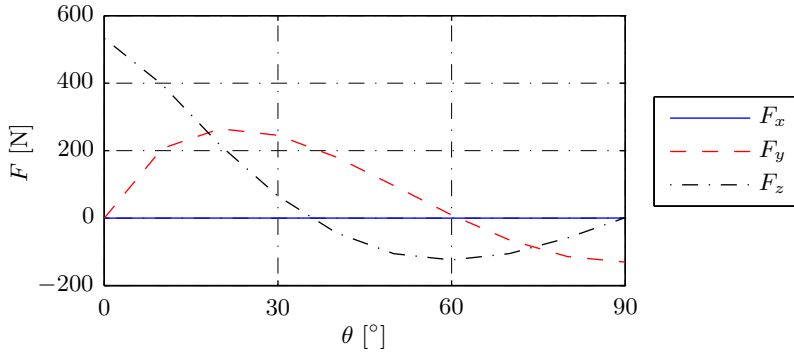


Figure 4.12: The force that occurs between the hemispherical permanent magnets during motion about the x -axis.

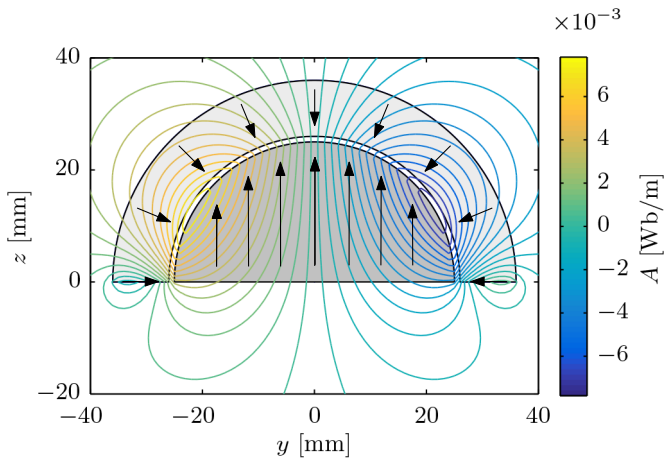


Figure 4.13: Flux lines of the radial-parallel magnetization combination in the initial position ($\theta = 0^\circ$).

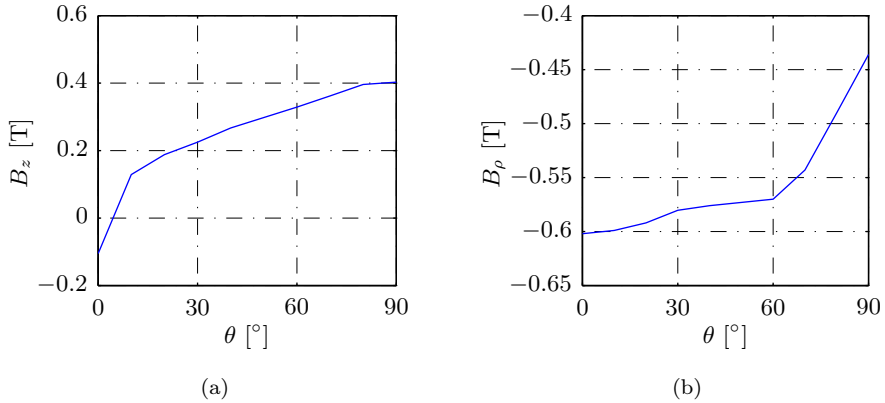


Figure 4.14: The minimal magnetic flux density in the direction of the magnetization as function of the rotation angle θ present in the hemispherical permanent magnets: (a) B_z for the inner magnet, (b) B_ρ for the outer magnet.

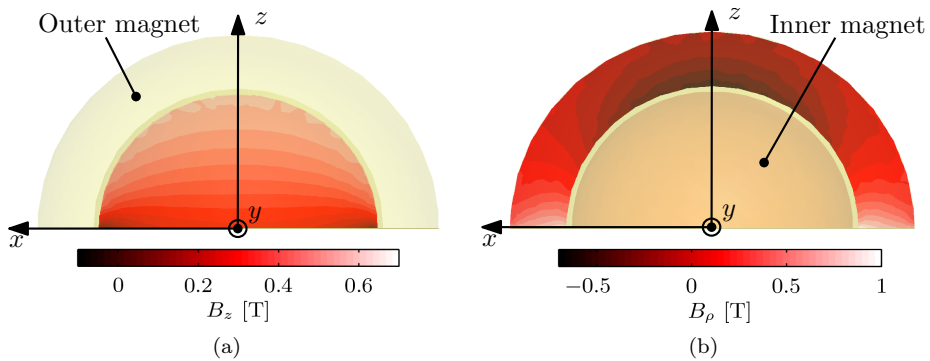


Figure 4.15: Magnetic flux density shown in a sectional view for the position with the highest risk of demagnetization for: (a) the inner hemispherical permanent magnet, (b) the outer hemispherical permanent magnet.

4.5 Manufacturability

For the design of the gravity compensator, the magnetic properties of sintered Nd-FeB permanent magnets are taken into account. This alloy has a high magnetic flux density with respect to other available materials such as ferrites, AlNiCo and samarium-cobalt [28]. The sintered manufacturing process uses a powdered permanent NdFeB alloy which is pressed into a shape while a bias field is applied to align all the elements in the powder. These permanent magnets are able to achieve a remanent magnetic flux density that can go up to 1.47 T [129]. For bonded permanent magnets a different manufacturing method is applied. Bonded permanent magnets are a mixture of permanent magnet material and other materials for example a plastic; hence it can be used for injection moulding. Due to this mixture the density of the magnetic material is lower and, therefore, a lower magnetic field can be created. Furthermore, the resulting magnetization is isotropic; hence, the magnet has no preferred magnetization direction. However, a magnetic field can be applied during the injection moulding process creating anisotropic material [28]. With the bonding method, exotic geometries are easier to accomplish compared to the sintered manufacturing method. However, a remanence of only 0.65 T can be achieved.

Spherical sintered permanent magnets are commercially available. Therefore, it is realistic to assume a remanence property of 1.3 T for the inner hemispherical permanent magnet. The outer hemispherical permanent magnet is more difficult to produce because it is hollow. Therefore, it may be interesting to create this with a bonded permanent magnet. Application of a bonded outer hemispherical permanent magnet ($B_r = 0.65$ T) combined with a sintered permanent magnet in the final design, as listed in Table 4.2, the torque amplitude reduces to 6.1 Nm. In the case both hemispherical permanent magnets are produced out of bonded material, the torque reduces to 3.0 Nm. Hence, the application of bonded permanent magnet significantly reduces the torque amplitude.

The hemispherical permanent magnet with the parallel magnetization can be created by machining it from a block of sintered NdFeB material. Because this material is very hard and brittle, machining methods such as wire eroding and vertical eroding are preferred over milling. The radial magnetization is more difficult than the parallel magnetization. Another method is approximating the radial magnetization with segmentation. This method uses a series of parallel magnetized permanent magnets to approximate the radial magnetization. The accuracy of this approximation is determined by the number and size of the segmented permanent magnets. This method allows fast prototyping and is, therefore, applied for the realized prototype design in Chapter 6. In this prototype design, the radial magnetization is approximated with 178 cylindrical permanent magnet with a radius of 2 mm and a height of 13 mm. These geometric parameters correspond to those of the final design as listed in Table 4.2. Due to the spherical shape,

this segmentation results in 74% less magnetic material resulting in an amplitude torque of 3.3 Nm.

Instead of a hemispherical shape for the inner permanent magnet, a full sphere can be used. This geometry is investigated in [91] for the gravity compensator design as presented in this chapter. According to this work the torque amplitude increases with 200% with respect to the hemispherical permanent magnet geometry. However, it is also shown that the sinusoidal torque characteristic only holds for hemispherical or full spherical shapes. Only the inner permanent magnet can be employed out of a full sphere. Otherwise, the range of motion cannot be achieved. However, a hemisphere is chosen for the inner permanent magnet array because it results in a more stable construction when mounted on the supporting structure.

4.6 Conclusions

A novel magnetic gravity compensator has been designed that is able to provide support in multiple degrees of freedom. A spherical magnetic spring is created with two concentric hemispherical permanent magnets. Different torque characteristics can be realized depending on the combination of parallel and radial magnetizations. It has been shown that a change of the hemisphere radii only results in a change in torque amplitude and not in the characteristic.

An arm-support system requires a sinusoidal torque characteristic. This characteristic corresponds to the combination of a radial magnetization for the outer hemispherical permanent magnet and a parallel magnetization of the inner spherical permanent magnet. An average torque requirement of 12 Nm has been found by identifying the human arm movements. By mapping the torque performance of the compensator for different inner and outer radii, an optimal torque density with respect to its volume has been found. Considering a permanent magnet grade with a remanent magnetic flux density of 1.3 T, a radius of 29 mm and a radius of 43 mm for the inner and outer permanent magnet have been obtained, respectively. Commercial spherical permanent magnets are available that can be used for the inner hemispherical permanent magnet. However, the manufacturing of the outer hemispherical permanent magnet is not evident. Furthermore, this permanent magnet has a risk of demagnetization when employed in the gravity compensator.

Chapter 5

Integrated design of a spherical actuator

Abstract - Actively controlled arm support systems provides more support for activities of daily living compared to passive arm support systems. Therefore, a spherical actuator with integrated gravity compensator is designed as a multi-degrees-of-freedom robotic joint. Because of the integration of the compensator, in an unconventional hemispherical actuator is designed. The gravity compensator is concentrically placed inside the actuator. These two devices are decoupled by a spherically shaped segmented back-iron which is positioned in between the devices. Multiple slotless actuator topologies are compared based on their predicted power dissipation. In addition, the power dissipation of the resulting design is further minimized. Finally, the design suitable for an arm support system is presented.

This chapter is based on

- B. van Nindhuis, B. L. J. Gysen, J. W. Jansen, and E. A. Lomonova, "Topology comparison of slotless permanent magnet semispherical actuators," IEEE Transactions on Magnetics, vol. 50, nr.11, 2014.

5.1 System topology and specifications

Actuated arm-support systems can provide more support during activities of daily living compared to passive systems. Usually, passive mobile systems only compensate for the gravity. At a certain stage, persons that suffer from a progressive neuromuscular disorder are limited by non-ideal phenomena such as friction in the arm-support system. An actuated system can compensate for these phenomena, and also provide support for the acceleration and deceleration of the arm. Furthermore, the gravity force of additional weight, for example a cup of coffee, can be actively compensated. Arm-support systems are usually mounted on an electric wheelchair; hence, mobility and power consumption are important aspects.

A multiple-degrees-of-freedom spherical actuator with integrated gravity compensator is proposed. The spherical actuator has a similar ball and socket joint as the compensator and has an equal number of degrees of freedom (DoF). These degrees of freedom are necessary to comply with the range of motion requirements. In this chapter, it is shown that a passive compensator can be integrated into a spherical actuator. A design is presented towards a smart mobile arm-support application.

5.1.1 Spherical actuation

There are several spherical actuator topologies described in the literature. The design of these actuators are often application specific. For example, a gyroscope for aerospace purposes is presented in [112]. This design has a completely encapsulated rotor which can rotate unlimitedly in three DoF. In most cases, contact with the rotor is required. For example in a sorting stage for a conveyor belt or in omni wheels [24]. These applications require a design with a stator that covers the rotor only partially. Some designs provide unlimited rotation about only one axis and a limited tilting motion about the other axes [69, 139]. Other applications need to exert a force in combination with a rod, such as a camera joint or a robotic manipulator. This rod is connected to the rotor of the spherical actuator and, therefore, the design has a limited rotation movement in two [139] or three [92] DoF.

The majority of the spherical actuators found in the literature use permanent magnets in combination with slotless coils and an interior rotor [47, 62, 66, 69, 112, 139, 140]. A permanent magnet spherical actuator with an exterior rotor is proposed in [66]. In addition, slotted topologies with an interior rotor are proposed by [132] and [56]. Typically, the spherical actuator designs provide a torque below 4 Nm with rotor radii ranging from 25.5 mm to 46.5 mm. The design presented by [56] has high number of permanent magnets (112) and slotted coils (96) and an interior rotor with a radius of 325 mm. This design provides a torque of more than 40 Nm in all degrees of freedom. Different techniques can be applied to produce

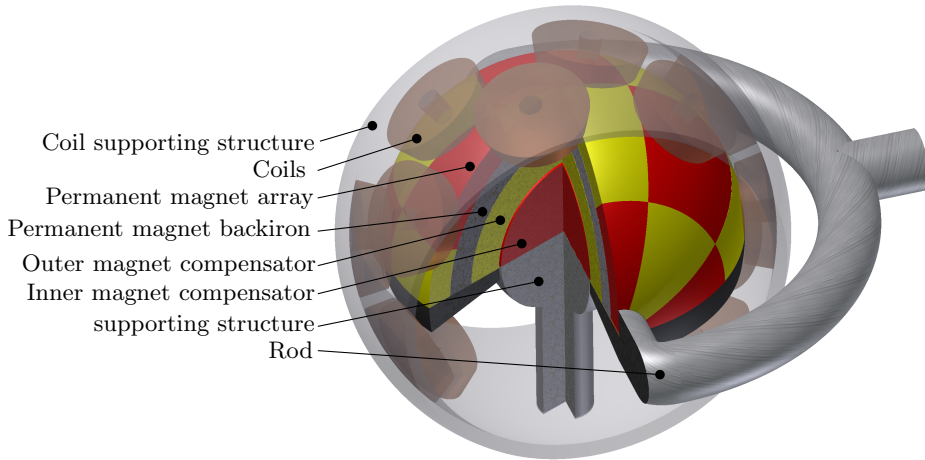


Figure 5.1: Initial design of the spherical actuator with integrated magnetic gravity compensator.

a torque with a spherical actuator. In [65, 70] a variable reluctance machine is designed capable of providing 3 DoF. The possibilities of an induction machine are explored in [22] and [24] in which several topologies are investigated. A spherical actuator with two DoF is presented in [63] using electromagnets for the rotor and stator.

In this chapter, a spherical actuator topology is investigated with an integrated gravity compensator capable of moving with a large range of motion. In this design, an unconventional hemispherical permanent magnet array is applied as depicted in Fig. 5.1. A set of specifications for the design are obtained from the shoulder joint analysis presented in Chapter 2. The analysis of rotary actuators in [26, 100] shows that permanent magnet technology provides the highest torque density. This technology is preferred because the volume can be minimized. The combination of the integrated gravity compensator and the specifications, result in mechanical constraints. Due to these constraints, the design deviates from the traditionally chosen full spherical structure for the permanent magnet array. The integrated topology has two airgaps, namely one in the compensator and one in the actuator. Multiple configurations of the hemispherical permanent magnet arrays, coil arrays and back-iron configurations are investigated. The power dissipation is predicted with the models derived in Chapter 3. Subsequently, the gravity compensator is integrated in the spherical actuator. Next, the geometry parameters of the spherical actuator topology are minimized and the thermal behavior is modeled.

5.1.2 User scenarios

A spherical actuator is designed towards the application in a smart arm-support system. These systems are usually mounted on a wheelchair where limited space is available. In addition, a small volume reduces the stigmatization and increases the social acceptance. Therefore, the optimization objective is to minimize the volume of the spherical actuator. This volume is determined by the torque specification and maximum allowable temperature on the outside of the actuator.

Each individual performs the activities of daily living differently and, therefore, require unique motion profiles to be followed by the actuator. Hence, the requested performance of an actuator in an arm support varies for each person. Therefore, the spherical actuator is designed to be suitable for multiple users. The torque specifications, as derived in Chapter 2, consider the torque required for certain positions. In practice, the human arm is at rest (zero torque is required) in between activities. In case an individual uses his arm (too) frequently, the muscles become tired and the person has to let his arm rest. This property of the arm should corresponds with the duty cycle of the spherical actuator.

There are two types of scenarios considered during the activities of daily living. The first scenario depicts an activity that can be repeated continuously. It is assumed that this scenario represents a worst case when maximal acceleration or deceleration is required every second with a bent elbow. Such a scenario should also cover activities such as drinking where the mass is higher but the repetition is lower. The second scenario is considered as an activity that requires a short peak torque and is not repeated often. For this scenario, the user should be able to stretch his arm for 20 s. This position requires additional gravity compensation from the spherical actuator.

5.1.3 Mechanics

The mechanical construction of the spherical actuator is constrained by the required range of motion and the integration of the gravity compensator. The rotor of the integrated actuator consists of the outer permanent magnet of the gravity compensator and the permanent magnet array of the actuator. This array is limited by a hemispherical shape, otherwise the range of motion cannot be achieved due to the obstructing supporting structure of the gravity compensator. For the robotic application, a rod has to be connected to the rotor to exert the produced torque. This rod and the range of motion requirements determine the maximum width of the coil array. According to Table 2.10 this range is 90° about each axis for the most essential activities of daily living. Rigid body dynamics are assumed, and consequently the superposition principle is applied to the force and torque calculations.

The dissipated power in the coils requires cooling. Possible cooling methods are forced air cooling, water cooling, and natural convection. Forced air cooling is undesirable due to possible sound production. Water cooling is impractical in the application because of the required additional pumping system with the additional risk of leakages. Hence, natural convection is preferred. For natural convection it is beneficial to place the heat source close to a convection surface which is as large as possible. Therefore, the coils are placed on the outside of the integrated actuator. Furthermore, placement of the coils on the outside is also beneficial of the torque production. Because the radius is larger a higher torque is produced with the same force production.

5.1.4 Specifications

The technical specifications for the spherical actuator with integrated gravity compensator are chosen for a continuous and peak torque. The continuous torque is obtained from the shoulder-joint analysis performed in Chapter 2. In this chapter it is found that to accelerate with 7.6 rad/s^2 , a torque of 2.7 Nm is required. This torque is required for 0.15 s to accelerate to a speed of $65^\circ/\text{s}$ with the elbow bent at 90° . This speed is estimated based on the ambulatory directly-on-the-joint actuator specifications as listed in Table 2.1. The repetition of the torque is every 1 s, resulting in a duty cycle of 15%. The produced torque has a quadratic relation with the dissipated power. Therefore, the continuous torque is obtained with

$$T_{con} = T\sqrt{\delta} \quad (5.1)$$

where T_{con} is the continuous torque, T is the peak torque, and δ is the duty cycle. The resulting continuous torque is 1.0 Nm.

The peak torque is based on the difference between the maximum gravity compensation required for an arm with a bent elbow at 90° and a stretched arm as listed in Table 2.8. This torque is 6 Nm and should be provided for a duration of 20 s and is not repeated for at least 2.5 hours.

The thermal specifications is defined as the temperature increase at the outside of the actuator. For the arm-support application, a maximum increase of 40°C is acceptable. When the user is able to directly contact the metal of the stator it can be required that this specification reduces to 20°C . All aforementioned design specifications for the spherical actuator are listed in Table 5.1.

Table 5.1: Technical specifications for the spherical actuator design

Specification	Value	Unit
Continuous torque	1.0	[Nm]
Duty cycle continuous mode	15	[%]
Peak torque	6.0	[Nm]
Maximum temperature rise	40	[deg]
Range of motion (all DoF)	90	[deg]

5.2 Analysis method

5.2.1 Flux density

Multiple actuator topologies are evaluated and compared based on the predicted power dissipation. A slotless coil topology is chosen for the spherical actuator design to avoid cogging torque. From a safety point of view, cogging is undesirable because it interferes with the sinusoidal torque characteristic of the gravity compensator. Hence, when a sudden power failure occurs, it is possible that the user is no longer capable of controlling the arm-support system. Nevertheless, the configuration with back-iron behind the coils is investigated in Section 5.7. It is shown that the power dissipation to compensate for the cogging torque does not justify the increase in magnetic flux density. Fig. 5.2 shows the integration of the gravity compensator and the geometric parameters which are listed in Table 5.2 and Table 5.3.

Table 5.2: Geometric parameters as defined in Fig. 5.2

Parameter	Value	Unit
Outer radius of the magnet array	63	[mm]
Outer radius of the coil array	74	[mm]
Magnet height, h_m	10	[mm]
Coil thickness, h_c	10	[mm]
Airgap length, g_a	1	[mm]
Remanent magnetic flux density, B_r	1.3	[T]
Assumed magnet relative permeability, μ_r	1	[-]

Spherical actuator topologies are evaluated with the developed magnetic charge model as presented in Chapter 3. Regions that consist of highly permeable material are modeled with spherical imaging. The back-iron for the permanent magnet

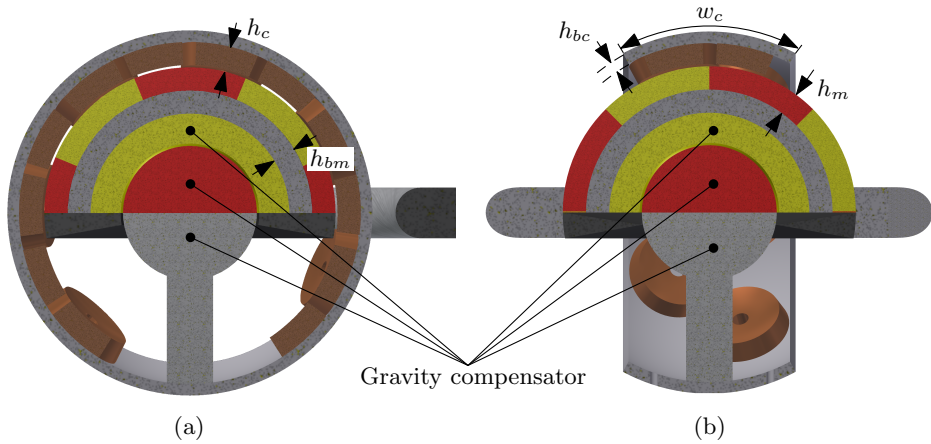


Figure 5.2: Sectional view of the spherical actuator with integrated gravity compensator: (a) side view, (b) front view.

array as indicated with h_{bm} in Fig. 5.2 has a partial spherical. A partial spherical region has been approximated with a full region by the magnetic charge model and spherical imaging. The accuracy of this approximation is validated with FEA. In this validation only the radial component is taken into account because it produces the torque according to the Lorentz force law in (3.23).

For the topology with a hemispherical permanent magnet array and a full sphere as back-iron for the magnets, the magnetic flux density predicted with the semi-analytical tool is shown in Fig. 5.3a. In this projection of the magnetic flux density, the permanent magnet array is positioned in the Cartesian coordinate system as presented in Chapter 3, Fig. 3.6. This full spherical permanent magnet array is cut in half at the zy -plane to create the hemispherical permanent magnet array. The discrepancy with FEA is shown in Fig. 5.3b and the amplitude difference between FEA and the semi-analytical analysis is 0.65%. Hence, both models are in good agreement. There is a discrepancy at the edge of the hemispherical permanent magnet, located at $\phi = 90^\circ$ and $\phi = 270^\circ$ in this figure. This is caused by the full sphere taken into account with the magnetic charge model instead of a hemispherical shape as modeled in FEA.

Modeling a hemispherical permanent magnet with two infinite permeable boundaries, to approximate the back-iron behind the magnet array and the coil in case it is present, results in a magnetic flux density as shown in Fig. 5.4a. In theory, an infinite number of images are required to predict the magnetic field. However, in practise only a limited number of images can be taken into account. therefore, the accuracy is investigated for two and four images. The back-iron for the coils covers the hemispherical permanent magnet array only partially, namely between $\theta = 62^\circ$ and $\theta = 124^\circ$ and is depicted with w_c in Fig. 5.2 (b). This back-iron

has a different interaction with the magnetic field of the permanent magnets when the position is changed. Hence, besides an increase in magnetic flux density in the airgap, this configuration introduces a cogging torque. To validate the correct prediction of the magnetic flux density, two positions are taken into account. The position with zero cogging torque at the initial position and the position with maximum cogging torque when rotated 15° in the θ -direction. The results are shown in Fig. 5.4b and Fig. 5.4c, respectively. It is found that in the region in which the coils are located, the amplitude discrepancy between the semi-analytical model and FEA is 9.11% and 4.5% with two and four images, respectively. Increasing the amount of images provides a higher accuracy with respect to FEA, however, this also increases the calculation time. The number of four images is considered to be a good compromise between accuracy and calculation time. The magnetic flux density amplitude with two infinitely permeable boundaries is 44% larger than the magnetic flux density with only back-iron behind the permanent magnets as shown in Fig. 5.3a.

5.2.2 Commutation algorithm

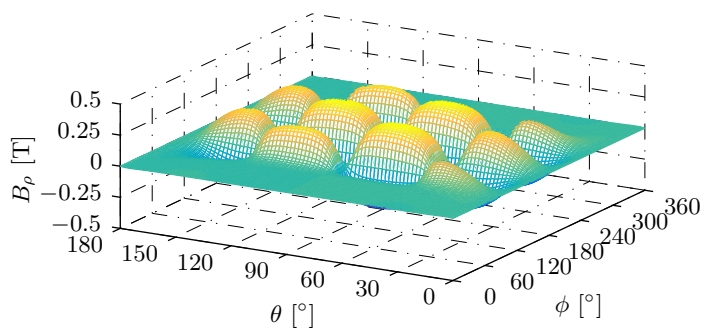
Due to the hemispherical permanent magnet array, the spherical actuator is not a balanced system. Furthermore, the actuator should be able to produce torque components in three directions independently. Hence, it is not possible to actuate the spherical actuator with a balanced three phase system. Consequently, each coil has to be separately excited. To determine the excitation of each coil, the current is decoupled from the torque with a mapping of the torque constants for each position of each coil resulting in a decoupling matrix defined as [51]

$$\vec{T} = \begin{bmatrix} T_x \\ T_y \\ T_z \end{bmatrix} = \begin{bmatrix} \Gamma_{1,x} & \Gamma_{2,x} & \dots & \Gamma_{n,x} \\ \Gamma_{1,y} & \Gamma_{2,y} & \dots & \Gamma_{n,y} \\ \Gamma_{1,z} & \Gamma_{2,z} & \dots & \Gamma_{n,z} \end{bmatrix} \begin{bmatrix} i_1 \\ i_2 \\ i_3 \\ \vdots \\ i_n \end{bmatrix} \quad (5.2)$$

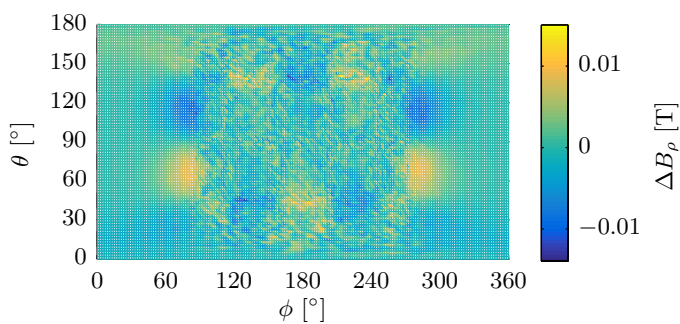
$$= \mathbf{\Gamma}(R_x, R_y, R_z) \vec{i} \quad (5.3)$$

where \vec{T} is the produced torque predicted with the Lorentz force equation 3.20, $\Gamma_{l,k}$ is the mapping of the torque and current for coil l about the k -axis, and i_l is the current through coil l . The torque model required for this method is validated in [92]. A two-norm minimization can be applied to find the current distribution through the coils with this decoupling matrix. This results in

$$\vec{i} = \left(\mathbf{\Gamma}^\top (\mathbf{\Gamma} \mathbf{\Gamma}^\top)^{-1} \right) \vec{T}_d \quad (5.4)$$



(a)



(b)

Figure 5.3: The magnetic flux density in the middle of the airgap is obtained at 69 mm with the magnetic charge model and spherical imaging to model a full back-iron behind the permanent magnets: (a) the predicted magnetic flux density, (b) discrepancy between the charge model and FEA.

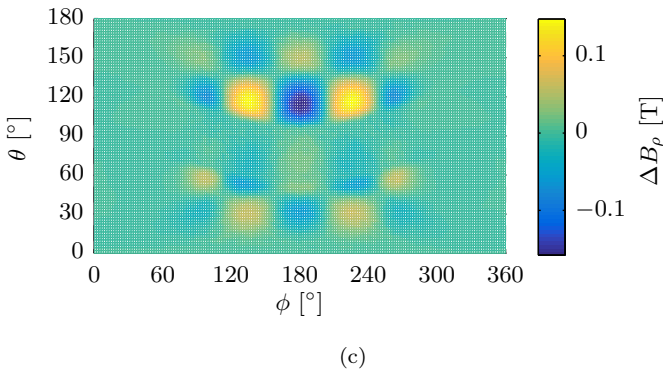
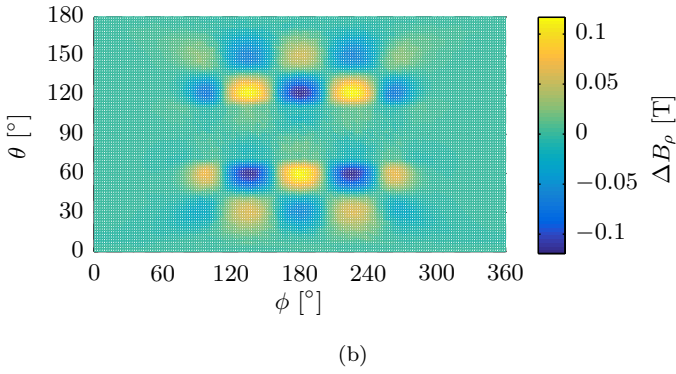
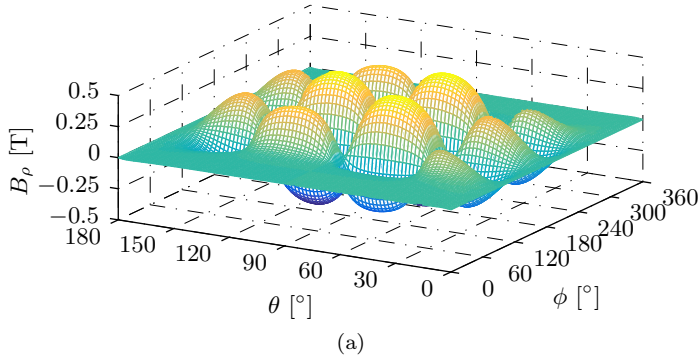


Figure 5.4: The magnetic flux density in the middle of the airgap at 69 mm of the magnetic charge model with in total four spherical images to model the back-iron behind the coils and permanent magnet array: (a) the predicted field, (b) discrepancy between the charge model and FEA at the position with zero cogging torque, and (c) discrepancy between the charge model and FEA at the position with maximum cogging torque.

where \vec{T}_d is the desired torque. This equation minimizes the ohmic losses and, consequently, the power dissipation of the actuator. The power dissipation is obtained by predicting the optimized current distribution through the individual coils for a predefined torque requirement. By averaging this power dissipation over the complete range of motion, the different actuator topologies are compared.

5.2.3 Optimization strategy

There are two optimizations performed for the spherical actuator design with integrated gravity compensator. Firstly, an optimization is performed to obtain the topology with the lowest power dissipation. Secondly, the geometric parameters are optimized to minimize the power dissipation further and the resulting design is verified with a thermal model. Finally, the resulting design is presented in a topology suitable for the smart arm-support system.

5.3 Topology optimization

In search for the optimal spherical actuator topology, multiple configurations of hemispherical permanent magnet arrays, coil shapes and coil arrays are evaluated. The objective is to minimize the average power dissipation by optimizing the coil to pole pitch ratio of the different topologies. These topologies are derived from permanent magnet rotary machine designs, planar actuator designs, and spherical actuator designs from the literature.

The structure to exert the torque, depicted as rod in Fig. 5.1, is neglected in the topology optimization. The design of the rod is highly dependant on material properties, required stiffness, mechanical construction and application. For the final design, the rod is taken into account because together with the required range of motion, it defines the maximum allowable coil pitch.

5.3.1 Permanent magnet arrays

The considered hemispherical permanent magnet arrays are chosen while taking mobility and the integration with the gravity compensator into account. For the mobility of the arm-support system, it is beneficial to reduce the number of permanent magnets in the array. The required number of coils decreases for a reduction in permanent magnets because there is a direct link between these two. Consequently, the amount of electronics, such as power amplifiers, decreases for a lower number of coils. Hence, less additional volume to control the spherical actuator. An asymmetric permanent magnet array is undesirable because it influences the symmetric torque production of the gravity compensator. Therefore, a layout

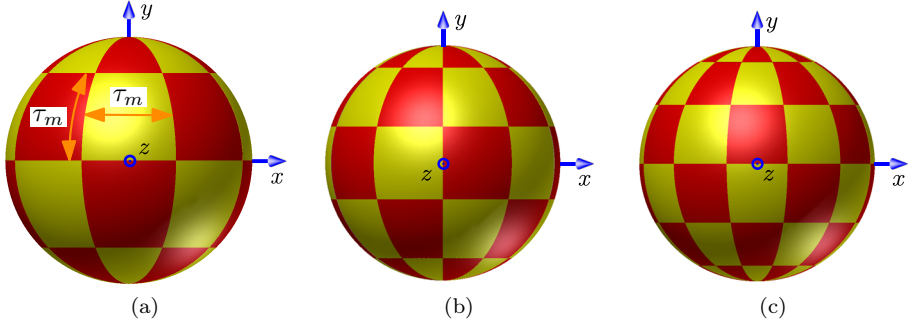


Figure 5.5: Investigated hemispherical permanent magnet arrays: (a) $\tau_m = 45^\circ$, (b) $\tau_m = 36^\circ$, and (c) $\tau_m = 30^\circ$.

with half sized permanent magnets on the edge of the array is used. This layout provides symmetry in the magnetic field and reduces the end effects.

Not all magnet sizes are equal due to the spherical shape of the permanent magnet array. Therefore, the pole pitch of the permanent magnet arrays are defined as an angle. Three hemispherical permanent magnet arrays are investigated with a pole pitch of $\tau_m = 45^\circ$, 36° , and 30° . These arrays are shown in Fig. 5.5. The power dissipation is predicted with the complete coil array to evaluate the actuator topologies. The effect of the variable magnet size is included by averaging the power dissipation over different positions covering the complete range of motion.

5.3.2 Coil arrays

For each coil array two different coil topologies are investigated, namely with a circular shape and an elongated shape. The circular coil topology is often used in combination with a spherical permanent magnet array [56, 64, 139, 140]. The elongated coil topology is employed in a similar actuation technology, i.e., the planar actuator [113]. The geometric parameters and variables of these topologies are listed in Table 5.2 and Table 5.3, respectively. The definition of these parameters and variables are shown in Fig. 5.6 and Fig. 5.2. The coils have a spherical shape to achieve a constant airgap. An array is constructed for both coil topologies as function of the coil pitch, τ_c , as illustrated in Fig. 5.7. To obtain the optimal ratio between pole pitch, τ_m and coil pitch τ_c , the comparison is made by varying the coil pitches for each defined hemispherical permanent magnet array. In this comparison, the coil height, h_c , is optimized and adapted for each permanent magnet array.

For the coil topology optimization, an initial ratio between the gap of the bobbin

G_w and the conductor bundle C_w of 25% is chosen, resulting in

$$G_w = \frac{1}{4}C_w. \quad (5.5)$$

Optimization and verification of this ratio is presented in Section 5.5. The placement of the coils in the array is defined in terms of the coil pitch as shown in Fig. 5.7. The radius of the circular coil topology is limited by the distance between the center of two coils. When the radius is larger than this diagonal the coils would overlap. Hence, the maximal coil radius can be calculated by

$$G_w + C_w = \frac{1}{2}\sqrt{\left(\frac{\tau_c}{2}\right)^2 + \left(\frac{\tau_c}{2}\right)^2} \quad (5.6)$$

$$= \frac{\sqrt{2}\tau_c}{4} \quad (5.7)$$

where τ_c is the coil pitch. To account for manufacturing tolerances, the outside radius is reduced by 10%.

The elongated coils are positioned such that the array results in a herringbone structure as illustrated in Fig. 5.7b. In this array, the coils are rotated in the opposite direction, $\alpha_c = 45^\circ$ and $\alpha_c = -45^\circ$, with respect to each other. The relation between the geometric variables and the coil pitch is

$$G_w + C_w = \frac{1}{4}\tau_c \quad (5.8)$$

where G_w is the elongated coil gap width. A similar coil distribution as the circular shape is achieved with this ratio. The maximum gap length, G_l , is obtained with the distance between the coil centers and is found by

$$G_l = \sqrt{\left(\frac{\tau_c}{2}\right)^2 + \left(\frac{\tau_c}{3}\right)^2} - 2C_wG_w. \quad (5.9)$$

The outer size is, similar to the circular coils, reduced by 10% to account for manufacturing tolerances.

5.3.3 Power dissipation

The power dissipation at multiple positions over the complete range of motion is obtained with a predefined torque, T_d . Subsequently, the results are averaged for each actuator topology. In these positions, one of the three torque components is set to $T_d = 1$ Nm and the other components are set to zero. This is done for each component x , y , and z resulting in a power dissipation P_x , P_y , and P_z .

The power dissipation for the topology with $\tau_m = 45^\circ$ and $\tau_c = 52^\circ$ is shown in Fig. 5.8. The results in this figure consider the rotations about the y -axis, R_y , and

Table 5.3: Geometric variables as defined in Fig. 5.2 and Fig. 5.6

Variable	Symbol/Value	Unit
Coil pitch	τ_c	[deg]
Pole pitch	τ_m	[deg]
Conductor bundle width	C_w	[deg]
Coil gap width	G_w	[deg]
Coil gap length	G_l	[deg]
Rotated angle elongated coil	α_c	[deg]
Coil back-iron height	h_{bc}	[m]
Coil height	h_c	[m]
Permanent magnet height	h_m	[m]
Permanent magnet back-iron height	h_{bm}	[m]

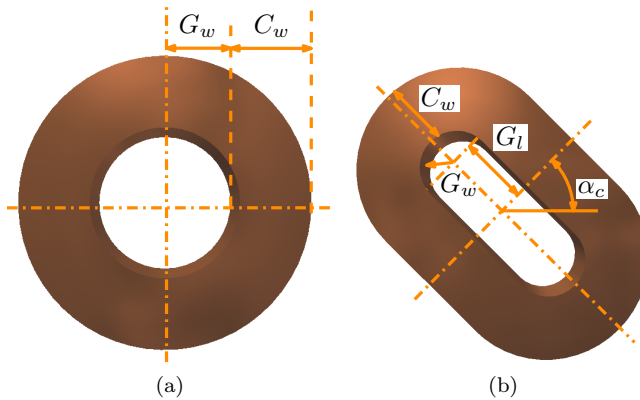


Figure 5.6: Coil topologies and their geometric variables: (a) circular coil, (b) elongated coil.

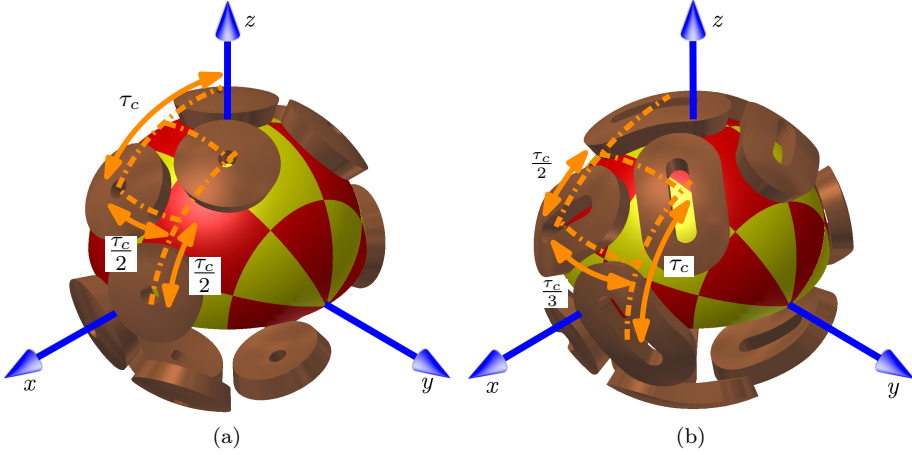


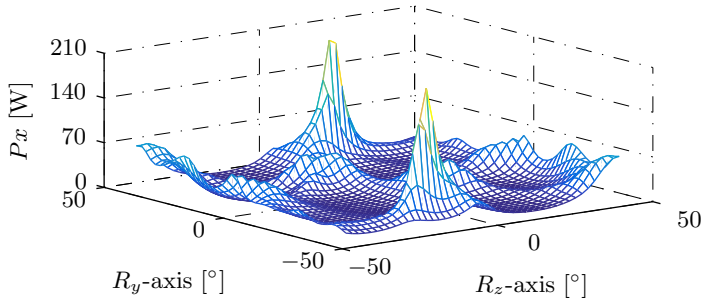
Figure 5.7: Investigated coil array topologies: (a) circular coil array, (b) elongated coil array.

about the z -axis, R_z . The figure shows peaks in the power dissipation at certain positions. It is investigated whether the peaks are singular points by determining the condition number of the torque matrix, $\mathbf{\Gamma}^-$, where

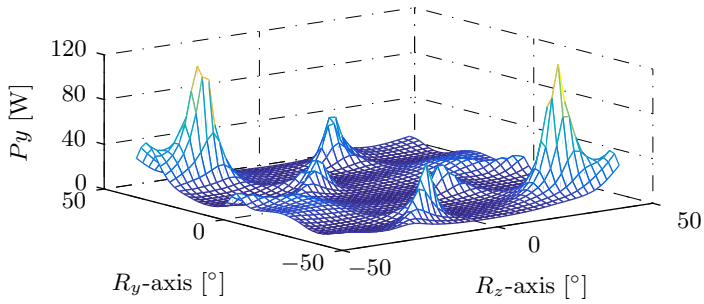
$$\mathbf{\Gamma}^- = \left(\mathbf{\Gamma}^\top (\mathbf{\Gamma}\mathbf{\Gamma}^\top)^{-1} \right). \quad (5.10)$$

The condition number of $\mathbf{\Gamma}^-$ is a measure for the sensitivity of the matrix inversion for small input changes [51]. The input of the inversion matrix is the mapping of the torque as function of the position and currents through the coils. If the condition number is sufficiently small, any torque can be accurately achieved. As a rule of thumb, if the condition number is 10^k , then k indicates the number of digits lost in accuracy [17]. The condition number of the torque matrix in these positions is in the order of 10, whereas for the other locations this is equal to 2.5. In addition, the positions at the peaks occur for P_x , P_y , and P_z are not the same. Hence, in these positions there is only torque in one direction that cannot be provided. This can be caused by, for example, coils with an opposite torque production or when only one coil is able to provide torque in this direction. It is chosen that the issues of the power dissipation peaks in the actuator design need to be solved in the kinematics and control algorithm by avoiding these positions for the arm support application.

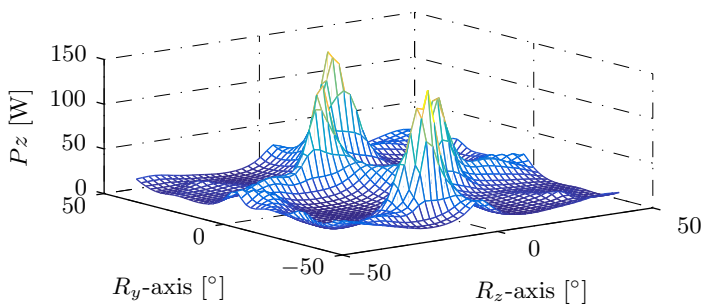
The power dissipation is obtained as function of the coil pitch for the different hemispherical permanent magnet arrays. This power dissipation is averaged over 3375 positions which corresponds to 15 rotations about each axis. The peaks in the power dissipation are included in the averaging with this resolution. Addition-



(a)



(b)



(c)

Figure 5.8: Power dissipation with one torque vector component set to 1 Nm and the others to 0 Nm with $\tau_m = 45^\circ$ and $\tau_c = 52^\circ$: (a) $T_x = 1$ Nm, P_x (b) $T_y = 1$ Nm, P_y (c) $T_z = 1$ Nm, P_z .

ally, the number of coils in the arrays are reduced for larger coil pitches to avoid overlapping coils. If such an overlap occurs, coils are removed at the back side of the hemispherical permanent magnet array (negative z -direction). The coil pitch of the circular coil topology ranges from $40^\circ \leq \tau_c \leq 51$ with 14 coils, $52^\circ \leq \tau_c \leq 60$ with 12 coils, and $61^\circ \leq \tau_c \leq 70$ with 10 coils. The elongated coil topology has a range of $30^\circ \leq \tau_c \leq 45$ with 16 coils, and $46^\circ \leq \tau_c \leq 60$ with 12 coils.

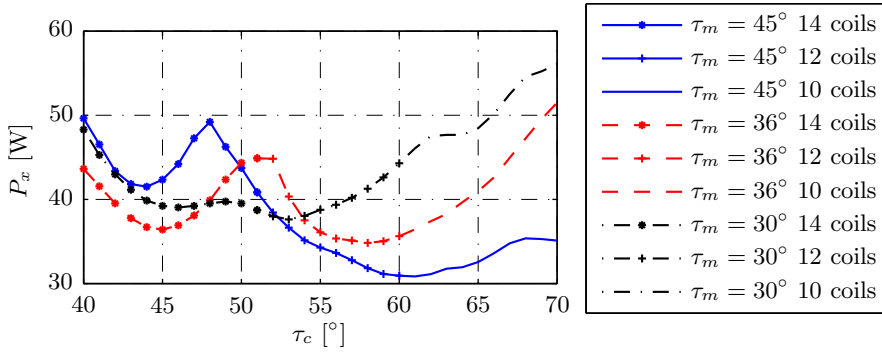
The average power dissipation over the specified range of motion is obtained for multiple back-iron configurations. These configurations are approximated with a full spherical region with an infinitely permeable boundary. Therefore, possible cogging torque is not taken into account. For the circular coil topology without back-iron, with back-iron for the permanent magnets and with back-iron for the magnets and coils, the power dissipation is shown in Fig. 5.9, Fig. 5.10, and Fig. 5.11, respectively. For the elongated coils these are shown in Fig. 5.12, Fig. 5.13, and Fig. 5.14, respectively. In each of these figures, a comparison of the power dissipation between the three hemispherical permanent magnet topologies, τ_m , are shown.

The power dissipation of the circular coil topology without back-iron, as presented in Fig. 5.9, has a minimum average power dissipation with a hemispherical permanent magnet topology of $\tau_m = 45^\circ$ and a coil pitch of $\tau_c = 58^\circ$. The power dissipation of the other two back-iron configurations as shown in Figs. 5.10 and 5.11 with a magnet pitch of $\tau_m = 45^\circ$ is the lowest for all coil pitches.

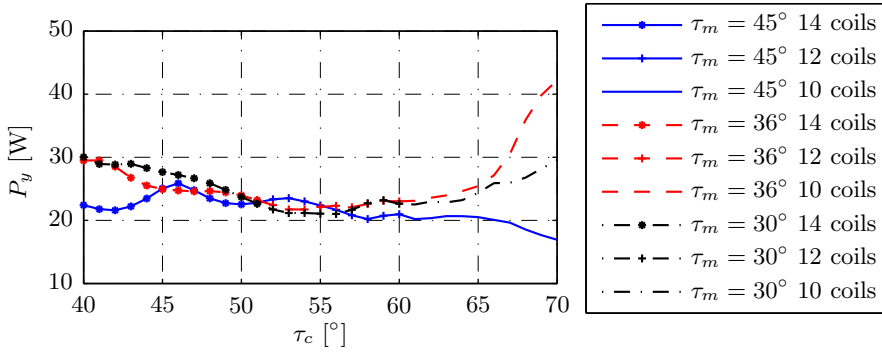
The elongated coil topology has the lowest power dissipation when the magnet pitch is $\tau_m = 45^\circ$. For the configuration without back-iron, this occurs for a coil pitch of $\tau_c = 57^\circ$ as shown in Fig. 5.12. The other configurations have the lowest power dissipation for all coil pitches with $\tau_m = 45^\circ$ as shown in Figs. 5.13 and 5.14. The power dissipation of the different back-iron configurations shows a similar trend for both the circular and elongated coil topologies as function of the coil pitch.

The topologies with the lowest power dissipation are listed in Table 5.4. The average of the three power dissipations, P_x , P_y , and P_z is given, and the ratio between the pole and coil pitch is included in this table. The actuator topologies with an equal pole pitch, τ_m , and coil topology have a similar result for this ratio. Hence, the back-iron has almost no influence on the pole to coil pitch ratio.

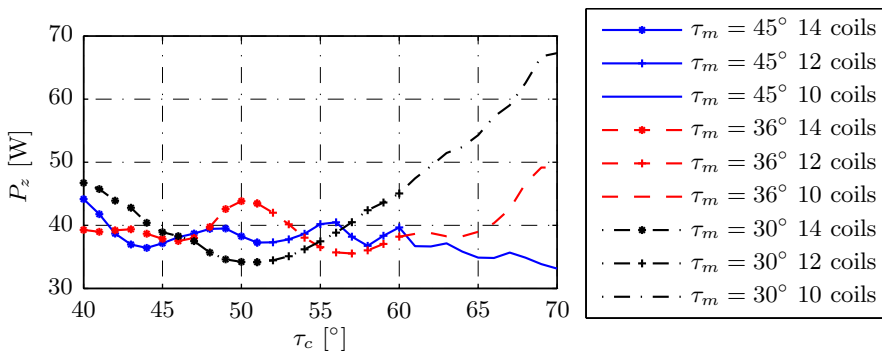
The relative change in power dissipation for the different magnet pitches, τ_m , increases for the different back-iron configurations. This change is caused by the different sizes of the permanent magnets. The hemispherical permanent magnet arrays with $\tau_m = 36^\circ$ and $\tau_m = 30^\circ$ have a higher number of magnets on the same surface of the rotor than the topology with $\tau_m = 45^\circ$. Therefore, the amplitude of the magnetic flux density in the airgap is lower. Consequently, the effect of adding back-iron reduces. This is visible in Table 5.5 where the decrease in the power dissipations becomes less when the pole pitch decreases. Therefore, the topology



(a)

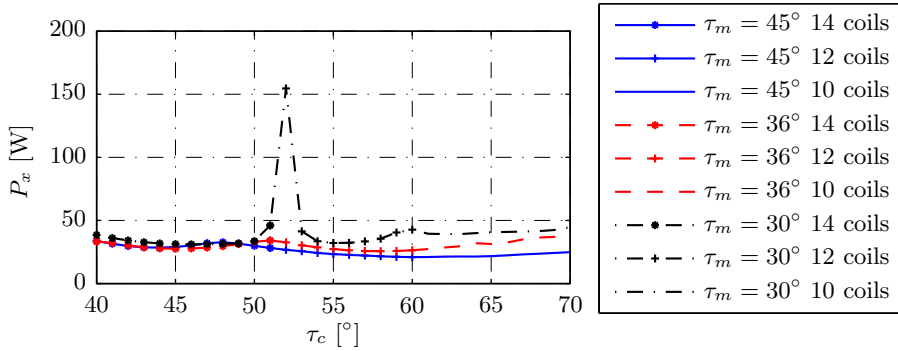


(b)

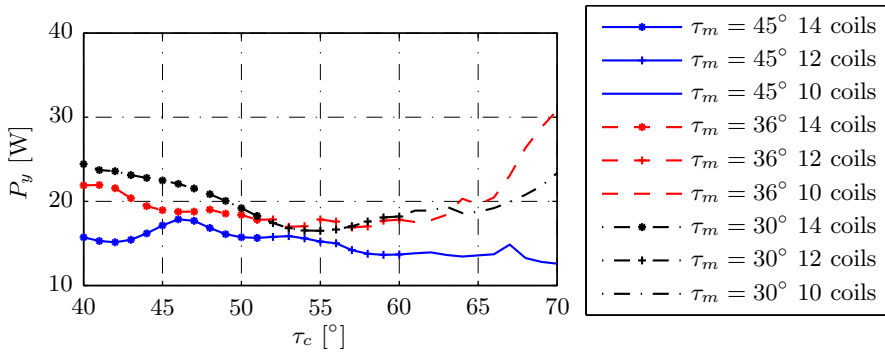


(c)

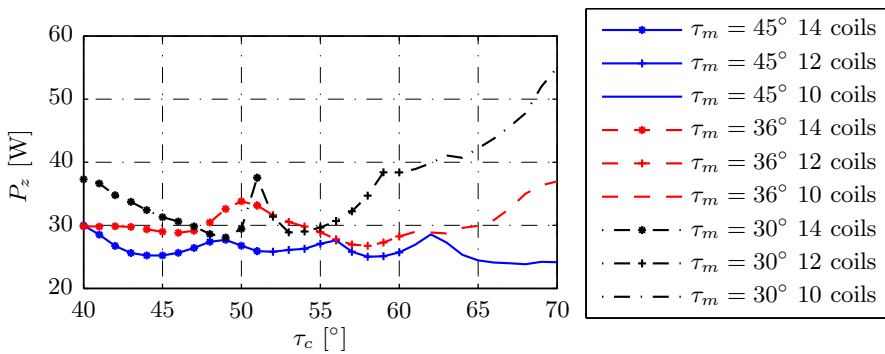
Figure 5.9: Average power dissipation over the complete range of motion as function of the coil pitch of the circular coil array without back-iron: (a) P_x , (b) P_y , and (c) P_z .



(a)

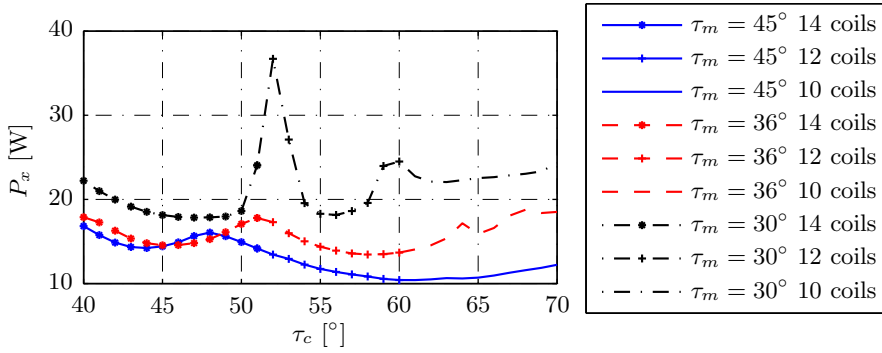


(b)

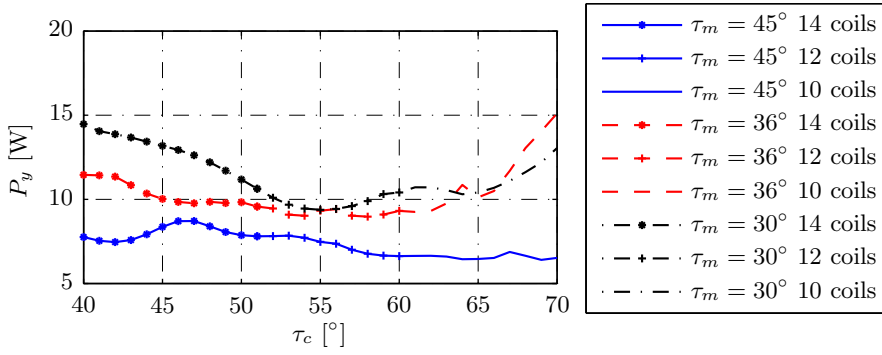


(c)

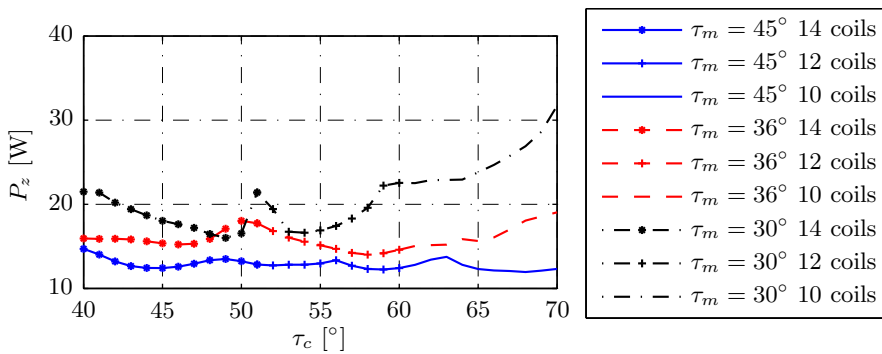
Figure 5.10: Average power dissipation over the complete range of motion as function of the coil pitch of the circular coil array with back-iron behind the permanent magnet array: (a) P_x , (b) P_y , and (c) P_z .



(a)



(b)



(c)

Figure 5.11: Average power dissipation over the complete range of motion as function of the coil pitch with back-iron behind of the circular coil array and permanent magnet array (cogging is not taken into account): (a) P_x , (b) P_y , and (c) P_z .

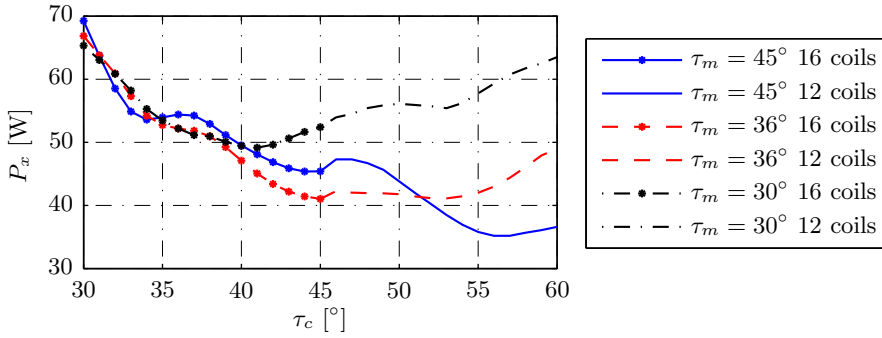
with a hemispherical permanent magnet of $\tau_m = 45^\circ$, represented by a full line in the figures, has the lower power dissipation for all coil pitches when back-iron is considered. In addition, the power dissipation P_y , is the lowest because the most coils are distributed about the y -axis. Furthermore, the circular coil topology provides a lower overall power dissipation in comparison to the elongated coil topology.

The decrease of power dissipation when adding back-iron can be predicted with the quadratic relation between the magnetic flux density and the power dissipation. Assuming an equal torque production, the increase in magnetic flux density results in a decrease in current density because of their linear relation as shown in the Lorentz force law (3.23). The applicability of this relation is validated with the prediction for the hemispherical permanent magnet array with $\tau_m = 45^\circ$. With respect to the configuration without back-iron, an increase of 26% and 80% (shown in Figs. 5.3a and 5.4a) is achieved when placing back-iron behind the permanent magnets, and behind the magnets and coils, respectively. A predicted decrease of 37% and 69% in power dissipation is obtained by the quadratic relation. Calculation of the decrease in power dissipation with the values presented in Table 5.4 results in 32% and 66%. These values are in good agreement with the prediction based on the magnetic flux density. The deviation of the predictions is caused by a difference in the spatial magnetic flux density characteristic between the back-iron configurations. Hence, when a region partially consists of highly permeable material, in case back-iron is segmented, the increase in magnetic flux density can be obtained with FEA. Subsequently, the power dissipation can be approximated with the magnetic charge model by applying this relation.

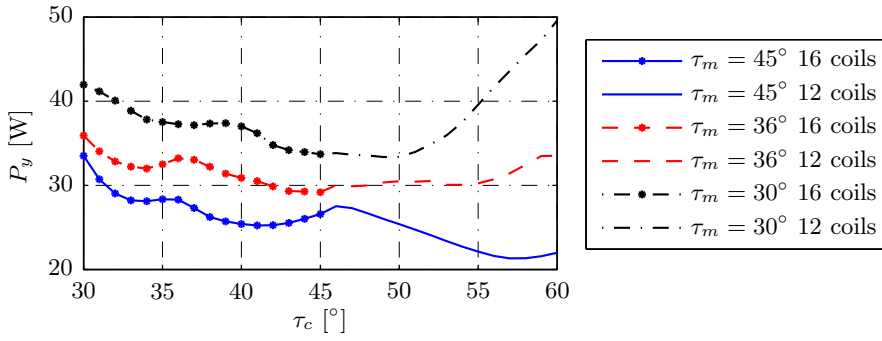
The configuration with back-iron for the permanent magnets, $\tau_m = 45^\circ$ and the circular coil shape is preferred. This topology has the lowest power dissipation with respect to the other actuator topologies. The configuration with back-iron behind the coils is not considered due to the cogging torque. However, this cogging torque is investigated in Fig. 5.7.

5.4 Integration of the gravity compensator

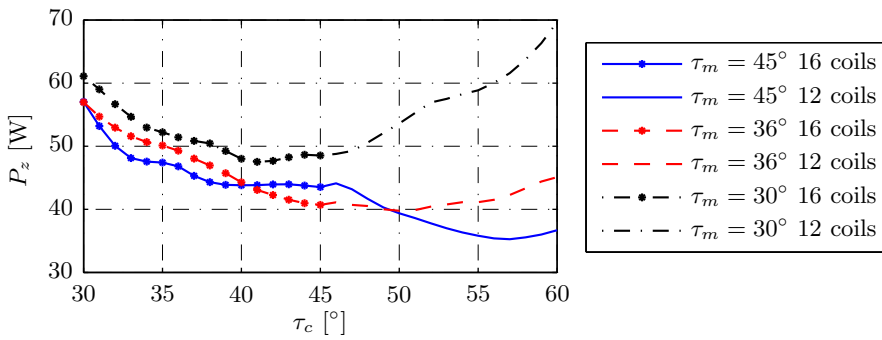
The selected spherical actuator design configuration has back-iron behind the permanent magnets. In the integrated actuator design, the gravity compensator is adjacent to this back-iron. Therefore, the influence that this back-iron has on the gravity compensator is investigation. This investigation is performed with non-linear 3D FEA and a back-iron height of $h_{bm} = 10$ mm. The gravity compensator should provide a sinusoidal torque characteristic with the gravity compensator when the actuator is not active. In case of a sudden power failure, the user has to be able to keep the smart arm-support system under control. When the torque characteristic is not sinusoidal a user with deteriorated muscles could be too weak



(a)

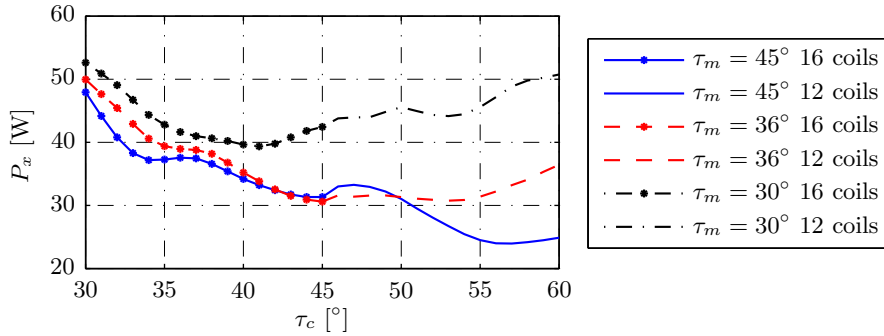


(b)

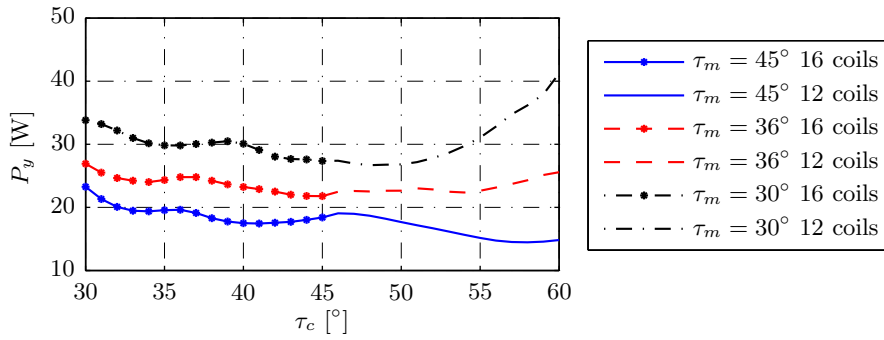


(c)

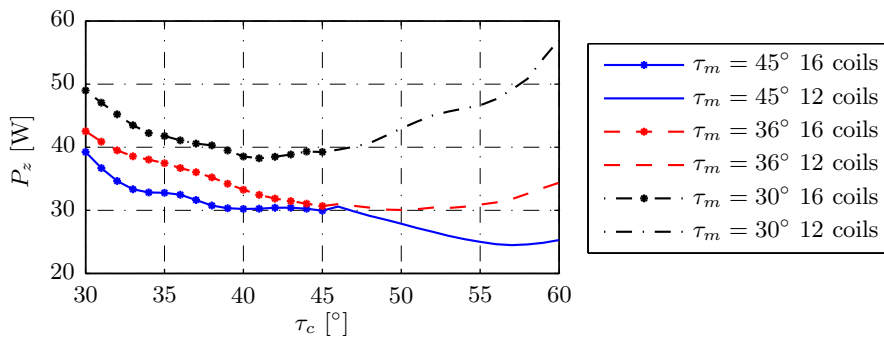
Figure 5.12: Average power dissipation over the complete range of motion as function of the coil pitch of the elongated coil array without back-iron: (a) P_x , (b) P_y , and (c) P_z .



(a)

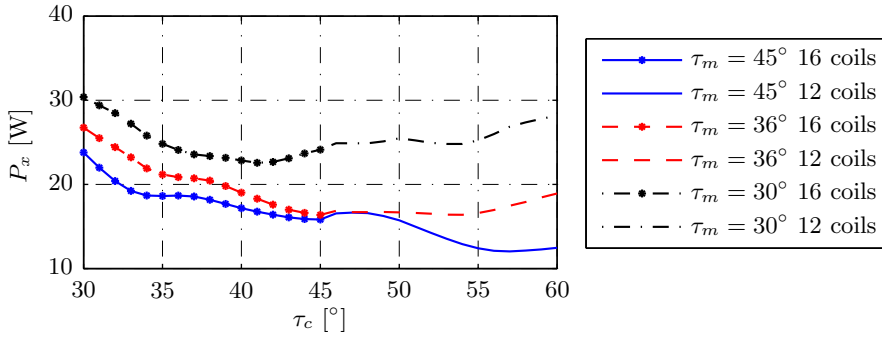


(b)

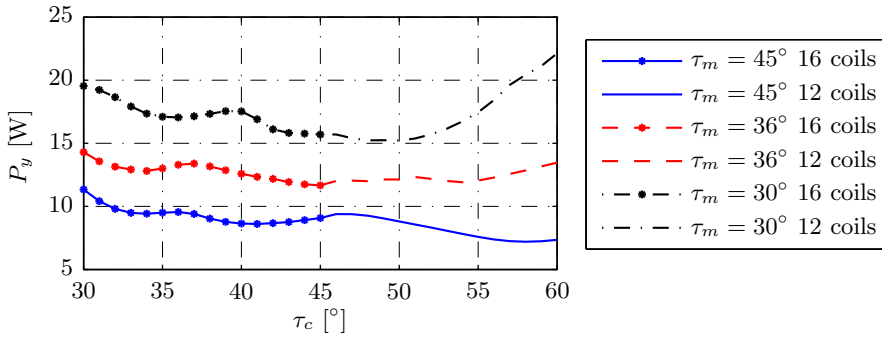


(c)

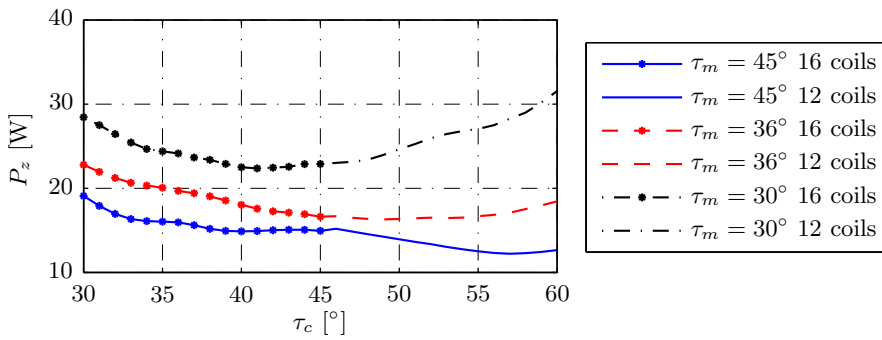
Figure 5.13: Average power dissipation over the complete range of motion as function of the coil pitch of the elongated coil array with back-iron behind the permanent magnet array: (a) P_x , (b) P_y , and (c) P_z .



(a)



(b)



(c)

Figure 5.14: Average power dissipation over the complete range of motion as function of the coil pitch with back-iron behind the elongated coil array and permanent magnet array (cogging is not taken into account): (a) P_x , (b) P_y , and (c) P_z .

Table 5.4: The average of the three power dissipations P_x , P_y , and P_z are given for the different coil and magnet pitch that have the lowest power dissipation

Coil topology	back-iron configuration	P [W]	τ_m	τ_c	τ_m/τ_c	
Circular	without	29.6	45°	58°	0.78	
		30.9	36°	57°	0.63	
		31.3	30°	53°	0.56	
	magnet	20.1	45°	60°	0.75	
		23.1	36°	58°	0.62	
		27.0	30°	48°	0.63	
		magnet and coil	9.8	45°	59°	0.76
			12.1	36°	58°	0.62
			15.2	30°	49°	0.61
	Circular	without	30.6	45°	57°	0.79
			37.4	36°	54°	0.67
			44.3	30°	41°	0.73
magnet		21.0	45°	57°	0.79	
		27.9	36°	54°	0.67	
		35.4	30°	42°	0.71	
		magnet and coil	10.6	45°	57°	0.79
			15.0	36°	54°	0.67
			20.4	30°	42°	0.71

Table 5.5: The decrease in power dissipation when back-iron is added with respect to the configuration without back-iron

Magnet array topology	PM back-iron	PM and Coil back-iron
$\tau_m = 45^\circ$	32%	66%
$\tau_m = 36^\circ$	22%	60%
$\tau_m = 30^\circ$	14%	51%

to keep the smart arm-support system in position.

A segmented back-iron for the hemispherical permanent magnet array is proposed as alternative to a full hemispherical back-iron. This segmentation is a compromise between no or a hemispherical back-iron. The outer permanent magnet of the gravity compensator and the spherical permanent magnet array of the actuator are mounted on a supporting structure. This supporting structure contains the back-iron of the hemispherical permanent magnet array and is attached to the rod that exerts the produced torque. A full and segmented hemispherical back-iron for the spherical permanent magnet array is illustrated in the sectional view of Fig. 5.15a and Fig. 5.15b, respectively.

The size of the back-iron segments is varied as indicated with ξ in Fig. 5.15b which results in a gravity compensator torque performance as shown in Fig. 5.16. The size of the segments is defined with ξ where 45° represents a full hemispherical back-iron and 0° represents no back-iron. For a full hemispherical back-iron, the gravity compensator does not provide an exact sinusoidal torque. This back-iron topology short circuits the magnetic field of the gravity compensator. In case of segmentation, the reluctance of the air is dominant with respect to the iron parts because of the high difference in relative permeability. The application of the segmented back-iron of $\xi = 35^\circ$ increases the torque production of the gravity compensator with 3%. However, the magnetic flux density in the airgap of the spherical actuator, produced by the hemispherical permanent magnet array, decreases due to the segmentation of the back-iron. Hence, a compromise is made between the segmentation size, sinusoidal torque of the compensator and the mechanical stiffness of the supporting structure. Furthermore, when the space between the elements is too small, the supporting structures is more difficult to realize due to manufacturing limitations. Consequently, a segment size of $\xi = 35^\circ$ is chosen. With this segmentation, the magnetic flux density in the airgap of the spherical actuator increases with 19% instead of 26% in case of a full hemispherical back-iron. Furthermore, for larger values of ξ the distance between the elements becomes very small. This distance defines the geometry of the supporting structure in which the elements are embedded.

To avoid saturation in the back-iron behind the permanent magnet arrays a height of $h_{bm} = 10$ mm is used. For comparison, the magnetic field in the back-iron is shown for a height of $h_{bm} = 5$ mm and $h_{bm} = 10$ mm in Fig. 5.18a and Fig. 5.18b, respectively. The maximum magnetic flux density for a height of 5 mm is 2.3 T and for a height of 10 mm is 1.6 T. In this case, there is a difference of 12% between the magnetic flux densities in the airgap due to the saturation effect. The back-iron of the coils shows a maximum magnetic flux density of 1.4 T with a height of $h_{bc} = 5$ mm. Hence, no saturation occurs and, therefore, a larger height is not investigated.

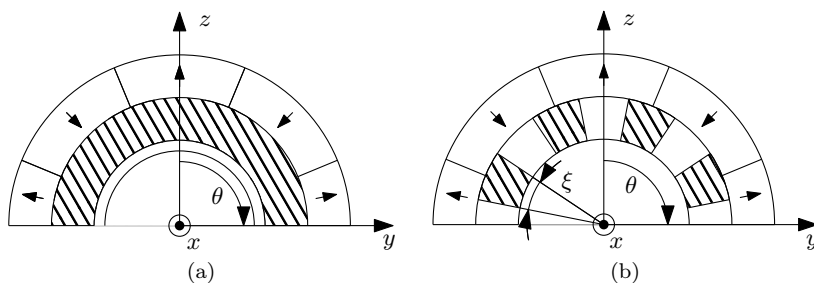


Figure 5.15: Sectional view of the spherical actuator integrated with the gravity compensator with: (a) full hemispherical back-iron, b) segmented spherical back-iron.

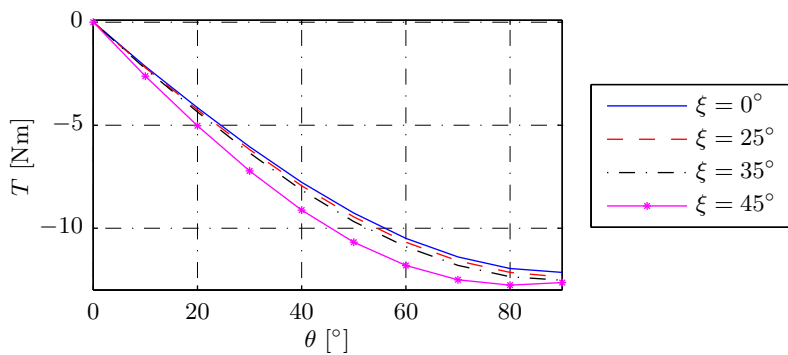


Figure 5.16: Torque performance of the gravity compensator for various back-iron segment sizes.

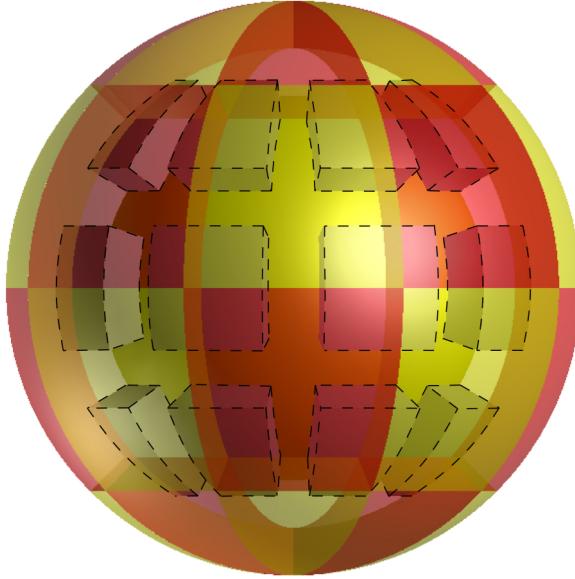


Figure 5.17: Segmented backiron in combination with the hemispherical permanent magnet array.

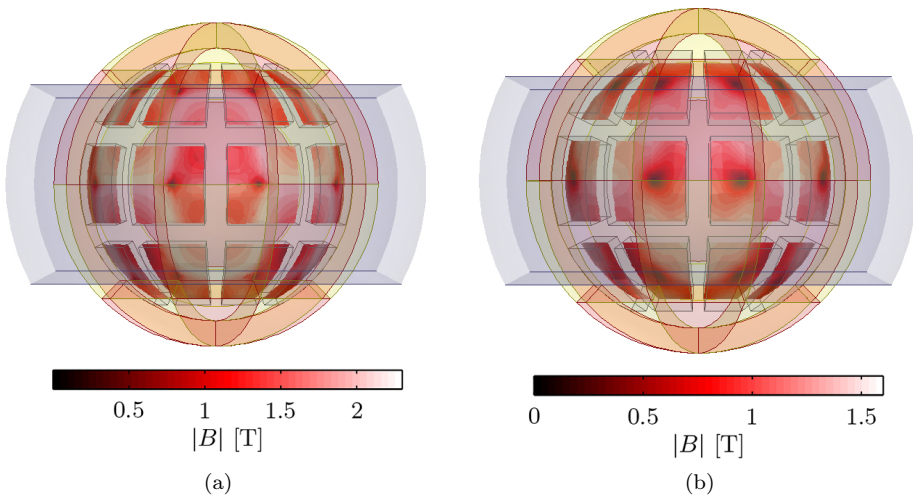


Figure 5.18: The total magnetic flux density in the middle of the permanent magnet back iron with a height of: (a) $h_{bm} = 5$ mm, (b) $h_{bm} = 10$ mm.

5.5 Optimization of the geometry

The goal for the final design of the spherical actuator with integrated gravity compensator is to minimize its volume without exceeding the thermal requirements. The topology with the lowest power dissipation has circular coils and a pole pitch of $\tau_m = 45^\circ$. The coil pitch is constrained by the diameter of the rod (depicted in Fig. 5.1) and the required range of motion. It is assumed that for the smart arm support system a rod diameter of 20 mm is sufficient. Hence, to comply with the range of motion requirements, the coil pitch is limited to 55° . Within this limited range, the power dissipation is the lowest with a coil pitch of $\tau_m = 52^\circ$.

The volume of the spherical actuator is minimized with a parametric search. This parametric search concerns the conductor bundle width, height of the coils, and the permanent magnet height. It is assumed that there is no coupling between the conductor bundle width and the other two parameters based on the separation of variables in (3.85). The power dissipation as function of the conductor bundle width is shown in Fig. 5.19. According to these results the power dissipation is minimal after a ratio of 0.75 between the conductor bundle width and the coil size.

The geometric parameters of the coil height and magnet height are optimized for two back-iron configurations. Both configurations have back-iron behind the permanent magnets, however, one is with and the other is without back-iron behind the coils. Furthermore, to model the segmentation of the back-iron behind the permanent magnet array, this analysis is performed with FEA. In the evaluation, three different positions are taken into account for the coil array, namely a rotation about the x -axis of 0° , 22.5° , and 45° . The influence of the hemispherical permanent magnet sizes, due to the spherical geometry, is averaged with these three positions.

In the parametric search for the optimal coil height, the radius of the permanent magnet array is kept constant. The radius of the back-iron behind the coils is adjusted for each coil height variation. The resulting power dissipation as function of the coil height is shown in Fig. 5.20a and Fig. 5.20b with and without back-iron behind the coils, respectively. The coil height for the configuration with back-iron behind the coils has the lowest power dissipation for $h_c = 9$ mm. The other configuration has the lowest power dissipation when $h_c = 13$ mm. However, the results in this figure shows a relative constant power dissipation for all three axis from a height of $h_c = 9$ mm. This height is preferred for the minimization of the volume.

The optimization of the permanent magnet array height, h_m , is shown in Fig. 5.21 for the two configurations. In the trade off between the increase in torque production, mass, and costs, a height of 10 mm is chosen as maximum for both topologies.

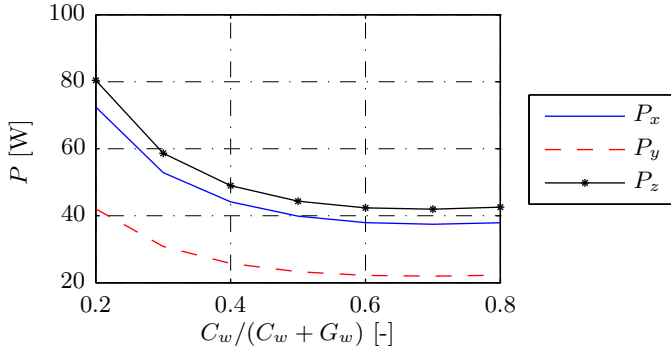


Figure 5.19: The power dissipation as function of conductor bundle width for the slotless spherical actuator topology with circular coils.

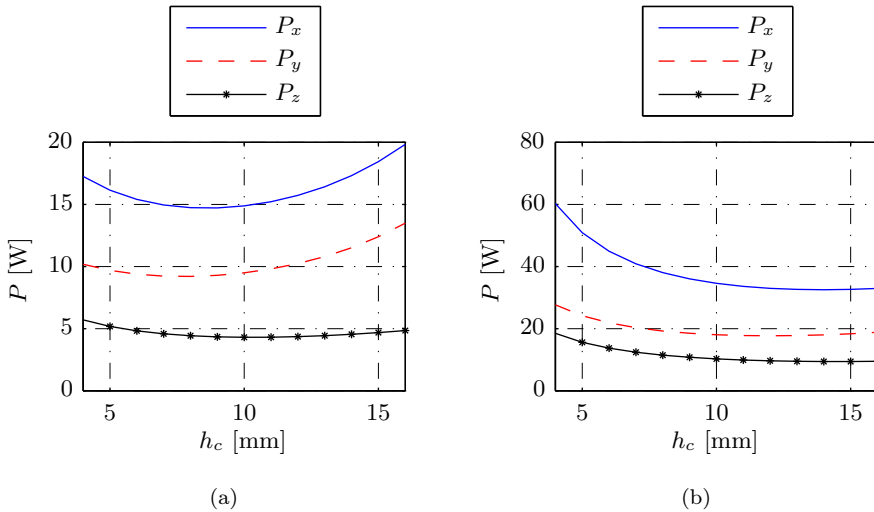


Figure 5.20: Obtained power dissipation as function of the coil height for the configuration: (a) with coil back-iron, (b) without coil back-iron.

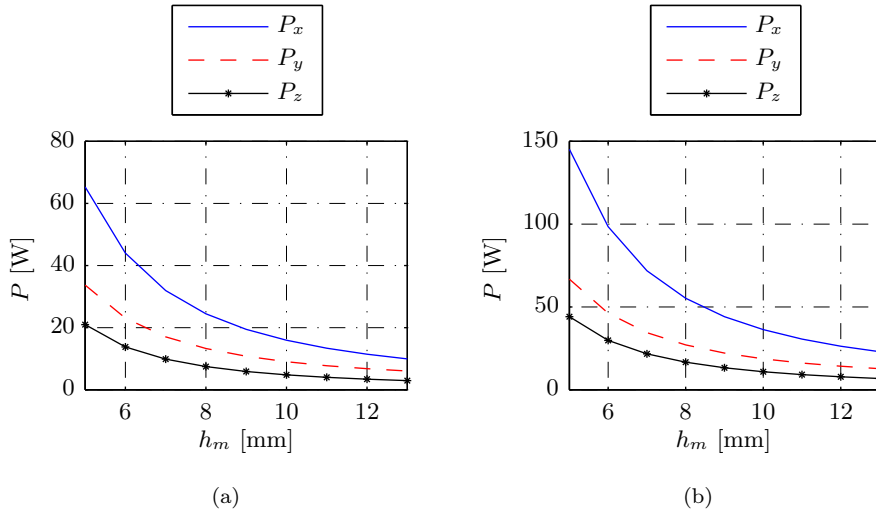


Figure 5.21: Obtained power dissipation as function of the permanent magnet height for the configuration: (a) with coil back-iron, (b) without coil back-iron.

5.6 Thermal analysis

The dissipation of power is constrained by the thermal requirement of the actuator. Therefore, a thermal model is used to determine the temperature rise during operation. The heat flow rate in the spherical actuator is caused by the power dissipation (ohmic losses) in the coils and the heat is conducted through the coils to the back-iron or support structure where the convection occurs. The material chosen for the support structure is aluminum. This material is non-magnetic and has a high thermal conductivity.

The configuration with only a segmented back-iron behind the permanent magnets is taken as the most suitable topology for the application. This topology provides the most magnetic flux density in the airgap without introducing a cogging torque. In this thermal analysis, the power dissipation is predicted by modeling the configuration without any back-iron. These results are adjusted knowing that the segmentation increases the magnetic flux density with 19% as shown in Section 5.4. This method allows a fast analysis over the complete range of motion with 3375 positions.

The thermal behavior of the continuous torque and peak torque modes are investigated. In the continuous torque mode, the actuator reaches its steady state

temperature. The relation of this temperature to the radius of the spherical actuator is analysed. The peak torque is produced by a short burst of power; hence, a peak current flows through the coils. This current causes a rise in the temperature as function of time. In addition, this temperature rise in combination with the cool down period determines the time that the peak current can be applied.

In the thermal analysis it is assumed that the main heat removal occurs through convection. Consequently, the rise in temperature reaching the steady state can be obtained by Newton's law [45]:

$$\Delta T = \frac{Q}{hA} \quad (5.11)$$

where Q is the heat flow rate, A is the area, ΔT is the temperature difference between the cooling medium and the surface being cooled, and h is the convection heat-transfer coefficient. This heat-transfer coefficient is a combination of radiation and convection which results in a value between $12 \text{ W}/(\text{m}^2\text{K})$ and $16 \text{ W}/(\text{m}^2\text{K})$ [119]. Every surface that is in contact with the surrounding environment is taken into account for the convection surface, A . It is assumed that the thermal resistance due to convection is dominant compared to the thermal resistance due to conduction inside the actuator. Therefore, thermal conduction is neglected. In this thermal analysis, the value for the heat-transfer coefficient is chosen conservatively, namely $h = 12 \text{ W}/(\text{m}^2\text{K})$.

According to Newton's law, the steady-state temperature of the spherical actuator is directly related to the outer surface of the stator. Therefore, the temperature is also directly related to the outer radius. This radius also influences the magnetic flux density in the airgap and, consequently, the torque production. Hence, for the analysis of the steady-state temperature with respect to the size, both these effects have to be included. In this analysis, the height of the permanent magnets, airgap length, coil height and coil supporting structure height is kept constant at, $h_m = 10 \text{ mm}$, $g_a = 1 \text{ mm}$, $h_c = 9 \text{ mm}$, and $h_{bc} = 5 \text{ mm}$, respectively. The resulting temperature rise, ΔT , as function of the outer radius of the actuator is shown in Fig. 5.22 for the continuous power dissipation of $Q = 30.3 \text{ W}$. These results show that with an outer radius of 78 mm , the actuator complies with the required thermal specification, $\Delta T = 40^\circ\text{C}$. Furthermore, these results shows that with an outer radius of 87 mm for the spherical actuator, the temperature rise stays within $\Delta T = 20^\circ\text{C}$. From this analysis, it is found that the torque has a quadratic relation as function of the outer spherical actuator radius for a constant ΔT . This corresponds with standard rotary electromechanical machines which have a torque as function of the radius and stack length of the machine for a constant temperature rise [44].

A transient thermal FEA is applied to model the temperature rise for the peak torque mode. The transient behavior is analysed with an axial symmetric 2D finite element model, as shown in Fig. 5.23, with the commercial software Flux

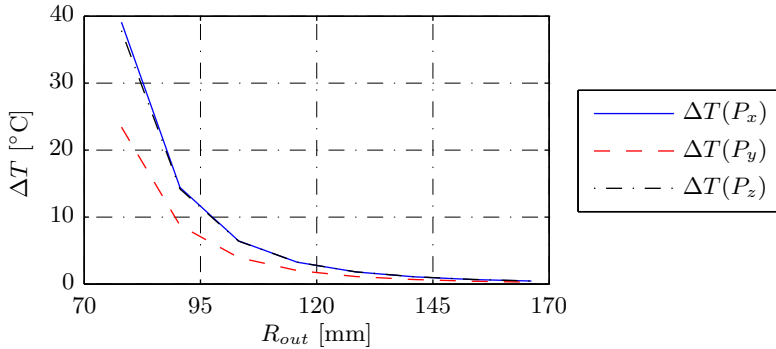


Figure 5.22: The steady state temperature rise as function of the outer radius of the actuator with a predefined torque of $T_d = 1$ Nm about the x , y , and z axis resulting in a power dissipation P_x , P_y , and P_z .

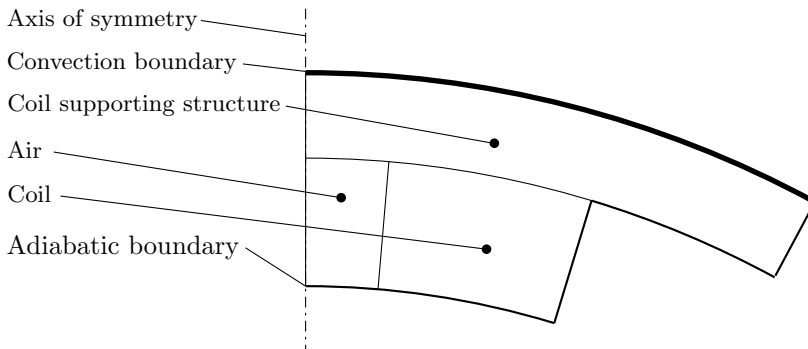


Figure 5.23: Transient axial symmetric finite element model applied for the thermal analysis representing $\frac{1}{12}$ of the spherical actuator.

[16]. In this model, the spherical actuator is simplified by considering only one coil and the convection boundary corresponds with $\frac{1}{12}$ part of the convection area of the spherical actuator. The thermal parameters used for this model are listed in Table 5.6.

The time the spherical actuator requires to cool down after providing a peak torque needs to comply with the specified duty cycle of 2.5 hours. This time depends on the thermal capacitance and on the duration the peak torque is applied. The spherical actuator with an outer radius of 78 mm dissipates 848 W when a peak torque of 6 Nm is produced. In the FEA, the coil is excited with $\frac{1}{12}$ of this power for one period of time and then set to zero to simulate the cool down period. The resulting cool down time for the different excitation times are listed

Table 5.6: Thermal parameters of the transient FEA

	Thermal conductivity [W/mK]	Specific heat [J/cm ³ K]
Coil	1	3.45
Aluminum	205	3.42

Table 5.7: The peak temperature increase, T_p , reached for several excitation times of the coils to achieve the peak torque and the time to cool down, t_{ambient} , to the ambient temperature afterwards for an outer radius of 78 mm.

Excitation time [s]	T_p [°]		t_{ambient} [hours]	
	Stator	Coils	Stator	Coils
5	2.2	6.4	1.25	1.25
10	5	15	1.8	1.8
15	8	23	2.2	2.2
20	11	30	2.5	2.5
25	14	37	2.6	2.6

in Table 5.7. These results show that the excitation time has a maximum of 20 s, otherwise the cool down time is larger than 2.5 hours which does not comply with the specifications. With this excitation time, the coils and their supporting structure have a transient behavior as shown in Fig. 5.24. In this figure, the maximum temperature rise of the supporting structure is $\Delta T = 11^\circ\text{C}$. The heat of the coils is transferred without a large increase of the temperature of the supporting structure because of its large heat capacitance. This results in a fast decrease in temperature of the coils with respect to the supporting structure until their temperature is almost equal. The peak of the temperature rise occurs after 4 min and, subsequently, the structure cools down to its initial temperature after 2.5 hours.

5.7 Cogging torque

There are two parasitic torques, namely a cogging and reluctance torque. The magnetic field produced by the coils is small with respect to the magnetic field produced by the permanent magnets. The height of the permanent magnets, 9 mm, which prevents the magnetic field of the coils to reach the back-iron of the permanent magnets. Therefore, the reluctance torque that the coils create with the back-iron can be neglected.

Although it is not preferred to introduce cogging in the actuator because of the

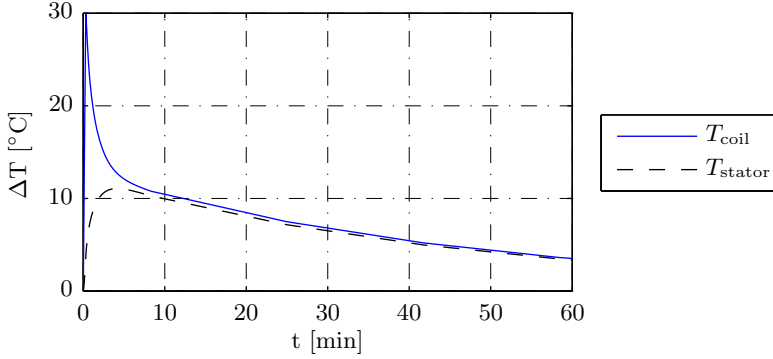


Figure 5.24: Temperature rise of the outside of the actuator and the coils with an excitation time of 15 s and an outer radius of 78 mm.

arm support application, it is investigated what the effects of introducing back-iron behind the coils are. High permeable material as back-iron for the permanent magnets and coils can be added to increase the magnetic flux density in the airgap. For the back-iron of the coils, a full sphere cannot be employed because otherwise the specified range of motion cannot be achieved. Therefore, the structure has two edges that interact with the magnetic field of the permanent magnets, which results in a cogging torque.

An additional torque is required to compensate for the cogging. This additional torque can be necessary to accelerate or compensate for an extra mass. Hence, a certain amount of the gained torque density by introducing back-iron is required to counteract the cogging torque. This amount determines if it is justified to add back-iron or that it provides an equal or lower performance. Therefore, several back-iron geometries are evaluated, to find a design with minimized cogging torque.

The proposed actuator design has a back-iron surrounding the spherical permanent magnet array completely about the y -axis. Hence, rotation about this angle does not change the energy in the system and, therefore, this motion produces no cogging torque. Furthermore, because of the symmetry of the spherical actuator, the initial position as shown in Fig. 5.25 has zero cogging torque. However, when the actuator rotates about the x or z -axis, cogging torque occurs. This cogging torque characteristic is equal for both rotation direction because of the spherical symmetry. Therefore, only the cogging torque about the x -axis is shown.

The cogging torque of the back-iron design of the initial actuator, as shown in Fig. 5.25, produces a cogging torque when rotated about the x -axis as shown in Fig. 5.27a. The results in this figure shows a sinusoidal characteristic. In addition, there is not much variation in amplitude for the different back-iron widths (indicated with an angle), w_c .

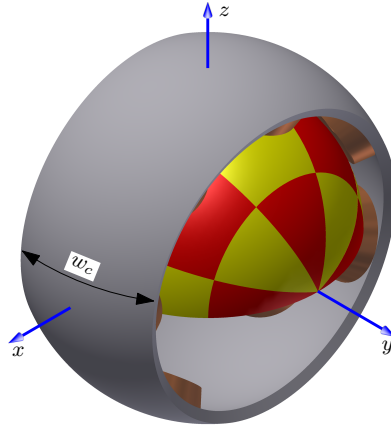


Figure 5.25: The spherical actuator without the gravity compensator and the initial design for the back-iron behind the coils.

Alternative shapes for the coil back-iron are proposed as shown in Fig. 5.26. The first shape consists out of two separated rings, and the second shape has undulated sides. The distance between the two separate rings is indicated with, s , in Fig. 5.26a. The width of the back-iron is kept at a constant $w_c = 56.8^\circ$ which corresponds with the width of the geometrically optimized spherical actuator. It is investigated whether the cogging torque caused by one edge can be counteracted by the cogging torque produced by the other edge. The undulated sides topology is an attempt to improve the smoothness of the transition of the back-iron with respect to the permanent magnets of the hemispherical array. The undulated shape corresponds with the location of the coils.

The two separated rings have a cogging torque as shown in Fig. 5.27b for different distances, s , between the rings. These results show an increasing cogging torque when enlarging the distance between the rings. This indicates a minimum cogging torque when the distance between the rings is zero. Therefore, the cogging torque can not be reduced with this topology.

The topology with the undulated sides has a cogging as shown in Fig. 5.27c for different width of the back-iron, w_c , as indicated in Fig. 5.26b. In contrast to the other two topologies, the undulated sides cause a cogging torque about all three axes. The amplitudes are the lowest of all three topologies, however, in total they present a comparable cogging torque with the other topologies.

For all three back-iron topologies, the cogging torque has an larger amplitude than the required continuous torque of 1 Nm. Therefore, it is concluded that the cogging torque is too high and a configuration without back-iron behind the coils is preferred.

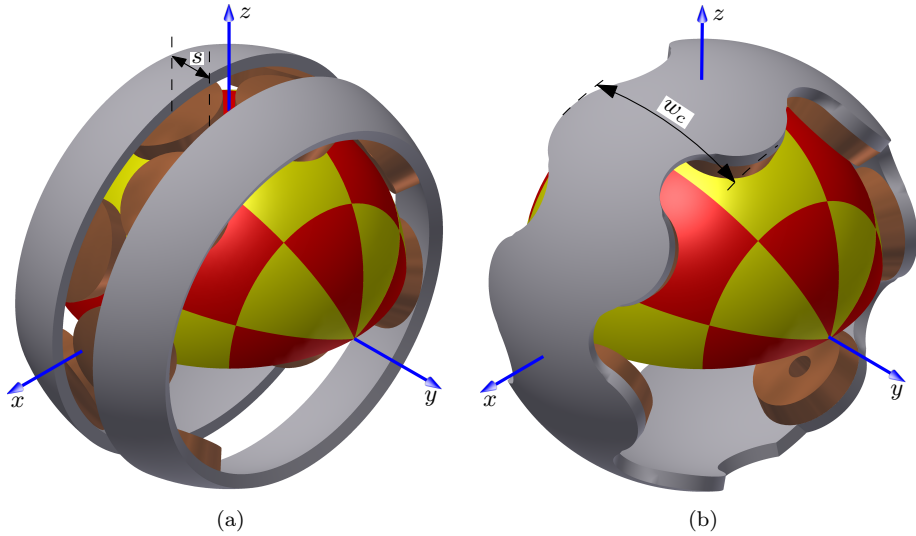


Figure 5.26: Alternative coil back-iron geometries consisting of: (a) two separate spherical rings, (b) undulated sides

5.8 Final design

The final design of the spherical actuator with integrated gravity compensator is presented in Fig. 5.28. The geometric parameters and specifications of this design are listed in Table 5.8. The spherical actuator with integrated gravity compensator is designed for a smart arm-support system. The compensator has to be positioned accounting for the gravity direction, whereas the spherical actuator has to be positioned to comply with the specified range of motion required for the activities of daily living. In the illustration of the final design, the rod is shown transparently to clearly visualize the position of the gravity compensator. The flat side of the inner hemispherical permanent magnet of the gravity compensator is aligned with the horizontal xy -plane. This magnet is supported by a construction positioned in an angle of 45° with the gravity direction. In this configuration the integrated actuator complies with the range of motion required for the activities of daily living.

The position of the integrated gravity compensator in the illustration (Fig. 5.28) corresponds with 90° flexion. This motion represents the rotation about the y -axis and is the motion in which the gravity compensator provides the sinusoidal torque characteristic. The other motions, horizontal flexion and rotation, can be supported with the rotation about the z - and x -axis, respectively. There is zero rotation stiffness for these rotations because the magnetization of the gravity

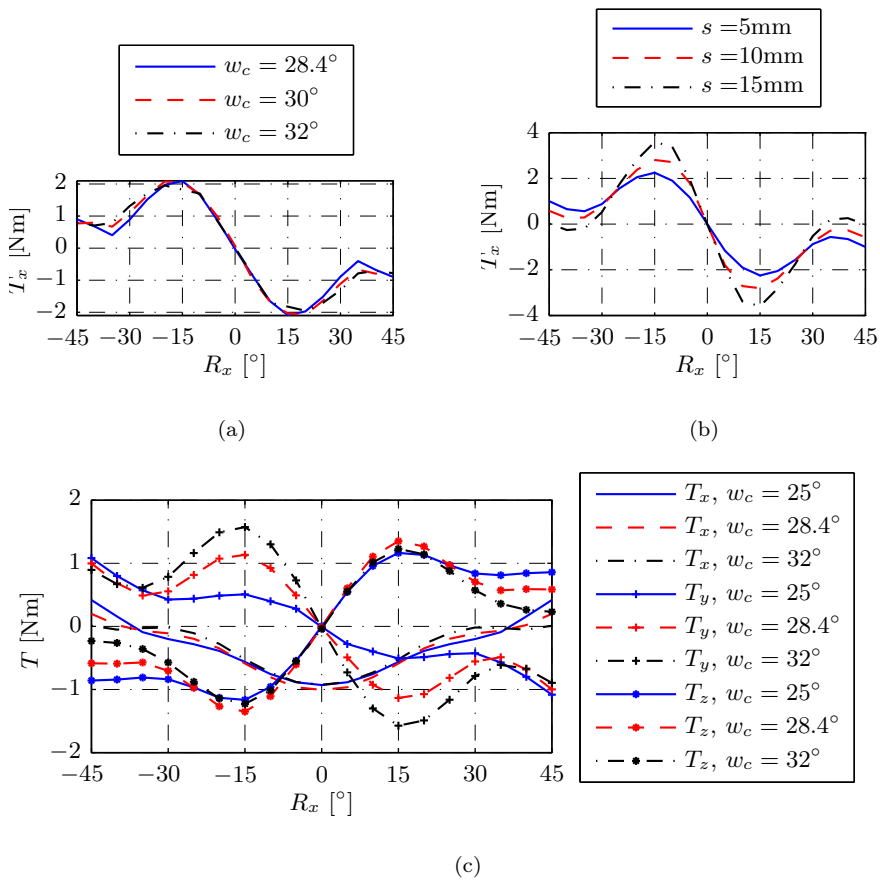


Figure 5.27: Rotation of the coil back-iron about the x -axis results in a: (a) cogging torque for the initial spherical actuator design which has only a non-zero x -component, (b) cogging torque for the spherical actuator design consisting of two separated rings which has only a non-zero x -component, and (c) cogging torque for all three components for the back-iron with the undulated sides.

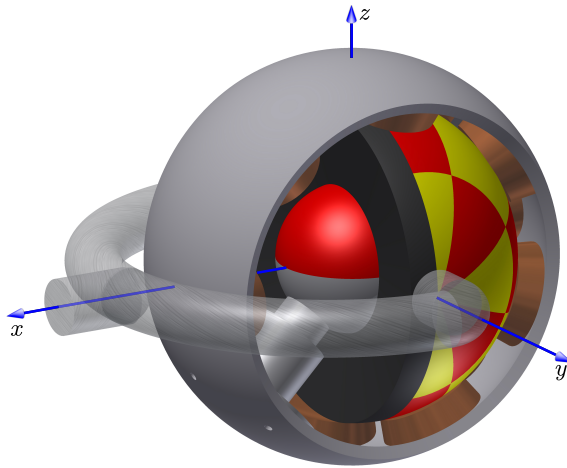


Figure 5.28: The final design of the spherical actuator with integrated gravity compensator.

compensatory is symmetrical.

For other robotic applications, the design can be different. Such as the placement of the gravity compensator with respect to the spherical actuator to change the range of motion. This novel integrated actuator topology is suitable in more applications than only mobile arm-support systems.

5.9 Conclusions

A spherical actuator with integrated gravity compensator has been designed for a smart arm-support system. The stator consists of the inner hemispherical permanent magnet of the gravity compensator and the coils of the spherical actuator. Both these elements are mounted on the same supporting structure. The rotor consists of the outer hemispherical permanent magnets of the compensator and the permanent magnet array of the actuator. These magnets are employed on a supporting structure that contains the segmented back-iron for the hemispherical permanent magnet array. The produced torque of the actuator is exerted through the supporting structure. The integrated design has two airgaps, namely the airgap of the gravity compensator and of the airgap of the spherical actuator.

The magnetic charge model is used to estimate the magnetic flux density of a hemispherical permanent magnet array for three configurations. The first configuration considers no back-iron, the second only behind the permanent magnet array and the third behind the magnet array and coils. The accuracy of the first

Table 5.8: Geometric parameters of the spherical actuator design

parameter	Symbol/Value	Unit
Outer radius of the magnet array	63	[mm]
Outer radius of the coil array	73	[mm]
Airgap length, g_a	1	[mm]
Coil height, h_c	9	[mm]
Coil supporting structure, h_{bc}	5	[mm]
Magnet height, h_m	10	[mm]
Coil pitch, τ_c	52	[deg]
Pole pitch, τ_m	45	[deg]
Conductor bundle width, C_w	14.7	[deg]
Coil gap radius, G_w	3.7	[deg]
Stator width, w_c	56.8	[deg]
Specifications		
Continuous torque	1.0	[Nm]
Peak torque	6.0	[Nm]
Temperature increase, ΔT	40	[°C]

configuration has been validated in Chapter 3. The second and third configurations have been approximated with the magnetic charge model combined with spherical imaging. This approximation requires to be validated with FEA. The magnetic flux density of the second configuration has been predicted with an amplitude discrepancy of 0.65%. In the third configuration, four spherical images have been applied to achieve an amplitude discrepancy of 4.5%. This prediction is only accurate in the region in which the coils are positioned.

The spherical actuator design has been minimized according to the requirements of the smart arm-support system. Multiple topologies have been compared based on their power dissipation. This power dissipation has been determined with the commutation algorithm. For the coil arrays, two different coil topologies have been included namely, circular and elongated. In this analysis it has been found that the circular coil topology has a lower average power dissipation than the elongated topology. The optimal coil and hemispherical permanent magnet topology applicable for the application are a coil pitch of $\tau_c = 52^\circ$ and a pole pitch of $\tau_m = 45^\circ$.

The inclusion of back-iron for the hemispherical permanent magnet array of the spherical actuator has been investigated. A full hemispherical shell short circuits the magnetic field of the gravity compensator and, therefore, influences its torque characteristic. To decouple both devices, the back-iron is segmented and segment

sizes of $\xi = 35^\circ$ have been employed. This back-iron structure has been configured such that any present interaction between the spherical actuator and gravity compensator is shielded to ensure the decoupling. The torque amplitude of the gravity compensator has been increased by 3%, and the magnetic flux produced by the hemispherical permanent magnet increased by 19% with this back-iron configuration.

By introducing back-iron for the supporting structure of the coils, a higher torque density can be achieved. However, the inclusion of this back-iron results in a cogging torque. To minimize this cogging, three different geometries have been investigated. Besides the initial geometry design, two alternative supporting structures, one with two separated rings and one with undulated sides, have been examined. A cogging torque that is larger than the continuous torque specifications has been found. Therefore, it has been concluded that back-iron behind the coils is not beneficial.

Chapter 6

Realization and experimental verification

Abstract - A scaled prototype of the spherical actuator with integrated gravity compensator is presented in this chapter. The torque characteristic of the novel gravity compensator and the spherical actuator are treated, and the torque production is measured and compared with the predictions. In addition, the applicability of the commutation algorithm combined with the theoretical results is validated. Subsequently, the torque production of the separated and integrated devices are compared. The coupling between both devices is quantified with this comparison.

6.1 Prototype design

The prototype is a scaled design of the gravity compensator and the spherical actuator as presented in Chapter 4. The design needs to be scaled due to manufacturing limitations. Commercially available permanent magnets are employed in the gravity compensator for the inner and outer hemispherical permanent magnet. Consequently, the size is determined by the largest parallel magnetized spherical permanent magnet available. The radial magnetization is approximated with a segmentation of multiple cylindrical permanent magnets.

The size of the spherical actuator is adjusted to the prototype design of the gravity compensator to investigate the interaction between both devices. Therefore, a different scaling is applied to the spherical actuator than to the gravity compensator. The spherical permanent magnet array of the actuator is constructed of cylindrically shaped permanent magnet pieces to approximate the spherical shape.

The realized prototypes allow experimental validation of their working principles. Furthermore, the design methods and theoretical predicted results are verified. In addition, any coupling between the compensator and actuator in the integrated device are identified.

6.2 Test benches

Two test benches are manufactured to perform measurements on the prototypes. The test benches for the gravity compensator and spherical actuator are shown in Fig. 6.1 and Fig. 6.2, respectively. These test benches have three rotation axes, x -, y - and, z as indicated in the figures. Each rotation axis can be locked to perform static measurements. The rotation about the x - and y -axis are realized with a stainless steel bush through the aluminum frames. There is a difference in the construction of the rotation about the z -axis between the test benches. This difference improves the dynamic behavior of the test setup for the spherical actuator. The rotation about the z -axis is realized by two aluminum disks rotating over each other for the gravity compensator. For the spherical actuator, there is a ring made of POM between the aluminum disks to reduce friction. The rotor can be locked in different positions with the test bench to keep it in position with respect to the stator for the measurements. In this setting, the spherical bearing is not included in gravity compensator to avoid alignment problems. Furthermore, due to the predefined sequence of rotation axes of the test benches, not every motion profile can be realized.

The measurement equipment used in the different test benches are almost the same. To measure the torque, an ATI delta SI-165-15 load cell is used. This load cell is capable of measuring six DoF, namely the forces and torques in the Cartesian

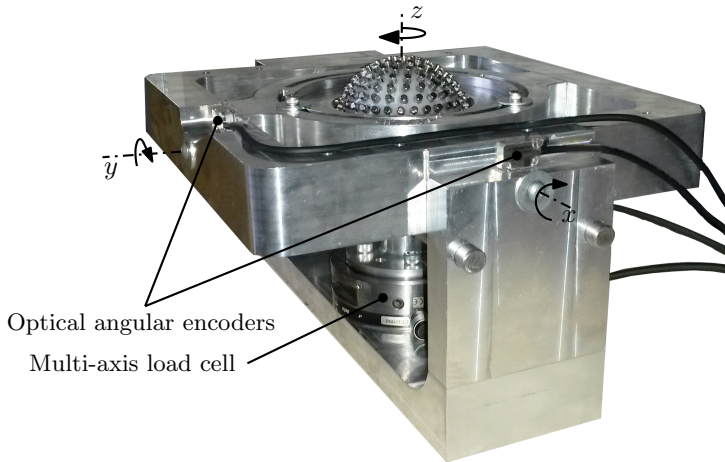


Figure 6.1: Test bench to measure the torque performance of the gravity compensator.

directions. The measurements of the load cell are provided through analog signals to a dSPACE system. The angular displacement of the rotation axes are measured with three optical Renishaw encoders. The rotations about the x - and y -axis, are measured with two incremental angular ATOM4T1-300 encoders and the rotation about the z -axis is measured with an incremental linear ATOM4T0-150 encoder. Both encoders have a resolution of $1\ \mu\text{m}$, and provide a digital to a dSPACE system. The measurements are performed with two different dSPACE systems, namely a 1104 system and a 1007 system for the gravity compensator and the spherical actuator, respectively. The dSPACE 1007 is also capable of controlling the single-phase three axes Prodrive PAD3AX59/6 PWM amplifiers to excite the coils. These amplifiers are capable of providing a continuous current of 2 A rms and a peak current of 6 A. They operate at a voltage of $\pm 59\ \text{V}$.

6.3 Magnetic gravity compensator

6.3.1 Construction

The realized prototype for the magnetic gravity compensator is shown in Fig. 6.3 and its geometry parameters are listed in Table 6.1. This prototype consists out of six parts as depicted in the exploded view shown in Fig. 6.4.

The inner hemispherical permanent magnet is created out of a full sphere of NdFeB grade N45 with a parallel magnetization and a radius of 25.4 mm. Wire eroding

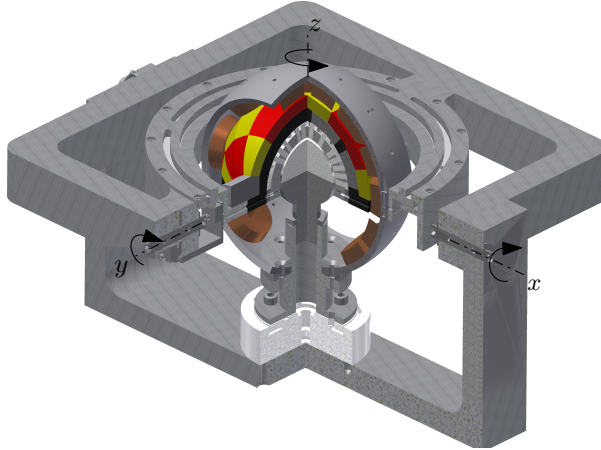


Figure 6.2: Test setup design for the spherical actuator with integrated gravity compensator.

Table 6.1: Dimensions of the prototyped gravity compensator topology, which are depicted in Fig. 4.4

Parameter	Value	Unit
Outer radius of the inner magnet, R_{in}	25.4	[mm]
Airgap length, g_a	2.5	[mm]
Outer radius of the outer magnet, R_{out}	40.4	[mm]
Height of the cylindrical magnets, h_{mc}	12.5	[mm]
Diameter of the cylindrical magnets, h_d	4	[mm]
Wall thickness, h_b	0.5	[mm]



Figure 6.3: Photo of the spherical gravity compensator prototype.

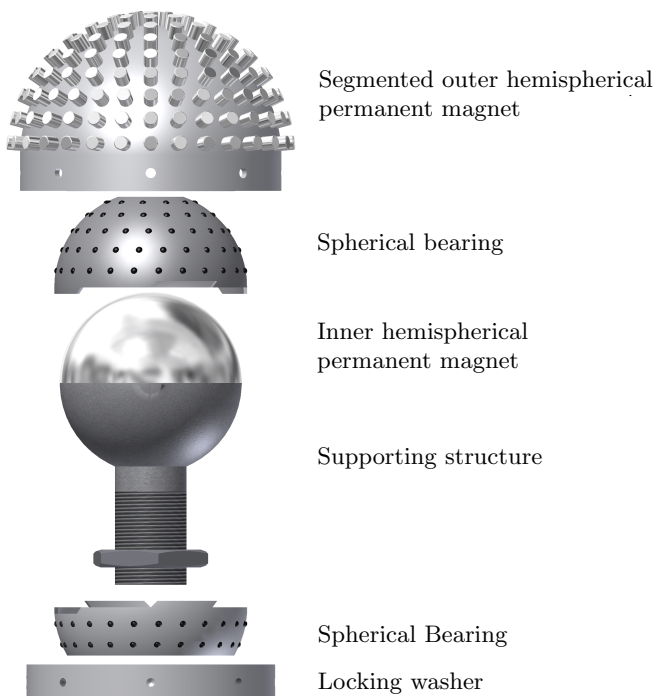


Figure 6.4: Exploded view of the gravity compensator prototype.

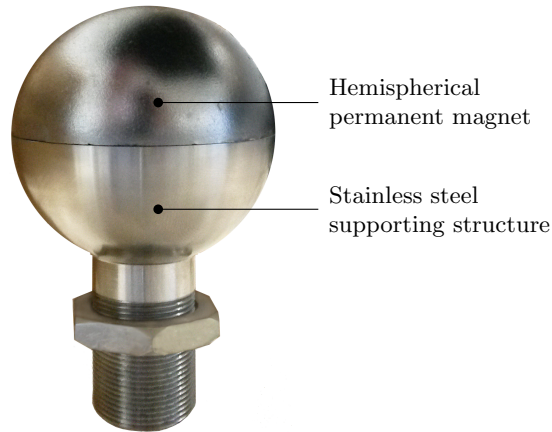


Figure 6.5: Inner hemispherical permanent magnet of the gravity compensator glued on the supporting structure.

is used to machine the NdFeB sphere into a hemisphere. For safety reasons, this permanent magnet was demagnetized by a decaying alternating magnetic field and afterwards magnetized again. The processed hemisphere is then glued on the supporting structure as depicted in the exploded view (Fig. 6.4). A photo of the realized part is shown in Fig. 6.5. Stainless steel, RVS304, is chosen for the material of the supporting structure because it has a low relative permeability ($\mu_r = 1.008$). Furthermore, this material has a higher hardness than aluminium which was required for the fine screw thread.

An approximation of the radial magnetization with a segmentation of 178 cylindrical permanent magnets allows fast prototyping. A photo of the realized structure is shown in Fig. 6.6a. The geometrical parameters of the cylindrical permanent magnets are listed in Table 6.1 and defined in the sectional view of this construction shown in Fig. 6.6b. This figure also shows that on the inside of the construction the cylindrical permanent magnets are close to each other, whereas on the outside there is more space between the cylindrical permanent magnets. This is due to the spherical shape and results in 68% less magnetic material compared to a full hemisphere for the specified radii in Table 6.1. The cylindrical permanent magnets are made of a N42 grade which specifications are listed in Table 6.2. These magnets are placed in a blind chamber of a supporting structure. These chambers are blind to provide a smooth surface for the spherical bearing. The wall thickness of the bearing cage, as indicated with h_b in Fig. 6.6b, is equal to 0.5 mm. This wall thickness together with the diameter of the bearing balls (2 mm), creates an airgap of 2.5 mm. The sectional view also shows the locking washer in combination with the supporting structure of the inner hemispherical permanent magnet array (depicted in a dashed line). The washer forms a cavity that encloses the

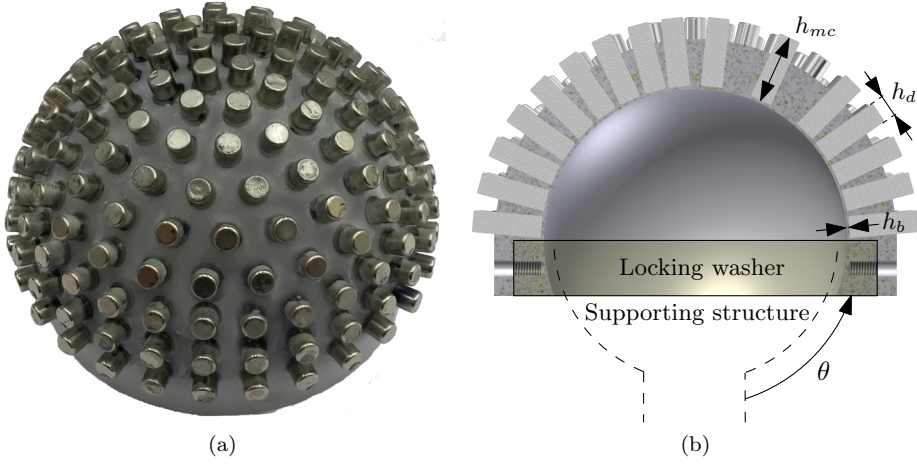


Figure 6.6: Segmented outer hemispherical permanent magnet: (a) realization, (b) sectional view

Table 6.2: Material properties of neodymium grades

NdFeB grade	B_r [T]	H_{cb} [kA/m]	H_{cj} [kA/m]
N45	1.32-1.37	860-955	≥ 955
N42	1.29-1.32	860-955	≥ 955

inner hemispherical permanent magnet with its spherical shape. The height of the washer is a trade off between the mechanical stresses to cope with and the required range of motion. With a larger washer, the mechanical stresses are more distributed, however, the angle between the bottom side of the washer and the supporting construction, depicted with θ in Fig. 6.6b, decreases.

A cylindrical permanent magnet with a diameter of 4 mm is chosen for the segmentation. This size is easy to handle during assembly but small enough to approximate the spherical shape. To determine the cylinder length, its relation to the torque is investigated as shown in Fig. 6.7. These results are obtained with the presented magnetic charge model in the spherical and cylindrical domain of Chapter 3. The amplitude of the sinusoidal torque characteristic of the gravity compensator is obtained for the different cylindrical permanent magnet heights. The figure shows that the torque converges at a height of 50 mm to a torque of 5.2 Nm. However, when this length is applied the majority of the outer hemispherical structure consists of non-magnetic material resulting in an inefficient use of volume. It is recommended to increase the amount of magnetic material in the outer hemispherical volume to improve the torque, for example, by a radial seg-

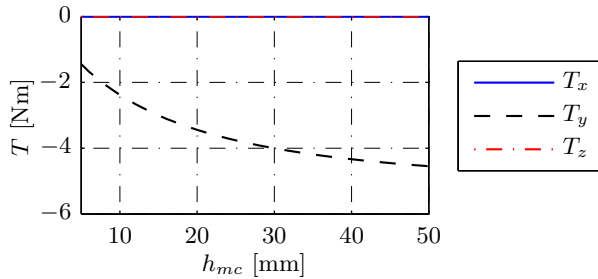


Figure 6.7: The torque as function of the cylindrical permanent magnet height.

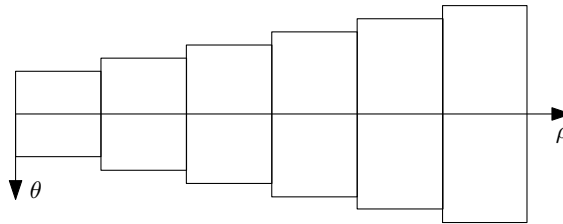


Figure 6.8: A radial segmentation to increase the torque performance of the spherical gravity compensator.

mentation as shown in Fig. 6.8 and also proposed in [138]. A compromise between efficient use of volume and torque performance is found in a commercially available size of $h_{mc}=12.5$ mm.

The predicted torque production of the prototype with the segmentation of the outer hemispherical permanent magnet is equal to 2.6 Nm. A torque production of 3.3 Nm can be achieved when the proposed segmentation is applied to a gravity compensator with the dimensions of the designed gravity compensator in Chapter 4. Hence, this segmentation causes a torque reduction of 72.5% with respect to the design specification of 12 Nm. The inner and outer radii of the prototype are 3.6 mm and 2.6 mm smaller with respect to the design presented in Chapter 4, respectively.

The segmented outer hemispherical permanent magnet array is the most susceptible for local permanent demagnetization. The demagnetization properties of the two magnet grades, N42 and N45, are listed in Table 6.2. The magnetic flux inside the permanent magnets is obtained with 3D FEA and shown in Fig. 6.9a and Fig. 6.9b for the cylindrical magnets and the hemispherical magnet, respectively. These figures show the worst case position in which the magnetization inside the magnets is the lowest. In the tip of the cylindrical permanent magnets the magnetic flux density reduces to 0 T. According to the permanent magnet properties,

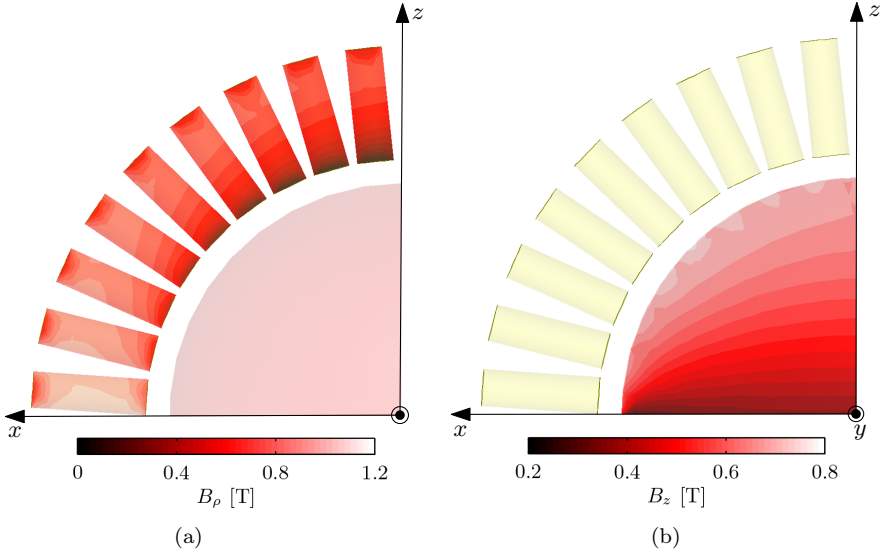


Figure 6.9: Magnetic flux density obtained with 3D FEA shown in a sectional view for the position with the highest risk of demagnetization: (a) cylindrical permanent magnets, (b) hemispherical permanent magnet.

local permanent demagnetization can occur here. The magnetic flux density inside the inner hemispherical permanent magnet is shown in Fig. 6.9b. This figure shows a maximum flux density of 0.3 T which poses no risks for permanent demagnetization.

To manage the mechanical stresses of the magnetic gravity compensator, a spherical ball bearing has been developed. The ball bearing is preferred over other possible bearings such as plain bearings or air bearings because it has less friction and does not require additional hardware outside the gravity compensator. A photo of the developed ball bearing is shown in Fig. 6.10a. To assemble the spherical bearing in the gravity compensator, the bearing has to be smaller than a hemisphere. Otherwise, it cannot be placed over the inner permanent magnet due to its spherical shape. Therefore, the bearing consists out of two parts. Assembled, this bearing provides a constant airgap over the complete range of motion of the gravity compensator. The hemispherical parts of the spherical bearing are visible in the exploded view of (Fig. 6.4). The ball bearing is constructed out of a cage and bearing balls with a diameter of 2 mm. To avoid magnetic interaction between the bearing balls and the compensator, a ceramic material is chosen for the balls. The principle of the cage is visualized in Fig. 6.10b. The cavities in the cage for

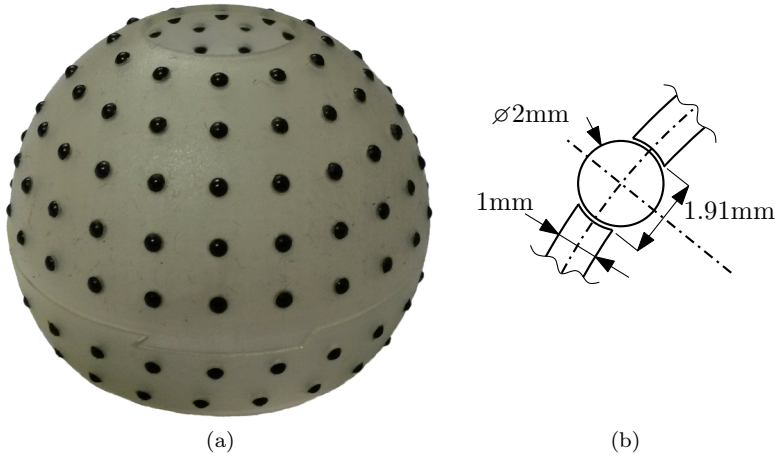


Figure 6.10: Spherical bearing: (a) photo of the realized prototype, (b) part of the sectional view to visualize the placement of the bearing balls.

the bearing balls are spherical with a slightly larger diameter (2.14 mm) such that the diameter of the entrance is 1.91 mm (which is smaller than the diameter of bearing balls of 2 mm). The cage is made out of UV cured acrylic polymer which is a flexible material. As a result, the bearing balls can be pressed in the cavity and are able to rotate freely without falling out of their cavity. To avoid contact between the cage and the inner and outer hemispheres which could result in friction or wear and tear, the wall thickness of the cage is smaller than the airgap namely, 1 mm as indicated in Fig. 6.10b. The cage is created with a 3D printer (Multijet modeling (MJM) process).

The airgap length depends on the smallest bearing ball diameter for which a cage can be manufactured. Therefore, the possibilities of manufacturing a cage with 3D print technology are explored. A cage is realized that can hold bearing balls with a diameter of 1 mm. This cage design has a wall thickness of 0.5 mm to avoid contact with the inner or outer hemispherical permanent magnet. The airgap length decreases from 2.5 mm to 1.5 mm with this spherical bearing design. Consequently, the torque increases with 12% to 2.9 Nm. However, there is a higher risks of making scores with 1 mm balls than with 2 mm balls. Hence, this spherical bearing is not considered for the prototype due to the expected risks for a little torque increase.

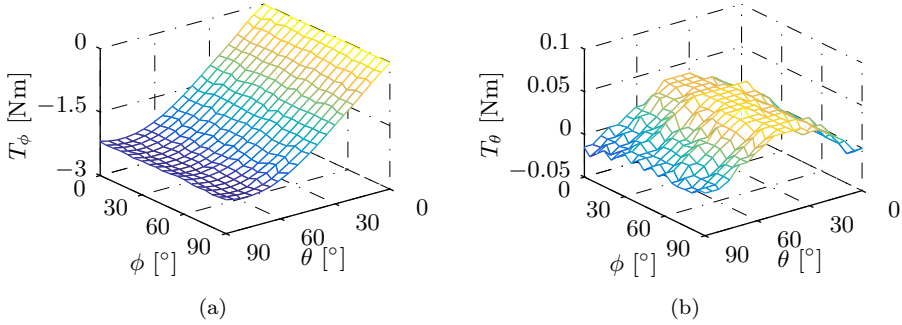


Figure 6.11: Measured torque of the gravity compensator prototype with the spherical coordinate system as defined in Fig. 4.2: (a) T_ϕ , (b) T_θ .

6.3.2 Measurement results

The measured torque of the prototyped gravity compensator is shown in Fig. 6.11. According to the results found in Chapter 4, a sinusoidal torque and zero torque is expected for T_ϕ and T_θ , respectively. The torque T_ϕ has a sinusoidal shape, however, the amplitude value is reached at approximately 80° instead of 90° . The torque T_θ shows a torque variation between 0 and 0.051 Nm as function of ϕ in Fig. 6.11b instead of an overall zero torque. This variation is 2.0% of the 2.4 Nm maximum torque of the prototype.

A comparison between the measurements, 3D FEA and the analytical magnetic charge model is shown in Fig. 6.12. The measurements show an error of 3.9% with FEA when the typical relative permeability of the permanent magnets is taken into account. The typical relative permeability for the permanent magnet grades N42 and N45 are $\mu_r = 1.11$ and $\mu_r = 1.14$, respectively. The measurements show a good agreement for the range of $\theta = 0^\circ - 80^\circ$ with FEA. The shifted peak from 90° to 80° is also visible in the FEA results. Therefore, this can be partially caused by the segmentation of the outer hemispherical permanent magnet. Because the last ring of cylindrical permanent magnet is not completely horizontal as is shown in Fig. 6.6, this approximation does not have a complete hemispherical shape. The error between the magnetic charge model and the measurements is equal to 16%. Comparison of the charge model with a FEA that considers a $\mu_r = 1$ shows a discrepancy of 2.3%. Hence, the error between the magnetic charge model and measurement is mainly caused by the relative permeability of $\mu_r = 1$ limitation of the magnetic charge model.

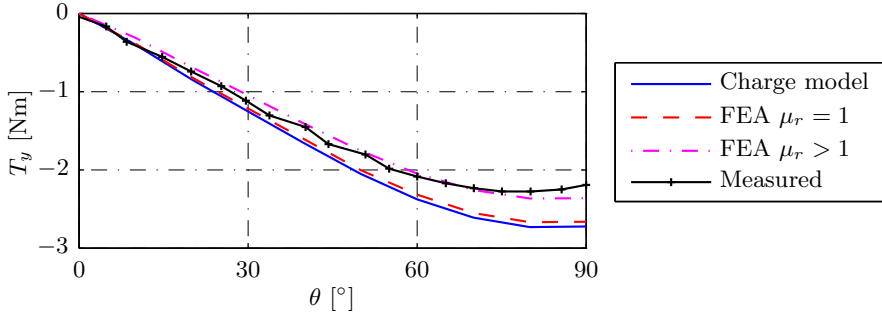


Figure 6.12: Comparison between the results of the measurements, analytical model, and with two FEA models with different relative permeabilities, namely $\mu_r = 1$ and the typical value belonging to the magnet grade.

6.4 Spherical actuator with gravity compensator

The realized spherical actuator with integrated gravity compensator mounted in the test setup is shown Fig. 6.13. An exploded view of the spherical actuator parts and the gravity compensator is shown in Fig. 6.14. This view shows that the stator consists of the coils and their support structure combined with the inside of the gravity compensator. The rotor is constructed of a supporting structure on which the permanent magnet array and outer magnet of the gravity compensator is mounted. For the assembly of the integrated actuator, the stator can be split up in two parts as indicated in the exploded view.

The back-iron segments slightly deviate from a spherical shape in the radial direction due to manufacturing limitations. The alternative shape is visible in the sectional view of the rotor of the actuator in Fig. 6.15a. It is found with 3D FEA investigation that this deviation only affects the torque production of the spherical actuator. These back-iron segments increase the magnetic flux density in the airgap with 17.6% instead of 19% compared to the configuration without back-iron. The alternative back-iron segments have more distance between each other on the outside of the supporting structure than on the inside. Hence, the magnetic flux density is affected because there is less highly permeable material in the supporting structure. The realized supporting structure for the hemispherical permanent magnet array is shown in a photo in Fig. 6.16a. In this figure, the back-iron segments can be distinguished from the aluminium support.

In the actuator prototype, the height of the support structure and the height of the permanent magnets are kept equal to the design in Chapter 5, namely $h_{bm} = 10$ mm and $h_m = 10$ mm. Hence, their radius is decreased with 2.6 mm to fit directly on the gravity compensator prototype. A cylindrical segmentation in

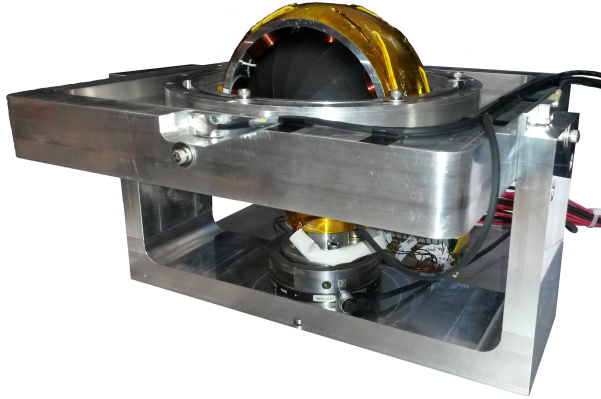


Figure 6.13: Photo of the spherical actuator with integrated gravity compensator prototype in the test bench.

one direction is applied to realize the hemispherical permanent magnet array. This segmentation results in a magnet array as shown in the sectional views of Fig. 6.16. These permanent magnet segments are machined out of a rectangular block of sintered NdFeB with wire eroding. This machining method is not capable to create the required spherically shaped permanent magnets. Therefore, cylindrical shaped segments are produced to approximate the permanent magnet array. It could be possible to approximate the spherical shape more accurately with additional machining, for example with vertical eroding. However, this possibility is not investigated.

The cylindrical permanent magnets are glued on the structure resulting in the hemispherical permanent magnet array in the photo shown in Fig. 6.16b. The airgap of the spherical actuator is not constant due to the segmentation. The minimum and maximum radii of the hemispherical permanent magnet array are equal to 60.4 mm and 61.58 mm, respectively. The maximum and minimum clearances are equal to 2.6 mm and 1.42 mm with respect to the inner coil array radius of 63 mm. Hence, the average airgap length is equal to 2 mm. The permanent magnet material used is VACODYM 633HR, and the properties are listed in Table 6.3.

For the coils a grade 1B wire is used with a bare copper diameter of 0.8 mm and they are wound orthogonally. The number of turns is equal to 208. The coils have a copper fill factor of 0.75. To achieve the spherical shape, the coils are pressed in a spherically shaped mould. These coil have a resistance of 0.6Ω and an inductance of $670 \mu\text{H}$.

The geometry parameters of the realized spherical actuator are listed in Table 6.3. The prototype geometry differentiates from the spherical actuator design presented

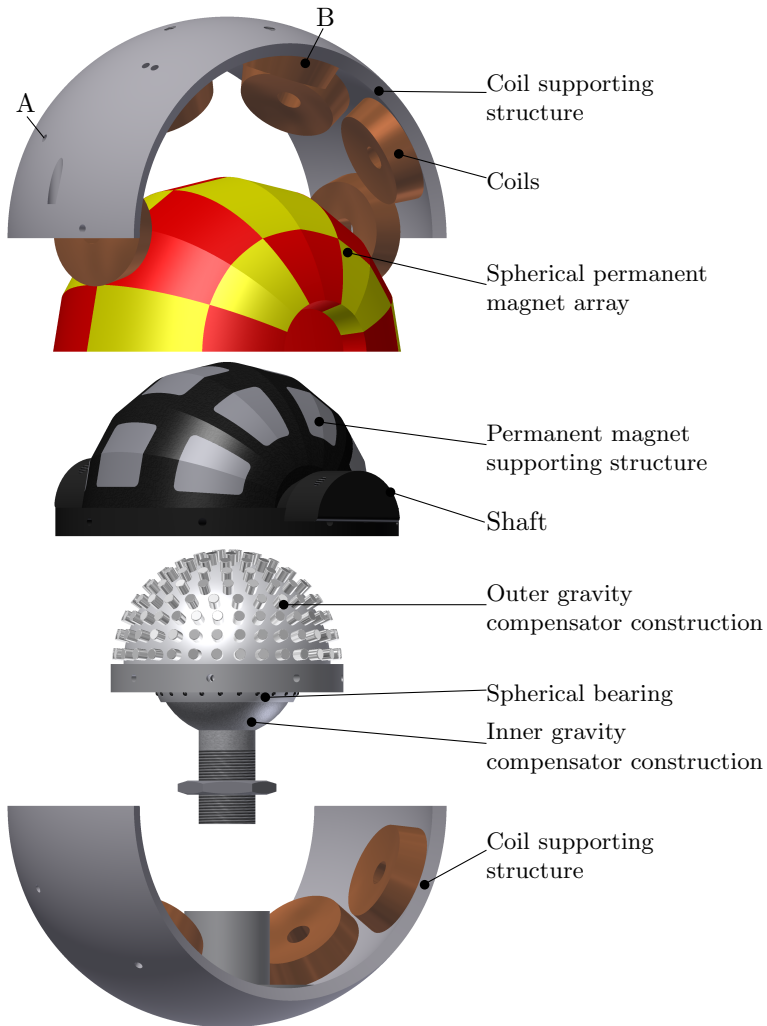


Figure 6.14: Elements of the spherical actuator with integrated gravity compensator.

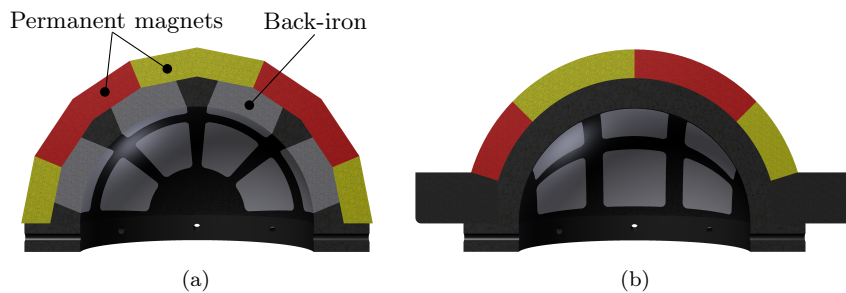


Figure 6.15: Different sectional views of the supporting structure and mounted spherical permanent magnet array: (a) front view, (b) side view.

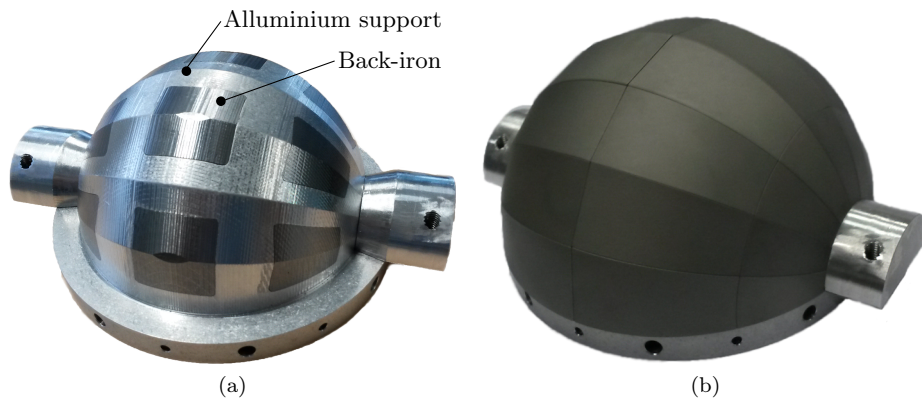


Figure 6.16: Realized: (a) supporting structure, (b) mounted spherical permanent magnet array.

Table 6.3: Geometric parameters of the spherical actuator prototype

parameter	Value	Unit
Outer radius of the magnet array	60.4 - 61.58	[mm]
Inner radius of the coil array	63	[mm]
Outer radius of the coil array	73	[mm]
Outer radius of the coil supporting structure	78	[mm]
Average airgap length, g_a	2	[mm]
Coil height, h_c	10	[mm]
Magnet height, h_m	10	[mm]
Supporting structure permanent magnets, h_{bm}	10	[mm]
Coil pitch, τ_c	50	[deg]
Pole pitch, τ_m	45	[deg]
Conductor bundle width, C_w	15.9	[deg]
Coil gap radius, G_w	4	[deg]
Total number of coils	12	[-]
Number of turns	208	[-]
Vacodym 633 HR [129]		
remnant magnetic flux density, B_r	1.35	[T]
Relative permeability, H_{cb}	1004	[kA/m]
Relative permeability, H_{cj}	1389	[kA/m]
Relative permeability, μ_r	1.078	[-]

in Chapter 5 because of manufacturing limitations. To avoid issues due to the realization in the coil shape, an average airgap of 2 mm is taken into account instead of 1 mm. The prototype has a pole pitch of 50° instead of 52° to account for manufacturing tolerances which could result in a limitation in the range of motion. Analysis on the geometry of the prototype resulted in an optimal coil height of 10 mm instead of 9 mm. The back-iron height, permanent magnet height, and the height of the coil supporting structure are kept equal to the presented design. As a result, the outer radius of the prototype is equal to 78 mm, which is the same as the outer radius of the designed spherical actuator. However, the torque production of the prototype is lower, namely 0.68 Nm instead of 1 Nm.

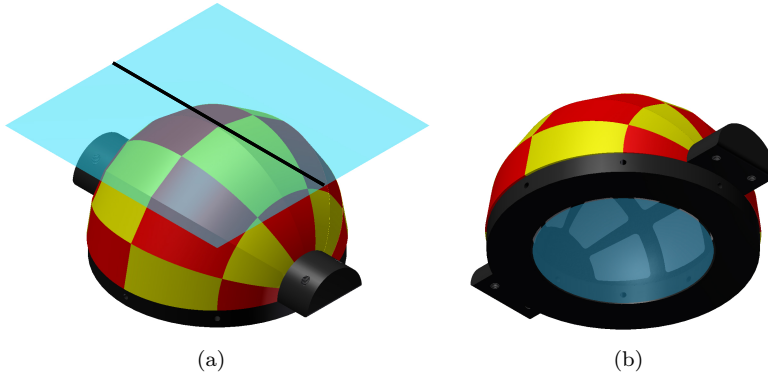


Figure 6.17: Indicated measurement areas of the magnetic flux density around the hemispherical permanent magnet array: (a) above, (b) below.

6.4.1 Spherical actuator measurement results

The gravity compensator is not completely integrated for the magnetic flux density and torque measurements of the spherical actuator. The segmented outer permanent magnet of the gravity compensator is assembled in the hemispherical permanent magnet array while the inner magnet is not present. Together with the coil array and their supporting structure, they are mounted in the test bench.

The measurements of the magnetic flux density of the hemispherical permanent magnet array is performed in a horizontal plane as depicted in Fig. 6.17a. In this plane, the probe is positioned at 1 mm with respect to the highest point of the array. Only a horizontal plane was possible due to the limitations of the measurement equipment. This measurement is done before and after the integration of the outer permanent magnet of the gravity compensator. In these measurements there is no change in magnetic flux density visible when the outer hemispherical permanent magnet of the gravity compensator is assembled. The measurement results are compared with the predicted magnetic flux density of the FEA as shown in Fig. 6.18. In the FEA, the cylindrical segmentation of the permanent magnet array and back-iron is included. The FEA has an error of 3.6% with the measurements; hence, both results are in good agreement.

The torque model is validated for two coils which are indicated with A and B in Fig. 6.14. These coils are chosen because of their position with respect to the hemispherical permanent magnet array. Coil A is positioned at the edge and coil B is positioned more in the center. These coils are chosen because at least one has a maximum deflection while the other moves only a little for the considered rotation axes.

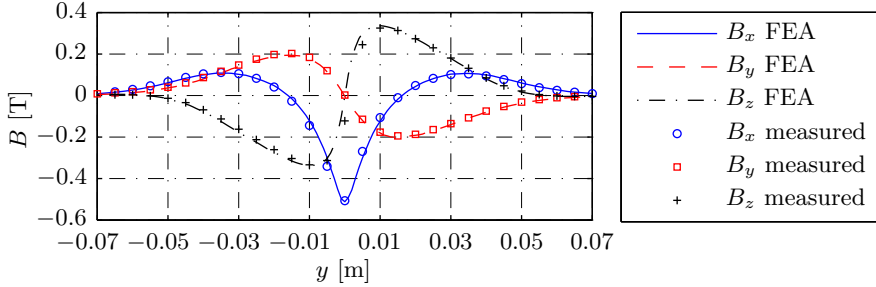
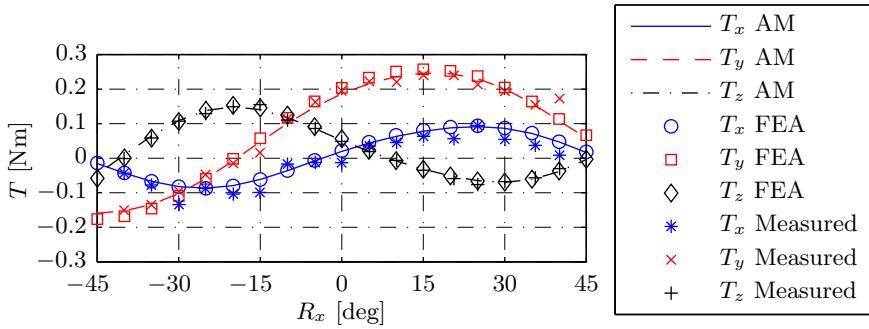


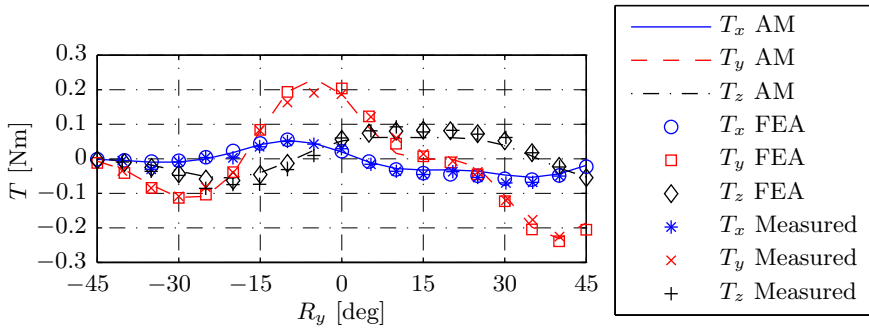
Figure 6.18: Comparison of measured magnetic flux density and predicted magnetic flux density with 3D FEA in the horizontal plane 1 mm above the hemispherical permanent magnet array according to the line depicted in Fig. 6.17a.

The torque measurement of coil A and B are shown in Fig. 6.19 and Fig. 6.20, respectively. In this figure, the torque predicted of the FEA and the analytical model is included. The rms error between the measurements and the models is equal to 7% and 11% for the FEA and the analytical model, respectively. The analytical model has a larger error because it assumes a relative permeability of $\mu_r = 1$. Nevertheless, the analytical model predicts the torque characteristics accurately.

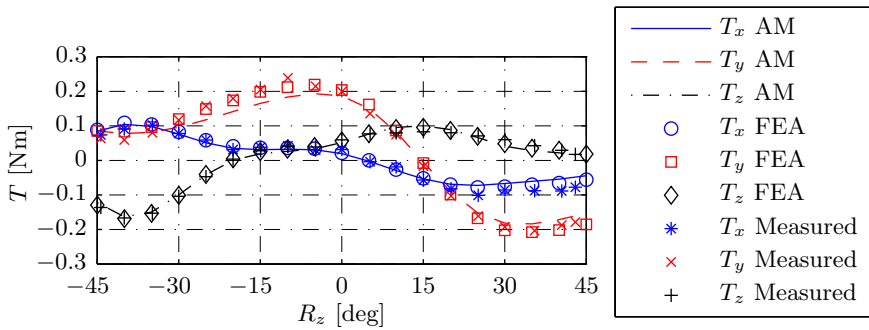
The coils in the spherical actuator are commutated with the two-norm minimization algorithm as presented in (5.4). The torque constants of each coil is obtained by the Lorentz law as used in the topology optimization of Section 5.3. In this method, the magnetic flux density is predicted with FEA to include the segmentation, material properties of the magnets, and the segmented back-iron. The coils are commutated to produce a torque about each Cartesian axis namely, $\vec{T}_d = [0.4; 0; 0]$ Nm, $\vec{T}_d = [0; 0.4; 0]$ Nm, and $\vec{T}_d = [0; 0; 0.4]$ Nm. The resulting torque is measured with the 6 DoF load cell. These measurements are performed over the full range of motion combining the rotation about the x - and y -axis and the z - and y -axis. The resulting torque is shown in Figs. 6.21, 6.22, and 6.23. For the rotation about the x - and y -axis, the test bench was not capable to reach some positions after $R_y = 35^\circ$. Therefore, there are 6 measurement points left out in the results. Furthermore, one position was not excitable by the amplifiers because too much power was required. This position is $R_x = 10^\circ$ $R_y = 10^\circ$ in the figures 6.23a, b, and c. The obtained measurements are averaged for the different rotations and desired torques and the results are listed in Table 6.4. These results are within 7.5% error with the desired torque. Hence, it can be concluded that the actuation in each of the three degrees of freedom is decoupled by the commutation algorithm.



(a)

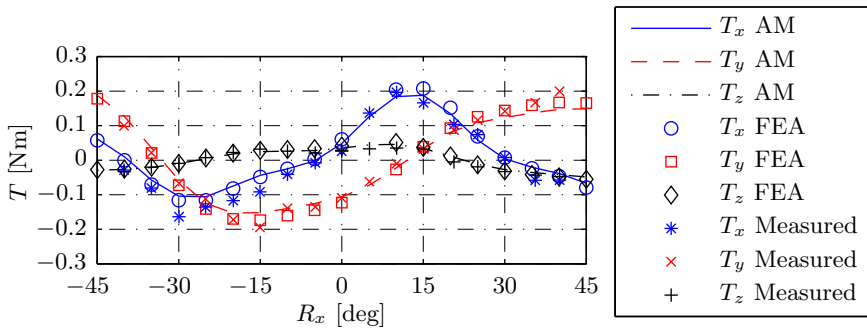


(b)

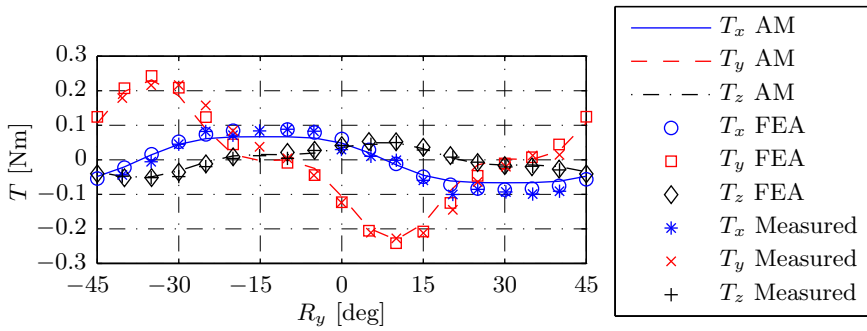


(c)

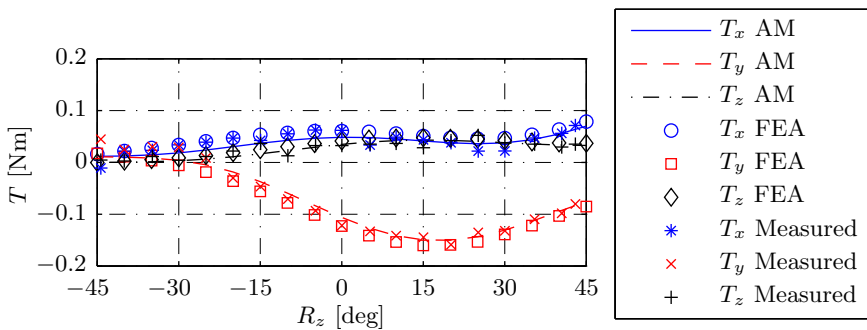
Figure 6.19: Comparison between the torque prediction with FEA, the analytical model, and the measurements of a single coil at the edge of the permanent magnet array for the rotation about the: (a) x -axis, (b) y -axis, and (c) z -axis.



(a)



(b)



(c)

Figure 6.20: Comparison between the torque prediction with FEA, the analytical model, and the measurements of a single coil in the middle of the permanent magnet array for the rotation about the: (a) x -axis, (b) y -axis, and (c) z -axis.

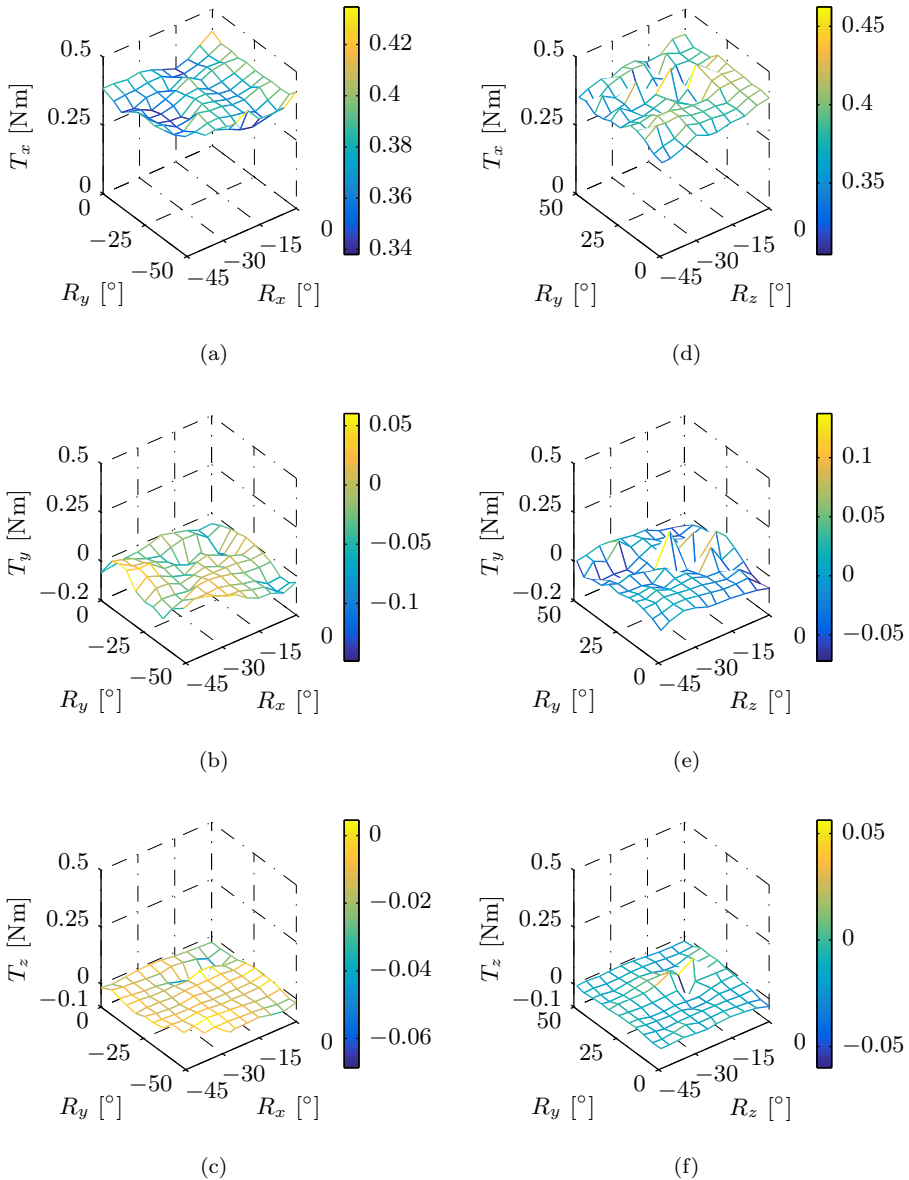


Figure 6.21: Torque measurements when a desired torque is commutated of $\vec{T}_d = [0.4 \ 0 \ 0]$ for the torque and rotation axes: (a) xy , (b) xy , (c) xy , and (d) zy , (e) zy , (f) zy .

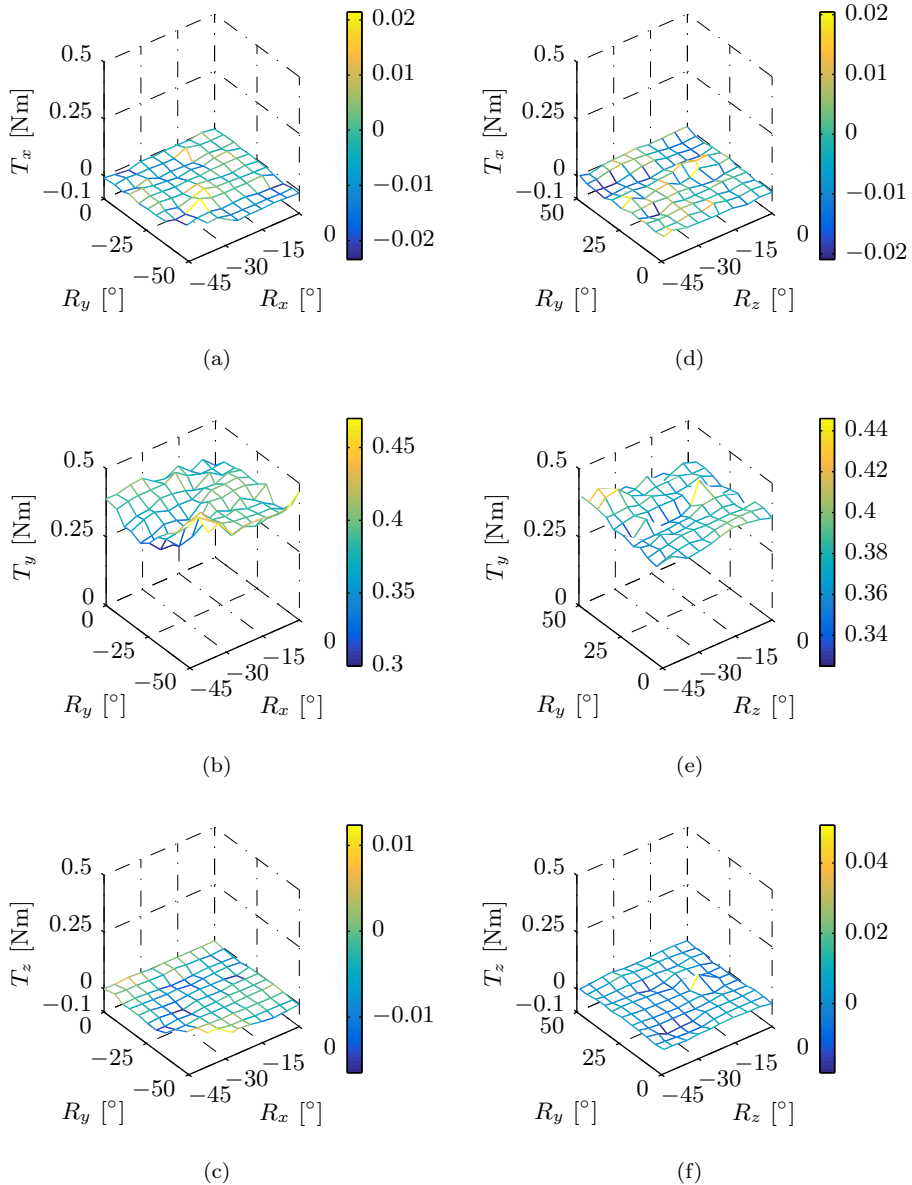


Figure 6.22: Torque measurements when a desired torque is commutated of $\vec{T}_d = [0 \ 0.4 \ 0]$ for the torque and rotation axes: (a) xy , (b) xy , (c) xy , and (d) zy , (e) zy , (f) zy .

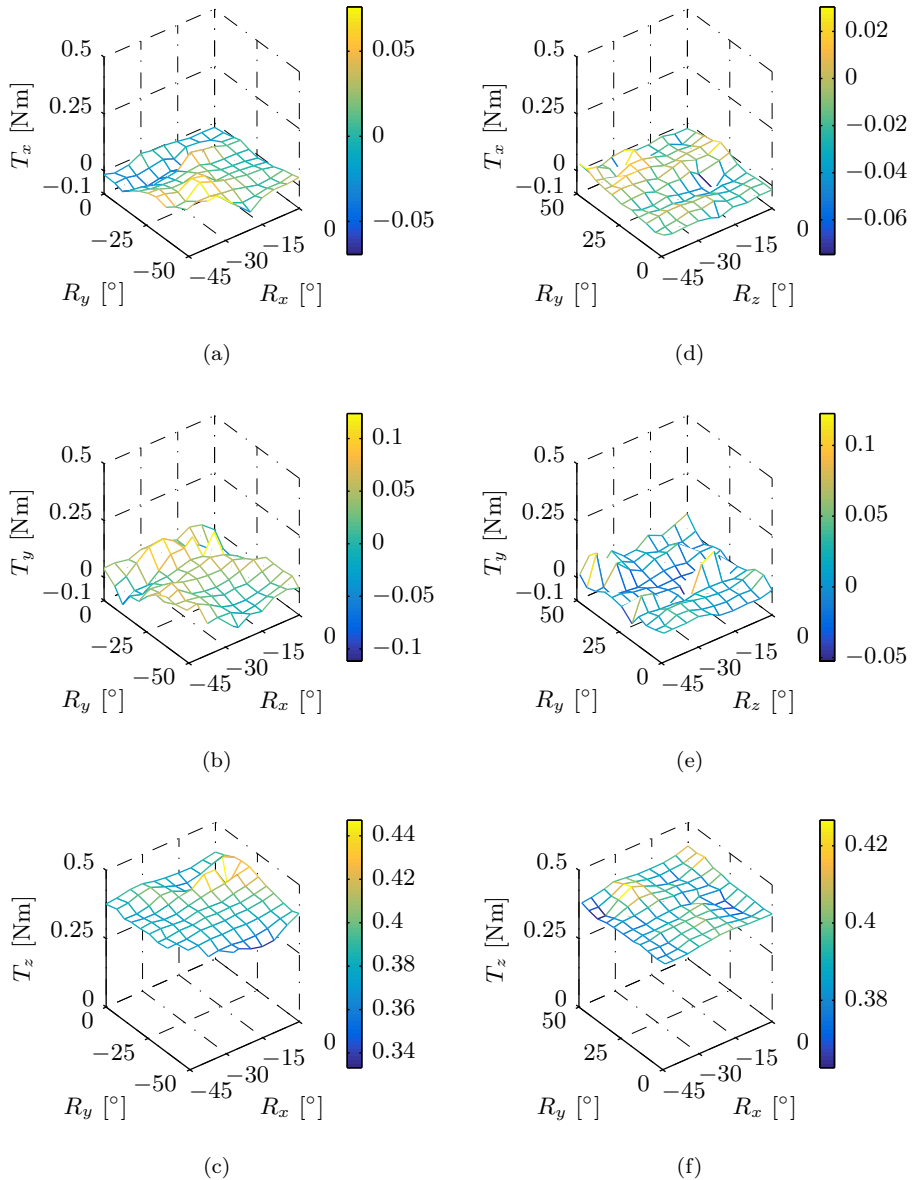


Figure 6.23: Torque measurements when a desired torque is commutated of $\vec{T}_d = [0 \ 0 \ 0.4]$ for the torque and rotation axes: (a) xy , (b) xy , (c) xy , and (d) zy , (e) zy , (f) zy .

Table 6.4: Comparison of the desired torque with the averaged torque measurements

Rotation axes	Desired torque \vec{T}_d [Nm]			Measured torque [Nm]		
	T_x	T_y	T_z	T_x	T_y	T_z
x and y	0.4	0	0	0.37	0.02	0.01
	0	0.4	0	0.00	0.38	0.00
	0	0	0.4	0.01	0.02	0.38
z and y	0.4	0	0	0.38	0.00	0.00
	0	0.4	0	0.00	0.37	0.00
	0	0	0.4	0.01	0.01	0.39

6.4.2 Integration

Several measurements have been carried out to investigate the decoupling between the gravity compensator and the spherical actuator. The magnetic flux density beneath the permanent magnet array of the actuator is measured to investigate the shielding property of the segmented back-iron. This measurement is performed at 1 mm beneath the array in a horizontal circular shaped plane as depicted in Fig. 6.17b. The resulting magnetic flux density measurements are shown in Fig. 6.24. The solid circle in these figures indicates the geometric dimension of the outer hemispherical permanent magnet of the gravity compensator. The results in the Figs. 6.24a, b, and c are measured before the integration. In these figures there is almost no magnetic flux density present inside the circle. Hence, the segmented back-iron shields a large part of the magnetic field produced by the permanent magnet array. After the integration, the magnetic flux density results in the measurements as shown in Figs. 6.24d, e, and f. In these results there is a magnetic flux density present inside the circle. This flux density is produced by the permanent magnet of the gravity compensator. This gives a first indications that the magnetic field of the permanent magnet array has no influence on the magnetic flux density in the airgap of the gravity compensator. However, torque measurements of the integrated and separated gravity compensator and spherical actuator are necessary to verify the decoupling.

The measured torque produced by the integrated gravity compensator is shown in Fig. 6.25. These results are compared to the torque prediction of FEA and the measured torque of the gravity compensator separated from the spherical actuator. The integrated compensator has a sinusoidal torque characteristic that is 20% larger than the separated compensator. This increase is caused by the back-iron of the spherical actuator. Without this amplitude difference and comparing solely the torque characteristic, the integrated and separated gravity compensator have an rms difference of 0.6%. Comparison with the FEA shows a deviation of the sinusoidal characteristic. The rms discrepancy between the FEA and the

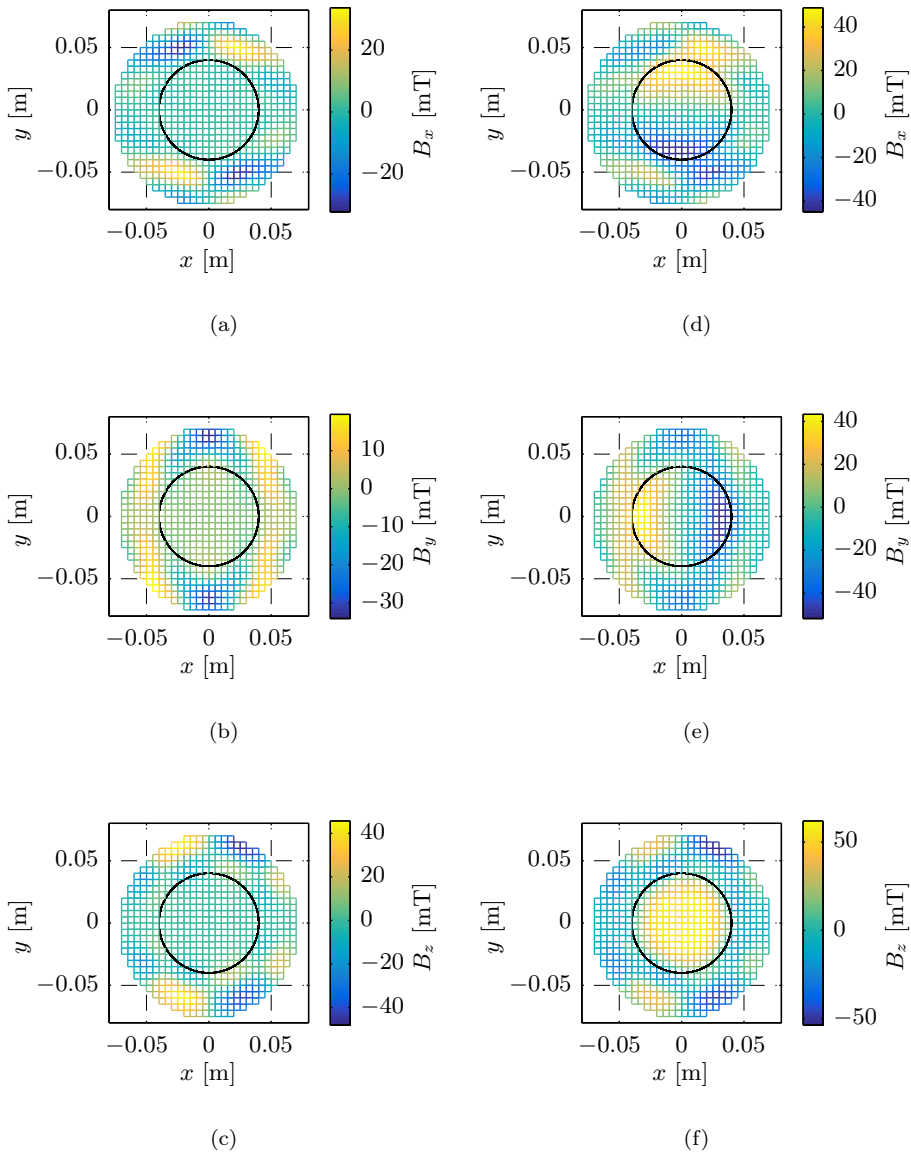


Figure 6.24: The magnetic flux density measured 1 mm beneath the hemispherical permanent magnet according to the plane depicted in Fig. 6.17b before and after the integration of the outer hemispherical permanent magnet of the gravity compensator: (a) B_x before integration, (b) B_y before integration, (c) B_z before integration, and (d) B_x after integration (e) B_y after integration, (f) B_z after integration.

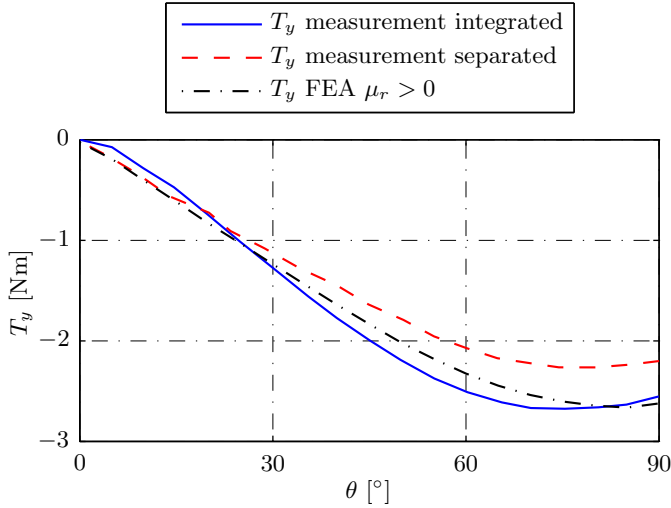
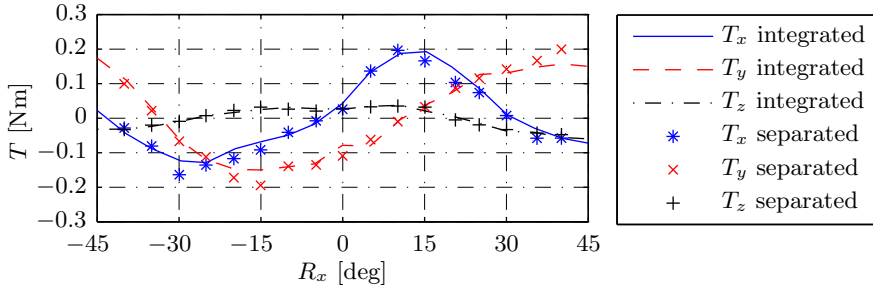


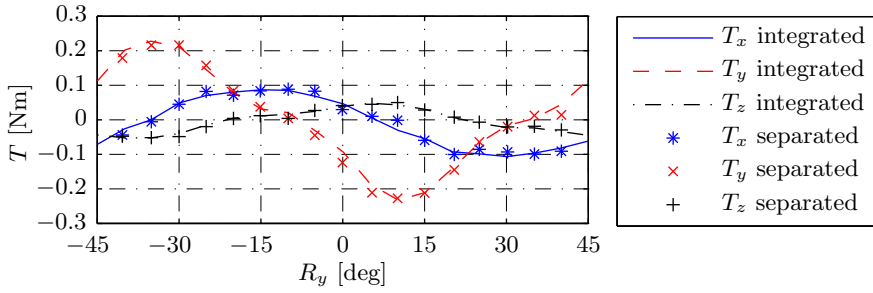
Figure 6.25: Comparison of the torque produces by the gravity compensator separated of and integrated in the spherical actuator and the torque prediction of FEA.

measurements is equal to 3.6%.

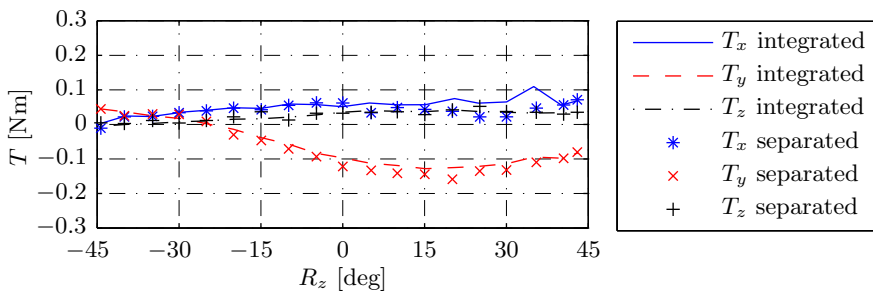
The torque production of two different coils are measured to determine the influence of the gravity compensator on the torque production of the spherical actuator. These coils are depicted in Fig. 6.14 as A and B. This influence is determined by comparing the torque measurements of these coils for a separated and integrated actuator. These measurements are shown in Fig. 6.26 and Fig. 6.27, respectively. The rms discrepancy between these figures is equal to 0.7%. Hence, the influence of the gravity compensator on the spherical actuator is small.



(a)

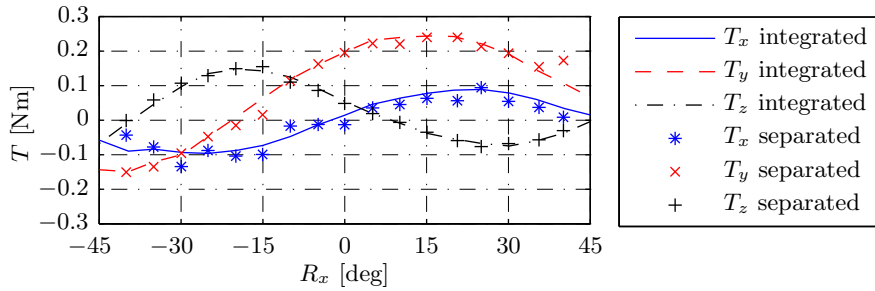


(b)

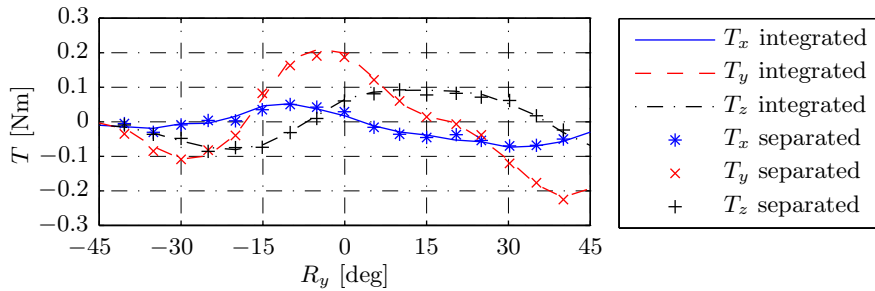


(c)

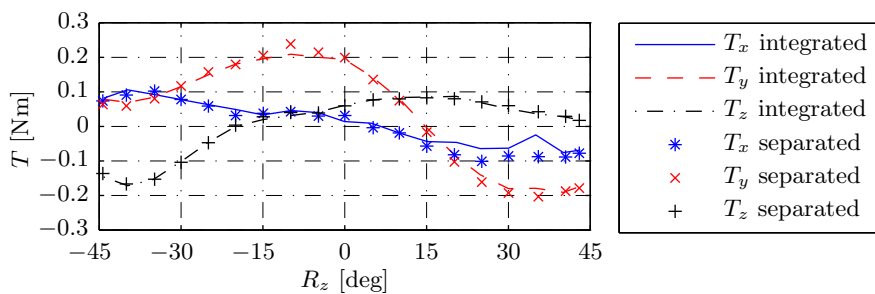
Figure 6.26: Comparison between the measurements of a single coil in the middle of the permanent magnet array for the rotation about the: (a) x -axis, (b) y -axis, and (c) z -axis.



(a)



(b)



(c)

Figure 6.27: Comparison between the measurements of a single coil at the edge of the permanent magnet array for the rotation about the: (a) x -axis, (b) y -axis, and (c) z -axis.

6.5 Conclusions

In this chapter the working principle of the gravity compensator has been demonstrated. In addition, the decoupling of the three degrees-of-freedom of the spherical actuator has been experimentally verified. Furthermore, the minimized interaction between the gravity compensator and the spherical actuator has been validated through measurements.

The prototype has been scaled with respect to the designed spherical actuator with integrated gravity compensator. In addition, some aspects of this design has been changed due to manufacturing limitations.

The gravity compensator consists of two concentrically spherically shaped permanent magnets. The inner permanent magnet has a hemispherical shape and a parallel magnetization. The radial magnetization of the outer permanent magnet has been approximated with a segmentation of cylindrical permanent magnets. In addition, a spherical bearing has been designed to demonstrate that a functional prototype outside the test bench is possible. Comparison between the FEA and the measurements showed a rms error of 3.9%. An rms error between the measurements and the magnetic charge of 16% has been found. The magnetic charge model has a larger error than FEA because this modeling tool can only take a relative permeability of $\mu_r = 1$ into account.

A spherical actuator prototype has been realized in which the created gravity compensator can be integrated. For this design, manufacturing limitations resulted in a cylindrical segmentation of the hemispherical permanent magnet array. Furthermore, the applied back-iron segments are not completely spherical in shape. Comparison of these measurements with the prediction of FEA and the analytical model showed an rms error of 7% and 11%, respectively. The averaged measurement results are within 7.5% error with respect to the desired torque when the coils are commutated with the two-norm minimization algorithm.

The torques of the gravity compensator and the spherical actuator are measured before and after their integration. The rms error between these measured characteristic is 0.6% and 0.7% for the gravity compensator and spherical actuator, respectively. In addition, the rms error between the integrated gravity compensator and FEA is equal to 3.6%.

Chapter 7

Conclusions and recommendations

This thesis concerns the three-dimensional modeling, analysis, realization and experimental verification of the integration of a gravity compensator and a spherical actuator in one device. This device has been designed towards the application in a smart arm-support system. Categorization of the actuated arm-support systems described in the literature and an analysis of the human shoulder-joint led to the formulation of the electromechanical specifications. The integration of a novel gravity compensator topology, created with a spherical magnetic spring, reduces the power consumption significantly and provides an equal number of degrees of freedom as the spherical actuator. The uniqueness and electromagnetic complexity of the integrated design called for a complex yet fast electromagnetic modeling. An extensive evaluation of integrated actuator topologies has been performed with the magnetic charge method and the spherical imaging technique. The theoretical analysis has been experimentally validated by measurements of the gravity compensator and spherical actuator, both separately and integrated.

This chapter provides a summary of the conclusions that correspond to the research objectives, as stated in section 1.2. Additionally, the scientific contributions of this thesis are addressed, and recommendations for future research are given.

7.1 Conclusions

7.1.1 Literature overview of actuated arm-support systems

The arm-support systems found in the literature have been categorized based on the design choices that influence the actuation requirements. Three applications of the arm support have been distinguished namely, at home (ambulatory), in rehabilitation centers, and in the industry. This defines their functionality: supporting, training, or enhancing of the human arm, respectively. These categories have been further arranged based on the employed actuation technology. Four technologies can be differentiated from the arm-support systems that have been found in the literature, namely electromechanical actuators, pneumatic actuators, hydraulic actuators, and semi-active dampers. Properties such as compliance or back-drivability can be inherently present or achieved with hardware or software. The actuators are placed in different ways in the mechanical construction, namely directly on the joint, positioned externally or a cable suspension is applied. This mechanical construction influences the required actuator specifications such as the range of motion, and the inertia of the system.

The torque requirements have been deducted from the analysis of the human shoulder joint. A static torque and dynamic torque specification have been obtained which are required to compensate for gravity and to accelerate the arm, respectively. The human body is different for each person and, therefore, a performance range is obtained. The range for the static torque is between 4.3 Nm and 16 Nm, and the dynamic torque ranges between 0.44 Nm and 3.2 Nm. Furthermore, to achieve the range of motion for a basic set of activities of daily living at least three degrees of freedom are necessary.

In the literature overview, it has been shown that there is a trade off between the actuated degrees of freedom and the mobility of the robotic arm. The actuation of a multi-degree-of-freedom joint is often implemented with a different actuator for each degree and this results in a large and cumbersome construction with a predefined sequence of axes. The specifications of arm-support systems show the need for gravity compensation to reduce the power consumption and the size of the system. In addition, multi-degree-of-freedom actuation with one device such as a spherical actuator is desirable to mimic a shoulder joint for the activities of daily living.

7.1.2 Electromagnetic modeling

For the optimization of spherical magnetic structures, the 3D semi-analytical models have been researched for a fast and accurate prediction of the torque of the spherical actuator with integrated gravity compensator. To obtain the magnetic field produced by spherically shaped permanent magnets, the scalar potential obtained from Maxwell's equations has been solved with the Green's function and with the method of separation of variables. This has resulted in a magnetic charge model and harmonic model, respectively.

A spherical harmonic model has been presented that can include an infinitely permeable boundary and is extended to account for uneven numbers of permanent magnets in the array in the θ - and ϕ -direction. In contrast to the magnetic charge model, the presented harmonic model cannot account for hemispherical permanent magnet arrays. It has been shown that for a parallel magnetization a maximum discrepancy of 4% with respect to FEA is achieved for a bounded and unbounded problem.

The magnetic charge model has been implemented in the spherical coordinate system to model parallel and radial magnetizations. The radial magnetization requires the inclusion of the magnetic volume charge density. Furthermore, these models are extended with spherical imaging by applying the method of inversion. Hence, the magnetic charge model can account for an infinitely permeable boundary. This modeling method obtains the field solution in an observation point for each permanent magnet individually, and by superposition the total field solution is found. Therefore, this method provides a high flexibility because hemispherical permanent magnet arrays can be taken into account. Validation of the model with FEA for multiple configurations for the magnetization and infinitely permeable boundary resulted in a maximum discrepancy of 1.6%. The magnetic flux density of hemispherical permanent magnet geometries such as used in the gravity compensator and in the actuator has been predicted with this method. In addition, the influence of placing a hemispherical back-iron behind the permanent magnet and coils in the spherical actuator has been approximated with spherical imaging in the magnetic charge model.

7.1.3 Spherical magnetic gravity compensator

A novel magnetic gravity compensator has been designed that is able to provide support in multiple degrees of freedom. A spherical magnetic spring has been created with two concentric hemispherical permanent magnets. Different torque characteristics can be realized depending on the combination of parallel and radial magnetizations. It has been shown that a change of the hemisphere radii only results in a change in torque amplitude and not in the characteristic.

An arm-support system requires a sinusoidal torque characteristic. This characteristic corresponds to the combination of a radial magnetization for the outer hemispherical permanent magnet and a parallel magnetization of the inner spherical permanent magnet. An average torque requirement of 12 Nm has been found by identifying the human arm movements. By mapping the torque of the compensator for different inner and outer radii, an optimal torque density with respect to its volume has been found. Considering a permanent magnet grade with a remanent magnetic flux density of 1.3 T, a radius of 29 mm and a radius of 43 mm for the inner and outer permanent magnet have been obtained, respectively. Commercial spherical permanent magnets are available that can be used for the inner parallel magnetized hemispherical permanent magnet. However, the manufacturing of the radially magnetized outer hemispherical permanent magnet is not evident. Furthermore, this permanent magnet has a risk of demagnetization when employed in the gravity compensator.

7.1.4 Spherical actuator design with integrated gravity compensator

A spherical actuator with integrated gravity compensator has been designed towards a smart arm-support system. The stator consists of the inner hemispherical permanent magnet of the gravity compensator and the coils of the spherical actuator. Both structures are mounted on a stationary support. The rotor is constructed out of a supporting structure with an embedded segmented back-iron to enhance the magnetic flux density produced by the hemispherical permanent magnet array of the actuator. On the inside of this supporting structure the outer hemispherical permanent magnet of the gravity compensator is mounted. The integrated design has two airgaps.

The power dissipation of several spherical actuator configurations has been analyzed to obtain the optimal topology. The power dissipation of these configurations has been predicted by applying a commutation algorithm that decouples the torques and currents. In this optimization, three permanent magnet arrays with different pole pitches have been investigated. For the coil arrays, two coil topologies have been included, namely circular and elongated. An optimal coil and hemispherical permanent magnet configuration suitable for the application has been obtained, namely a coil pitch of $\tau_c = 52^\circ$ and a permanent magnet pitch of $\tau_m = 45^\circ$.

To minimize the influence of the spherical actuator design on the gravity compensator the back-iron behind the permanent magnets has been segmented. It has been shown that a full hemispherical shell short-circuits the magnetic field of the gravity compensator. A compromise has been found in a segment size of $\xi = 35^\circ$ for the integrated design. This segment size results in an increased torque amplitude of the gravity compensator of 3% without influencing the sinusoidal torque

characteristic. The magnetic flux density of the hemispherical permanent magnet array increases with 19%. The inclusion of back-iron behind the coils introduces cogging which is undesirable for the arm support application. It has been found that this configuration has a higher power dissipation due to the required compensation for the cogging than the configuration with only a segmented back-iron behind the hemispherical permanent magnet array.

A spherical actuator with an integrated gravity compensator has been designed according to a set specifications. In this integrated design, the gravity compensator provides the required sinusoidal torque characteristic. The actuator is optimized to have a minimum power dissipation providing a continuous torque of 1 Nm and a peak torque of 6 Nm. The steady state temperature for continuous torque operation is $\Delta T = 40^\circ\text{C}$ when the outer radius for the integrated actuator design is equal to 78 mm.

7.1.5 Experimental verification

The working principle of the designed spherical actuator with integrated gravity compensator has been experimentally verified with a scaled prototype.

The gravity compensator consists of two concentric spherically shaped permanent magnets. The inner permanent magnet has a hemispherical shape and a parallel magnetization. The radial magnetization of the outer permanent magnet has been approximated with a segmentation of cylindrical permanent magnets. In addition, a spherical bearing has been designed to demonstrate that a functional prototype outside the test bench is possible. The torque has been measurement of this prototype and comparison between the FEA a rms error of 3.9%. An rms error between the measurements and the magnetic charge of 16% has been found. The magnetic charge model has a larger error than FEA because this modeling tool can only take a relative permeability in the permanent magnet material of $\mu_r = 1$ into account.

A spherical actuator prototype has been realized in which the created gravity compensator can be integrated. Manufacturing limitations resulted in a segmentation of 32 permanent magnets to construct the hemispherical permanent magnet array. Furthermore, the applied back-iron segments are not completely spherical in shape. Comparison of these measurements with the prediction of FEA and the analytical model showed an rms error of 7% and 11%, respectively. The averaged measurement results are within 7.5% error with respect to the desired torque when the coils are commutated.

The torques of the gravity compensator and the spherical actuator are measured before and after their integration. The rms error between these measured characteristic is 0.6% and 0.7% for the gravity compensator and spherical actuator,

respectively. In addition, the rms error between the integrated gravity compensator and FEA is equal to 3.6%.

7.2 Scientific contributions

The main scientific contributions of the performed research as presented in this thesis can be summarized as:

- *The development, design, and experimental verification of a passive multi-degree-of-freedom gravity compensator using two hemispherical permanent magnets.* A spherical magnetic spring has been created, and the torque characteristic by combining permanent magnets with different magnetizations has been investigated. The spring topology with a sinusoidal torque characteristic has been designed as a gravity compensator and integrated in a spherical actuator. A scaled version of this design has been manufactured and the working principle has been verified by means of measurements on a working prototype. A patent has been granted for the concept of a spherical magnetic spring [93].
- *The integration of the magnetic gravity compensator in a spherical actuator design, and the experimental verification of this concept.* A novel spherical actuator has been created with an integrated gravity compensator. The power consumption can be reduced significantly in applications that need to compensator for the gravity of a static load with this device. The spherical actuator has been designed with a hemispherical permanent magnet array such that is able to provide a large range of motion without interfering with the compensator. The interaction between both devices has been minimized to guarantee that both devices do not influence each other's torque output. A prototype of this design has been manufactured and validated with measurements.
- *The extension of the three-dimensional magnetic charge modeling for the evaluation of spherical springs and coreless spherical actuators.* The magnetic charge model has been applied in the spherical coordinate system, and is able to predict the magnetic field produced by spherically shaped magnetic structures. The magnetic volume charge density has been included to model the radial magnetization. This magnetization has been applied in three of the four spherical spring topologies. The modeling of back-iron in the spherical actuator has been solved by implementing the spherical imaging technique. Hence, multiple infinitely permeable boundaries can be taken into account.
- *The extension of the three-dimensional spherical harmonic modeling technique to model spherical magnetic structures.* The spherical harmonic model

has been extended by modeling spherical permanent magnet arrays with an uneven number of permanent magnets, and by including an infinitely permeable boundary can be included.

7.3 Recommendations

7.3.1 Development of a design for clinical test

Validation of the concept of the spherical actuator with integrated gravity compensator and its performance to mimic the shoulder joint in an arm-support system are necessary to ultimately perform clinical trials in rehabilitation and home environments. For this validation, the integrated actuator has to be built according to the specifications which were not achieved with the prototype. Implementation in an arm-support system also requires compact power electronics to excite the coils of the spherical actuator, a three-degree-of-freedom position sensor, and an integrated bearing. Furthermore, a robust control solution is required to guarantee the safety of the user.

7.3.2 Spherical actuator analytical design tools

The development of the analytical modeling tools is focused on the design of a gravity compensator, a slotless spherical actuator, and the integration of these devices. This analytical approach resulted in several design decisions made during the research. Improvements can be made to increase the accuracy, decrease the calculation time, and to enlarge the applicability of these tools for spherical electromagnetic designs such as a slotted spherical actuator. These improvements can be summarized as:

- Magnetic charge model:
 - Include the relative permeability of the permanent magnets [15, 61, 114].
 - Improve the numerical implementation of the model, for example, approximate the numerical integration with elliptic integrals.
- Extend the spherical harmonic model to include hemispherical permanent magnet structures.
- Include the modeling of regions which consist partially of highly permeable material such as slotted structures [21, 102].

7.3.3 A spherical gravity compensator design with variable torque

The torque produced by the gravity compensator should be made adaptable because the weight of the upper limb varies for each individual user. However, the proposed gravity compensator can only be designed for a fixed load. With the integration of the spherical actuator, a torque can be produced to compensate for limited variations, maximal 10%, of the load. To cope with a larger variation, an investigation on gravity compensator designs with a variable airgap is required.

7.3.4 Realization of the gravity compensator

The gravity compensator is realized with one layer of cylindrical permanent magnet to achieve the radial magnetization of the outer hemispherical permanent magnet. Consequently, the torque density of the device has been decreased by this segmentation. To improve the torque density of the gravity compensator a production process has to be developed that is able to produce or better approximate radially magnetized hemispherical permanent magnets.

Appendix A

Definition of the Spherical coordinate system

The analytical tools to predict the torque produced by the gravity compensator and spherical actuator are implemented in the spherical domain. There are several definitions of the spherical coordinate system, however, the definition used in this thesis is defined as shown in Fig. A.1. This definition is quite commonly used in physics. In mathematics the angle variables θ and ϕ are switched, because in this way the angle θ is defined the same as in the cylindrical coordinate system.

According to the defined spherical coordinate system conversion can be made using for vectors,

$$\begin{aligned}\vec{\rho} &= \sin(\theta) \cos(\phi) \vec{e}_x + \sin(\theta) \sin(\phi) \vec{e}_y + \cos(\theta) \vec{e}_z, \\ \vec{\theta} &= \cos(\theta) \cos(\phi) \vec{e}_x + \cos(\theta) \sin(\phi) \vec{e}_y - \sin(\theta) \vec{e}_z, \\ \vec{\phi} &= -\sin(\phi) \vec{e}_x + \cos(\phi) \vec{e}_y,\end{aligned}\tag{A.1}$$

and

$$\begin{aligned}\vec{x} &= \sin(\theta) \cos(\phi) \vec{e}_\rho + \cos(\theta) \cos(\phi) \vec{e}_\theta - \sin(\phi) \vec{e}_\phi, \\ \vec{y} &= \sin(\theta) \sin(\phi) \vec{e}_\rho + \cos(\theta) \sin(\phi) \vec{e}_\theta + \cos(\phi) \vec{e}_\phi, \\ \vec{z} &= \cos(\theta) \vec{e}_\rho - \sin(\theta) \vec{e}_\theta.\end{aligned}\tag{A.2}$$

For points in the free space the conversion is,

$$x = \rho \sin(\theta) \cos(\phi),\tag{A.3}$$

$$y = \rho \sin(\theta) \sin(\phi),\tag{A.4}$$

$$z = \rho \cos(\theta),\tag{A.5}$$

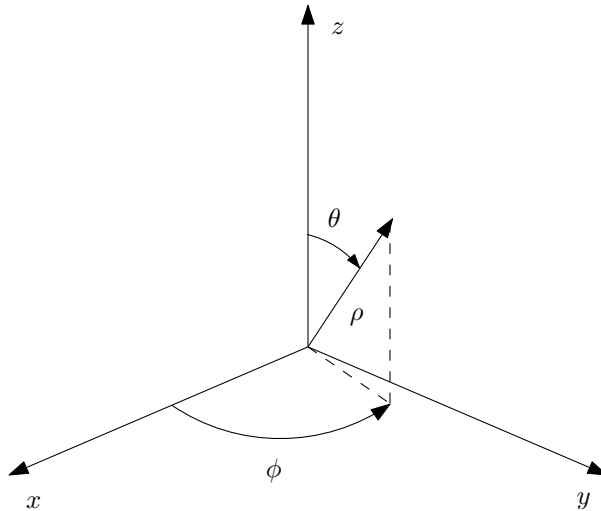


Figure A.1: Definition of the spherical coordinate system in the Cartesian coordinate system.

and,

$$\rho = \sqrt{x^2 + y^2 + z^2}, \quad (\text{A.6})$$

$$\theta = \arctan\left(\frac{y}{x}\right), \quad (\text{A.7})$$

$$\phi = \arccos\left(\frac{z}{\rho}\right). \quad (\text{A.8})$$

Further the volume element for the spherical domain is,

$$dv = \rho^2 \sin(\phi) d\rho d\theta d\phi, \quad (\text{A.9})$$

where the different surface areas are given by,

$$ds(\vec{r}') = \begin{cases} \rho'^2 \sin(\theta') d\theta' d\phi' & \text{if constant } \rho', \\ \rho' \sin(\theta) d\rho' d\phi' & \text{if constant } \theta', \\ \rho' d\rho' d\theta' & \text{if constant } \phi', \end{cases} \quad (\text{A.10})$$

Appendix B

Spherical vector analysis

The gradient operant in the spherical coordinate system is written as

$$\nabla f = \frac{\partial f}{\partial \rho} \vec{e}_\rho + \frac{1}{\rho} \frac{\partial f}{\partial \theta} \vec{e}_\theta + \frac{1}{\rho \sin(\theta)} \frac{\partial f}{\partial \phi} \vec{e}_\phi \quad (\text{B.1})$$

the divergence is defined as

$$\nabla \cdot \vec{A} = \frac{1}{\rho^2} \frac{\partial(\rho^2 A_\rho)}{\partial \rho} + \frac{1}{\rho \sin(\theta)} \frac{\partial(\sin(\theta) A_\theta)}{\partial \theta} + \frac{1}{\rho \sin(\theta)} \frac{\partial A_\phi}{\partial \phi} \quad (\text{B.2})$$

Further, The jacobian for a spherical volume volume is given by

$$dv = d\rho \cdot \rho d\theta \cdot \rho \sin(\phi) d\phi, \quad (\text{B.3})$$

where the different surface areas can be written as

$$ds_\rho = \rho^2 \sin(\theta) d\theta d\phi \quad (\text{constant } \rho) \quad (\text{B.4})$$

$$ds_\theta = \rho \sin(\theta) d\rho d\phi \quad (\text{constant } \theta) \quad (\text{B.5})$$

$$ds_\phi = \rho d\rho d\theta \quad (\text{constant } \phi). \quad (\text{B.6})$$

The Laplacian equation of the spherical domain is given by

$$\nabla^2 f = \frac{1}{\rho^2} \frac{\partial}{\partial \rho} \left(\rho^2 \frac{\partial f}{\partial \rho} \right) + \frac{1}{\rho^2 \sin(\theta)} \frac{\partial}{\partial \theta} \left(\sin(\theta) \frac{\partial f}{\partial \theta} \right) + \frac{1}{\rho^2 \sin^2(\theta)} \frac{\partial^2 f}{\partial \phi^2} \quad (\text{B.7})$$

Appendix C

Definition of the Cylindrical coordinate system

In the cylindrical coordinate system a radius, ρ , an angle ϕ , and a height z are used to define a point in space. A coordinate system as defined in Fig. C.1 is applied in this thesis.

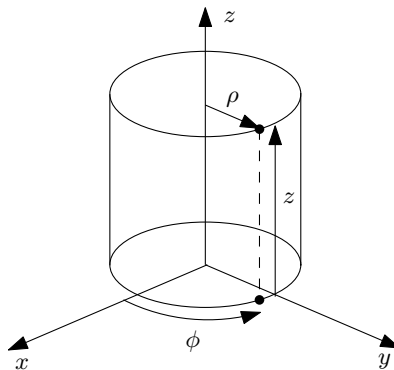


Figure C.1: Definition of the cylindrical coordinate system.

Bibliography

- [1] “DINED 2004 (20-60 years),” June 2011, <http://dined.io.tudelft.nl/en,dined2004>, 304.
- [2] *Maxon Program 2010/2011*. Maxon motor, Sachseln, Switzerland.
- [3] A. Alutei, A. Vaida, D. Mandru, and M. Tatar, “Development of an active upper-limb orthosis,” in *In Proceedings of the International Conference on Advancements of Medicine and Health Care through Technology*, ser. IFMBE Proceedings, vol. 26. Springer Berlin Heidelberg, 2009, pp. 405–408.
- [4] P. Artemiadis and K. Kyriakopoulos, “Emg-based position and force control of a robot arm: Application to teleoperation and orthosis,” in *In Proceedings of the IEEE/ASME international conference on advanced intelligent mechatronics*, Sept. 2007, pp. 1–6.
- [5] K. D. Bachovchin, J. F. Hoburg, and R. F. Post, “Stable levitation of a passive magnetic bearing,” *IEEE Transactions on Magnetics*, vol. 49, no. 1, pp. 609–617, Jan 2013.
- [6] S. Ball, I. Brown, and S. Scott, “Medarm: a rehabilitation robot with 5dof at the shoulder complex,” in *In Proceedings of the IEEE/ASME International conference on Advanced intelligent mechatronics*, Sept. 2007, pp. 1–6.
- [7] N. Benjuya and S. Kenney, “Hybrid arm orthosis,” *Journal of Prosthetics and Orthotics*, vol. 2, no. 2, pp. 155–163, 1990.
- [8] M. Bergamasco, B. Allotta, L. Bosio, L. Ferretti, G. Parrini, G. Prisco, F. Salsedo, and G. Sartini, “An arm exoskeleton system for teleoperation and virtual environments applications,” in *In Proceedings of the International Conference on Robotics and Automation*, vol. 2, may 1994, pp. 1449–1454.
- [9] M. Bergamasco, F. Salsedo, S. Marcheschi, and N. Lucchesi, “A novel actuation module for wearable robots,” in *In Proceedings of the Advances in Robot Kinematics: Motion in Man and Machine*. Springer Netherlands, 2010, pp. 117–125.

- [10] T. L. Brooks, "Telerobotic response requirements," in *International Conference on Systems, Man and Cybernetics*, 1990, pp. 113–120.
- [11] M. Brown, N. Tsagarakis, and D. Caldwell, "Exoskeletons for human force augmentation," *Industrial Robot: An International Journal*, vol. 30, no. 6, pp. 592–602, Jun. 2003.
- [12] D. Caldwell and N. Tsagarakis, "Biomimetic actuators in prosthetic and rehabilitation applications," *Technology and Health Care*, vol. 10, no. 2, pp. 107–120, 2002.
- [13] C. R. Carignan, M. P. Naylor, and S. N. Roderick, "Controlling shoulder impedance in a rehabilitation arm exoskeleton," in *International Conference on Robotics and Automation (ICRA)*, May 2008, pp. 2453–2458.
- [14] D. Case, B. Taheri, and E. Richer, "Design and characterization of a small-scale magnetorheological damper for tremor suppression," *Transactions on Mechatronics (ASME)*, vol. 18, no. 1, pp. 96–103, Feb. 2013.
- [15] D. T. E. H. van Casteren, J. J. H. Paulides, and E. A. Lomonova, "3-d numerical surface charge model including relative permeability : the general theory," *IEEE Transactions on Magnetics*, vol. 50, no. 11, 2014.
- [16] *Flux 12 User's guide*, release 12 ed., Cedrat Corporation, Grenoble, 2016.
- [17] E. Cheney and D. Kincaid, *Numerical Mathematics and Computing*. Cengage Learning, 2007, ISBN: 978-0-495-11475-8.
- [18] W. Chou, T. Wang, and J. Xiao, "Haptic interaction with virtual environment using an arm type exoskeleton device," in *In Proceedings of the International Conference on Robotics and Automation*, vol. 2, 2004, pp. 1992–1997.
- [19] W. Cloud, "Man amplifiers: Machines that let you carry a ton," *Popular Science*, vol. 187, no. 5, pp. 70–73, 1965.
- [20] J. J. Craig, *Introduction to Robotics*. addison-wesley, 2nd ed. 1989, ISBN: 0-13-123629-6.
- [21] C. H. H. M. Custers, T. T. Overboom, J. W. Jansen, and E. A. Lomonova, "2-d semianalytical modeling of eddy currents in segmented structures," *IEEE Transactions on Magnetics*, vol. 51, no. 11, pp. 1–4, Nov 2015.
- [22] K. Davey, G. Vachtsevanos, and R. Powers, "The analysis of fields and torques in spherical induction motors," *IEEE Transactions on Magnetics*, vol. 23, no. 1, pp. 273–282, Jan 1987.
- [23] S. Davis, N. Tsagarakis, J. Canderle, and D. G. Caldwell, "Enhanced modelling and performance in braided pneumatic muscle actuators," *International Journal of Robotics research*, vol. 22, no. 3/4, pp. 213–227, 2003.

- [24] B. Dehez, D. Grenier, and B. Raucent, "Development of a spherical induction motor with two degrees of freedom," *IEEE Transactions on Magnetics*, vol. 42, no. 8, pp. 2077–2089, Aug 2006.
- [25] J. Detriche, "Innovations in dismantling robotics," *Nuclear Engineering and Design*, vol. 182, no. 3, pp. 267–276, 1998.
- [26] M. Ehsani, Y. Gao, and J. Miller, "Hybrid electric vehicles: Architecture and motor drives," *Proceedings of the IEEE*, vol. 95, no. 4, pp. 719–728, April 2007.
- [27] M. Frey, D. Johnson, and J. Hollerbach, "Full-arm haptics in an accessibility task," in *Symposium on Haptic interfaces for virtual environment and teleoperator systems*, 2008, pp. 405–412.
- [28] E. P. Furlani, *Permanent Magnet and Electromechanical Devices*. Rochester, New York: Academic Press, 2001.
- [29] E. Garcia, M. A. Jimenez, P. De Santos, and M. Armada, "The evolution of robotics research," *IEEE Robotics Automation Magazine*, vol. 14, no. 1, pp. 90–103, March 2007.
- [30] J. Gibbs, "Fourier series," *Nature*, vol. 59, no. 200 and 606, 1899.
- [31] A. Gmerek, "The virtual reality system used for upper extremity rehabilitation," in *International Conference on Methods and Models in Automation and Robotics (MMAR)*, Aug. 2012, pp. 312–314.
- [32] R. A. R. C. Gopura and K. Kiguchi, "Mechanical designs of active upper-limb exoskeleton robots: State-of-the-art and design difficulties," in *In Proceedings of the International Conference on Rehabilitation Robotics (ICORR)*, 2009, pp. 178–187.
- [33] R. A. R. C. Gopura, K. Kiguchi, and Y. Li, "Sueful-7: A 7dof upper-limb exoskeleton robot with muscle-model-oriented emg-based control," in *In Proceedings of the International Conference on Intelligent Robots and Systems (IROS)*, Oct. 2009, pp. 1126–1131.
- [34] R. Gopura and K. Kiguchi, "Development of a 6dof exoskeleton robot for human upper-limb motion assist," in *In Proceedings of the International Conference on Information and Automation for Sustainability (ICIAFS)*, Dec. 2008, pp. 13–18.
- [35] D. J. Griffiths, *Introduction to Quantum Mechanics*. Upper Saddle River, New Jersey: Pearson Education, 2005.
- [36] E. Guizzo and H. Goldstein, "The rise of the body bots [robotic exoskeletons]," *IEEE Spectrum*, vol. 42, no. 10, pp. 50–56, Oct. 2005.

- [37] B. L. J. Gysen, "Generalized harmonic modeling technique for 2d electromagnetic problems : applied to the design of a direct-drive active suspension system," Ph.D. dissertation, Technische Universiteit Eindhoven, 2011.
- [38] B. L. J. Gysen, K. J. Meessen, J. J. H. Paulides, and E. A. Lomonova, "General formulation of the electromagnetic field distribution in machines and devices using fourier analysis," *IEEE Transactions on Magnetics*, vol. 46, no. 1, pp. 39–52, Jan. 2010.
- [39] M. Haraguchi, T. Kikuchi, M. Mihara, M. Hatakenaka, I. Miyai, and J. Furusho, "Development of evaluation system of the motor function for upper limbs using 3-d rehabilitation robot "emul" and near-infrared spectroscopy "nirs"," in *In Proceedings of the International Conference on Rehabilitation Robotics (ICORR)*, June 2009, pp. 566–570.
- [40] J. Hartmann, H. Tunnemann, and P. Klovora, *Fitness and Strength Training for All Sports : Theory, Methods, Programs*. Sport Books Publishers, 2000.
- [41] W. Harwin, T. Rahman, and R. Foulds, "A review of design issues in rehabilitation robotics with reference to north american research," *Transactions on Rehabilitation Engineering*, vol. 3, no. 1, pp. 3–13, Mar. 1995.
- [42] Y. Hayashi, R. Dubey, and K. Kiguchi, "Torque optimization for a 7dof upper-limb power-assist exoskeleton robot," in *Workshop on Robotic Intelligence In Informationally Structured Spacecarignan (RiiSS)*, April 2011, pp. 49–54.
- [43] L. Van der Heide, B. van Nihuijs, A. Bergsma, G. Gelderblom, D. van der Pijl, and L. de Witte, "An overview and categorization of dynamic arm supports for people with decreased arm function," *Prosthetics and orthotics international*, vol. 38, no. 4, pp. 287–302, 2014.
- [44] J. R. Hendershot and T. J. E. Miller, *Design of Brushless permanent-magnet machines*. 102 Triano Circle, Venice, Florida 34292, USA: USB by Motor Design Books LLC, 2010, ISBN 978-0-9840687-0-8.
- [45] J. R. Hendershot and T. J. E. Miller, *Design of Brushless permanent-magnet Motors*. Magna Physics Publishing and Clarenon Press, 1994, ISBN: 1-881855-03-1.
- [46] J. L. Herder, N. Vrijlandt, M. Antonides, T. Cloosterman, and M. P. L., "Principle and design of a mobile arm support for people with muscular weakness," *Journal of Rehabilitation Research and Development*, vol. 43, no. 5, pp. 591–604, Sept. 2006.
- [47] S. Ikejiri, K. Hirata, and S. Maeda, "Proposal of electromagnetic spherical actuator with 3-dof," *COMPEL: The International Journal for Computation*

- and Mathematics in Electrical and Electronic Engineering*, vol. 29, no. 4, pp. 994–1003, 2010.
- [48] G. Ivanova, S. Bulavintsev, J.-H. Ryu, and J. Poduraev, “Development of an exoskeleton system for elderly and disabled people,” in *In Proceedings of the International Conference on Information Science and Applications (ICISA)*, April 2011, pp. 1–7.
- [49] A. Jackson, P. Culmer, S. Makower, M. Levesley, R. Richardson, A. Cozens, M. Williams, and B. Bhakta, “Initial patient testing of ipam - a robotic system for stroke rehabilitation,” in *In Proceedings of the International Conference on Rehabilitation Robotics (ICORR)*, June 2007, pp. 250–256.
- [50] J. D. Jackson, *Classical Electrodynamics*. John Wiley & Sons Ltd., 1962, cited on page 35.
- [51] J. W. Jansen, C. M. M. Van Lierop, E. A. Lomonova, and A. J. A. Vandemput, “Magnetically levitated planar actuator with moving magnets,” *Transactions on Industry Applications*, vol. 44, no. 4, pp. 1108–1115, 2008.
- [52] M. Jansen, J. Burgers, M. Jannink, N. van Alfen, and I. J. M. de Groot, “Upper limb training with dynamic arm support in boys with duchenne muscular dystrophy: A feasibility study,” *International Journal of Physical Medicine & Rehabilitation*, vol. 3, no. 256, 2015.
- [53] J. L. G. Janssen, “Extended analytical charge modeling for permanent-magnet based devices : practical application to the interactions in a vibration isolation system,” Ph.D. dissertation, Eindhoven University of Technology, 2011.
- [54] J. L. G. Janssen, J. J. H. Paulides, and E. A. Lomonova, “Passive limitations for a magnetic gravity compensator,” *Journal of system design and Dynamics*, vol. 3, no. 4, pp. 671–680, 2009.
- [55] G. R. Johnson, D. A. Carus, G. Parrini, S. Scattereggia Marchese, and R. Valeggi, “The design of a five-degree-of-freedom powered orthosis for the upper limb,” *In Proceedings of the Institution of Mechanical Engineers, Part H: Journal of Engineering in Medicine*, vol. 215, no. 3, pp. 275–284, 2001.
- [56] K. Kahlen, I. Voss, C. Priebe, and R. W. De Doncker, “Torque control of a spherical machine with variable pole pitch,” *IEEE Transactions on Power Electronics*, vol. 19, no. 6, pp. 1628–1634, Nov. 2004.
- [57] I. A. Kapandji, *The Physiology of the Joints (Upper Extremities)*, 5th ed. Churchill Livingstone, 1982.

- [58] C.-H. Kim, J. Lim, C. Ahn, J. Park, and D. Y. Park, "Control design of passive magnetic levitation tray," in *International Conference on Electrical Machines and Systems (ICEMS)*, Oct 2013, pp. 1978–1980.
- [59] G. Kramer, G. R. B. Romer, and H. J. A. Stuyt, "Design of a dynamic arm support (das) for gravity compensation," in *International Conference on Rehabilitation Robotics (ICORR)*, 2007, pp. 1042–1048.
- [60] H. Krebs, N. Hogan, M. Aisen, and B. Volpe, "Robot-aided neurorehabilitation," *Transactions on Rehabilitation Engineering*, vol. 6, no. 1, pp. 75–87, 1998.
- [61] M. F. J. Kremers, J. J. H. Paulides, E. Ilhan, J. L. G. Janssen, and E. A. Lomonova, "Relative permeability in a 3d analytical surface charge model of permanent magnets," *IEEE Transactions on Magnetics*, vol. 49, no. 5, pp. 2299–2302, May 2013.
- [62] H. Lee, H. Park, S. Won, G. Ryu, and J. Lee, "Improvements of performance of multi-dof spherical motor by double air-gap feature," *Journal of Electrical Engineering & Technology*, vol. 8, no. 1, pp. 90–96, Jan 2013.
- [63] J.-S. Lee, D. kyong Kim, S. whang Baek, S.-H. Rhyu, and B.-I. Kwon, "Newly structured double excited two-degree-of-freedom motor for security camera," *IEEE Transactions on Magnetics*, vol. 44, no. 11, pp. 4041–4044, Nov 2008.
- [64] K.-M. Lee and H. Son, "Distributed multipole model for design of permanent-magnet-based actuators," *IEEE Transactions on Magnetics*, vol. 43, no. 10, pp. 3904–3913, Oct. 2007.
- [65] K.-M. Lee, R. B. Roth, and Z. Zhou, "Dynamic modeling and control of a ball-joint-like variable-reluctance spherical motor," *ASME Journal of Dynamic Systems, Measurement, and Control*, vol. 118, pp. 29–40, 1996.
- [66] K.-M. Lee, K. Bai, and J. Lim, "Dipole models for forward/inverse torque computation of a spherical motor," *IEEE/ASME Transactions on Mechatronics*, vol. 14, no. 1, pp. 46–54, feb. 2009.
- [67] T. Lenzi, N. Vitiello, S. M. M. De Rossi, S. Roccella, F. Vecchi, and M. Carrozza, "Neuroexos: A variable impedance powered elbow exoskeleton," in *In Proceedings of the International Conference on Robotics and Automation (ICRA)*, May 2011, pp. 1419–1426.
- [68] B. Li, G.-D. Li, and H.-F. Li, "Magnetic field analysis of 3-dof permanent magnetic spherical motor using magnetic equivalent circuit method," *IEEE Transactions on Magnetics*, vol. 47, no. 8, pp. 2127–2133, Aug. 2011.

- [69] H. Li, C. Xia, and T. Shi, "Spherical harmonic analysis of a novel halbach array pm spherical motor," in *Robotics and Biomimetics. ROBIO. IEEE International Conference on*, Dec. 2007, pp. 2085–2089.
- [70] Z. Li, W. Jun, D. Min, and Z. Qiang, "Mechanism study for magnetic levitation spherical reluctance driving joint to produce magnetic power and torque," in *International Conference on Consumer Electronics, Communications and Networks (CECNet)*, April 2011, pp. 5046–5049.
- [71] H. S. Lo and S. Q. Xie, "Exoskeleton robots for upper-limb rehabilitation: State of the art and future prospects," *Medical Engineering & Physics*, vol. 34, no. 3, pp. 261–268, 2012.
- [72] R. Loureiro, F. Amirabdollahian, M. Topping, B. Driessen, and W. Harwin, "Upper limb robot mediated stroke therapy - gentle/s approach," *Autonomous Robots*, vol. 15, no. 1, pp. 35–51, 2003.
- [73] R. Loureiro and T. Smith, "Design of the robin system: Whole-arm multi-model sensorimotor environment for the rehabilitation of brain injuries while sitting or standing," in *In Proceedings of the International Conference on Rehabilitation Robotics (ICORR)*, July 2011, pp. 1–6.
- [74] R. Loureiro, W. Harwin, K. Nagai, and M. Johnson, "Advances in upper limb stroke rehabilitation: a technology push," *Medical & Biological Engineering & Computing*, vol. 49, pp. 1103–1118, 2011.
- [75] Y. Mao and S. Agrawal, "Transition from mechanical arm to human arm with carex: A cable driven arm exoskeleton (carex) for neural rehabilitation," in *In Proceedings of the International Conference on Robotics and Automation (ICRA)*, May 2012, pp. 2457–2462.
- [76] L. Marchal-Crespo and D. J. Reinkensmeyer, "Review of control strategies for robotic movement training after neurologic injury," *NeuroEngineering and Rehabilitation*, vol. 6, no. 20, pp. 1–15, 2009.
- [77] F. Martinez, I. Retolaza, A. Pujana-Arrese, A. Cenitagoya, J. Basurko, and J. Landaluze, "Design of a five actuated dof upper limb exoskeleton oriented to workplace help," in *In Proceedings of the International Conference on Biomedical Robotics and Biomechatronics (BioRob)*, Oct. 2008, pp. 169–174.
- [78] B. Mastenbroek, E. de Haan, M. van den Berg, and J. L. Herder, "Development of a mobile arm support (armon): Design evolution and preliminary user experience," in *International Conference on Rehabilitation Robotics (ICORR)*, June 2007, pp. 1114–1120.
- [79] A. Mayr, M. Kofler, and L. Saltuari, "An electromechanical robot for upper limb training following stroke. a prospective randomised controlled pilot study," *Handchir Mikrochir plast Chir*, vol. 40, no. 1, pp. 66–73, Jan. 2008.

- [80] K. J. Meessen, "Electromagnetic fields and interactions in 3d cylindrical structures : modeling and application," Ph.D. dissertation, Eindhoven University of Technology, 2012.
- [81] K. J. Meessen, J. J. H. Paulides, and E. A. Lomonova, "Analysis of a novel magnetization pattern for 2-dof rotary-linear actuators," *IEEE Transactions on Magnetism*, vol. 48, no. 11, pp. 3867–3870, 2012.
- [82] R. Morales, F. Badesa, L. M. Domenech, N. Garcia-Aracil, J. Sabater, M. Menchofn, and E. Fernandez, "Design and control of a rehabilitation robot driven by pneumatic swivel modules," in *In Proceedings of the International Conference on Biomedical Robotics and Biomechatronics (BioRob)*, Sept. 2010, pp. 566–571.
- [83] K. Nagai, I. Nakanishi, H. Hanafusa, S. Kawamura, M. Makikawa, and N. Tejima, "Development of an 8 dof robotic orthosis for assisting human upper limb motion," in *In Proceedings of the International Conference on Robotics and Automation*, vol. 4, May 1998, pp. 3486–3491.
- [84] A. Nakai, T. Ohashi, and H. Hashimoto, "7 dof arm type haptic interface for teleoperation and virtual reality systems," in *In Proceedings of the Intelligent Robots and Systems (IEEE/RSJ)*, vol. 2, Oct 1998, pp. 1266–1271.
- [85] A. Nakai, T. Ohashi, and H. Hashimoto, "7 dof arm type haptic interface for teleoperation and virtual reality systems," in *In Proceedings of the International Conference on Intelligent Robots and Systems*, vol. 2, 1998, pp. 1266–1271.
- [86] T. Nef, M. Mihelj, G. Colombo, and R. Riener, "Armin - robot for rehabilitation of the upper extremities," in *In Proceedings of the International Conference on Robotics and Automation*, 2006, pp. 3152–3157.
- [87] V. L. Nickel, J. R. Kachak, and J. R. Allen, "Electrically powered orthotic systems," *Journal of Bone and Joint Surgery*, vol. 51-A, no. 2, pp. 343–351, 1969.
- [88] B. van Nindhuijs, T. E. Motoasca, and E. A. Lomonova, "Accurate analytical computation of magnetic flux density of spherical permanent magnet arrays," in *XXth International Conference on Electrical Machines (ICEM)*, Sept 2012, pp. 2746–2751.
- [89] B. van Nindhuijs, T. E. Motoasca, D. J. van der Pijl, P. Verstegen, and E. A. Lomonova, "Development of a smart arm support for daily-life activities and entertainment," *Gerontechnology*, vol. 11, no. 2, pp. 226–227, 2012.
- [90] B. van Nindhuijs, L. A. van der Heide, J. W. Jansen, B. L. J. Gysen, D. J. van der Pijl, and E. A. Lomonova, "Overview of actuated arm support systems and their applications," *Actuators*, vol. 2, no. 4, pp. 86–110, 2013.

-
- [91] B. van Nindhuijs, J. W. Jansen, B. L. J. Gysen, and E. A. Lomonova, "Multi-degree-of-freedom spherical permanent-magnet gravity compensator for mobile arm support systems," *IEEE Transactions on Industry Applications*, vol. 50, no. 6, pp. 3628–3636, Nov. 2014.
- [92] B. van Nindhuijs, J. W. Jansen, B. L. J. Gysen, and E. A. Lomonova, "Topology comparison of slotless permanent magnet semispherical actuators," *IEEE Transactions on Magnetics*, vol. 50, no. 11, pp. 1–4, 2014.
- [93] B. van Nindhuijs, B. L. J. Gysen, J. W. Jansen, and E. A. Lomonova, "Gravitation compensation using a spherical magnetic spring," patent 2015/0 137 923, 2015.
- [94] W. Nunes, L. Rodrigues, L. Oliveira, J. Ribeiro, J. Carvalho, and R. S. Goncalves, "Cable-based parallel manipulator for rehabilitation of shoulder and elbow movements," in *In Proceedings of the International Conference on Rehabilitation Robotics (ICORR)*, July 2011, pp. 1–6.
- [95] J. Oblak and Z. Matjajic, "Design of a series visco-elastic actuator for multi-purpose rehabilitation haptic device," *Journal of NeuroEngineering and Rehabilitation*, vol. 8, no. 3, Jan 2011.
- [96] J. Oblak, I. Cikaĵlo, and Z. Matjajic, "Haptic robot for arm and wrist rehabilitation," in *World Congress on Medical Physics and Biomedical Engineering*, ser. IFMBE Proceedings. Springer Berlin Heidelberg, Sept. 2009, vol. 25/9, pp. 20–23.
- [97] B. E. Paden, C. Chen, and O. J. Fiske, "Magnetic spring and actuators with multiple equilibrium positions," United states of America Patent US 7 265 470 B1, 2007.
- [98] F. C. Park and R. W. Brockett, "Kinematic dexterity of robotic mechanisms," *The International Journal of Robotics Research*, vol. 13, no. 1, pp. 1–15, 1994.
- [99] H.-S. Park, Y. Ren, and L.-Q. Zhang, "Intelliarm: An exoskeleton for diagnosis and treatment of patients with neurological impairments," in *In Proceedings of the International Conference on Biomedical Robotics and Biomechanics (BioRob)*, Oct. 2008, pp. 109–114.
- [100] J. Paulides, B. Gysen, K. Meessen, Y. Tang, and E. Lomonova, "Influence of multiple air gaps on the performance of electrical machines with (semi) halbach magnetization," *IEEE Transactions on Magnetics*, vol. 47, no. 10, pp. 2664–2667, Oct 2011.
- [101] J. Perry, J. Rosen, and S. Burns, "Upper-limb powered exoskeleton design," *Transactions on Mechatronics (ASME)*, vol. 12, no. 4, pp. 408–417, Aug. 2007.

- [102] K. J. W. Pluk, J. W. Jansen, and E. A. Lomonova, "3-D hybrid analytical modeling: 3-D fourier modeling combined with mesh-based 3-D magnetic equivalent circuits," *IEEE Transactions on Magnetics*, vol. 51, no. 12, pp. 1–14, Dec. 2015.
- [103] D. Ragonesi, S. Agrawal, W. Sample, and T. Rahman, "Series elastic actuator control of a powered exoskeleton," in *In Proceedings of the International Conference on Engineering in Medicine and Biology Society (EMBC)*, 2011, pp. 3515–3518.
- [104] M. Rahman, T. K-Ouimet, M. Saad, J.-P. Kenne, and P. Archambault, "Nonlinear control of an upper-limb exoskeleton robot," in *In Proceedings of the International Conference on Electronics, Circuits and Systems (ICECS)*, 2011, pp. 772–775.
- [105] H. Rakotoarison, J. Yonnet, and B. Delinchant, "Using coulombian approach for modeling scalar potential and magnetic field of a permanent magnet with radial polarization," *IEEE Transactions on Magnetics*, vol. 43, no. 4, pp. 1261–1264, April 2007.
- [106] D. Reinkensmeyer, P. Lum, and J. Winters, *In Emerging and Accessible Telecommunications, Information and Healthcare Technologies*. Arlington, VA, USA: RESNA Press, 2002, ch. Emerging Technologies for Improving Access to Movement Therapy following Neurologic Injury.
- [107] D. J. Reinkensmeyer, "Robotic assistance for upper extremity training after stroke," *Studies in Health technology informatics*, vol. 145, pp. 25–39, 2009.
- [108] R. Riener, T. Nef, and G. Colombo, "Robot-aided neurorehabilitation of the upper extremities," *Medical and Biological Engineering and Computing*, vol. 43, pp. 2–10, 2005.
- [109] W. Robertson, B. Cazzolato, and A. Zander, "A multipole array magnetic spring," *IEEE Transactions on Magnetics*, vol. 41, no. 10, pp. 3826–3828, Oct 2005.
- [110] E. Rocon, J. Belda-Lois, A. Ruiz, M. Manto, J. Moreno, and J. Pons, "Design and validation of a rehabilitation robotic exoskeleton for tremor assessment and suppression," *Transactions on Neural Systems and Rehabilitation Engineering*, vol. 15, no. 3, pp. 367–378, Sept. 2007.
- [111] G. Rosati, P. Gallina, and S. Masiero, "Design, implementation and clinical tests of a wire-based robot for neurorehabilitation," *Transactions on Neural Systems and Rehabilitation Engineering*, vol. 15, no. 4, pp. 560–569, Dec. 2007.

- [112] L. Rossini, O. Chetelat, E. Onillon, and Y. Perriard, "Force and torque analytical models of a reaction sphere actuator based on spherical harmonic rotation and decomposition," *IEEE/ASME Transactions on Mechatronics*, vol. 18, no. 3, pp. 1006–1018, June 2013.
- [113] J. M. M. Rovers, J. W. Jansen, and E. A. Lomonova, "Multiphysical analysis of moving-magnet planar motor topologies," *IEEE Transactions on Magnetics*, vol. 49, no. 12, pp. 5730–5741, Dec 2013.
- [114] J. M. M. Rovers, J. W. Jansen, and E. A. Lomonova, "Modeling of relative permeability of permanent magnet material using magnetic surface charges," *IEEE Transactions on Magnetics*, vol. 49, no. 6, pp. 2913–2919, June 2013.
- [115] A. Ruiz, A. Forner-Cordero, E. Rocon, and J. L. Pons, "Exoskeletons for rehabilitation and motor control," in *In Proceedings of the International Conference on Biomedical Robotics and Biomechanics (BioRob)*, Feb. 2006, pp. 601–606.
- [116] A. Schiele and G. Hirzinger, "A new generation of ergonomic exoskeletons - the high-performance x-arm-2 for space robotics telepresence," in *In the proceedings of the international Conference on Intelligent Robots and Systems*, Sept. 2011, pp. 2158–2165, iROS.
- [117] M. Seki, Y. Matsumoto, H. Iijima, T. Ando, Y. Kobayashi, M. Fujie, and M. Nagaoka, "Development of robotic upper limb orthosis with tremor suppressibility and elbow joint movability," in *In Proceedings of the International Conference on Systems, Man, and Cybernetics (SMC)*, Oct. 2011, pp. 729–735.
- [118] P. van der Smagt, M. Grebenstein, H. Urbanek, N. Fligge, M. Strohmayer, G. Stillfried, J. Parrish, and A. Gustus, "Robotics of human movements," *Journal of Physiology-Paris*, vol. 103, no. 3-5, pp. 119–132, 2009.
- [119] J. P. C. Smeets, "Contactless transfer of energy: 3d modeling and design of a position-independent inductive coupling integrated in a planar motor," Ph.D. dissertation, Eindhoven University of Technology, 2015.
- [120] J. P. C. Smeets, T. T. Overboom, J. W. Jansen, and E. A. Lomonova, "Three-dimensional analytical modeling technique of electromagnetic fields of air-cored coils surrounded by different ferromagnetic boundaries," *IEEE Transactions on Magnetics*, vol. 49, no. 12, pp. 5698–5708, Dec 2013.
- [121] A. H. A. Stienen, E. E. G. Hekman, A. C. Schouten, F. C. T. van der Helm, and van der Kooij h., "Suitability of hydraulic disk brakes for passive actuation of upper-extremity rehabilitation exoskeleton," *Applied Bionics and Biomechanics*, vol. 6, no. 2, 2009.

- [122] A. H. A. Stienen, E. E. G. Hekman, H. ter Braak, A. M. M. Aalsma, F. C. T. Van der Helm, and H. van der Kooij, "Design of a rotational hydroelastic actuator for a powered exoskeleton for upper limb rehabilitation," *Transactions on Biomedical Engineering*, vol. 57, no. 3, pp. 728–735, March 2010.
- [123] A. H. A. Stienen, J. McPherson, A. Schouten, and J. P. A. Dewald, "The act-4d: A novel rehabilitation robot for the quantification of upper limb motor impairments following brain injury," in *In Proceedings of the International Conference on Rehabilitation Robotics (ICORR)*, July 2011, pp. 1–6.
- [124] T. Sugar, J. He, E. Koeneman, J. Koeneman, R. Herman, H. Huang, R. Schultz, D. Herring, J. Wanberg, S. Balasubramanian, P. Swenson, and J. Ward, "Design and control of rupert: A device for robotic upper extremity repetitive therapy," *IEEE Transactions on Neural Systems and Rehabilitation Engineering*, vol. 15, no. 3, pp. 336–346, Sept. 2007.
- [125] A. Toth, G. Fazekas, G. Arz, M. Jurak, and M. Horvath, "Passive robotic movement therapy of the spastic hemiparetic arm with REHAROB: report of the first clinical test and the follow-up system improvement," in *In Proceedings of the International Conference on Rehabilitation Robotics (ICORR)*, 2005, pp. 127–130.
- [126] N. G. Tsagarakis and D. G. Caldwell, "Development and control of a soft-actuated exoskeleton for use in physiotherapy and training," *Autonomous Robots*, vol. 15, no. 1, pp. 21–33, July 2003.
- [127] A. Umemura, Y. Saito, and K. Fujisaki, "A study on power-assisted rehabilitation robot arms operated by patient with upper limb disabilities," in *In Proceedings of the IEEE International Conference on Rehabilitation Robotics (ICORR)*, June 2009, pp. 451–456.
- [128] Y. Umetani, Y. Yamada, T. Morizono, T. Yoshida, and S. Aoki, "'skil mate' wearable exoskeleton robot," in *In Proceedings of the International Conference on Systems, Man, and Cybernetics (SMC)*, vol. 4, 1999, pp. 984–988.
- [129] VacuumSchmelze, "Rare earth permanent magnets, vacodym - vacomax," Hanau, Germany, 2007.
- [130] I. Vanderniepen, R. Van Ham, M. Van Damme, and D. Lefeber, "Design of a powered elbow orthosis for orthopaedic rehabilitation using compliant actuation," in *In Proceedings of the International Conference on Biomedical Robotics and Biomechatronics (BioRob)*, 2008, pp. 801–806.
- [131] L. Visser, R. Carloni, and S. Stramigioli, "Energy-efficient variable stiffness actuators," *IEEE Transactions on Robotics*, vol. 27, no. 5, pp. 865–875, Oct. 2011.

- [132] Q. Wang, Z. Li, Y. Ni, and K. Xia, "3D magnetic field analysis and torque calculation of a PM spherical motor," in *Proceedings of the Eighth International Conference on Electrical Machines and Systems (ICEMS)*, vol. 3, Sept. 2005, pp. 2116–2120.
- [133] W. Wang, J. Wang, G. W. Jewell, and D. Howe, "Design and control of a novel spherical permanent magnet actuator with three degrees of freedom," *IEEE/ASME Transactions on Mechatronics*, vol. 8, no. 4, pp. 457–468, Dec. 2003.
- [134] E. Wolbrecht, J. Leavitt, D. Reinkensmeyer, and J. Bobrow, "Control of a pneumatic orthosis for upper extremity stroke rehabilitation," in *In Proceedings of the International Conference of Engineering in Medicine and Biology Society*, Sept. 2006, pp. 2687–2693.
- [135] C. K. Wong, K. Jordan, and M. King, "Robotic arm skate for stroke rehabilitation," in *In Proceedings of the International Conference on Rehabilitation Robotics (ICORR)*, July 2011, pp. 1–6.
- [136] H. Woodson and J. Melcher, *Electromechanical dynamics, Part II: Field, Forces, and Motion*. New York, NY, USA: John Wiley & Sons, Inc., 1968.
- [137] Y. Xiong, C. Xiong, X. Jiang, R. Sun, X. Huang, and Y. Xiong, "Control methods for exoskeleton rehabilitation robot driven with pneumatic muscles," *Industrial Robot: An International Journal*, vol. 36, no. 3, pp. 210–220, 2009.
- [138] L. Yan, I. M. Chen, C. Lim, G. Yang, and K. M. Lee, "Empirical formulation of torque output for spherical actuators with low-cost rotor poles," in *IEEE/ASME International Conference on Advanced Intelligent Mechatronics (AIM)*, July 2009, pp. 1625–1630.
- [139] L. Yan, I.-M. Chen, G. Yang, and K.-M. Lee, "Analytical and experimental investigation on the magnetic field and torque of a permanent magnet spherical actuator," *Transactions on Mechatronics (ASME)*, vol. 11, no. 4, pp. 409–419, Aug. 2006.
- [140] T. Yano, "Proposal of a truncatedoctahedron-dodecahedron based spherical stepping motor," in *XIX International Conference on Electrical Machines (ICEM)*, Sept. 2010, pp. 1–6.
- [141] R. Zanis, E. Motoasca, and E. Lomonova, "Trade-offs in the implementation of rigid and intrinsically compliant actuators in biorobotic applications," in *International Conference on Biomedical Robotics and Biomechanics (BioRob)*, 2012, pp. 100–105.

- [142] H. Zhang, B. Kou, Y. Jin, H. Zhang, and L. Zhang, "Research on a low stiffness passive magnetic levitation gravity compensation system with opposite stiffness cancellation," *IEEE transaction on magnetics*, vol. 50, no. 11, Nov. 2014.

Acknowledgements

Het geeft een heerlijk gevoel om toegekomen te zijn aan het schrijven van mijn dankwoord. Hiermee is er dan toch een einde gekomen aan jaren van hard werk en toewijding. Het was tot op het laatste moment een innoverende ervaring en met trots kijk ik terug op wat we allemaal bereikt hebben.

Allereerst wil ik Elena bedanken voor de kans die ze me gegeven heeft. Tijdens mijn studie heb ik me altijd voorgehouden om de industriële wereld op te zoeken nadat ik klaar was op de universiteit. Dit veranderde na mijn buitenlandse stage waar mijn interesse voor onderzoek is gewekt. Deze interesse heeft door Elena's vertrouwen mogen uitgroeien tot een promotietraject. Ik heb dan ook geen spijt van mijn jaren als promovendus en heb ik een aantal mooie en uitdagende jaren mogen doormaken.

Mijn copromotoren Helm en Bart wil ik graag bedanken voor al hun input en het zogenaamde duwtje in de juiste richting. Bart, zonder jou was ik waarschijnlijk nog steeds bezig geweest (het maakt niet uit wanneer je deze tekst leest). Ook je hulp bij de realisatie van het prototype heeft het van een concept naar werkelijkheid gebracht. Helm, de vele discussies met jou hebben mij altijd erg geholpen in het onderzoek. Ik kon dan ook met alle vragen bij jou terecht en het was zeldzaam als je geen antwoord kon geven. Dit geldt ook voor zaken die niet gerelateerd zijn aan dit boekje. Zonder jouw expertise was ik zeker niet zo ver gekomen. Ik heb misschien op het laatste stukje nogal wat gemopperd, maar dit heeft je nooit weerhouden om me te helpen. Misschien heeft het je juist aangemoedigd bij de reviews van dit boekje. Desalniettemin het werd er altijd beter op na jouw feedback. Bedankt!

Furthermore, I would like to thank my committee members Prof.dr. Stramagioli, Prof.dr Ito, Prof.dr. Bouten and dr. Dehez for willing to spend time to read my thesis. Despite the busy times, you provided me with valuable feedback. In addition, I would like to thank you for taking the time to travel to Eindhoven for my defense.

Ik wil graag alle McArm project partners bedanken voor hun directe en indirecte hulp. Zeker mijn medepromovendus, Loek, die ik vanaf het eerste uur ken. De discussies met jou hebben mij altijd geholpen om het project in het juiste kader te zetten. Verder wil ik graag de mensen bij Focal Meditech B.V. bedanken. Paul en Paul, zonder jullie hulp was dit resultaat nooit gekomen tot wat het nu is. Ook het maken van het prototype was zonder jullie niet gelukt. Dick, als ik vragen had van medische aard kon ik altijd bij jou terecht. Voor de problemen van mechanische aard ben ik altijd goed geholpen door Erik en gelukkig was Ralf ook altijd bereid om even mee te denken. Een speciaal woordje van dank voor Eric en Leo voor het maken van alle onderdelen van mijn prototype. Dankzij hun inzet hebben we nog mooie metingen mogen toevoegen in dit boekje.

Promoveren in de EPE groep is een hele beleving waarin je altijd kan rekenen op hulp van je collega's. Een speciaal woord van dank voor mijn kamergenoten. Johan en Timo, bij jullie kon ik altijd terecht met vragen over de ongeschreven "protocollen" in onze groep zelfs toen jullie druk bezig waren jullie eigen promotie. Kevin en Dave die nooit te beroerd waren om me even te vertellen waar het allemaal fout ging. Niet te vergeten de rest, Esin, Reyhan, Marko, Sultan en Maarten, waarmee ik een hoop technische en niet-technische gerelateerde conversaties mee heb mogen voeren. Nancy, ook jij hebt me enorm geholpen met heel veel administratieve zaken en hebt me daarmee veel werk uit handen genomen. Verder wil ik ook onze labtechnici Marijn en Rutger bedanken. Marijn, jouw hulp en wijze raad zijn me altijd goed van pas gekomen in het lab en Rutger misschien af en toe wat minder wijze raad, maar zeker niet minder behulpzaam.

Tech United wil ik graag bedanken voor alle mooie toernooien die ik heb mogen meemaken. Het zijn een aantal hele mooie herinneringen geworden voor mij. Het is ongelofelijk wat de voetbaltechniek van onze robots is gegroeid in de jaren dat ik heb mogen meedraaien.

De drumbandrepetitie op de woensdagavond brak de week ook altijd mooi in twee. Als Limburgse kampioenen hebben we de repetities natuurlijk niet meer nodig, maar ach, anders heeft Leon niets meer te doen op woensdagavond. De laatste tijd was ik misschien meer afwezig dan aanwezig, maar dat gaat bij deze zeker verandering in komen. Zeker het gezellige stuk na de repetitie was altijd een mooi moment om de wereldproblemen eens te analyseren. Hiervoor wil ik graag een woord van dank uiten voor mijn medeslagwerkgroep/drumbandleden, Ton, Ruud, Guido, Wouter, Gerrit, Frans en Christel die ook nooit te beroerd waren om mijn geklaag aan te horen. Natuurlijk mag ik mijn medeslagwerker Ard niet vergeten die me enorm geholpen heeft met het cover design.

Buiten de verenigingen zijn natuurlijk ook de "Bearkes" Kevin, Ralph, Roel, Stefan en Tom (en niet te vergeten de aanhang) belangrijk geweest in het stukje ontspanning na werktijd. Meestal was er wel iemand te vinden om zo nu en dan iets mee te gaan drinken. Ook de diverse concerten die we bezochten waren altijd een succes.

Mijn familie, Thijs en Lieke, Carlien en Freek, Jurre, Levi, Cas, Mexie en al de rest die nog mag volgen, het is altijd gezellig als we bij elkaar komen. Het waren dan ook altijd mijn lieve neefjes en nichtje die me weer met beide voeten op de grond zetten. De spontane etentjes in het restaurant "op de Baarloseweg" zijn altijd een heerlijk moment om elkaar weer te zien. Een speciaal woord van dank voor mijn ouders, want zonder jullie steun, vertrouwen en aanmoediging was ik nooit tot dit punt gekomen. Ik had nooit durven dromen dat me dit ooit zou lukken en daarvoor ben ik jullie eeuwig dankbaar.

Natuurlijk mag ik mijn liefste Caro niet vergeten, want zonder jouw onvoorwaardelijke steun was dit boekje me zeker niet gelukt. Je hebt mijn leven dragelijk gemaakt als het weer eens tegenzat tijdens mijn promotie. Door jou kreeg ik iedere keer weer de energie en moed om door te gaan en het af te maken, zeker de laatste loodjes waren zwaar.

Bob van Nindhuijs, 3 mei 2016

Curriculum Vitae

Bob van Nindhuijs was born on 28th of October 1986 in Helden, the Netherlands. In 2011, he received his M.Sc. degree in Electrical Engineering at the Eindhoven University of Technology. In 2010, he was a trainee at the Austrian Institute of Technology, Vienna, Austria, where he did research on the losses which occur in the permanent magnets of synchronous machines. He conducted his Master thesis in the Electromechanics and Power Electronics group (EPE) at Eindhoven University of Technology, starting in December 2010. This work was carried out in cooperation with Focal Meditech B.V. on the topic of "Feasibility study of a spherical actuator in an arm support". Since September 2011, he has joined the Electromechanics and Power Electronics group (EPE) at the Eindhoven University of Technology as a Ph.D. candidate, where he has performed research on a spherical actuator with an integrated magnetic gravity compensator for arm support systems. In April 2015 he received a grant from the Swedish Promobilia foundation to accomplish a spherical actuator with integrated gravity compensator prototype. Since 2013, he has been a member of the Tech United Mid-size league Robocup team and became world champion in 2014.